CMS Physics Technical Design Report: Addendum on High Density QCD with Heavy Ions

D. d'Enterria, M. Ballintijn, M. Bedjidian, D. Hofman, O. Kodolova, C. Loizides, I. P Lokthin, C. Lourenço, C. Mironov, S. V Petrushanko, et al.

LABORATOIRE EUROPÉEN POUR LA PHYSIQUE DES PARTICULES
CERN EUROPEAN LABORATORY FOR PARTICLE PHYSICS

CERN/LHCC 2007-009
CMS TDR 8.2-Add1
5 March 2007

CMS

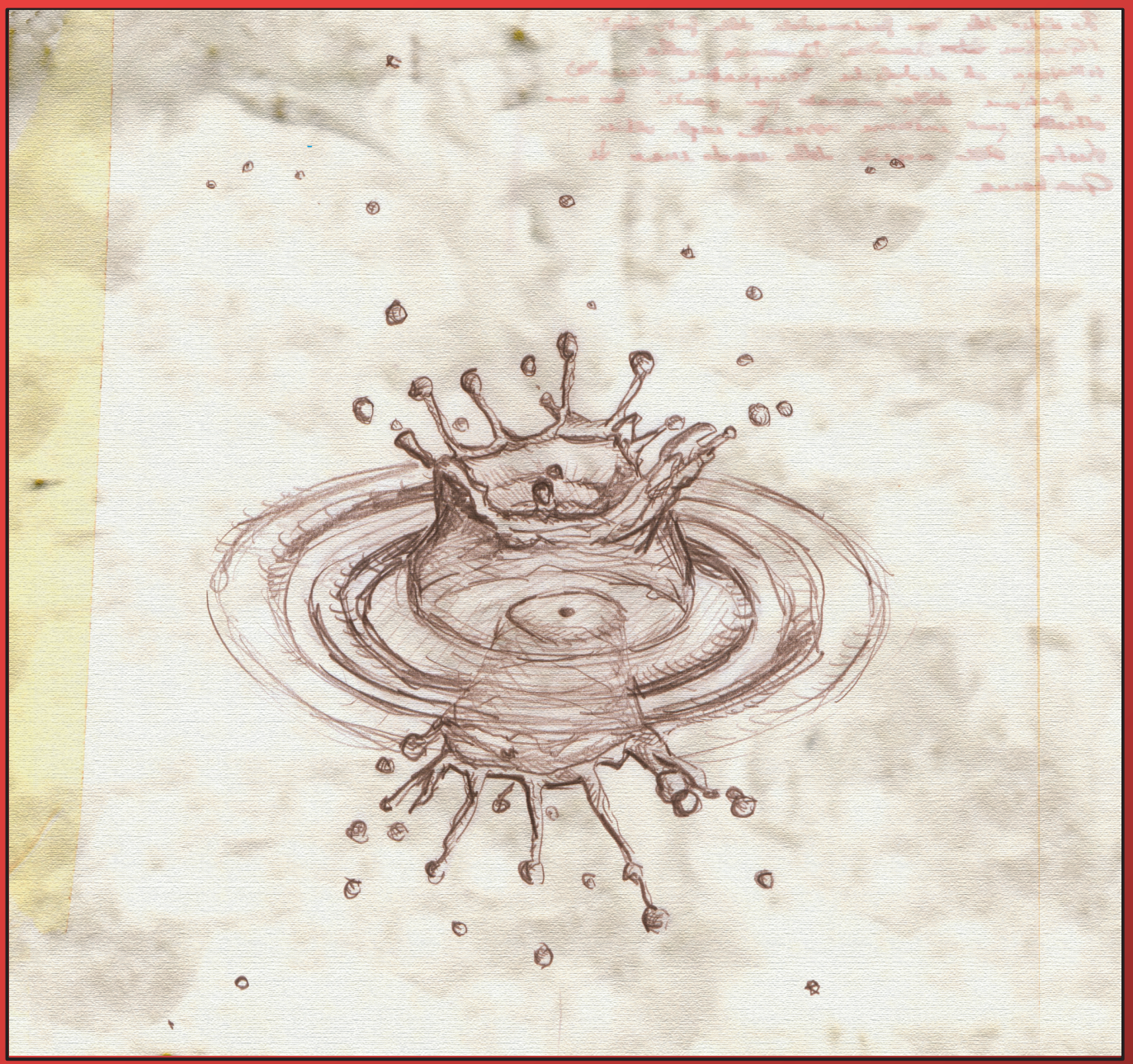

High Density QCD with Heavy Ions

Physics Technical Design Report, Addendum 1

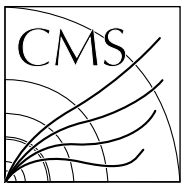

CERN/LHCC 2007-009
CMS TDR 8.2-Add1
5 March 2007

CMS

Physics Technical Design Report

Addendum on

High Density QCD with Heavy Ions

CMS Software and Physics, Reconstruction and Selection (PRS) Projects		
CMS Spokesperson	Tejinder Virdee, Imperial College London, CERN	Tejinder.Virdee@cern.ch
CMS Technical Coordinator	Austin Ball, CERN	Austin.Ball@cern.ch
CMS Collaboration Board Chair	Lorenzo Foa, Pisa	Lorenzo.Foa@cern.ch
CPT Project Manager	Paraskevas Sphicas, CERN and Athens	Paraskevas.Sphicas@cern.ch
CMS Heavy-Ions Coordinators	Bolek Wyslouch, MIT	Bolek.Wyslouch@cern.ch
	David d'Enterria, CERN	David.d'Enterria@cern.ch

Editor

D. d'Enterria

Chapter Editors

M. Ballintijn, M. Bedjidian, D. d'Enterria, D. Hoffman, O. Kodolova, C. Loizides, I. P. Lokthin, C. Lourenço, C. Mironov, S. V. Petrushanko, C. Roland, G. Roland, F. Sikler, G. Veres

Cover Design

S. Cittolin

Acknowledgments

We acknowledge fruitful contributions from the following colleagues: O. Barannikova, V. Korotikh, G.J. Kunde, I. Park and J. Snyder.

For their constructive comments and guidance, we would like to thank the internal reviewers Daniel Denegri and Klaus Rabbertz, as well as Joe Kapusta for an "external" reading of the full document.

For their patience in meeting sometimes impossible demands, we wish to thank the CMS Secretariat: K. Aspola, M. Azeglio, N. Bogolioubova, D. Denise, D. Hudson, G. Martin, and M.C. Pelloux.

We also would like to thank G. Alverson and L. Taylor for their invaluable technical assistance in the preparation of this manuscript.

Finally, we wish to thank the CMS management for their strong support and encouragement.

ISBN 978-92-9083-289-8

Also available at: `http://cmsdoc.cern.ch/cms/cpt/tdr/`

CMS Collaboration

Yerevan Physics Institute, Yerevan, ARMENIA
S. Chatrchyan, G. Hmayakyan, A.M. Sirunyan

Institut für Hochenergiephysik der OeAW, Wien, AUSTRIA
W. Adam, T. Bergauer, M. Dragicevic, J. Erö, M. Friedl, R. Fruehwirth, V. Ghete, P. Glaser, J. Hrubec, M. Jeitler, M. Krammer, I. Magrans, I. Mikulec, T. Noebauer, M. Pernicka, H. Rohringer, J. Strauss, A. Taurok, W. Waltenberger, G. Walzel, E. Widl, C.-E. Wulz

National Centre for Particle and High Energy Physics, Minsk, BELARUS
V. Chekhovsky, O. Dvornikov, I. Emeliantchik, A. Litomin, I. Marfin, V. Mossolov, N. Shumeiko, A. Solin, R. Stefanovitch, J. Suarez Gonzalez, A. Tikhonov

Research Institute for Nuclear Problems, Minsk, BELARUS
A. Fedorov, M. Korzhik, O. Missevitch, R. Zuyeuski

Vrije Universiteit Brussel, Brussel, BELGIUM
J. D'Hondt, S. De Weirdt, R. Goorens, J. Heyninck, S. Lowette, S. Tavernier, W. Van Doninck[**1], L. Van Lancker

Université Libre de Bruxelles, Bruxelles, BELGIUM
O. Bouhali, B. Clerbaux, G. De Lentdecker, J.P. Dewulf, T. Mahmoud, P.E. Marage, S. Rugovac, V. Sundararajan, C. Vander Velde, P. Vanlaer, J. Wickens

Université Catholique de Louvain, Louvain-la-Neuve, BELGIUM
S. Assouak, J.L. Bonnet, G. Bruno, J. Caudron, B. De Callatay, J. De Favereau De Jeneret, S. De Visscher, P. Demin, D. Favart, E. Feltrin, E. Forton, A. Giammanco, G. Grégoire, S. Kalinin, D. Kcira, T. Keutgen, V. Lemaitre, Y. Liu, F. Maltoni, D. Michotte, O. Militaru, A. Ninane, S. Ovyn, T. Pierzchala, K. Piotrzkowski, V. Roberfroid, X. Rouby, O. Van der Aa

Université de Mons-Hainaut, Mons, BELGIUM
E. Daubie, P. Herquet

Universiteit Antwerpen, Wilrijk, BELGIUM
W. Beaumont, M. Cardaci, E. De Langhe, E.A. De Wolf, L. Rurua, P. Van Mechelen

Centro Brasileiro de Pesquisas Fisicas, Rio de Janeiro, BRAZIL
G. Alves, M.H.G. Souza, M.E. Pol

Instituto de Fisica - Universidade Federal do Rio de Janeiro, Rio de Janeiro, BRAZIL
M. Vaz

Universidade do Estado do Rio de Janeiro, Rio de Janeiro, BRAZIL
D.R. Da Silva Di Calafiori, D. Meirelles Martinho, V. Oguri, A. Santoro, A. Sznajder, A. Vilela Pereira

Instituto de Fisica Teorica-Universidade Estadual Paulista, Sao Paulo, BRAZIL
E.M. Gregores, S.F. Novaes

Institute for Nuclear Research and Nuclear Energy, Sofia, BULGARIA
T. Anguelov, G. Antchev, I. Atanasov, J. Damgov, N. Darmenov[**1], L. Dimitrov, V. Genchev[**1], P. Iaydjiev, B. Panev, S. Piperov, S. Stoykova, G. Sultanov, I. Vankov

University of Sofia, Sofia, BULGARIA
A. Dimitrov, V. Kozhuharov, L. Litov, M. Makariev, A. Marinov, E. Marinova, S. Markov, M. Mateev, B. Pavlov, P. Petkov, C. Sabev, Z. Toteva[**1], V. Verguilov

Institute of High Energy Physics, Beijing, CHINA
J. Bai, G.M. Chen, H.S. Chen, Y.N. Guo, K.L. He, C.H. Jiang, Z.J. Ke, B. Li, J. Li, W.G. Li, H.M. Liu, G. Qin, J.F. Qiu, X.Y. Shen, G. Sun, H.S. Sun, C. Teng, Y.Y. Wang, Z. Xue, X. Yue, S.Q. Zhang, Y. Zhang, W.R. Zhao, G.Y. Zhu, H.L. Zhuang

Peking University, Beijing, CHINA
Y. Ban, J. Cai, S. Liu, S.J. Qian, Z.C. Yang, Y.L. Ye, J. Ying

University for Science and Technology of China, Hefei, Anhui, CHINA
J. Wu, Z.P. Zhang

Universidad de Los Andes, Bogota, COLOMBIA
C.A. Carrillo Montoya

Technical University of Split, Split, CROATIA
N. Godinovic, I. Puljak, I. Soric

University of Split, Split, CROATIA
Z. Antunovic, M. Dzelalija, K. Marasovic

Institute Rudjer Boskovic, Zagreb, CROATIA
V. Brigljevic, K. Kadija, S. Morovic, M. Planinic[**2]

University of Cyprus, Nicosia, CYPRUS
C. Nicolaou, A. Papadakis, F. Ptochos, P.A. Razis, D. Tsiakkouri

National Institute of Chemical Physics and Biophysics, Tallinn, ESTONIA
A. Hektor, M. Kadastik, K. Kannike, E. Lippmaa, M. Müntel, M. Raidal

Laboratory of Advanced Energy Systems, Helsinki University of Technology, Espoo, FINLAND
P.A. Aarnio

Helsinki Institute of Physics, Helsinki, FINLAND
S. Czellar, A. Heikkinen, J. Härkönen, V. Karimäki, R. Kinnunen, T. Lampén, K. Lassila-Perini, S. Lehti, T. Lindén, P.R. Luukka, S. Michal[**1], T. Mäenpää, J. Nystén, E. Tuominen, J. Tuominiemi, L. Wendland

Lappeenranta University of Technology, Lappeenranta, FINLAND
G. Polese, T. Tuuva

Laboratoire d'Annecy-le-Vieux de Physique des Particules, IN2P3-CNRS, Annecy-le-Vieux, FRANCE
J.P. Guillaud, P. Nedelec, D. Sillou

DSM/DAPNIA, CEA/Saclay, Gif-sur-Yvette, FRANCE
M. Anfreville, E. Bougamont, P. Bredy, R. Chipaux, M. Dejardin, D. Denegri, J. Descamps, B. Fabbro, J.L. Faure, S. Ganjour, F.X. Gentit, A. Givernaud, P. Gras, G. Hamel de Monchenault, P. Jarry, F. Kircher, M.C. Lemaire, B. Levesy[**1], E. Locci, J.P. Lottin, I. Mandjavidze, M. Mur, E. Pasquetto, A. Payn, J. Rander, J.M. Reymond, F. Rondeaux, A. Rosowsky, J.Y.A. Rousse, Z.H. Sun, P. Verrecchia

Laboratoire Leprince-Ringuet, Ecole Polytechnique, IN2P3-CNRS, Palaiseau, FRANCE
S. Baffioni, M. Bercher, C. Bernet, U. Berthon, S. Bimbot, J. Bourotte, P. Busson, M. Cerutti, D. Chamont, C. Charlot, C. Collard, D. Decotigny, L. Dobrzynski, A.M. Gaillac, Y. Geerebaert, J. Gilly, M. Haguenauer, A. Karar, A. Mathieu, G. Milleret, P. Miné, P. Paganini, T. Romanteau, I. Semeniouk, Y. Sirois

Institut Pluridisciplinaire Hubert Curien, IN2P3-CNRS - ULP, UHA Mulhouse, Strasbourg,

FRANCE
J.L. Agram, J. Andrea, J.D. Berst, D. Bloch, J.M. Brom, F. Didierjean, F. Drouhin[**1], J.C. Fontaine[**3], U. Goerlach[**4], P. Graehling, L. Gross[**1], L. Houchu, P. Juillot, A. Lounis[**4], C. Maazouzi, D. Mangeol, C. Olivetto, T. Todorov, P. Van Hove, D. Vintache

Institut de Physique Nucléaire, IN2P3-CNRS, Université Claude Bernard Lyon 1, Villeurbanne, FRANCE
M. Ageron, G. Baulieu, M. Bedjidian, J. Blaha, A. Bonnevaux, G. Boudoul[**1], E. Chabanat, E.C. Chabert, C. Combaret, D. Contardo[**1], R. Della Negra, P. Depasse, T. Dupasquier, H. El Mamouni, N. Estre, J. Fay, S. Gascon, N. Giraud, C. Girerd, R. Haroutunian, J.C. Ianigro, B. Ille, M. Lethuillier, N. Lumb[**1], H. Mathez, G. Maurelli, S. Perries, O. Ravat, P. Verdier

Institute of Physics Academy of Science, Tbilisi, GEORGIA
V. Roinishvili

RWTH, I. Physikalisches Institut, Aachen, GERMANY
R. Adolphi, R. Brauer, W. Braunschweig, H. Esser, L. Feld, W. Karpinski, K. Klein, C. Kukulies, J. Olzem, A. Ostapchuk, D. Pandoulas, G. Pierschel, F. Raupach, S. Schael, G. Schwering, M. Thomas, M. Weber, B. Wittmer, M. Wlochal

RWTH, III. Physikalisches Institut A, Aachen, GERMANY
A. Adolf, P. Biallass, M. Bontenackels, M. Erdmann, H. Fesefeldt, T. Hebbeker, G. Hilgers, K. Hoepfner[**1], C. Hof, S. Kappler, M. Kirsch, P. Kreuzer, D. Lanske, B. Philipps, H. Reithler, M. Sowa, H. Szczesny, D. Teyssier, O. Tsigenov

RWTH, III. Physikalisches Institut B, Aachen, GERMANY
F. Beissel, M. Davids, M. Duda, G. Flügge, T. Franke, M. Giffels, T. Hermanns, D. Heydhausen, S. Kasselmann, G. Kaussen, T. Kress, A. Linn, A. Nowack, M. Poettgens, O. Pooth, A. Stahl, D. Tornier, M.H. Zoeller

Deutsches Elektronen-Synchrotron, Hamburg, GERMANY
A. Flossdorf, B. Hegner, J. Mnich, C. Rosemann

University of Hamburg, Hamburg, GERMANY
F. Bechtel, E. Butz, G. Flucke, U. Holm, R. Klanner, U. Pein, N. Schirm, P. Schleper, G. Steinbrück, M. Stoye, R. Van Staa, K. Wick

Institut für Experimentelle Kernphysik, Karlsruhe, GERMANY
P. Blüm, V. Buege, A. Cakir[**5], W. De Boer, G. Dirkes, M. Fahrer, M. Feindt, U. Felzmann, M. Frey, A. Furgeri, F. Hartmann[**1], S. Heier, C. Jung, B. Ledermann, Th. Müller, M. Niegel, A. Oehler, T. Ortega Gomez, C. Piasecki, G. Quast, K. Rabbertz, A. Sabellek, C. Saout, A. Scheurer, D. Schieferdecker, F.P. Schilling, A. Schmidt, H.J. Simonis, A. Theel, A. Vest, W. Wagner, M. Weber, C. Weiser, J. Weng[**1], V. Zhukov[**6]

Institute of Nuclear Physics "Demokritos", Aghia Paraskevi, GREECE
G. Anagnostou, M. Barone, T. Geralis, K. Karafasoulis, A. Koimas, A. Kyriakis, S. Kyriazopoulou, D. Loukas, A. Markou, C. Markou, C. Mavrommatis, K. Theofilatos, G. Vermisoglou, A. Zachariadou

University of Athens, Athens, GREECE
G. Karapostoli[**1], P. Katsas, M. Lebeau, A. Panagiotou, C. Papadimitropoulos

University of Ioánnina, Ioánnina, GREECE
I. Evangelou, P. Kokkas, N. Manthos, I. Papadopoulos, F.A. Triantis

KFKI Research Institute for Particle and Nuclear Physics, Budapest, HUNGARY
G. Bencze[**1], L. Boldizsar, G. Debreczeni, C. Hajdu[**1], D. Horvath[**7], K. Krajczar, A. Laszlo, G. Odor, G. Patay, F. Sikler, N. Toth, G. Vesztergombi, P. Zalan

Institute of Nuclear Research ATOMKI, Debrecen, HUNGARY
J. Molnar

University of Debrecen, Debrecen, HUNGARY
N. Beni, A. Kapusi, G. Marian, P. Raics, Z. Szabo, Z. Szillasi, G. Zilizi

Panjab University, Chandigarh, INDIA
H.S. Bawa, S.B. Beri, V. Bhandari, V. Bhatnagar, P. Jindal, M. Kaur, R. Kaur, J.M. Kohli, A. Kumar, J.B. Singh

University of Delhi, Delhi, INDIA
S. Bhattacharya[**8], S. Chatterji, S. Chauhan, B.C. Choudhary, P. Gupta, M. Jha, K. Ranjan, R.K. Shivpuri, A.K. Srivastava

Bhabha Atomic Research Centre, Mumbai, INDIA
S. Borkar, R.K. Choudhury, V. Datar, M. Dixit, D. Dutta, M. Ghodgaonkar, S.K. Kataria, S.K. Lalwani, V. Mishra, A.K. Mohanty, L. Pant, S. Suryanarayana, A. Topkar

Tata Institute of Fundamental Research - EHEP, Mumbai, INDIA
T. Aziz, S. Banerjee, S. Bose, S. Chendvankar, P.V. Deshpande, M. Guchait[**9], A. Gurtu, M. Maity[**10], G. Majumder, K. Mazumdar, A. Nayak, M.R. Patil, S. Sharma, K. Sudhakar

Tata Institute of Fundamental Research - HECR, Mumbai, INDIA
B.S. Acharya, S. Banerjee, S. Bheesette, S. Dugad, S.D. Kalmani, V.R. Lakkireddi, N.K. Mondal, N. Panyam, P. Verma

Institute for Studies in Theoretical Physics & Mathematics (IPM), Tehran, IRAN
M. Arabgol, H. Arfaei, M. Hashemi, M. Mohammadi, M. Mohammadi Najafabadi, A. Moshaii, S. Paktinat Mehdiabadi

University College Dublin, Dublin, IRELAND
M. Felcini[**1], M. Grunewald

Università di Bari, Politecnico di Bari e Sezione dell' INFN, Bari, ITALY
M. Abbrescia, L. Barbone, A. Colaleo[**1], D. Creanza, N. De Filippis, M. De Palma, G. Donvito, L. Fiore, D. Giordano, G. Iaselli, F. Loddo, G. Maggi, M. Maggi, N. Manna, B. Marangelli, M.S. Mennea, S. My, S. Natali, S. Nuzzo, G. Pugliese, V. Radicci, A. Ranieri, F. Romano, G. Selvaggi, L. Silvestris[**1], P. Tempesta, R. Trentadue, G. Zito

Università di Bologna e Sezione dell' INFN, Bologna, ITALY
G. Abbiendi, W. Bacchi, C. Battilana, A. Benvenuti, D. Bonacorsi, S. Braibant-Giacomelli, P. Capiluppi, A. Castro, F.R. Cavallo, C. Ciocca, G. Codispoti, I. D'Antone, G.M. Dallavalle, F. Fabbri, A. Fanfani, P. Giacomelli[**11], C. Grandi, M. Guerzoni, L. Guiducci, S. Marcellini, G. Masetti, A. Montanari, F. Navarria, F. Odorici, A. Perrotta, A. Rossi, T. Rovelli, G. Siroli, R. Travaglini

Università di Catania e Sezione dell' INFN, Catania, ITALY
S. Albergo, V. Bellini, M. Chiorboli, S. Costa, M. Galanti, R. Potenza, C. Sutera, A. Tricomi, C. Tuve

Università di Firenze e Sezione dell' INFN, Firenze, ITALY
G. Ciraolo, V. Ciulli, C. Civinini, R. D'Alessandro, E. Focardi, C. Genta, G. Landi, P. Lenzi, A. Macchiolo, N. Magini, F. Manolescu, C. Marchettini, L. Masetti, S. Mersi, M. Meschini, S. Paoletti, G. Parrini, M. Sani, G. Sguazzoni

Laboratori Nazionali di Frascati dell' INFN, Frascati, ITALY
L. Benussi, M. Bertani, S. Bianco, M. Caponero, D. Colonna[**1], F. Fabbri, A. La Monaca, M. Pallotta, A. Paolozzi

Università di Genova e Sezione dell' INFN, Genova, ITALY
M. Bozzo, P. Fabbricatore, S. Farinon, F. Ferro, M. Greco

Istituto Nazionale di Fisica Nucleare e Universita Degli Studi Milano-Bicocca, Milano, ITALY
G. Cattaneo, A. De Min, M. Dominoni, F.M. Farina, F. Ferri, A. Ghezzi, P. Govoni, R. Leporini, S. Magni, M. Malberti, S. Malvezzi, S. Marelli, D. Menasce, L. Moroni, P. Negri, M. Paganoni, D. Pedrini, A. Pullia, S. Ragazzi, N. Redaelli, M. Rovere, L. Sala, S. Sala, R. Salerno, T. Tabarelli de Fatis, S. Vigano'

Istituto Nazionale di Fisica Nucleare de Napoli (INFN), Napoli, ITALY
G. Comunale, F. Fabozzi, D. Lomidze, S. Mele, P. Paolucci, D. Piccolo, C. Sciacca

Università di Padova e Sezione dell' INFN, Padova, ITALY
P. Azzi, N. Bacchetta[**1], M. Bellato, M. Benettoni, D. Bisello, E. Borsato, A. Candelori, P. Checchia, E. Conti, F. Dal Corso, M. De Mattia, T. Dorigo, U. Dosselli, V. Drollinger, F. Gasparini, U. Gasparini, P. Giubilato, F. Gonella, A. Kaminskiy, S. Karaevskii, V. Khomenkov, S. Lacaprara, I. Lippi, M. Loreti, O. Lytovchenko, M. Mazzucato, A.T. Meneguzzo, M. Michelotto, F. Montecassiano[**1], M. Nigro, D. Pantano, A. Parenti, M. Passaseo, M. Pegoraro, G. Rampazzo, P. Ronchese, M. Sgaravatto, E. Torassa, S. Vanini, S. Ventura, M. Verlato, M. Zanetti, P. Zotto, G. Zumerle

Università di Pavia e Sezione dell' INFN, Pavia, ITALY
G. Belli, U. Berzano, C. De Vecchi, A. Grelli, M.M. Necchi, S.P. Ratti, C. Riccardi, G. Sani, P. Torre, P. Vitulo

Università di Perugia e Sezione dell' INFN, Perugia, ITALY
F. Ambroglini, E. Babucci, D. Benedetti, M. Biasini, G.M. Bilei[**1], B. Caponeri, B. Checcucci, L. Fanò, M. Giorgi, P. Lariccia, G. Mantovani, D. Passeri, P. Placidi, V. Postolache, A. Santocchia, L. Servoli, D. Spiga, D. Tonoiu

Università di Pisa, Scuola Normale Superiore e Sezione dell' INFN, Pisa, ITALY
P. Azzurri, G. Bagliesi, A. Basti, L. Benucci, J. Bernardini, T. Boccali, A. Bocci, L. Borrello, F. Bosi, F. Calzolari, A. Carboni, R. Castaldi, C. Cerri, A.S. Cucoanes, R. Dell'Orso, S. Dutta, L. Foà, S. Gennai[**12], A. Giassi, D. Kartashov, F. Ligabue, S. Linari, T. Lomtadze, G.A. Lungu, B. Mangano, G. Martinelli, M. Massa, A. Messineo, A. Moggi, F. Palla, F. Palmonari, G. Petrucciani, F. Raffaelli, A. Rizzi, G. Sanguinetti, G. Segneri, D. Sentenac, A.T. Serban, A. Slav, P. Spagnolo, R. Tenchini, G. Tonelli[**1], A. Venturi, P.G. Verdini, M. Vos

Università di Roma I e Sezione dell' INFN, Roma, ITALY
S. Baccaro[**13], L. Barone, A. Bartoloni, F. Cavallari, S. Costantini, I. Dafinei, D. Del Re, M. Diemoz, C. Gargiulo, E. Longo, P. Meridiani, G. Organtini, A. Palma, R. Paramatti, S. Rahatlou, C. Rovelli, F. Santanastasio, V. Valente

Università di Torino e Sezione dell' INFN, Torino, ITALY
R. Arcidiacono, S. Argiro, R. Bellan, C. Biino, S. Bolognesi, N. Cartiglia, G. Cerminara, M. Cordero, M. Costa, D. Dattola[**1], G. Dellacasa, N. Demaria, C. Mariotti, S. Maselli, P. Mereu, E. Migliore, V. Monaco, M. Nervo, M.M. Obertino, N. Pastrone, G. Petrillo, A. Romero, R. Sacchi, A. Staiano, P.P. Trapani

Università di Trieste e Sezione dell' INFN, Trieste, ITALY
S. Belforte, F. Cossutti, G. Della Ricca, B. Gobbo, C. Kavka

Kyungpook National University, Daegu, KOREA
D.H. Kim, E.J. Kim, J.C. Kim, W.Y. Kim, S.K. Oh, S.R. Ro, D.C. Son

Konkuk University, Seoul, KOREA
S.Y. Jung, J.T. Rhee

Korea University, Seoul, KOREA
B.S. Hong, S.J. Hong, K.S. Lee, D.H. Moon, S.K. Park, K.S. Sim

Centro de Investigacion y de Estudios Avanzados del IPN, Mexico City, MEXICO
H. Castilla Valdez, A. Sanchez Hernandez

Universidad Iberoamericana, Mexico City, MEXICO
S. Carrillo Moreno

Benemerita Universidad Autonoma de Puebla, Puebla, MEXICO
H.A. Salazar Ibarguen

Universidad Autonoma de San Luis Potosi, San Luis Potosi, MEXICO
A. Morelos Pineda

University of Auckland, Auckland, NEW ZEALAND
R.N.C. Gray, D. Krofcheck

University of Canterbury, Christchurch, NEW ZEALAND
A.J. Bell, N. Bernardino Rodrigues, P.H. Butler, S. Churchwell, J.C. Williams

National Centre for Physics, Quaid-I-Azam University, Islamabad, PAKISTAN
Z. Aftab, U. Ahmad, I. Ahmed, M.I. Asghar, S. Asghar, M. Hafeez, H.R. Hoorani, M. Iftikhar, M.S. Khan, A. Osman, T. Solaija, A.R. Zafar

Institute of Nuclear Physics, Polish Academy of Sciences, Cracow, POLAND
J. Blocki, A. Cyz, E. Gladysz-Dziadus, S. Mikocki, J. Turnau, Z. Wlodarczyk[**14], P. Zychowski

Institute of Experimental Physics, Warsaw, POLAND
K. Bunkowski, H. Czyrkowski, R. Dabrowski, W. Dominik, K. Doroba, A. Kalinowski, M. Konecki, J. Krolikowski, I.M. Kudla, M. Pietrusinski, K. Pozniak[**15], W. Zabolotny[**15], P. Zych

Soltan Institute for Nuclear Studies, Warsaw, POLAND
M. Bluj, R. Gokieli, M. Górski, L. Goscilo, K. Nawrocki, P. Traczyk, G. Wrochna, P. Zalewski

Laboratório de Instrumentação e Física Experimental de Partículas, Lisboa, PORTUGAL
R. Alemany-Fernandez, C. Almeida, N. Almeida, A. Araujo Trindade, P. Bordalo, R. Bugalho De Moura, P. Da Silva Rodrigues, J. Gomes, M. Husejko, P. Ingenito, A. Jain, M. Kazana, P. Musella, S. Ramos, J. Rasteiro Da Silva, P.Q. Ribeiro, M. Santos, J. Semiao, P. Silva, I. Teixeira, J.P. Teixeira, J. Varela[**1], N. Vaz Cardoso

Joint Institute for Nuclear Research, Dubna, RUSSIA
K. Babich, D. Bardin, I. Belotelov, P. Bunin, S. Chesnevskaya, V. Elsha, Y. Ershov, I. Filozova, M. Finger, M. Finger, A. Golunov, I. Golutvin, N. Gorbounov, V. Kalagin, A. Kamenev, V. Karjavin, S. Khabarov, V. Khabarov, Y. Kiryushin, V. Konoplyanikov, V. Korenkov, A. Kurenkov, A. Lanev, V. Lysiakov, A. Malakhov, I. Melnitchenko, V.V. Mitsyn, K. Moisenz, P. Moisenz, S. Movchan, E. Nikonov, D. Oleynik, V. Palichik, V. Perelygin, A. Petrosyan, E. Rogalev, V. Samsonov, M. Savina, R. Semenov, S. Shmatov, S. Shulha, V. Sluneckova, V. Smirnov, D. Smolin, A. Tcheremoukhine, O. Teryaev, E. Tikhonenko, S. Vassiliev, A. Vishnevskiy, A. Volodko, N. Zamiatin, A. Zarubin, E. Zubarev

Petersburg Nuclear Physics Institute, Gatchina (St Petersburg), RUSSIA
N. Bondar, G. Gavrilov, V. Golovtsov, Y. Ivanov, V. Kim, V. Kozlov, V. Lebedev, G. Makarenkov, G. Obrant, E. Orishchin, A. Shchetkovskiy, A. Shevel, V. Sknar, I. Smirnov, V. Sulimov, V. Tarakanov, L. Uvarov, G. Velichko, S. Volkov, A. Vorobyev

Institute for Nuclear Research, Moscow, RUSSIA

Yu. Andreev, A. Anisimov, S. Gninenko, N. Golubev, D. Gorbunov, A. Ivashkin, M. Kirsanov, A. Kovzelev, N. Krasnikov, V. Matveev, A. Pashenkov, A. Pastsyak, V.E. Postoev, A. Sadovski, A. Solovey, A. Solovey, D. Soloviev, A. Toropin

Institute for Theoretical and Experimental Physics, Moscow, RUSSIA
V. Gavrilov, N. Ilina, V. Kaftanov, I. Kiselevich, V. Kolosov, M. Kossov[**1], A. Krokhotin, S. Kuleshov, A. Oulianov, G. Safronov, S. Semenov, V. Stolin, E. Vlasov[**1], V. Zaytsev

Moscow State University, Moscow, RUSSIA
E. Boos, M. Dubinin[**16], L. Dudko, A. Ershov, G. Eyyubova, R. Gloukhov, A. Gribushin, V. Ilyin, V. Klyukhin[**1], O. Kodolova, N.A. Kruglov, A. Kryukov, I. Lokhtin, V. Mikhaylin, S. Petrushanko, L. Sarycheva, V. Savrin, L. Shamardin, A. Sherstnev, A. Snigirev, K. Teplov, I. Vardanyan

P.N. Lebedev Physical Institute, Moscow, RUSSIA
E. Devitsin, A.M. Fomenko, N. Konovalova, V. Kozlov, A.I. Lebedev, N. Lvova, S. Potashov, S.V. Rusakov, A. Terkulov

State Research Center of Russian Federation - Institute for High Energy Physics, Protvino, RUSSIA
V. Abramov, S. Akimenko, A. Ashimova, I. Azhgirey, S. Bitioukov, O. Chikilev, K. Datsko, A. Filine, A. Godizov, P. Goncharov, V. Grishin, A. Inyakin[**17], V. Kachanov, A. Kalinin, A. Khmelnikov, D. Konstantinov, A. Korablev, E. Kozlovskiy, V. Krychkine, A. Levine, I. Lobov, V. Lukanin, V. Petrov, V. Petukhov, V. Pikalov, P. Ponomarev, R. Ryutin, V. Shelikhov, V. Skvortsov, S. Slabospitsky, O. Soumaneev, A. Sytine, V. Talov, L. Tourtchanovitch, S. Troshin, N. Tyurin, A. Uzunian, A. Volkov, S. Zelepoukine[**18]

Vinca Institute of Nuclear Sciences, Belgrade, SERBIA
P. Adzic, D. Krpic[**19], D. Maletic, P. Milenovic, J. Puzovic[**19], N. Smiljkovic[**1], M. Zupan

Centro de Investigaciones Energeticas Medioambientales y Tecnologicas (CIEMAT), Madrid, SPAIN
M. Aguilar-Benitez, J. Alberdi, J. Alcaraz Maestre, M. Aldaya Martin, P. Arce[**1], J.M. Barcala, C. Burgos Lazaro, J. Caballero Bejar, E. Calvo, M. Cardenas Montes, M. Cerrada, M. Chamizo Llatas, N. Colino, M. Daniel, B. De La Cruz, A. Delgado Peris, C. Fernandez Bedoya, A. Ferrando, M.C. Fouz, P. Garcia-Abia, O. Gonzalez Lopez, J.M. Hernandez, M.I. Josa, J.M. Luque, J. Marin, G. Merino, A. Molinero, J.J. Navarrete, J.C. Oller, E. Perez Calle, L. Romero, C. Villanueva Munoz, C. Willmott, C. Yuste

Universidad Autónoma de Madrid, Madrid, SPAIN
C. Albajar, J.F. de Trocóniz, E. Delmeire, I. Jimenez, R.F. Teixeira

Universidad de Oviedo, Oviedo, SPAIN
J. Cuevas, J. Lopez-Garcia, H. Naves Sordo, J.M. Vizan Garcia

Instituto de Física de Cantabria (IFCA), CSIC-Universidad de Cantabria, Santander, SPAIN
A. Calderon, D. Cano Fernandez, I. Diaz Merino, M. Fernandez, J. Fernandez Menendez[**20], L.A. Garcia Moral, G. Gomez, I. Gonzalez Caballero, J. Gonzalez Sanchez, A. Lopez Virto, J. Marco, R. Marco, C. Martinez Rivero, P. Martinez Ruiz del Arbol, F. Matorras, A. Patino Revuelta[**1], T. Rodrigo, D. Rodriguez Gonzalez, A. Ruiz Jimeno, L. Scodellaro, M. Sobron Sanudo, I. Vila, R. Vilar Cortabitarte

CERN, European Organization for Nuclear Research, Geneva, SWITZERLAND
D. Abbaneo, S.M. Abbas[**21], I. Ahmed[**21], M.I. Akhtar[**21], S. Akhtar, M.E. Alonso Rodriguez, N. Amapane, B. Araujo Meleiro, S. Ashby, P. Aspell, E. Auffray, M. Axer, A. Ball, N. Bangert, D. Barney, S. Beauceron, F. Beaudette[**22], W. Bialas, C. Bloch, P. Bloch, S. Bonacini, M. Bosteels, V. Boyer, A. Branson, A.M. Brett, H. Breuker, R. Bruneliere, O. Buchmuller, D. Campi, T. Camporesi,

E. Cano, A. Cattai, R. Chierici, T. Christiansen, S. Cittolin, E. Corrin, M. Corvo, B. Curé, C. D'Ambrosio, D. D'Enterria, A. De Roeck, C. Delaere, D. Delikaris, M. Della Negra, L.M. Edera, A. Elliott-Peisert, M. Eppard, F. Fanzago, R. Folch, S. Fratianni, W. Funk, A. Gaddi, J.V. Galan Chiner, M. Gastal, J.C. Gayde, H. Gerwig, K. Gill, A.S. Giolo-Nicollerat, F. Glege, R. Gomez-Reino Garrido, R. Goudard, J. Gutleber, M. Hansen, A. Hees, A. Hervé, H.F. Hoffmann, A. Holzner, A. Honma, M. Huhtinen, G. Iles, V. Innocente, W. Jank, P. Janot, K. Kloukinas, C. Lasseur, P. Lecoq, C. Leonidopoulos, M. Letheren, L. Linssen, C. Ljuslin, R. Loos, C. Lourenco, G. Magazzu, L. Malgeri, M. Mannelli, A. Marchioro, F. Meijers, E. Meschi, L. Mirabito, R. Moser, M. Mulders, J. Nash, R.A. Ofierzynski, A. Oh, P. Olbrechts, A. Onnela, L. Orsini, I. Pal, P. Palau Pellicer, G. Papotti, G. Passardi, B. Perea Solano, G. Perinic, P. Petagna, A. Petrilli, A. Pfeiffer, M. Pimiä, R. Pintus, M. Pioppi, A. Placci, H. Postema, R. Principe, J. Puerta Pelayo, A. Racz, R. Ranieri, J. Rehn, S. Reynaud, D. Ricci, M. Risoldi, P. Rodrigues Simoes Moreira, G. Rolandi, F.J. Ronga, P. Rumerio, H. Sakulin, D. Samyn, E. Sarkisyan-Grinbaum, W.D. Schlatter, C. Schwick, C. Schäfer, I. Segoni, A. Sharma, P. Siegrist, N. Sinanis, P. Sphicas[**23], M. Spiropulu, F. Szoncsó, O. Teller, J. Troska, E. Tsesmelis, D. Tsirigkas, A. Tsirou, D. Ungaro, M. Vander Donckt, F. Vasey, M. Vazquez Acosta, L. Veillet, P. Vichoudis, P. Wertelaers, M. Wilhelmsson, I.M. Willers, A. Zabi[**24]

Paul Scherrer Institut, Villigen, SWITZERLAND
W. Bertl, K. Deiters, W. Erdmann, K. Gabathuler, R. Horisberger, Q. Ingram, H.C. Kaestli, D. Kotlinski, S. König, D. Renker, T. Rohe

Institute for Particle Physics, ETH Zurich, Zurich, SWITZERLAND
B. Betev, Z. Chen, G. Davatz, G. Dissertori, M. Dittmar, L. Djambazov, C. Eggel[**25], J. Ehlers, R. Eichler, G. Faber, K. Freudenreich, J.F. Fuchs[**1], C. Grab, W. Hintz, U. Langenegger, P. Lecomte, P.D. Luckey, W. Lustermann, J.D. Maillefaud[**1], F. Moortgat, A. Nardulli, F. Nessi-Tedaldi, L. Pape, F. Pauss, T. Punz, U. Röser, D. Schinzel, A. Sourkov[**26], A. Starodumov[**27], F. Stöckli, H. Suter, L. Tauscher, P. Trüb[**25], J. Ulbricht, G. Viertel, H.P. von Gunten, M. Wensveen[**1]

Universität Zürich, Zürich, SWITZERLAND
E. Alagoz, C. Amsler, V. Chiochia, C. Regenfus, P. Robmann, T. Rommerskirchen, T. Speer, S. Steiner, L. Wilke

National Central University, Chung-Li, TAIWAN
S. Blyth, Y.H. Chang, E.A. Chen, A. Go, C.C. Hung, C.M. Kuo, W. Lin

National Taiwan University (NTU), Taipei, TAIWAN
P. Chang, Y. Chao, K.F. Chen, Z. Gao[**1], Y. Hsiung, Y.J. Lei, J. Schümann, J.G. Shiu, K. Ueno, Y. Velikzhanin, P. Yeh

Cukurova University, Adana, TURKEY
S. Aydin, M.N. Bakirci, S. Cerci, I. Dumanoglu, S. Erturk[**28], E. Eskut, A. Kayis Topaksu, P. Kurt, H. Ozkurt, A. Polatöz, K. Sogut[**29], H. Topakli, M. Vergili, G. Önengüt

Middle East Technical University, Physics Department, Ankara, TURKEY
H. Gamsizkan, A.M. Guler, C. Ozkan, S. Sekmen, M. Serin-Zeyrek, R. Sever, E. Yazgan, M. Zeyrek

Bogaziçi University, Department of Physics, Istanbul, TURKEY
K. Cankocak[**30], M. Deliomeroglu, D. Demir[**5], E. Gülmez, E. Isiksal[**31], M. Kaya[**32], O. Kaya[**32], S. Ozkorucuklu[**33], N. Sonmez[**34]

Institute of Single Crystals of National Academy of Science, Kharkov, UKRAINE
B. Grinev, V. Lyubynskiy, V. Senchyshyn

National Scientific Center, Kharkov Institute of Physics and Technology, Kharkov, UKRAINE
L. Levchuk, A. Nemashkalo

University of Bristol, Bristol, UNITED KINGDOM
J.J. Brooke, R. Croft, D. Cussans, D. Evans, N. Grant, M. Hansen, G.P. Heath, H.F. Heath, C. Hill, B. Huckvale, C. Lynch, C.K. Mackay, S. Metson, D.M. Newbold[**35], V.J. Smith, R.J. Tapper

Rutherford Appleton Laboratory, Didcot, UNITED KINGDOM
K.W. Bell, R.M. Brown, B. Camanzi, D.J.A. Cockerill, J. Cole, J.A. Coughlan, P.S. Flower, V.B. Francis, M. French, J. Greenhalgh, R. Halsall, J. Hill, L. Jones, B.W. Kennedy, L. Lintern, Q. Morrissey, P. Murray, S. Quinton, J. Salisbury, C. Shepherd-Themistocleous, B. Smith, M. Sproston, R. Stephenson, S. Taghavirad, I.R. Tomalin, J. Williams

Imperial College, University of London, London, UNITED KINGDOM
F. Arteche, R. Bainbridge, G. Barber, P. Barrillon, R. Beuselinck, F. Blekman, D. Britton, D. Colling, G. Daskalakis, G. Davies, S. Dris, C. Foudas, J. Fulcher, D. Futyan, S. Greder, G. Hall[**1], J. Hays, J. Jones, J. Leaver, B.C. MacEvoy, A. Nikitenko[**27], M. Noy, A. Papageorgiou, M. Pesaresi, K. Petridis, D.M. Raymond, M.J. Ryan, C. Seez, P. Sharp[**1], G. Sidiropoulos, M. Stettler[**1], A. Tapper, C. Timlin, T. Virdee[**1], S. Wakefield, M. Wingham, Y. Zhang, O. Zorba

Brunel University, Uxbridge, UNITED KINGDOM
C. Da Via, I. Goitom, P.R. Hobson, P. Kyberd, C. Munro, J. Nebrensky, I. Reid, C. Siamitros, R. Taylor, L. Teodorescu, S.J. Watts, I. Yaselli

Boston University, Boston, Massachusetts, USA
E. Hazen, A.H. Heering, A. Heister, D. Lazic, D. Osborne, J. Rohlf, L. Sulak, S. Wu

Brown University, Providence, Rhode Island, USA
L. Christofek, D. Cutts, S. Esen, R. Hooper, G. Landsberg

University of California, Davis, Davis, California, USA
R. Breedon, M. Case, M. Chertok, J. Conway, P.T. Cox, R. Erbacher, J. Gunion, B. Holbrook, W. Ko, R. Lander, A. Lister, D. Pellett, J. Smith, A. Soha, M. Tripathi, R. Vogt

University of California, Los Angeles, Los Angeles, California, USA
V. Andreev, K. Arisaka, D. Cline, R. Cousins, S. Erhan[**1], J. Hauser, M. Ignatenko, B. Lisowski, D. Matlock, C. Matthey, B. Mohr, J. Mumford, S. Otwinowski, G. Rakness, P. Schlein, Y. Shi, J. Tucker, V. Valuev, R. Wallny, H.G. Wang, X. Yang, Y. Zheng

University of California, Riverside, Riverside, California, USA
R. Clare, D. Fortin, J.W. Gary, M. Giunta[**1], G. Hanson, G.Y. Jeng, S.C. Kao, H. Liu, G. Pasztor[**36], A. Satpathy, B.C. Shen, R. Stringer, V. Sytnik, R. Wilken

University of California, San Diego, La Jolla, California, USA
J.G. Branson, E. Dusinberre, J. Letts, D. MacFarlane, T. Martin, M. Mojaver, H.P. Paar, H. Pi, M. Pieri, A. Rana, V. Sharma, A. White, F. Würthwein, A. Yagil

University of California, Santa Barbara, Santa Barbara, California, USA
A. Affolder, C. Campagnari, M. D'Alfonso, A. Dierlamm, J. Incandela, S.A. Koay, D. Kovalskyi, V. Krutelyov, S. Kyre, J. Lamb, J. Richman, D. Stuart, D. White

California Institute of Technology, Pasadena, California, USA
T. Azim, A. Bornheim, J. Bunn, J. Chen, G. Denis, P. Galvez, M. Gataullin, E. Hughes, Y. Kuznetsova, T. Lee, I. Legrand, V. Litvine, Y. Ma, D. Nae, I. Narsky, H.B. Newman, S. Ravot, C. Rogan, S. Shevchenko, C. Steenberg, X. Su, M. Thomas, V. Timciuc, F. van Lingen, J. Veverka, B.R. Voicu[**1], A. Weinstein, R. Wilkinson, Y. Xia, Y. Yang, L.Y. Zhang, K. Zhu, R.Y. Zhu

Carnegie Mellon University, Pittsburgh, Pennsylvania, USA
T. Ferguson, M. Paulini, J. Russ, N. Terentyev, H. Vogel, I. Vorobiev

University of Colorado at Boulder, Boulder, Colorado, USA
M. Bunce, J.P. Cumalat, W.T. Ford, D. Johnson, U. Nauenberg, K. Stenson, S.R. Wagner

Cornell University, Ithaca, New York, USA
L. Agostino[**1], J. Alexander, D. Cassel, S. Das, L.K. Gibbons, B. Heltsley, C.D. Jones, V. Kuznetsov, J.R. Patterson, D. Riley, A. Ryd, W. Sun, J. Thom, P. Wittich

Fairfield University, Fairfield, Connecticut, USA
C.P. Beetz, G. Cirino, V. Podrasky, C. Sanzeni, D. Winn

Fermi National Accelerator Laboratory, Batavia, Illinois, USA
S. Abdullin[**27], M.A. Afaq[**1], M. Albrow, G. Apollinari, M. Atac, W. Badgett, J.A. Bakken, B. Baldin, L.A.T. Bauerdick, A. Baumbaugh, P.C. Bhat, M. Binkley, F. Borcherding, K. Burkett, J.N. Butler, H.W.K. Cheung, G. Chevenier[**1], I. Churin, S. Cihangir, M. Demarteau, D.P. Eartly, J.E. Elias, V.D. Elvira, D. Evans, I. Fisk, J. Freeman, P. Gartung, F.J.M. Geurts, L. Giacchetti, D.A. Glenzinski, E. Gottschalk, D. Green, Y. Guo, O. Gutsche, A. Hahn, J. Hanlon, R.M. Harris, A. Heavey, T. Hesselroth, S.L. Holm, B. Holzman, S. Iqbal, E. James, M. Johnson, U. Joshi, B. Klima, S. Kossiakov, J. Kowalkowski, T. Kramer, S. Kwan, E. La Vallie, M. Larwill, S. Los, L. Lueking, P. Lukens, G. Lukhanin, S. Lusin[**1], K. Maeshima, P. McBride, S. Moccia, S.J. Murray, V. O'Dell, M. Paterno, D. Petravick, R. Pordes, O. Prokofyev, V. Rasmislovich, N. Ratnikova, A. Ronzhin, V. Sekhri, E. Sexton-Kennedy, T. Shaw, D. Skow, R.P. Smith, W.J. Spalding, L. Spiegel, M. Stavrianakou, G. Stiehr, A.L. Stone, I. Suzuki, P. Tan, W. Tanenbaum, S. Tkaczyk[**1], S. Veseli, R. Vidal, H. Wenzel, J. Whitmore, W.M. Wu, Y. Wu, J. Yarba, J.C. Yun, A. Zatzerklyany, J.K. Zimmerman

University of Florida, Gainesville, Florida, USA
D. Acosta, P. Avery, V. Barashko, P. Bartalini, D. Bourilkov, R. Cavanaugh, A. Drozdetskiy, R.D. Field, Y. Fu, L. Gray, D. Holmes, B.J. Kim, S. Klimenko, J. Konigsberg, A. Korytov, K. Kotov, P. Levchenko, A. Madorsky, K. Matchev, G. Mitselmakher, Y. Pakhotin, C. Prescott, P. Ramond, J.L. Rodriguez, M. Schmitt, B. Scurlock, H. Stoeck, J. Yelton

Florida International University, Miami, Florida, USA
W. Boeglin, V. Gaultney, L. Kramer, S. Linn, P. Markowitz, G. Martinez, B. Raue, J. Reinhold

Florida State University, Tallahassee, Florida, USA
A. Askew, O. Atramentov, M. Bertoldi, W.G.D. Dharmaratna, Y. Gershtein, S. Hagopian, V. Hagopian, M. Jenkins, K.F. Johnson, H. Prosper, H. Wahl

Florida Institute of Technology, Melbourne, Florida, USA
M. Baarmand, L. Baksay[**37], S. Guragain, M. Hohlmann, H. Mermerkaya, R. Ralich, I. Vodopiyanov

University of Illinois at Chicago (UIC), Chicago, Illinois, USA
M.R. Adams, L. Apanasevich, R.R. Betts, E.J. Garcia-Solis, C.E. Gerber, D.J. Hofman, R. Hollis, A. Iordanova, C. Mironov, E. Shabalina, C. Smith, T.B. Ten, N. Varelas

The University of Iowa, Iowa City, Iowa, USA
U. Akgun, A.S. Ayan, R. Briggs, A. Cooper, P. Debbins, F. Duru, M. Fountain, N. George, E. McCliment, J.P. Merlo, A. Mestvirishvili, M.J. Miller, C.R. Newsom, E. Norbeck, Y. Onel, L. Perera, I. Schmidt, S. Wang, T. Yetkin

Iowa State University, Ames, Iowa, USA
E.W. Anderson, J.M. Hauptman, J. Lamsa

Johns Hopkins University, Baltimore, Maryland, USA
B.A. Barnett, B. Blumenfeld, C.Y. Chien, A. Gritsan, D.W. Kim, P. Maksimovic, S. Spangler, M. Swartz

The University of Kansas, Lawrence, Kansas, USA
P. Baringer, A. Bean, J. Chen, O. Grachov, M. Murray, J.G. Snyder, J.S. Wood, V. Zhukova

Kansas State University, Manhattan, Kansas, USA
D. Bandurin, T. Bolton, A. Khanov, Y. Maravin, D. Onoprienko, R. Sidwell, N. Stanton, E. Von Toerne

Lawrence Livermore National Laboratory, Livermore, California, USA
C.H. Cheng, J. Gronberg, D. Lange, D. Wright

University of Maryland, College Park, Maryland, USA
D. Baden, R. Bard, S.C. Eno, T. Grassi, N.J. Hadley, R.G. Kellogg, S. Kunori, F. Ratnikov, A. Skuja

Massachusetts Institute of Technology, Cambridge, Massachusetts, USA
B. Alver, M. Ballintijn, G. Bauer, W. Busza, P. Harris, I. Kravchenko, W. Li, C. Loizides, S. Nahn, C. Paus, S. Pavlon, C. Reed, C. Roland, G. Roland, G. Stephans, K. Sumorok, S. Vaurynovich, G. Veres, E.A. Wenger, B. Wyslouch

University of Minnesota, Minneapolis, Minnesota, USA
D. Bailleux, P. Cushman, A. De Benedetti, A. Dolgopolov, P.R. Dudero, R. Egeland, G. Franzoni, W.J. Gilbert, D. Gong, J. Grahl, J. Haupt, Y. Kubota, J. Mans, R. Rusack, A. Singovsky, J. Zhang

University of Mississippi, University, Mississippi, USA
L.M. Cremaldi, R. Godang, R. Kroeger, J. Reidy, D.A. Sanders, D. Summers

University of Nebraska-Lincoln, Lincoln, Nebraska, USA
K. Bloom, B. Bockelman, D.R. Claes, A. Dominguez, M. Eads, D. Johnston, C. Lundstedt, S. Malik, G.R. Snow, A. Sobol

State University of New York at Buffalo, Buffalo, New York, USA
U. Baur, K.M. Ecklund, I. Iashvili, A. Kharchilava, A. Kumar, M. Strang

Northeastern University, Boston, Massachusetts, USA
G. Alverson, E. Barberis, O. Boeriu, G. Eulisse, Y. Musienko[**38], S. Muzaffar, I. Osborne, S. Reucroft, J. Swain, L. Taylor, L. Tuura, D. Wood

Northwestern University, Evanston, Illinois, USA
B. Gobbi, M. Kubantsev, M. Schmitt, E. Spencer, S. Stoynev, M. Velasco

University of Notre Dame, Notre Dame, Indiana, USA
B. Baumbaugh, N.M. Cason, M. Hildreth, C. Jessop, D.J. Karmgard, T. Kolberg, N. Marinelli, R. Ruchti, J. Warchol, M. Wayne

The Ohio State University, Columbus, Ohio, USA
B. Bylsma, L.S. Durkin, J. Gilmore, J. Gu, R. Hughes, P. Killewald, K. Knobbe, T.Y. Ling, B.L. Winer

Princeton University, Princeton, New Jersey, USA
P. Elmer, D. Gerbaudo, V. Halyo, D. Marlow, P. Piroué, D. Stickland, C. Tully, T. Wildish, S. Wynhoff, Z. Xie

University of Puerto Rico, Mayaguez, Puerto Rico, USA
X.T. Huang

Purdue University, West Lafayette, Indiana, USA
A. Apresyan, K. Arndt, K. Banicz, V.E. Barnes, G. Bolla, D. Bortoletto, A. Bujak, A.F. Garfinkel, L. Gutay, N. Ippolito, Y. Kozhevnikov[**1], A.T. Laasanen, C. Liu, V. Maroussov, P. Merkel, D.H. Miller, N. Neumeister, A. Sedov, I. Shipsey

Purdue University Calumet, Hammond, Indiana, USA
N. Parashar

Rice University, Houston, Texas, USA
G. Eppley, S.J. Lee, J. Liu, M. Matveev, T. Nussbaum, B.P. Padley, J. Roberts, A. Tumanov, P. Yepes

University of Rochester, Rochester, New York, USA
A. Bodek, H. Budd, Y.S. Chung, P. De Barbaro[**1], R. Demina, G. Ginther, Y. Gotra, U. Husemann, S. Korjenevski, W. Sakumoto, P. Slattery, P. Tipton, M. Zielinski

The Rockefeller University, New York, New York, USA
A. Bhatti

Rutgers, the State University of New Jersey, Piscataway, New Jersey, USA
E. Bartz, J. Doroshenko, E. Halkiadakis, P.F. Jacques, M.S. Kalelkar, D. Khits, A. Lath, A. Macpherson[**1], R. Plano, K. Rose, S. Schnetzer, S. Somalwar, R. Stone, G. Thomson, T.L. Watts

Texas A&M University, College Station, Texas, USA
A. Aurisano, A. Golyash, T. Kamon, A. Safonov, D. Toback, M. Weinberger

Texas Tech University, Lubbock, Texas, USA
N. Akchurin, K.W. Carrell, K. Gumus, C. Jeong, H. Kim, Y. Roh, A. Sill, M. Spezziga, E. Washington, R. Wigmans

Vanderbilt University, Nashville, Tennessee, USA
T. Bapty, D. Engh, W. Johns, T. Keskinpala, E. Luiggi Lopez, S. Neema, S. Nordstrom, S. Pathak, P. Sheldon, E.W. Vaandering, M. Webster

University of Virginia, Charlottesville, Virginia, USA
M.W. Arenton, S. Conetti, B. Cox, R. Hirosky, R. Imlay, A. Ledovskoy, D. Phillips II, H. Powell, M. Ronquest, D. Smith, R. Yohay

University of Wisconsin, Madison, Wisconsin, USA
Y.W. Baek, J.N. Bellinger, D. Bradley, P. Cannarsa[**1], D. Carlsmith, I. Crotty[**1], S. Dasu, F. Feyzi, T. Gorski, M. Grothe[**39], W. Hogg, M. Jaworski, P. Klabbers, A. Lanaro, R. Loveless, M. Magrans de Abril, A. Mohapatra, D. Reeder, W.H. Smith, D. Wenman

---

**1: Also at CERN, European Organization for Nuclear Research, Geneva, Switzerland
**2: Also at University of Zagreb, Zagreb, Croatia
**3: Also at Université de Haute-Alsace, Mulhouse, France
**4: Also at Université Louis Pasteur, Strasbourg, France
**5: Also at Izmir Institute of Technology (IYTE), Izmir, Turkey
**6: Also at Moscow State University, Moscow, Russia
**7: Also at Institute of Nuclear Research ATOMKI, Debrecen, Hungary
**8: Also at University of California, San Diego, La Jolla, USA
**9: Also at Tata Institute of Fundamental Research - HECR, Mumbai, India
**10: Also at University of Visva-Bharati, Santiniketan, India
**11: Also at University of California, Riverside, Riverside, USA
**12: Also at Centro Studi Enrico Fermi, Roma, Italy
**13: Also at ENEA - Casaccia Research Center, S. Maria di Galeria, Italy
**14: Also at Institute of Physics, Swietokrzyska Academy, Kielce, Poland
**15: Also at Warsaw University of Technology, Institute of Electronic Systems, Warsaw, Poland
**16: Also at California Institute of Technology, Pasadena, USA
**17: Also at University of Minnesota, Minneapolis, USA
**18: Also at Institute for Particle Physics, ETH Zurich, Zurich, Switzerland
**19: Also at Faculty of Physics of University of Belgrade, Belgrade, Serbia

**20: Also at Institut für Experimentelle Kernphysik, Karlsruhe, Germany
**21: Also at National Centre for Physics, Quaid-I-Azam University, Islamabad, Pakistan
**22: Also at Laboratoire Leprince-Ringuet, Ecole Polytechnique,
IN2P3-CNRS, Palaiseau, France
**23: Also at University of Athens, Athens, Greece
**24: Also at Imperial College, University of London, London, United Kingdom
**25: Also at Paul Scherrer Institut, Villigen, Switzerland
**26: Also at State Research Center of Russian Federation - Institute for High Energy
Physics, Protvino, Russia
**27: Also at Institute for Theoretical and Experimental Physics, Moscow, Russia
**28: Also at Nigde University, Nigde, Turkey
**29: Also at Mersin University, Mersin, Turkey
**30: Also at Mugla University, Mugla, Turkey
**31: Also at Marmara University, Istanbul, Turkey
**32: Also at Kafkas University, Kars, Turkey
**33: Also at Suleyman Demirel University, Isparta, Turkey
**34: Also at Ege University, Izmir, Turkey
**35: Also at Rutherford Appleton Laboratory, Didcot, United Kingdom
**36: Also at KFKI Research Institute for Particle and Nuclear Physics, Budapest, Hungary
**37: Also at University of Debrecen, Debrecen, Hungary
**38: Also at Institute for Nuclear Research, Moscow, Russia
**39: Also at Università di Torino e Sezione dell' INFN, Torino, Italy

Executive Summary

The Large Hadron Collider at CERN will open a new energy frontier in ultrarelativistic heavy-ion physics. The collisions of heavy nuclei at energies $\sqrt{s_{NN}}$ = 5.5 TeV, thirty times larger than previous experiments at RHIC, will probe quark and gluon matter at unprecedented values of energy density. The prime goal of this research programme is to study the fundamental theory of the strong interaction — Quantum Chromodynamics (QCD) — in extreme conditions of temperature, density and parton momentum fraction (low-x). Such studies — with impressive experimental and theoretical advances in recent years thanks to the wealth of high-quality data collected at RHIC and the SPS — address not only basic aspects of the strong interaction, such as the nature of confinement or the mechanism of mass generation via chiral symmetry breaking, but shed light on a wide variety of fundamental physics problems such as the high-energy limit of all scattering cross sections involving hadronic objects, the inner structure of compact stellar objects, the evolution of the early universe between the electroweak transition and primordial nucleosynthesis, etc. To carry out this research programme, the Compact Muon Solenoid (CMS) experiment must be prepared to deal with the large particle multiplicities expected in nucleus-nucleus collisions, be able to measure low momentum observables which provide information on the bulk properties of the produced medium and, most importantly, be capable of triggering on and reconstructing the rare perturbative probes expected to yield the most direct insights into the properties of the produced high-density strongly-interacting matter.

The principal aim of this Technical Design Report is to present the capabilities of the CMS experiment to explore the rich heavy-ion physics programme offered by the LHC. This document updates and extends the first comprehensive studies carried out within the CMS collaboration a few years ago ("Heavy Ion Physics in CMS" CMS-NOTE-2000-060). A recent description of the CMS detector configuration and performance — including track and jet reconstruction in the high particle-multiplicity environment of nucleus-nucleus collisions — has been presented in the CMS Physics Technical Design Report, Volume 1. In Volume 2 of the same report, a benchmark heavy-ion physics probe, the measurement of the charmonium ($\mathrm{J}/\psi, \psi'$) and bottomonium ($\Upsilon, \Upsilon', \Upsilon''$) resonances in PbPb collisions at 5.5 TeV, was also described. This report covers in detail the potential of the CMS experiment to address physics with lead beams at the LHC based on a series of representative measurements simulated and reconstructed within the official CMS software framework.

Structure of the Report

Chapter 1, the Introduction, presents the physics interest of heavy-ion collisions at LHC energies to address important open questions on high-density QCD matter.

Chapters 2–4 describe the bulk observables — charged particle multiplicity, low p_{T} inclusive hadron identified spectra and elliptic flow — which provide information on the collective properties of the system and which are accessible with a standard "minimum bias" trigger in CMS. The PbPb level-1 trigger and the method to determine the reaction centrality are also

outlined.

Chapter 5 presents the hard probes physics reach and triggering capabilities. Hard probes constitute privileged perturbative "tomographic" probes of the hottest and densest phases of the reaction, and Chapters 6 and 7 detail the capabilities for the measurement of quarkonia, heavy-quarks, jets and high p_{T} hadrons.

Chapter 8 discusses the CMS capabilities for measuring photon-induced processes in electromagnetic (ultraperipheral) nucleus-nucleus interactions which will allow us to study the small-x gluon distribution in the nuclei in an unexplored domain. Finally, Chapter 9 outlines a few other observables which can certainly be measured in CMS but for which no (fast or slow) simulation studies are available at the time of writing this report.

Contents

Chapter 1

Introduction

1.1 Physics motivation

The study of the fundamental theory of the strong interaction — Quantum Chromodynamics (QCD) — in extreme conditions of temperature, density and parton momentum fraction (low-x) has attracted an increasing experimental and theoretical interest during the last 20 years. Indeed, QCD is not only a quantum field theory with an extremely rich dynamical content — such as asymptotic freedom, infrared slavery, (approximate) chiral symmetry, non-trivial vacuum topology, strong CP violation problem, $\mathrm{U}_A(1)$ axial-vector anomaly, colour superconductivity, ... — but also the only sector of the Standard Model (SM) whose full *collective* behaviour — phase diagram, phase transitions, thermalisation of fundamental fields — is accessible to scrutiny in the laboratory. The study of the many-body dynamics of high-density QCD covers a vast range of fundamental physics problems (Fig. 1.1).

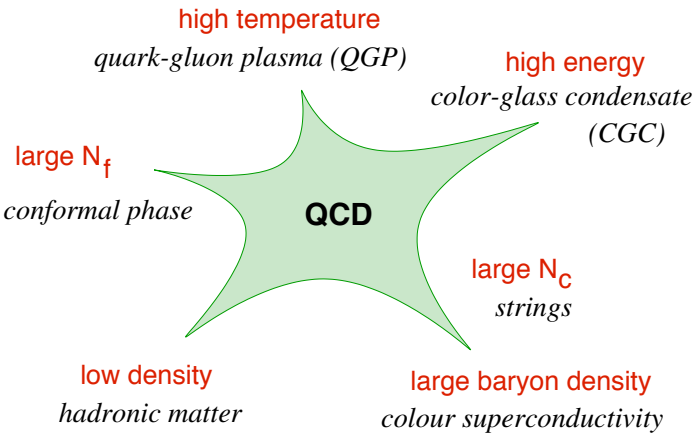

Figure 1.1: Many-body dynamics of QCD in different physics limits (adapted from [1]).

Deconfinement and chiral symmetry restoration

Lattice QCD calculations [2] predict a new form of matter at energy densities (well) above a critical value — $\epsilon_c = (6 \pm 2) T_c^4 \approx 1$ GeV/fm^3 (Fig. 1.2), where $T_c \approx 150$–190 MeV [3, 4] is the critical temperature — consisting of an extended volume of deconfined and current-mass quarks and gluons: the Quark-Gluon Plasma (QGP) [5, 6]. The vanishing of the chiral condensate at T_c and the sudden liberation of quark and gluon degrees of freedom are clearly visible in Fig. 1.2. The scrutiny of this new state of matter — equation-of-state (EoS), order of

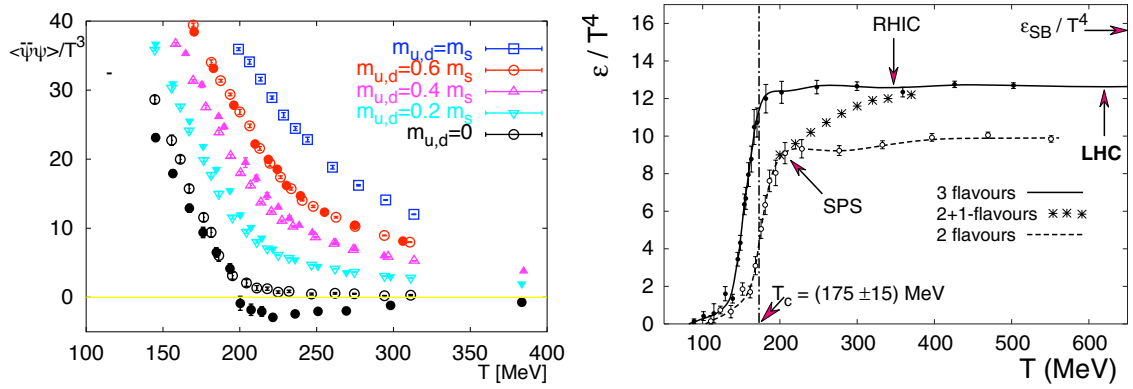

Figure 1.2: Left: The light quark chiral condensate versus the temperature computed in lattice QCD with various number of flavours and values of the u, d, s quark masses [7]. Right: The energy density in QCD with 0, 2 and 3 degenerate quark flavours as well as with two light and one heavier (strange) quarks. The horizontal arrow shows the value of the Stefan-Boltzmann limit for an ideal quark-gluon gas [2].

the phase transition, transport properties, etc. — promises to shed light on basic aspects of the strong interaction such as the nature of confinement, the mechanism of mass generation (chiral symmetry breaking, structure of the QCD vacuum) and hadronization, which still evade a thorough theoretical description [8, 9] due to their highly non-perturbative nature.

Early universe cosmology

The quark-hadron phase transition took place some 10 μs after the Big Bang and is believed to have been the most important event in the Universe between the electroweak (or SUSY) transition and Big Bang Nucleosynthesis (BBN), see Fig. 1.3. Depending on the order of the transition[1], several cosmological implications have been postulated [10] such as the formation of strangelets and cold dark-matter (WIMP) clumps, relic magnetic fields, primordial black holes, or baryon fluctuations leading to inhomogeneous nucleosynthesis. In any event, the thermodynamics of the QCD transition epoch plays a background role in the determination of various hypothetical dark-matter relic densities (axion, WIMP, ... see Fig. 1.3, bottom) [11, 12].

Parton structure and evolution at small-x

HERA results [13, 14] indicate that when probed at high energies, hadrons consist of a very dense system of gluons with small (Bjorken) momentum $x = p_{\rm parton}/p_{\rm hadron}$. At low x, the probability to emit an extra gluon is large, proportional to $\alpha_s \ln(1/x)$, and gluon-gluon fusion processes will eventually dominate the parton evolution in the hadronic wavefunctions. At high virtualities Q^2 and moderately low x, such evolution is described by linear DGLAP [15–17] or BFKL [18–20] equations, suitable for a dilute parton regime. At $x \lesssim 10^{-2}$, and for Q values below an energy-dependent saturation momentum Q_s, hadrons are however more appropriately described as dense, saturated parton systems in the context of the "Colour-Glass Condensate" (CGC) [21] effective theory with the corresponding non-linear JIMWLK [22–24] (or BK [25]) evolution equations (Fig. 1.4). Low-x gluons in nuclei overlap and, so, saturation effects are expected to set in earlier for ultrarelativistic heavy nuclei (for

[1]The order itself is not exactly known: the transition — which is 1$^{\rm st}$-order in pure SU(3) gluodynamics and of a fast cross-over type for N_f = 2+1 quarks [2] — is still sensitive to lattice extrapolations to the continuum limit.

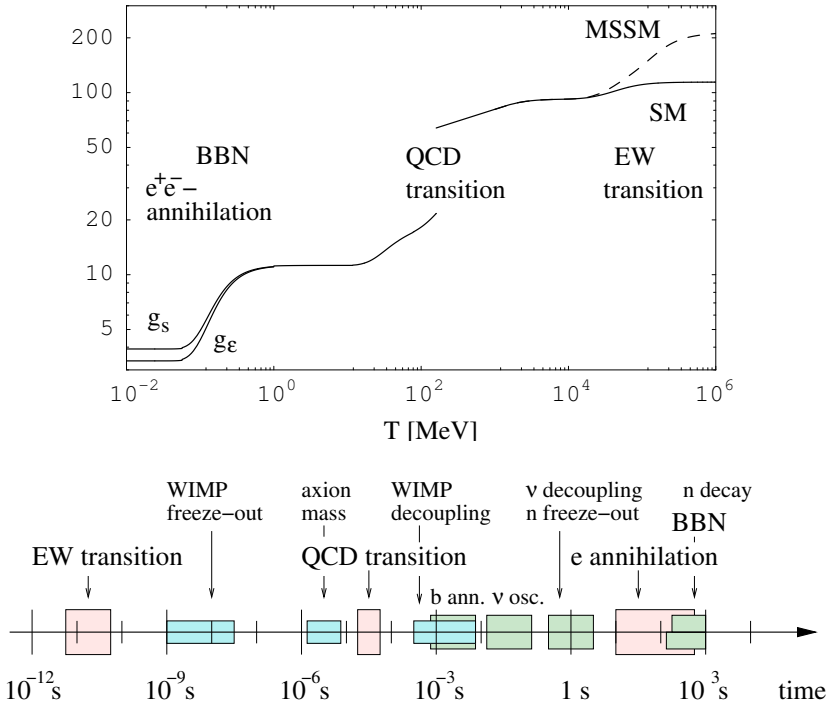

Figure 1.3: Top: Effective number of degrees of freedom $g_\varepsilon(T) = \varepsilon(T)/(\pi^2/30\,T^4)$ predicted by the Standard Model (the dashed line is a minimal supersymmetric extension of the SM) [10]. Bottom: Sequence of significant events in the early Universe until the Big Bang Nucleosynthesis epoch: electroweak and QCD transitions, decoupling of several SM and hypothetical particles, $e^\pm$ annihilation, etc. [10, 12].

which $Q_s^2 \propto A^{1/3}$, with A the number of nucleons) than for free nucleons.

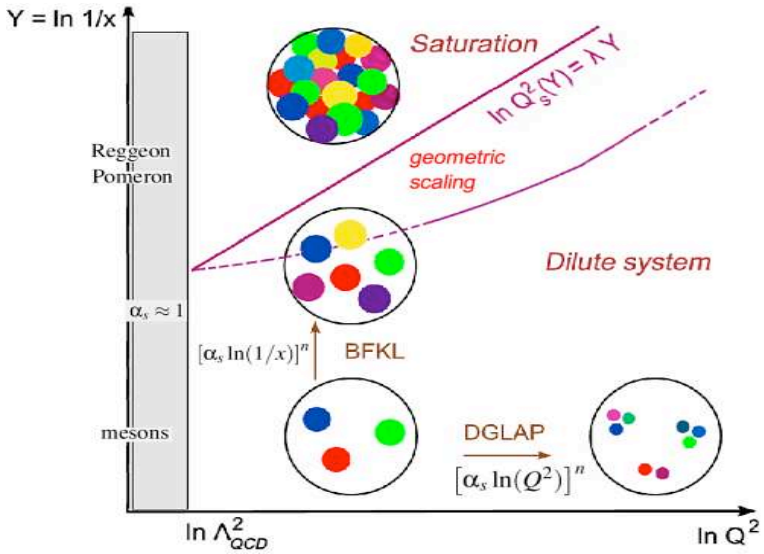

Figure 1.4: QCD phase diagram in the $1/x, Q^2$ plane (each circle represents a parton with transverse area $\sim 1/Q^2$ and fraction x of the hadron momentum). The different evolution regimes (DGLAP, BFKL, saturation) are indicated, as well as the saturation scale and geometric scaling curves between the dense and dilute domains [26, 27].

Gauge/String duality

Theoretical applications of the Anti-de Sitter/Conformal-Field-Theory (AdS/CFT) correspondence [28, 29] provide results in strongly coupled (i.e. large 't Hooft coupling $\lambda = g^2\, N_c \gg 1$) SU($N_c$) gauge theories in terms of a weakly-coupled dual gravity theory. Recent applications of this formalism for QCD-like ($\mathcal{N} = 4$ super Yang-Mills) theories have led to the determination of transport properties accessible to experimental study — such as the QGP viscosity [30], the jet quenching parameter $\langle \hat{q} \rangle$ [31], or the heavy-quark diffusion coefficient [32–34] — from black hole thermodynamics calculations. Such results provide valuable insights on *dynamical* properties of strongly-coupled QCD that cannot be easily treated by perturbative or lattice methods, and open novel phenomenological and experimental directions in high-energy heavy-ion physics.

Compact object astrophysics

At high baryon densities and not too high temperatures, the attractive force between (colour antisymmetric) quarks can lead to the formation of bound $\langle qq \rangle$ condensates of Cooper pairs. Cold and dense matter is thus expected to behave as a *colour superconductor* with a non-trivial quark pairing structure due to the combination of the various quantum numbers involved (spin, colour, flavour) [35]. This regime, currently beyond the direct reach of accelerator-based research — except indirectly in the region of large baryon densities around the QCD critical point, Fig. 1.5 — may be realised in the core of compact stars (neutron, hybrid or other exotic stars) and, thus, open to study through astronomical observation.

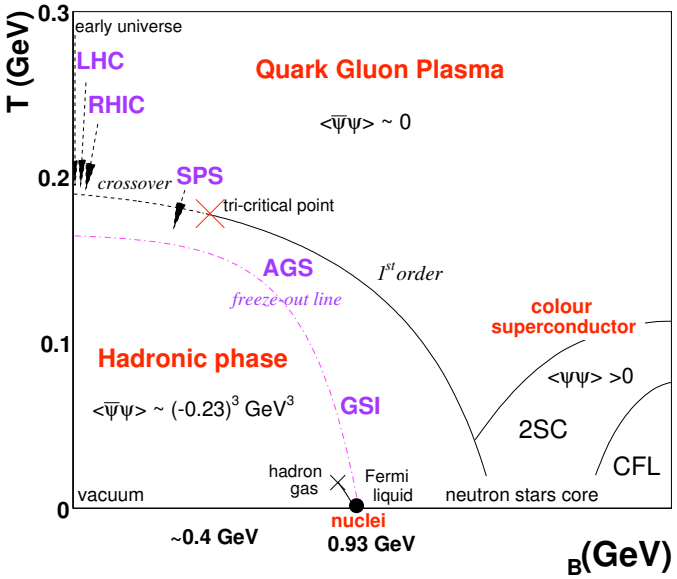

Figure 1.5: QCD phase diagram in the temperature vs. baryochemical potential (T, μ_B) plane. The arrows indicate the expected crossing through the deconfinement transition during the expansion phase in heavy-ion collisions at different accelerators. The (dashed) freeze-out curve indicates where hadro-chemical equilibrium is attained in the final stage of the collision [36]. The ground-state of nuclear matter at $T = 0$ and $\mu_B = 0.93$ GeV and the approximate position of the QCD critical point at $\mu_B \approx 0.4$ GeV [37] are also indicated.

1.2 High-energy nucleus-nucleus collisions

The only experimental means available so far to investigate the (thermo)dynamics of a multi-parton system involves colliding large atomic nuclei at ultrarelativistic energies. Figure 1.6 left, shows the total centre-of-mass energy available for particle production (i.e. subtracting the rest mass of the colliding hadrons) at different accelerators as a function of the first operation year ("Livingston plot") [38]. The exponential increase in performance translates into an energy doubling every 2 (3) years for the ion ($\bar{\mathrm{p}}$,p) beams. Head-on collisions of heavy ions (AA) can produce extremely hot and dense QCD matter by concentrating a substantial amount of energy — $\mathcal{O}$(1 TeV) at mid-rapidity at the LHC, see Fig. 1.6-right — in an *extended* cylindrical volume, $V = \pi R_A^2 \tau_0 \approx 150$ fm^3 for a typical large nucleus with radius $R_A = 6.5$ fm, at thermalisation times of $\tau_0 = 1$ fm/c.

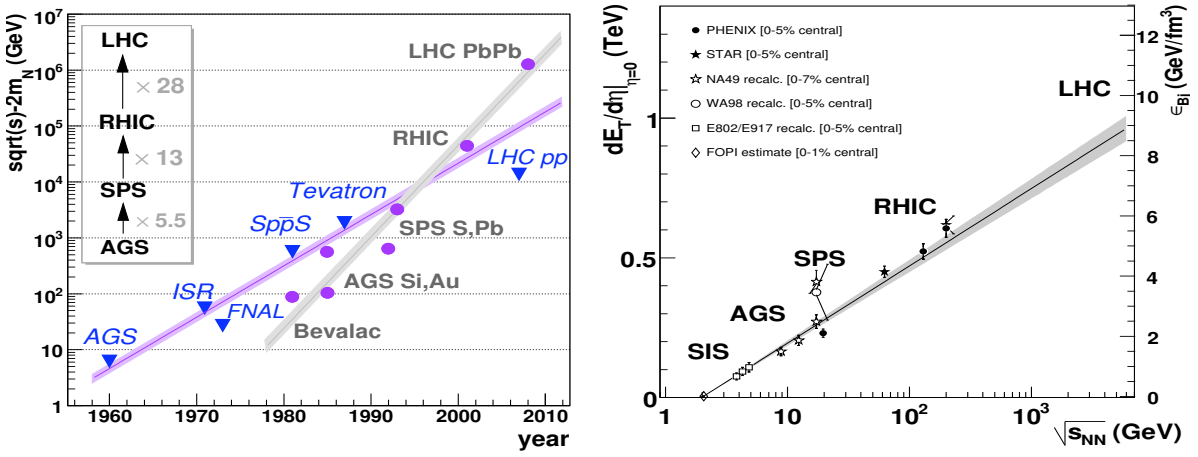

Figure 1.6: Left: "Livingston plot" for (anti)proton and ion accelerators in the period 1960-2008 (adapted from [38]). Right: Measured transverse energy per unit rapidity at $\eta = 0$ and corresponding Bjorken energy density $\epsilon_{\mathrm{Bj}}(\tau_0 = 1\ \mathrm{fm}/c)$ [39], in central heavy-ion collisions at various c.m. energies [40, 41], fitted to a logarithmic parametrisation.

The hot and dense systems produced in high-energy AA collisions are not prepared under controlled thermodynamical conditions but follow a dynamical trajectory along the phase diagram shown in Fig. 1.5. After the collision, the system (with a temperature profile decreasing from the centre) expands with relativistic longitudinal (transverse) velocities $\langle\beta\rangle \approx 1.0$ (0.5) and cools as a function of time as $T \propto \tau^{-1/n}$, with $n = 3$ for a longitudinal-only expansion [39]. When T reaches $T_c \approx 190$ MeV, the quark matter undergoes a phase transition into hadrons. The produced hadronic gas stops self-interacting collectively at freeze-out times $\tau \approx$ 10–20 fm/c [42]. At the initial stages of the reaction (1 fm/c after impact), the commonly used "Bjorken estimate" [39] gives energy densities attained at mid-rapidity of $\epsilon_{\mathrm{Bj}} = \mathrm{d}E_{\mathrm{T}}/\mathrm{d}\eta|_{\eta=0}/(\pi R_A^2\, \tau_0) \approx 5$ and 10 GeV/fm^3, at RHIC and the LHC, respectively (Fig. 1.6 right). Although these values can only be considered as a lower limit since they are obtained in a simple 1+1 D expansion scenario ignoring any effects from longitudinal work, they are already about 5 and 10 times larger, respectively, than the QCD critical energy density for deconfinement. High-energy heavy-ion colliders provide therefore the appropriate conditions for the study of highly excited quark-gluon matter.

At the LHC, the ion-ion centre of mass energies will exceed those at RHIC by nearly a factor of 30, providing access to a completely uncharted regime. Our current understanding is that this regime will be characterised by the following properties [43]:

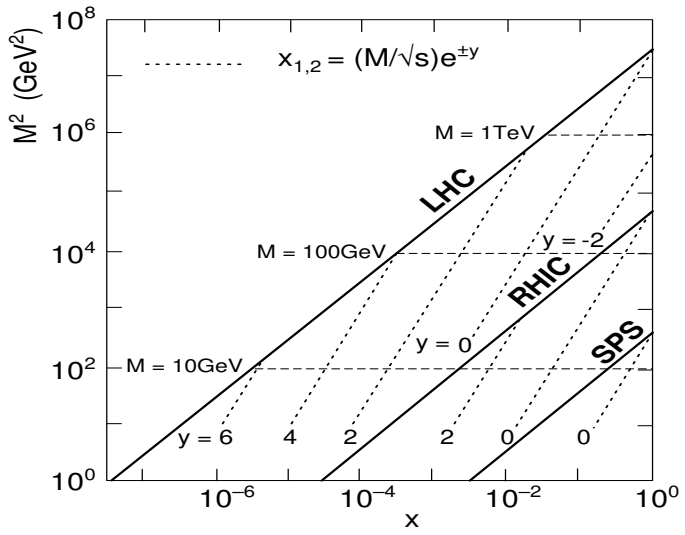

Figure 1.7: Parton kinematic range in the (x, M^2) plane for PbPb at $\sqrt{s_{NN}}$ = 5.5 TeV, compared to that of the highest RHIC and SPS energies [43].

1. An initial-state dominated by high-density (saturated) parton distributions. The relevant range of parton momentum fraction x probed at LHC will be as low as 10^{-5} (Fig. 1.7) and the characteristic saturation momentum, $Q_s^2 \approx$ 5–10 GeV^2 [48], will be a factor of 2–3 larger than at RHIC, accessing a novel perturbative regime where deviations from the standard linear evolutions in Q^2 and x are expected. Important aspects of particle production and the early time evolution of the system should be governed by classical chromodynamics, as described in the Colour-Glass-Condensate framework.

2. Hard probes — such as jets, high-p_{T} hadrons, heavy-quarks, heavy-quarkonia — will be produced abundantly (Table 1.1). The cross sections for these processes can be calculated using the perturbative QCD framework and their potential attenuation in the medium will provide precise "tomographic" information about the hottest and densest phases of the reaction.

3. Weakly-interacting perturbative probes (direct photons, dileptons, Z^0 and $W^{\pm}$ bosons) unaffected by final-state interactions in the medium will be produced with large yields (Table 1.1), providing direct information on the parton distributions of the colliding ions and an undistorted reference when produced back-to-back with (quenched) jets.

4. Parton dynamics will dominate a significant fraction of the medium evolution. The initial energy density, temperature, volume, and lifetime of the QGP state is expected to be much larger than at RHIC. Partonic degrees of freedom will thus dominate the fireball expansion and the collective features of the hadronic final state.

1.3 The CMS detector

The CMS experiment [49, 50] at the LHC is a general purpose detector designed to explore the physics at the TeV energy scale. The primary goals of the experiment are to reveal the electroweak (EWK) symmetry breaking mechanism and provide evidence of physics beyond the SM in proton-proton collisions at $\sqrt{s}$ = 14 TeV, as well as to study the properties of the

Table 1.1: The expected yield of several hard probes in 10^6 s PbPb and pPb LHC runs.

	PbPb $\sqrt{s_{NN}} = 5.5$ TeV $\mathcal{L} = 5 \times 10^{26}$ cm^{-2}s^{-1}		pPb $\sqrt{s_{NN}} = 8.8$ TeV $\mathcal{L} = 1.4 \times 10^{30}$ cm^{-2}s^{-1}	
Process	Yield/10^6 s	Ref.	Yield/10^6 s	Ref.
$\|\eta\| \leq 2.4$				
jet ($p_{\mathrm{T}} > 50$ GeV/c)	2.2×10^7	[44]	1.5×10^{10}	[45]
jet ($p_{\mathrm{T}} > 250$ GeV/c)	2.2×10^3	[44]	5.2×10^6	[45]
Z^0	3.2×10^5	[46]	6.8×10^6	[45]
W^+	5.0×10^5	[46]	1.1×10^7	[45]
W^-	5.3×10^5	[46]	1.1×10^7	[45]
all phase space				
$c\bar{c}$	9.0×10^{10}	[43]	2.0×10^{12}	[43]
$b\bar{b}$	3.6×10^9	[43]	8.2×10^{10}	[43]
$\mathrm{J}/\psi \to \mu^+\mu^-$	2.4×10^7	[47]	5.5×10^8	[47]
$\Upsilon \to \mu^+\mu^-$	1.5×10^5	[47]	3.5×10^6	[47]
$\Upsilon' \to \mu^+\mu^-$	3.7×10^4	[47]	8.4×10^5	[47]
$\Upsilon'' \to \mu^+\mu^-$	2.2×10^4	[47]	5.2×10^5	[47]

strongly interacting matter produced in PbPb collisions at the highest energy densities ever reached in the laboratory. When running in the heavy-ion mode, the LHC will collide two lead beams (as well as lighter ions in a second phase), circulating in opposite directions, at an energy of 2.75 TeV each (centre-of-mass energy $\sqrt{s_{NN}}$ = 5.5 TeV per nucleon pair). Since the detector subsystems have been designed with a resolution and granularity adapted to cope with the extremely high luminosities expected in the proton-proton running mode ($\mathcal{L} \sim 10^{34}\,\mathrm{cm}^{-2}\,\mathrm{s}^{-1}$ at 14 TeV) with up to 25 simultaneous (pile-up) pp collisions per bunch crossing, CMS can also deal with the large particle multiplicities (see Fig. 1.8) anticipated for PbPb collisions at 5.5 TeV (where $\mathcal{L} \sim 10^{27}\,\mathrm{cm}^{-2}\,\mathrm{s}^{-1}$).

The CMS apparatus measures roughly 22 m in length, 15 m in diameter and 12 500 metric tons in weight. A drawing of the detector can be seen in Fig. 1.9. Figure 1.10 shows schematic representations of the response to various types of particles superimposed on a transverse slice through the detector. A detailed description of the construction and performance of each detector system can be found in Ref. [51]. Its central feature is a 4 T solenoid, 13 m in length and 6 m in diameter. Along with the central silicon pixel and microstrip tracking detector, the electromagnetic ($|\eta| < 3$) and hadronic ($|\eta| < 5$) calorimeters are contained within the solenoid coil. Muon detectors ($|\eta| < 2.4$) are embedded in the flux return iron yoke of the magnet. Two other detectors cover the very forward hemisphere (Fig. 1.11): CASTOR ($5.3 < |\eta| < 6.6$) and the Zero-Degree Calorimeters (ZDC, $|\eta| > 8.3$ for neutrals). The TOTEM experiment, which shares the interaction point with CMS, provides two extra trackers at forward rapidities (T1 at $3.1 < |\eta| < 4.7$ and T2 at $5.5 < |\eta| < 6.6$).

The innermost tracking is accomplished with three layers of silicon pixel detectors (at radii of 4.4, 7.3 and 10.2 cm) with a total area of approximately 1 m^2, composed of 66 million 100×150 μm^2 area pixels. The remaining tracking layers are composed of 9.3 million single- and double-sided silicon microstrip detectors covering a total of 200 m^2 of detectors, organised in an inner barrel (TIB) with 4 layers within the 20–50 cm radius range, an outer barrel (TOB)

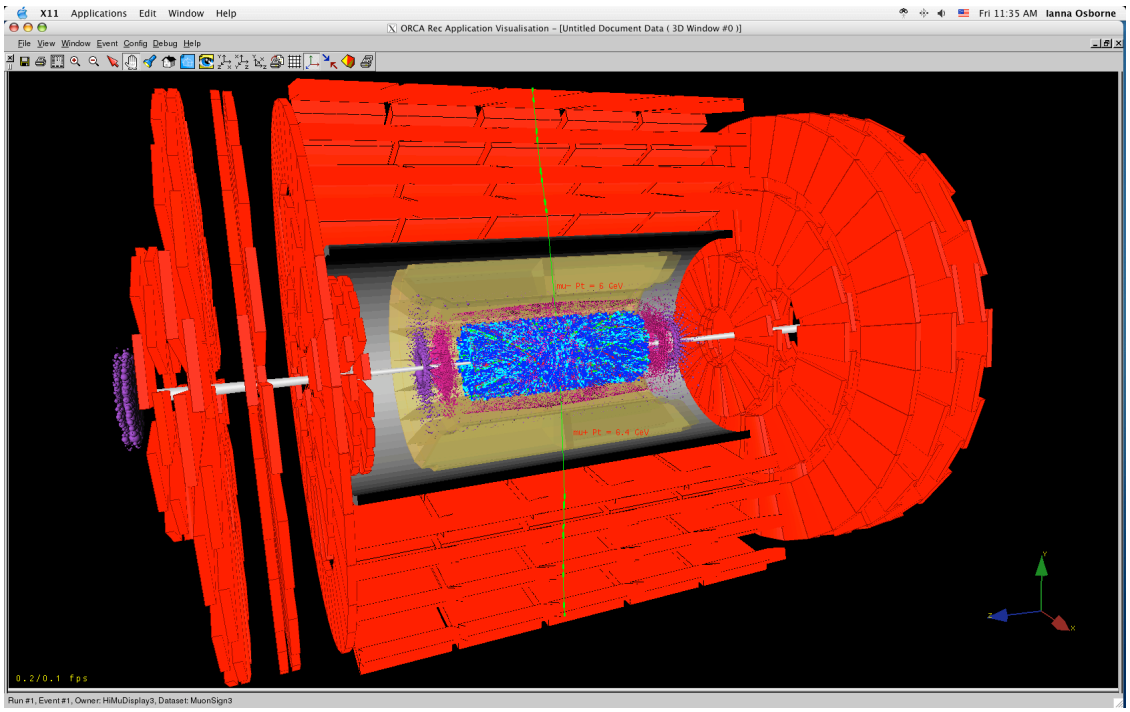

Figure 1.8: CMS event display of a simulated $\Upsilon \rightarrow \mu^+\mu^-$ produced in a PbPb collision at $\sqrt{s_{NN}}$ = 5.5 TeV with charged multiplicities at mid-rapidity $\mathrm{d}N_{\mathrm{ch}}/\mathrm{d}\eta|_{\eta=0}$ = 3500.

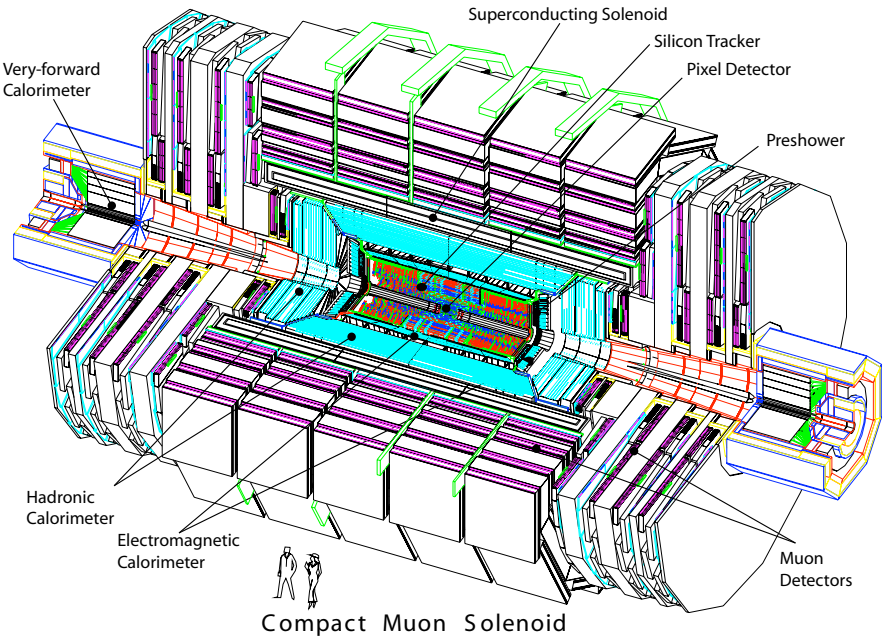

Figure 1.9: The CMS detector.

with 6 layers within the 55–120 cm radius range, and two endcap detectors (TEC and TID).

The electromagnetic calorimeter consists of $\sim$76 000 Lead-Tungstate crystals ($\sim 25\, X_0$ with granularity $\Delta\eta \times \Delta\phi = 0.0174 \times 0.0174$) read out by Avalanche Photodiodes, plus $\sim$6000 endcap silicon pre-shower detectors. Hadronic calorimetry is achieved with scintillators embed-

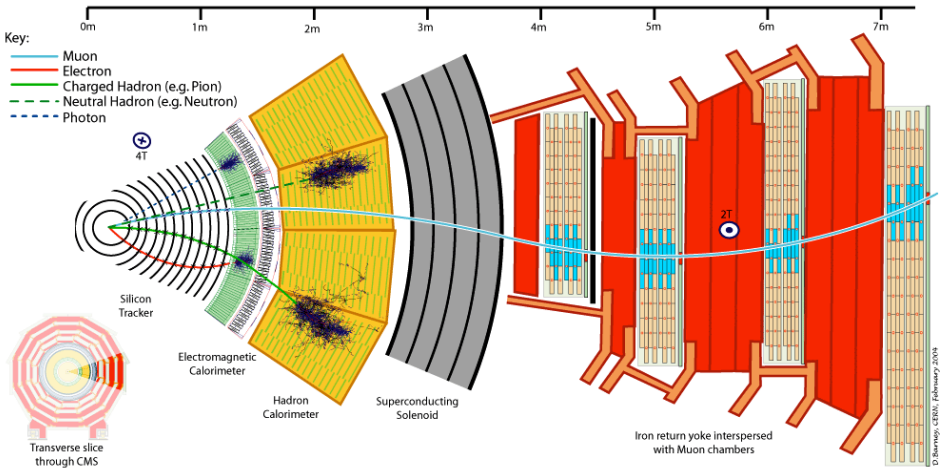

Figure 1.10: A transverse slice through one segment of the CMS detector indicating the responses of the various detecting systems to different types of particles.

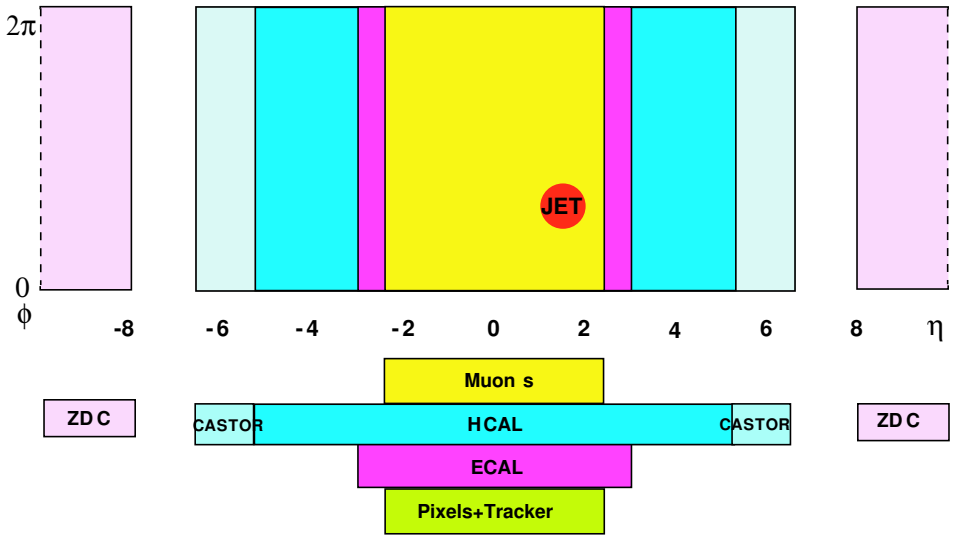

Figure 1.11: CMS acceptance of tracking, calorimetry, and muon identification in pseudorapidity (η) and azimuth (ϕ). The size of a jet with cone $R = 0.5$ is also depicted for illustration.

ded in a brass absorber (9072 readout channels for a granularity of $\Delta\eta \times \Delta\phi = 0.087 \times 0.087$ at central rapidities and $\Delta\eta \times \Delta\phi = 0.175 \times 0.175$ at forward rapidities), where the light is read out using Hybrid Photodiodes (HPD).

The CMS muon system, covering the pseudorapidity window $|\eta| < 2.4$, is made of three detector technologies: Drift Tubes (DT) are used in the CMS barrel, Cathode Strip Chambers (CSC) in the endcaps, and Resistive Plate Chambers (RPC) are used in parallel with the other detectors, both in the barrel and in the endcaps. In total, the muon system contains about 25 000 m^2 of active detection planes, and nearly 1 million electronic channels.

The CASTOR and ZDC detectors are tungsten plus quartz sampling Čerenkov calorimeters with hadronic and electromagnetic sections and a few hundred readout channels in total.

1.4 Heavy-ion observables with CMS

The aim of this section is to give a concise experimental and phenomenological overview of the heavy-ion observables that can be measured in CMS. Emphasis is put on those measurements which can help clarify some of the current open issues at RHIC [52]. Chapters 2–8 describe in detail the analyses and physics reach for the sample of measurements introduced here.

1.4.1 PbPb rapidity density: low-x gluon saturation

The charged-particle multiplicity per unit rapidity at mid-rapidity, $\mathrm{d}N_{\mathrm{ch}}/\mathrm{d}\eta|_{\eta=0}$, is related to the produced entropy density in the PbPb collision and fixes the global properties of the produced medium. Before the start up of RHIC, extrapolations from SPS measurements at $\sqrt{s_{_{NN}}} \approx 20$ GeV varied widely, mostly overestimating the result [53]. The bulk hadron multiplicity measured in central AuAu at $\sqrt{s_{_{NN}}} = 200$ GeV, $\mathrm{d}N_{\mathrm{ch}}/\mathrm{d}\eta|_{\eta=0} \approx 700$, is comparatively lower than the $\mathrm{d}N_{\mathrm{ch}}/\mathrm{d}\eta|_{\eta=0} \approx 1000$ expectations of "minijet"-dominated scenarios [54], soft Regge models [55] (without accounting for strong shadowing effects [56]), or extrapolations from an incoherent sum of proton-proton collisions [53]. On the other hand, Colour Glass Condensate (CGC) approaches [57, 58] which effectively take into account a reduced initial number of scattering centres in the nuclear PDFs, $f_{a/A}(x,Q^2) < A\, f_{a/N}(x,Q^2)$, can reproduce the RHIC data. In the saturation models, non-linear effects (gluon-gluon fusion processes at low values of x) become important and saturate the parton densities when the area occupied by the partons becomes similar to that of the hadronic system, πR_A^2. For a nucleus with A nucleons, radius $R_A \sim A^{1/3}$ and total gluon distribution $xG_A(x,Q^2) = A\, xg(x,Q^2)$, where $g(x,Q^2)$ is the gluon density in a single nucleon, this condition translates into the following "saturation momentum" [59, 60]:

$$Q_s^2(x) \simeq \alpha_s \frac{1}{\pi R_A^2}\, xG_A(x,Q^2) \sim A^{1/3}\, x^{-\lambda} \sim A^{1/3}(\sqrt{s})^{\lambda} \sim A^{1/3} e^{\lambda y}, \tag{1.1}$$

with $\lambda \approx 0.2$–0.3 [57]. The mass number dependence implies that, at comparable energies, non-linear effects will be $A^{1/3} \approx 6$ times larger in a heavy nucleus ($A \sim 200$ for Au or Pb) than in a proton. Based on the general expression (1.1), CGC-based models can reproduce the centrality and c.m. energy dependences of the bulk AA hadron production (Fig. 1.12-left). Compared to RHIC, the relevance of low-x QCD effects will certainly be enhanced at the LHC due to the increased centre-of-mass energy and rapidity of the produced partons [27, 44]. The expected hadron multiplicities at midrapidity are of the order $\mathrm{d}N/\mathrm{d}\eta|_{\eta=0} \approx 2000$ (Fig. 1.12-right), much lower than the $\mathrm{d}N/\mathrm{d}\eta|_{\eta=0} \approx 8000$ predictions before RHIC results.

1.4.2 Soft spectra: baryochemical potential, freeze-out temperature

Measurements of hadron momentum spectra and ratios at low p_{T} ($p_{\mathrm{T}} \lesssim 2$ GeV/c) are an important tool to determine the amount of collective radial flow generated and the thermal and chemical conditions in the final (freeze-out) phase of the reaction. The measured single hadron p_{T} spectra at RHIC and SPS have an inverse slope parameter T_{eff} larger than that measured in pp collisions, increasing with reaction centrality and with hadron mass, as expected if collective expansion blue-shifts the hadron spectra. Phenomenological fits of the spectra to "blast wave" models ($T_{\mathrm{eff}} \approx T + \langle\beta_{\mathrm{T}}\rangle^2\, m$) yield transverse flow velocities $\langle\beta_{\mathrm{T}}\rangle \approx 0.6$ [65]. Full hydrodynamical calculations which start with a partonic phase very shortly after impact ($\tau_0 < 1$ fm/c) develop the amount of collective radial flow needed to accurately reproduce all the measured hadron spectra (Fig. 1.13).

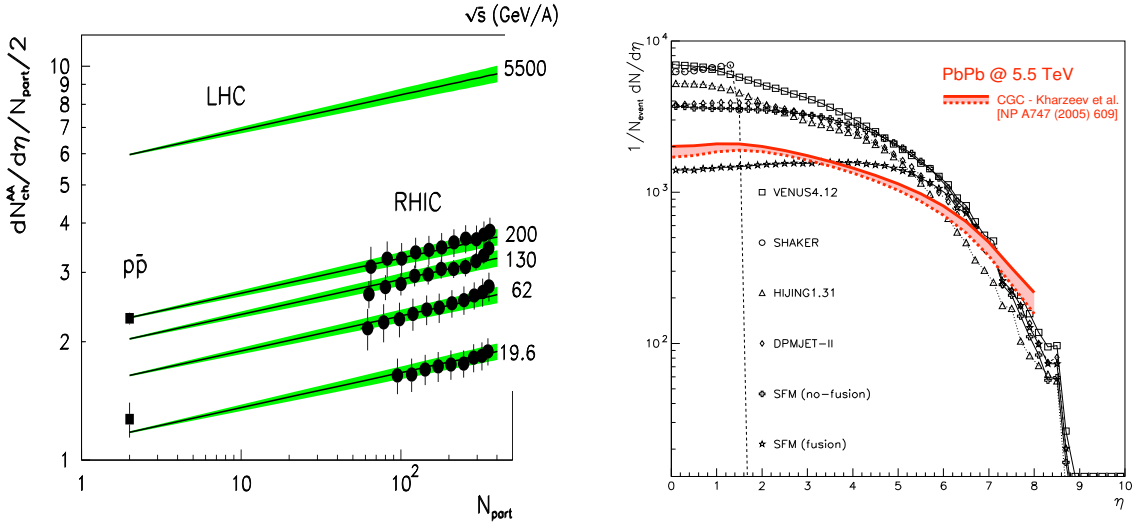

Figure 1.12: Left: Collision energy and centrality dependences of the charged particle multiplicity at mid-rapidity, $\mathrm{d}N_{\mathrm{ch}}/\mathrm{d}\eta|_{\eta=0}$ ($\mathrm{d}N_{\mathrm{ch}}/\mathrm{d}\eta|_{\eta=0}$ is normalised by the number of participating nucleon pairs, $N_{\mathrm{part}}/2$, and the centrality is given in terms of N_{part}): the PHOBOS data [61] is compared to the gluon saturation model prediction of Ref. [58]. Right: Model predictions for $dN/d\eta$ in central PbPb at $\sqrt{s_{NN}}$ = 5.5 TeV [48, 56].

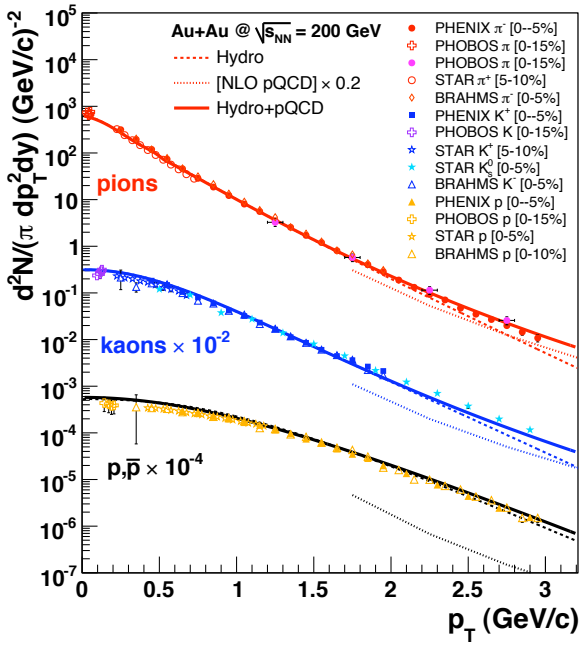

Figure 1.13: Transverse momentum spectra for pions, kaons, and (anti)protons measured at RHIC below $p_{\mathrm{T}} \approx 3$ GeV/c in 0-10% most central AuAu collisions at $\sqrt{s_{NN}}$ = 200 GeV compared to hydrodynamics calculations [62]. Above $p_{\mathrm{T}} \approx 2$ GeV/c the expected perturbative contributions of hard scattering products [63, 64] (scaled as described in [62]) are also shown.

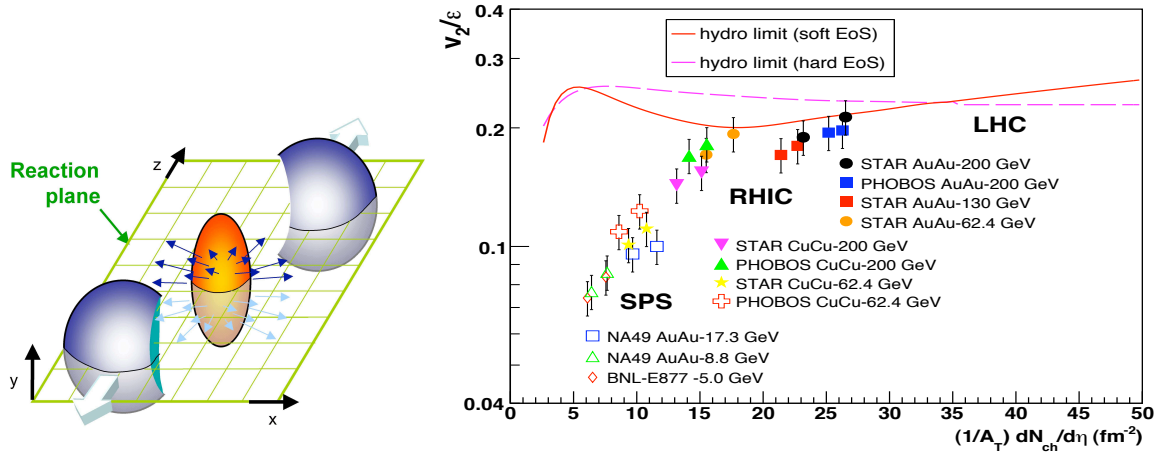

Figure 1.14: Left: Spatial asymmetry with respect to the reaction plane of the produced "fireball" in non-central nucleus-nucleus collisions. Right: Elliptic flow (normalised by the participant eccentricity) [66] v_2/ϵ, as a function of the charged hadron rapidity density, $\mathrm{d}N_{\mathrm{ch}}/\mathrm{d}\eta|_{\eta=0}$, normalised by the reaction overlap area $A_{\perp}$, measured at SPS [67, 68] and RHIC [68, 69], compared to the "hydrodynamical limit" expectations for a fully thermalized system with hard (hadron-gas like) or soft (QGP-like) EoS [70–72]. Adapted from [69] (10% errors have been added to account for the v_2 and ϵ systematic uncertainties).

Measurement of the bulk pion, kaon and (anti)proton spectra in PbPb at 5.5 TeV and their comparison to the hydrodynamical predictions will provide the first estimates of the thermodynamical conditions characterising the initial- (thermalisation time, baryochemical potential) and final- (freeze-out temperature) states of the produced medium. In particular, the abundance of strange hadrons or the $\mathrm{p}/\bar{\mathrm{p}}$ ratio at mid-rapidity, determine the strangeness undersaturation factor γ_s or the baryo-chemical potential, μ_B, respectively of the thermalized fireball. At the LHC, the expected formation of a virtually baryon-free system with μ_B close to zero at mid-rapidity, will result in a $\mathrm{p}/\bar{\mathrm{p}} \approx 1$ at $y = 0$. In addition, the possibility to identify various hadron species and measure their yield with respect to the reaction plane (see next section) will more strongly constrain the equation of state and dynamical evolution of the system.

1.4.3 Elliptic flow: thermalisation time, medium shear viscosity

The initial-state in nucleus-nucleus collisions with non-zero impact parameter is characterised by an anisotropic distribution in coordinate-space given by the lenticular- or almond-like shape of the overlapping zone (Fig. 1.14-left). If the produced system behaves collectively, the initial spatial anisotropy translates into a final elliptical asymmetry in momentum-space with respect to the reaction plane because the pressure gradient is larger for directions parallel to the smallest dimension of the lens. As a result, the final azimuthal distributions, $\mathrm{d}N/\mathrm{d}\Delta\phi$, of the produced hadrons ($\Delta\phi = \phi - \Phi_{RP}$) show a strong harmonic modulation with a preferential "in-plane" emission in non-central collisions. The strength of this asymmetry is quantified via the second Fourier coefficient, $v_2(p_{\mathrm{T}}, y) \equiv \langle\cos(2\Delta\phi)\rangle$, of the azimuthal decomposition of single inclusive hadron spectra relative to the reaction plane [73, 74],

$$E\frac{\mathrm{d}^3N}{\mathrm{d}^3p} = \frac{1}{2\pi}\frac{\mathrm{d}^2N}{p_{\mathrm{T}}\,\mathrm{d}p_{\mathrm{T}}\,\mathrm{d}y}\left(1 + 2\sum_{n=1}^{\infty} v_n\,\cos[n(\phi - \Phi_{RP})]\right). \tag{1.2}$$

At RHIC, a large v_2 value has been measured (Fig. 1.14-right), $v_2 \approx 0.2$, indicative of a strong degree of collectivity (pressure gradients) building up in the first instants of the collision. Such a strong v_2 is not consistent with the much lower values, $v_2 \lesssim 0.06$, expected by transport models of hadronic matter [75] or for a partonic system rescattering with perturbative cross sections ($\sigma_{gg} \approx 3$ mb) [76]. The magnitude, and the $p_{\rm T}$ and hadron mass dependences of the radial and elliptic flows below $p_{\rm T} \approx 2$ GeV/c are, on the other hand, well described by *ideal* hydrodynamic models whose space-time evolution starts with a realistic QGP equation of state (EoS) with initial energy densities $\varepsilon_0 \approx 30$ GeV/fm^3 at thermalisation times $\tau_0 \approx 0.6$ fm/c [42, 72, 77, 78] (Fig. 1.14-right). Such a degree of accord between relativistic hydrodynamics and the data was absent at lower CERN-SPS energies [67]. Figure 1.14-right shows the particle-density dependence of the v_2 parameter (scaled by the eccentricity of the reaction ϵ to remove centrality-dependent geometrical effects) in semi-central nucleus-nucleus collisions at different c.m. energies. RHIC v_2 data in the range $\sqrt{s_{NN}} \approx$ 62–200 GeV [68, 69, 79] are close to the hydrodynamical limit curves [70, 71] estimated for a completely thermalized system.

The robust collective flow generated in the first instants of the reaction, the fast (local) thermalisation times, and the good agreement of the data with *ideal* relativistic hydrodynamic models which assume a fluid evolution with zero viscosity (i.e. with negligible internal shear stress), have been presented as evidence that the matter formed at RHIC is a *strongly interacting* QGP (sQGP) [80–84]. This new state of matter with *liquid*-like properties, challenges the anticipated paradigm [5, 6] of a weakly interacting gas of relativistic partons, lending support to the application of strongly-coupled-gauge/weakly-coupled-gravity duality techniques [30–34] to compute relevant sQGP parameters (see Section 1.1). It is worth noting that in the range of temperatures attained at RHIC, $T \lesssim 2\,T_c$, lattice QCD predictions for the pressure and energy-density are still far from fulfilling the expected $P \approx \varepsilon/3$ ideal-gas relation. Figure 1.15 shows recent calculations [85] of the *interaction measure* $I = (\varepsilon - 3P)$, normalised by T^4, which clearly deviate from the ideal-gas $I \approx 0$ value in the range $T \lesssim 3\,T_c$. This result shows that strong interactions between the plasma constituents persist in the deconfined phase at several times T_c. The initial temperatures in central PbPb collisions at the LHC[2] will be of the order of $T \approx 3\,T_c$ where the interaction measure approaches its asymptotic value. The measurement of the differential elliptic flow properties in PbPb collisions at the LHC will be of primary importance to confirm or reject the sQGP interpretation as well as to search for a possible weakening of v_2, indicative of the existence of a weakly-interacting QGP phase at higher temperatures than those of the liquid-like state found at RHIC [86, 87]. In addition, at LHC energies the contribution from the QGP phase to the collective particle flow(s) is expected to be much larger than at RHIC or SPS and, therefore, v_2 will be less dependent on the details of the late hadronic phase.

1.4.4 Hard processes: "tomographic" probes of QCD matter

Among all available experimental observables, the so-called hard probes (particles with large transverse momentum $p_{\rm T}$ and/or high mass [52, 88]) are of crucial importance for several reasons (Fig. 1.16): (i) they originate from parton scattering with large momentum transfer Q^2 and thus are directly coupled to the fundamental QCD degrees of freedom; (ii) their production timescale is very short, $\tau \approx 1/p_{\rm T} \lesssim 0.1$ fm/c, allowing them to propagate through,

[2] A particle multiplicity in central PbPb of $\mathrm{d}N_{\rm ch}/\mathrm{d}y|_{y=0} \approx 2000$, corresponds to an energy density $\varepsilon_0 \approx (0.5\,\rho)^{4/3} \approx [0.5\,\mathrm{d}N_{\rm ch}/\mathrm{d}y|_{y=0}/(\tau_0\,A_\perp)]^{4/3} \approx 100$ GeV/fm^3 at an initial time τ_0 = 0.3 fm/c. A fully equilibrated QGP at these energy densities would have a temperature of $T_0 \approx (\varepsilon_0/12)^{1/4} \approx 0.52$ GeV.

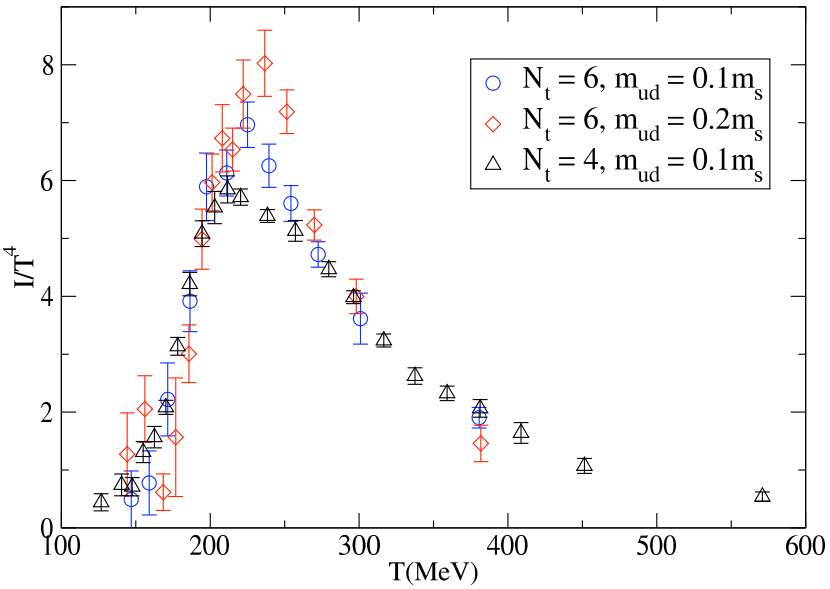

Figure 1.15: Lattice QCD calculations of the "interaction measure", $I/T^4 = (\varepsilon - 3P)/T^4$, as a function of the temperature for various lattice spacings $N_t = 4, 6$ and quark masses $m_{u,d} = 0.1, 0.2 m_s$ [85], with $T_c \approx 170$ MeV.

and potentially be affected by, the medium; (iii) their cross sections can be theoretically predicted using the perturbative QCD (pQCD) framework. Hard processes thus constitute experimentally- and theoretically-controlled (self-generated) "tomographic" probes of the hottest and densest phases of the reaction.

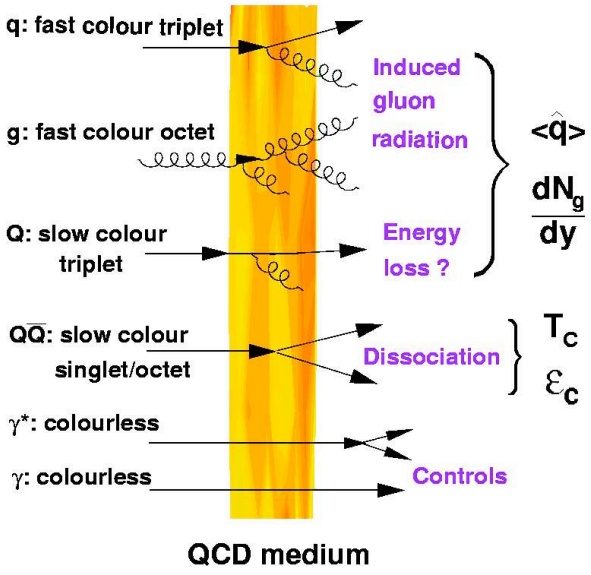

Figure 1.16: Examples of hard probes whose modifications in high-energy AA collisions provide direct information on properties of QCD matter such as the medium transport coefficient $\langle \hat{q} \rangle$, the initial gluon rapidity density $\mathrm{d}N_g/\mathrm{d}y$, and the critical temperature and energy density [52].

1.4.5 Jets and high-p_{T} hadrons: parton number density and medium transport coefficient

Among the most exciting results of the RHIC physics programme is the factor $\sim$5 suppression of high-p_{T} leading hadrons in central AuAu [89] compared to an incoherent superposition of pp collisions (Fig. 1.17). Such a result is consistent with the predicted attenuation of the parent quark and gluon jets due to energy loss in a dense QCD medium ("jet quenching") [90, 91]. The dominant contribution to the energy loss is believed to be of non-Abelian radiative nature ("gluon-strahlung") as described in the GLV [92, 93] and BDMPS [94–97] formalisms. In the GLV approach, the initial gluon density $\mathrm{d}N_g/\mathrm{d}y$ of the expanding plasma (with transverse area $A_\perp$ and length L) can be estimated from the measured energy loss ΔE,

$$\Delta E \propto \alpha_S^3 \, C_R \, \frac{1}{A_\perp} \frac{\mathrm{d}N_g}{\mathrm{d}y} \, L \, , \tag{1.3}$$

where C_R is the Casimir colour factor of the parton (4/3 for quarks, 3 for gluons). In the BDMPS framework, the transport coefficient $\langle \hat{q} \rangle$, characterising the scattering power of the medium[3], can be derived from the average energy loss according to

$$\langle \Delta E \rangle \propto \alpha_S \, C_R \, \langle \hat{q} \rangle \, L^2. \tag{1.4}$$

From Eqs. (1.3) and (1.4), very large initial gluon rapidity densities, $\mathrm{d}N_g/\mathrm{d}y \approx 1100 \pm 300$ [93], or, equivalently, transport coefficients $\langle \hat{q} \rangle \approx 11 \pm 3$ GeV^2/fm [98–101], are required in order to explain the observed amount of hadron suppression at RHIC, as quantified by the *nuclear modification factor*:

$$R_{AA}(p_T, y; b) \, = \, \frac{\mathrm{d}^2 N_{AA}/\mathrm{d}y\mathrm{d}p_T}{\langle T_{AA}(b) \rangle \, \times \, \mathrm{d}^2\sigma_{pp}/\mathrm{d}y\mathrm{d}p_T}, \tag{1.5}$$

which measures the deviation of AA at impact parameter b from a simple incoherent superposition of NN collisions. In Eq. (1.5), $T_{AB}(b)$ (normalised to $A \cdot B$) is the nuclear overlap function at b determined within a geometric Glauber eikonal model using the known Woods-Saxon distribution for the colliding nuclei [102]. The corresponding predictions for the inclusive charged hadron suppression at LHC are shown in Fig. 1.17.

Most of the empirical properties of the quenching factor for light-flavour hadrons — the magnitude, p_{T}, centrality, and the $\sqrt{s_{NN}}$ dependences of the suppression — are in quantitative agreement with the predictions of non-Abelian parton energy loss models [106]. However, the fact that the high-p_{T} $e^{\pm}$ spectrum from semi-leptonic D and B decays is as suppressed as the light hadrons in central AuAu [107, 108] is in apparent conflict with the robust $\Delta E_Q < \Delta E_q < \Delta E_g$ prediction of radiative energy loss models. In order to reproduce the measured high-p_{T} open charm/beauty suppression, jet quenching models require either initial gluon rapidity densities ($\mathrm{d}N_g/\mathrm{d}y \approx 3000$ [109]) inconsistent with the total hadron multiplicities ($\mathrm{d}N_g/\mathrm{d}y \approx 1.8\,\mathrm{d}N_{\mathrm{ch}}/\mathrm{d}\eta|_{\eta=0}$ [106]) or with the values ($\mathrm{d}N_g/\mathrm{d}y \approx 1100$) needed to describe the quenched light hadron spectra, or they need a smaller relative contribution of B relative to D mesons than theoretically expected in the measured p_{T} range [100]. This discrepancy may point to an additional contribution from elastic energy loss for heavy quarks [110–112], so far considered negligible [91]. At the LHC, the original capability to fully reconstruct jets [44], to tag them with unscathed prompt γ [113] or Z^0 [114], and to

[3]The $\hat{q}$ parameter is the squared average momentum transfer of the hard parton per unit distance, $\hat{q} = \langle k_{\mathrm{T}}^2 \rangle / \lambda$, and can be identified [31] with the coefficient in the exponential of an adjoint Wilson loop averaged over the medium length L: $\langle W^A(\mathcal{C}) \rangle \equiv \exp\left[(-1/4\sqrt{2})\hat{q}L^- L^2\right]$.

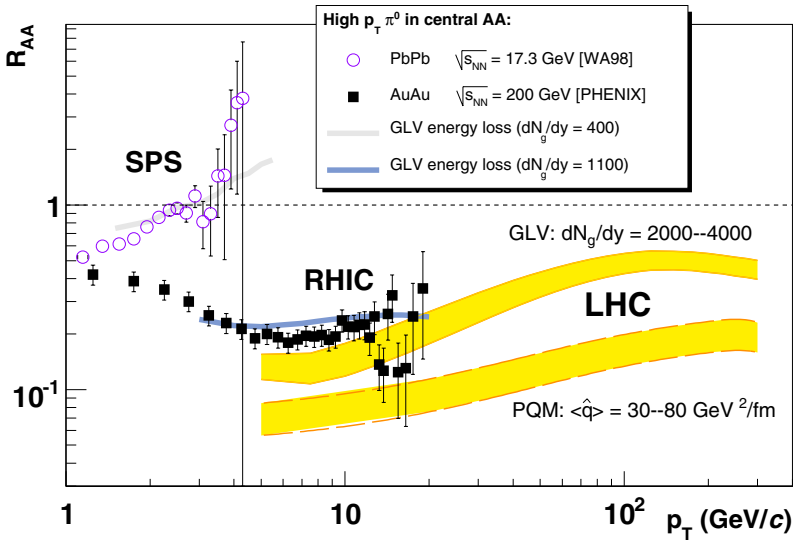

Figure 1.17: Nuclear modification factor, $R_{AA}(p_{\mathrm{T}})$, for high-p_{T} neutral pions at CERN-SPS [103, 104] and RHIC [105] compared to the predictions of the GLV parton energy loss model [93] for two values of the initial gluon rapidity density, $\mathrm{d}N_g/\mathrm{d}y$. The bottom bands show the expected suppression of inclusive high-p_{T} charged hadrons in central PbPb collisions at 5.5 TeV as given by the GLV ($\mathrm{d}N_g/\mathrm{d}y$ = 2000–4000) and the PQM ($\langle\hat{q}\rangle \approx$ 30–80 GeV^2/fm) [98, 101] models.

carry out high-statistics studies in the heavy-flavour sector [47], will be very valuable to clarify the apparently conflicting results at RHIC and to provide accurate information on the transport properties of QCD matter.

1.4.6 Quarkonia: critical temperature and energy density

The study of heavy-quark bound states in high-energy AA collisions has long been proposed as a sensitive probe of the thermodynamical properties of the produced medium [115]. Analysis of quarkonia correlators and potentials in finite-T lattice QCD indicate that the different charmonium and bottomonium states dissociate at temperatures for which the colour (Debye) screening radius of the medium falls below their corresponding $Q\overline{Q}$ binding radii. Recent lattice analyses of the quarkonia spectral functions [116–119] indicate that the ground states (J/ψ and Υ) survive at least up to $T \approx 2\,T_c$ whereas the less bound χ_c and ψ' melt near T_c. Experimental confirmation of such a threshold-like dissociation pattern would provide a direct means to determine the transition temperature reached in the system and their comparison to *ab initio* lattice QCD predictions. A significant amount of experimental data on J/ψ production in different proton-(deuteron-)nucleus and nucleus-nucleus collisions have been collected at SPS [120–122] and at RHIC [123]. The corresponding nuclear modification factors, compiled in Ref. [124], are shown in Fig. 1.18 as a function of N_{part}. The surprisingly similar amount of J/ψ suppression observed at SPS and RHIC energies (with expected temperature differences of a factor of $\sim$2) has been interpreted in a sequential-dissociation scenario [125] where the J/ψ survives up to $T \approx 2\,T_c$ in agreement with the lattice predictions, and the observed suppression at both c.m. energies is due to the absence of feed-down decay contributions from $\chi_c(1P)$ ($\sim$30%) and $\psi'(2S)$ ($\sim$10%) resonances which melt at $T \approx T_c$. The confirmation of such an interpretation would set an upper limit of $T \lesssim 2\,T_c \approx 400$ MeV for the temperatures reached at RHIC.

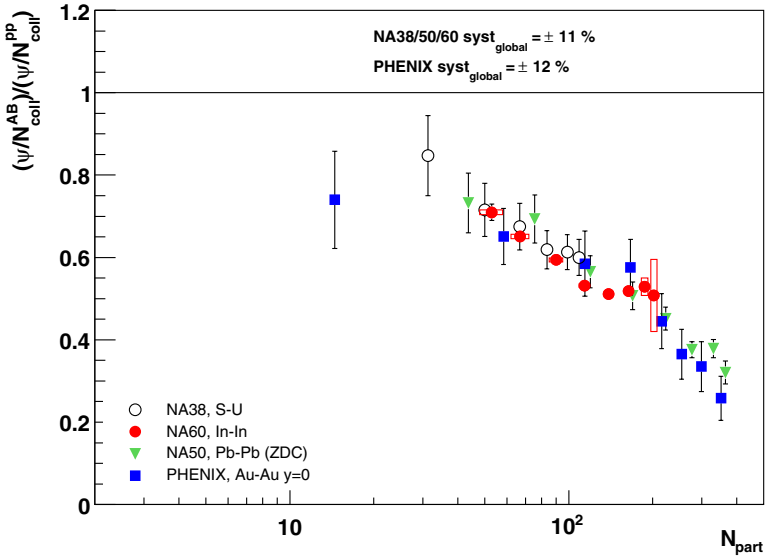

Figure 1.18: J/ψ nuclear modification factor versus centrality [124] (given by the number of participant nucleons in the collision) measured in nucleus-nucleus collisions at the SPS [120–122] and RHIC [123].

Other explanations of the comparatively low depletion of J/ψ yields at RHIC have been put forward based on a much stronger direct J/ψ suppression (at temperatures close to T_c) combined with $c\bar{c} \rightarrow \mathrm{J}/\psi$ regeneration from the abundant charm quarks[4] in the dense medium [126]. The LHC measurements will be also crucial to resolve this issue. A strongly suppressed J/ψ yield in PbPb at 5.5 TeV — where the expected initial temperatures will be well above $2\,T_c$ — would support the sequential-screening scenario, whereas recombination models predict a strong enhancement due to the larger density of $c\bar{c}$ pairs in the medium. In addition, the abundant production of the $\Upsilon(1S, 2S, 3S)$ states at LHC energies will open up a unique opportunity to study the threshold dissociation behaviour of the whole bottomonium family. The Υ is expected to survive up to $4T_c$ and, therefore, *direct* suppression of the $b\bar{b}$ ground state would be indicative of medium temperatures around 1 GeV at the LHC.

1.4.7 Electromagnetic PbPb interactions: high-energy photoproduction

Lead nuclei accelerated to ultrarelativistic energies at the LHC are a powerful source of quasi-real photons due to the coherent action of the $Z = 82$ proton charges and the Lorentz contraction factor $\gamma \approx 2900$ of the electromagnetic field at such high energies. In ultra-peripheral collisions (UPCs) of heavy-ions at impact parameters larger than twice the nuclear radius, where no nucleon-nucleon collisions occur, a strong flux of photons is generated that can be used for high-energy photoproduction ($\gamma\,\mathrm{A}$, $\gamma\,\gamma$) studies, as shown schematically in Fig. 1.19 [127–129]. The equivalent photon spectrum flux in UPCs increases with Z^2/E_γ and, thus, for Pb there is a $Z^2 \sim 7000$ enhancement factor compared to electron or proton beams. The upper bound in the equivalent photon energy spectrum is of the order of the inverse Lorentz-contracted radius R_A of the charge: $\omega_{\max} \approx \gamma/R_A$. The requirement that all the charges act coherently in the generation of the equivalent quasi-real photon imposes very small virtualities for the photoproduction process. Therefore, the beam charges are barely deflected in the process and any produced particles have very low transverse momenta of

[4] On average, 10 charm pairs are produced in a central AuAu collision at the top RHIC energy.

the order of $p_{\mathrm{T}} < 2/R_A \approx 50$ MeV/c or $p_{\mathrm{T}} \sim m_X/\gamma \approx 30$ MeV/c. At the LHC, lead beams at 2.75 TeV/nucleon have Lorentz factors γ = 2930 leading to maximum (equivalent) photon energies $\omega_{\max} \approx 80$ GeV. These photons can then collide either with the other incoming nucleus at maximum c.m. energies of $W_{\gamma\mathrm{Pb}}^{\max} \approx 1$ TeV/nucleon (3–4 times larger than those of equivalent ep collisions at HERA), or they can interact with another similarly-radiated photon leading to two-photon collisions at $W_{\gamma\gamma}^{\max} \approx 160$ GeV, comparable to (or slightly higher than) those studied at LEP.

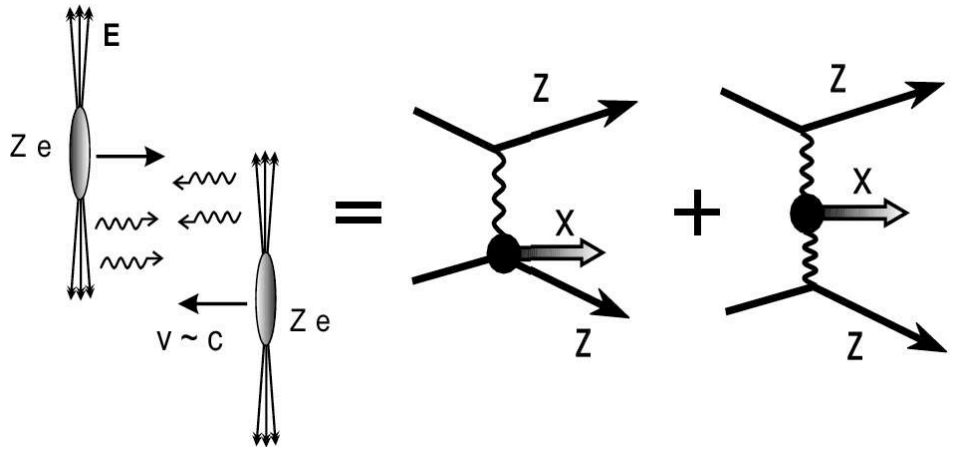

Figure 1.19: Schematic diagram of an ultraperipheral collision (UPC) of two ions, leading to two typical photoproduction processes (γ A and $\gamma\,\gamma$ collisions).

The physics interest of ultraperipheral PbPb collisions at LHC is twofold. On the one hand, γ A collisions open up the possibility to carry out precision QCD studies [130] — e.g. of the gluon distribution function in the nucleus or of (photoproduced) vector-meson absorption in cold nuclear matter — with a low background and much simpler initial state than in equivalent pA or AA studies. On the other hand, photon-photon collisions provide the conditions to study QED in a non-perturbative regime (with $\alpha_{\mathrm{em}}Z \sim$0.6), as well as the production of $\mathcal{C}$-even heavy mesons ($c\bar{c}, b\bar{b}$) or the physics of quartic gauge couplings ($\gamma\,\gamma W^+W^-$) [131]. The feasibility of such studies has been proven at RHIC energies where the existing UPC measurements include ρ^0 [132] and J/ψ [133] photoproduction in photon-gold collisions as well as low- [134] and high-mass [133] dielectron production in two-photon processes.

1.4.8 Forward physics: low-x partons, baryon-rich QCD matter, and the cosmic-ray connection

Forward coverage is essential for measurements of the low-x parton distribution functions, particularly the gluon distributions, in protons and nuclei. Indeed, from leading-order kinematics the rapidities and momentum fractions of two colliding partons are related via

$$x_2 = (p_{\mathrm{T}}/\sqrt{s}) \cdot (e^{-y_1} + e^{-y_2}) \quad \text{and} \quad x_1 = (p_{\mathrm{T}}/\sqrt{s}) \cdot (e^{y_1} + e^{y_2})\,, \tag{1.6}$$

and the *minimum* momentum fractions probed in a $2 \to 2$ process with a particle of momentum p_{T} produced at pseudo-rapidity η are [135]

$$x_2^{\min} = \frac{x_{\mathrm{T}}\, e^{-\eta}}{2 - x_{\mathrm{T}}\, e^{\eta}}\,, \quad x_1^{\min} = \frac{x_2\, x_{\mathrm{T}}\, e^{\eta}}{2x_2 - x_{\mathrm{T}}\, e^{-\eta}}\,, \text{ where } \quad x_{\mathrm{T}} = 2\,p_{\mathrm{T}}/\sqrt{s}\,. \tag{1.7}$$

$x_2^{\min}$, in particular, decreases by a factor of about 10 every 2 units of (pseudo)rapidity. At LHC energies, the relevant x values in AA and pA collisions will be 30–45 times lower than

at RHIC: $x_2 \approx 10^{-5}$–10^{-6} for processes with a hard scale of a few GeV^2 at rapidities $\eta \approx 5$–6 (see Fig. 1.7), far exceeding the reach of previous parton distribution measurements. In this kinematic regime, the nonlinear evolution of the parton densities can be fully mapped out, thereby clarifying the nature of the gluon saturation predicted by CGC models.

In addition, the study of the bulk particle and energy flow in AuAu and p(d)Au collisions at forward rapidities has proven of great interest at RHIC to fully characterise the longitudinal dependence of the properties of the produced medium [136, 137]. On the one hand, several measurements [138–140] have given evidence for the existence of an extended longitudinal scaling (also called "limiting fragmentation" [141]) region close to beam rapidity, which increases with $\sqrt{s_{NN}}$ (Fig. 1.20-left). On the other hand, measurements in the forward region can be used to study baryon density effects on particle production, essentially changing the chemistry of the produced quark-gluon system [142, 143]. Thermal and chemical analyses of the current data in different rapidity slices indicate that the system has larger baryo-chemical potential, less transverse flow and fewer degrees of freedom at forward rapidity [144]. Based on extrapolations from BRAHMS data (Fig. 1.20-right), the maximum net baryon density at the LHC is expected in the pseudorapidity region $\eta \approx 5$–6. Studies of baryon production in the forward rapidities will thus shed light on the mechanism of baryon stopping and transport as well as of partonic matter over a wide range of baryo-chemical potentials.

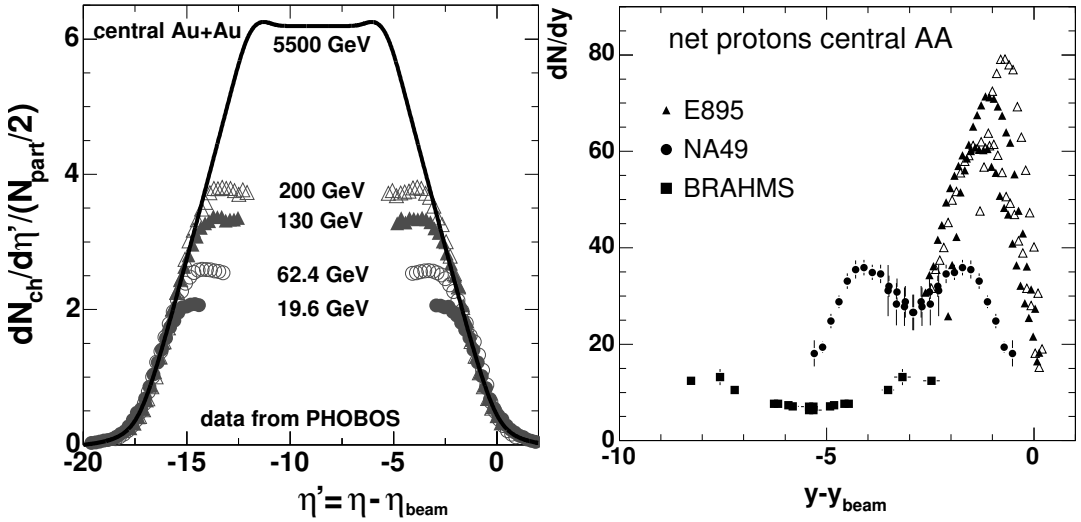

Figure 1.20: Left: Pseudorapidity distributions, $dN_{\rm ch}/d\eta'$, normalised by the number of participating nucleon pairs, for primary charged hadrons in central AuAu collisions at RHIC ($\sqrt{s_{NN}}$ = 19–200 GeV) and extrapolation for PbPb at LHC ($\sqrt{s_{NN}}$ = 5500) [136, 137]. Right: Rapidity distribution ($y' = y - y_{\rm beam}$ where $y_{\rm beam} = \ln(\sqrt{s}/m_N)$ is the beam rapidity) of net protons ($N_{\rm p} - N_{\bar{\rm p}}$) in central AuAu and PbPb collisions at RHIC and SPS energies (compiled in Refs. [137, 142]).

Last, but not least, the interest in hadron production at forward rapidities in pA and AA collisions at LHC energies has interesting connections with cosmic-ray physics. First, knowledge of the particle multiplicities and energy flow in proton and nucleus collisions at forward rapidities is a prerequisite for calibrating the existing hadronic codes used to study the interaction of ultra-high energy (UHE, $E > 100$ PeV) cosmic rays[5] in the upper atmosphere [145]. The only way currently known to study UHE cosmic rays is via extended air-showers in the atmosphere whose cascade development is dominated by forward and soft

[5]The c.m. energy in pp collisions at the LHC corresponds to a 100 PeV fixed-target collision in the air.

QCD interactions, which are poorly known at such high energies. The LHC data will help constrain the models and validate their extrapolation up to the highest cosmic-ray energies measured. Second, emulsion experiments at high altitudes have observed exotic cosmic-rays events with energies $E \sim 10^{15}$–10^{17} eV featuring a very low production of electromagnetic secondaries [146]. Such "Centauro" events have been interpreted in some theoretical scenarios [147] as due to the disintegration of a small lump of strange quark matter (strangelets), a hypothetical state consisting of roughly equal numbers of u, d and s quarks, or as due to the formation and decay of a Disoriented Chiral Condensate [148], a region of matter where the quark condensate is misaligned with respect to the physical vacuum and results in coherent excitations of the pion fields along particular directions in isospin space. Accelerator searches of signatures of any such unusual objects at the Sp$\bar{\text{p}}$S [149, 150], Tevatron [151], SPS [152, 153] or RHIC [154] have been unsuccessful so far. The much higher energies and rapidities attainable at the LHC should provide more favourable conditions for such investigations [155].

1.5 Physics schedule

The timescale with which the various physics topics presented here can be addressed is determined by the machine luminosity and by the beam time allocated to the different running modes at the LHC. Table 1.2 shows the estimated plan for the LHC heavy-ion physics programme. Using increasing luminosity a range of physics topics starting with basic global event properties and moving on to more and more rare processes can be addressed. A preliminary schedule of physics goals is shown in Table 1.3. The heavy-ion (HI) label includes planned proton-nucleus (pPb at $\sqrt{s_{NN}}$ = 8.8 TeV) and light ion (ArAr) runs.

Table 1.2: The projected run schedule at the LHC with proton and ion beams.

Calendar Year	Beam
2007	Pilot pp
2008	Physics pp, low luminosity Pilot HI
2009	Physics pp, towards full luminosity Physics HI, at 1/20 luminosity
2010	Physics pp Physics HI full luminosity
2011	Physics pp full luminosity Physics HI pp at HI beam energy (5.5 TeV)
2012	Physics pp Physics HI (pPb or ArAr)

The discussion presented in the next chapters will clearly demonstrate the significant capabilities of the CMS detector to perform the important measurements for heavy-ion physics discussed in this chapter. Experience at other recent collider facilities (LEP, Fermilab, RHIC) has shown the importance of having multiple detectors addressing a particular physics topic. However, the contribution of CMS to the heavy-ion effort will go well beyond a mere complementary role to ALICE, the dedicated heavy-ion detector at the LHC. Instead, inclusion

Table 1.3: A preliminary schedule for the physics goals of the CMS heavy ion programme at the LHC.

Calendar Year	Physics Goals
2007	Monte Carlo simulations: • Capabilities of the detector for HI • Trigger performance for HI 900 GeV pp data: • First opportunity to test detector and trigger performance • pp charged multiplicity, particle and jet spectra
2008	Reference pp data: • pp charged multiplicity • pp particle and jet spectra • pp jet studies: dijet, jet+γ, jet+Z^0 • pp quarkonium and heavy quark measurements First HI data: • Charged particle multiplicity and energy flow • Collective elliptic flow • Spectra of charged particles to $p_{\mathrm{T}} < 100$ GeV/c • Observation of jets
2009	Increased statistics reference pp data. Increased statistics HI data: • Charged multiplicity and flow vs centrality • Charged particle spectra to $p_{\mathrm{T}} <$ multi-100 GeV/c • First J/ψ, Υ family observation • Jet studies for jets with $E_{\mathrm{T}} <$ multi-100 GeV • Initial c- and b-quark jets studies
2010	Further statistics for pp and HI data: • Detailed jet fragmentation studies, multi-jets • Detailed J/ψ, Υ family, centrality dependence • First jet+γ and jet+Z^0 observations • Detailed c- and b-quark jets studies
2011	Further statistics for pp and light-ion (ArAr) data: • Detailed jet fragmentation, multi-jet studies • Detailed J/ψ, Υ family, centrality dependence • Jet+γ, jet+Z^0 studies, centrality dependence
2012	pp reference at 5.5 TeV: • Refined analysis with improved pp reference Increased statistics HI data: • Detailed studies of all rare channels, centrality dependence

of CMS provides a number of unique capabilities. These include:

- Acceptance: Significantly broader coverage than ALICE near midrapidity (full ϕ, $|\eta| < 2.5$) for layered detection of charged and neutral hadrons as well as muons, electrons and photons, over a wide range of p_{T}.
- Resolution: The best dimuon mass resolution of any LHC detector, leading to a

clean separation of the various quarkonia (J/ψ, Υ) states and an improved signal over background ratio. Significantly better (than ALICE) charged track momentum resolution over a much wider range of acceptance.

- Calorimetry: Full electromagnetic and hadronic calorimetry for complete jet triggering and reconstruction over a very large solid angle, leading to large statistics measurements of single jet and jet+X channels, where X is another jet, a (virtual) γ or a Z^0.
- Forward coverage: Unparalleled forward physics capabilities thanks to the forward hadronic calorimeters ($3 < |\eta| < 5$), CASTOR-TOTEM ($5.3 < |\eta| < 6.6$), and the ZDCs ($|\eta| \gtrsim 8.3$ for neutrals).
- Trigger: The DAQ is capable of delivering almost every PbPb event to the High Level Trigger (with an equivalent ~ 50 TFlops computing power), allowing maximum flexibility to select rare probes. Having the event selection implemented in the software makes it easy to update, improve, and modify for a variety of physics programmes or to react to new discoveries.

Chapter 2

Global observables and event characterisation

2.1 Introduction

Our current understanding of how bulk QCD matter behaves with increasing energy density is based on results from heavy-ion collisions up to a maximum energy of $\sqrt{s_{NN}}$ = 200 GeV, currently achievable at the Relativistic Heavy-Ion Collider (RHIC). Measurements at RHIC suggest that the initial state described by the concept of parton saturation is directly reflected in the multiplicity of produced hadrons and their phase-space distribution. These global features of multiparticle production, measured by PHOBOS and others [61, 65, 144, 156], exhibit great simplicity, such as factorisation into separate dependencies on energy and collision geometry as well as the general feature of extended longitudinal scaling over a large fraction of the rapidity range [138, 139]. In CMS, the high tracking efficiency and low rate of fake tracks, together with a large calorimetric coverage, provide a precise measurement of global event characteristics, event by event. Forward angle coverage is essential for studying the complete longitudinal distribution as well as pushing to the lowest possible x values. An extrapolation of existing results for the energy dependence of hadron production predicts a much lower multiplicity at the LHC, $\mathrm{d}N_{\mathrm{ch}}/\mathrm{d}\eta|_{\eta=0} \approx 1300$ [136, 137], than can be accommodated by most current models. Confirmation of, or disagreement with, these expectations will undoubtedly severely constrain our understanding of the initial conditions and early evolution of the dense matter formed in heavy-ion collisions.

Experience at SPS and RHIC has demonstrated that global variables, such as the charged-particle pseudorapidity density ($\mathrm{d}N_{\mathrm{ch}}/\mathrm{d}\eta$), transverse energy (both E_{T} and $\mathrm{d}E_{\mathrm{T}}/\mathrm{d}\eta$), and energy of neutral spectators are essential for event categorisation (i.e. to estimate the attained initial parton and energy densities in a nucleus-nucleus collision at a given centrality) in various analyses, as well as for placing important constraints on fundamental properties of particle production. The large coverage of the CMS tracking and muon detectors ($|\eta| < 2.5$) and the nearly full coverage of the CMS calorimeters ($|\eta| \lesssim 6.3$) provides access to all these measurements with high precision. In particular, the large acceptance will allow detailed studies of trigger and event selection biases. The resulting event-characterisation observables will be available on an event-by-event basis for all other studies, allowing detailed measurements as a function of the centrality, collision volume, and related (derivable) quantities such as the number of nucleon participants and nucleon-nucleon collisions.

What follows is a brief overview of how we can measure event-by-event charged particle multiplicities in PbPb collisions using the innermost layers of the silicon pixel tracker, how to determine the centrality in heavy-ion collisions, and what would be the optimal Level-1

minimum-bias (interaction) trigger to measure these global observables in both pp and PbPb collisions.

2.2 Event-by-event charged particle multiplicity with the silicon tracker

The measurement of the primary charged particle pseudorapidity density in PbPb collisions, versus the centrality of the collision, will be one of the initial measurements of the CMS collaboration. A method for determination of the primary charged-particle multiplicity in heavy-ion events at CMS is outlined. Further details of the analysis can be found in Ref. [157].

The technique is based on the relation between the pseudorapidity distribution of reconstructed clusters in the innermost layer of the pixel tracker ($|\eta| < 2.5$) and that of charged-particle tracks originating from the primary vertex. This study is performed using a set of 100 PbPb heavy-ion events, with a midrapidity charged particle yield of $\mathrm{d}N_{\mathrm{ch}}/\mathrm{d}\eta|_{\eta=0} \approx 5000$, generated using the HIJING Monte Carlo [54, 158] (with default settings) and run through the GEANT3-based CMS detector simulation (CMSIM 125). Hits from all charged particles in the first layer of the pixel barrel detector are first connected into clusters of hits to incorporate the possibility that a single charged particle could deposit energy in more than one pixel. This clustering algorithm is still effective for multiplicities as high as $\mathrm{d}N_{\mathrm{ch}}/\mathrm{d}\eta \approx 5000$ at midrapidity, i.e. much larger than expected in central PbPb collisions at the LHC, as the occupancy in that scenario remains less than 2%.

As the amount of energy deposited is proportional to the length traversed in the silicon, charged particle tracks with longer path lengths will deposit more energy. Thus, at higher pseudorapidities, or shallower angles, the charged particle path length from the "true" interaction point through the silicon in the barrel region is longer, resulting in a $\cosh\eta$ dependence of the energy deposited with pseudorapidity η, see Fig. 2.1-left. Background (or secondary) particles originating from dead material (e.g. the beam-pipe) produced at an effective high η will deposit less energy as they will primarily be emitted perpendicular to the beam z-axis and thus will traverse less silicon. These background particles can be removed from the analysis via a cut in $\cosh\eta$ that selects only energy loss in the silicon consistent with particles emanating from the true collision vertex, see Fig. 2.1-right.

Once the background component of the secondaries is removed, the measured data can be corrected back to the number of primary charged particles via a correction function determined from Monte Carlo studies. The correction factor is essentially a ratio of $\mathrm{d}N_{\mathrm{ch}}/\mathrm{d}\eta$ for primary tracks to $\mathrm{d}N_{\mathrm{ch}}/\mathrm{d}\eta$ for reconstructed hits in layer 1 of the silicon pixel tracker — where the effect of background secondaries at higher η has been removed as discussed previously. The average correction factor from these studies is found to be $\sim$0.83 for PbPb roughly independent of pseudorapidity, see Fig. 2.2-left, where spikes in the correction function are the result of gaps in the detector for the chosen nominal interaction point of the colliding Pb ions. It is worth noting that if all secondary particle hits are removed in the simulation, the baseline of the correction factor is found to be close to one, illustrating that the geometrical coverage of CMS is uniform and complete. The correction factor shown is thus primarily a consequence of the secondary particles produced in the collision. It will be necessary to apply this correction to the data in order to extract the primary charged particle production.

The results of this analysis applied to one PbPb event is shown in Fig. 2.2-right. On an event-

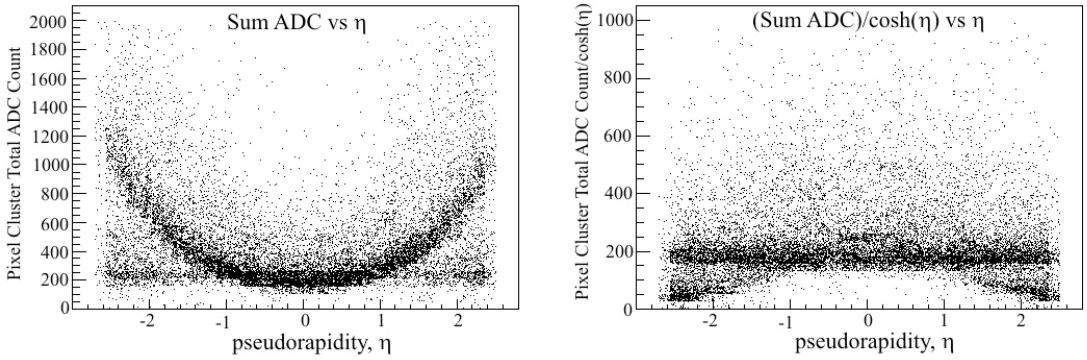

Figure 2.1: Total ADC count for reconstructed hits in the first layer of the silicon pixel detector as a function of pseudorapidity, η, which is calculated event-by-event relative to that event's primary vertex. Left: Energy deposition in the pixel clusters, which varies as $\cosh\eta$ for tracks originating from the primary vertex and is largely flat for background particles at high η. Right: Same distribution with the $\cosh\eta$ dependence factored out such that a simple cut can be utilised to remove hits at high η from the other (non-primary) sources.

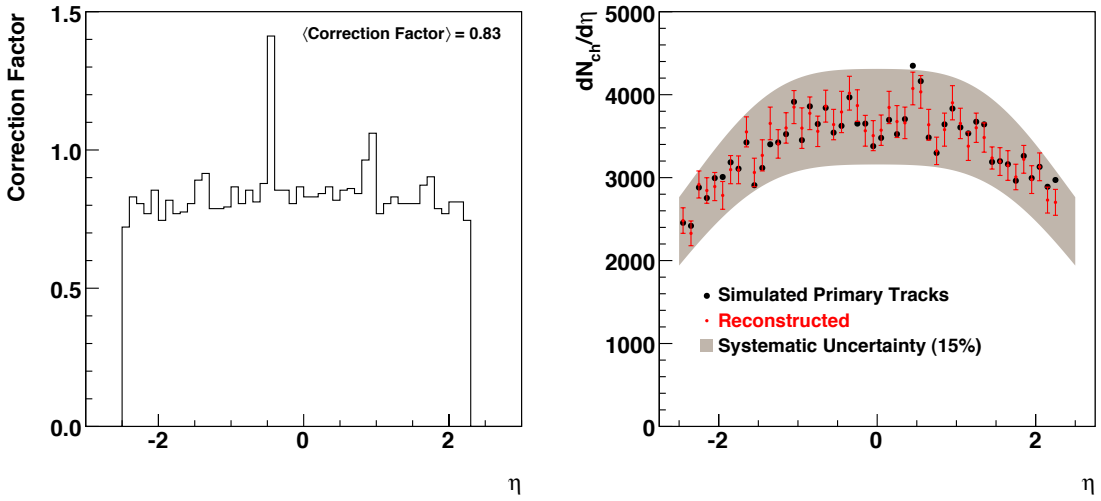

Figure 2.2: Left: The η-dependent correction factor used to convert the measured $\mathrm{d}N_{\mathrm{ch}}/\mathrm{d}\eta|_{\eta=0}$, which include secondaries, to the primary charged particle multiplicity. Right: Comparison of the original distribution of primary simulated tracks (black large points) to the estimate obtained from the reconstructed hits in layer 1 of the Si pixel tracker (red smaller points with statistical error bars, the grey band indicates a somewhat conservative systematical uncertainty of Ref. [157]).

by-event basis, the charged particle multiplicity estimated from the innermost layer of the silicon tracker using this technique is within $\sim$2% of the true (simulated) primary multiplicity. Final systematic uncertainties are estimated to be below 10%, based on experience with a similar analysis using the PHOBOS detector at RHIC [159].

2.3 Centrality determination

Determining the impact parameter, b, or centrality of a heavy-ion collision is extremely important for event characterisation. Knowledge of the reaction centrality provides a geomet-

rical scale of the overlapping region between the colliding nuclei for use in any studies of the underlying collision dynamics and affords the possibility of a meaningful comparison to baseline data from simpler proton-proton or proton-nucleus collisions. The primary event centrality in high-energy nucleus-nucleus collisions is determined by measuring the charged particle multiplicities or transverse energies in various regions of pseudorapidity. These signals, through bins in the percentage of total cross section, provide a measure of centrality. The validity of this technique is based on the assumption that there is a monotonic relation between the charged particle multiplicity or the transverse energy and the amount of nucleus-nucleus overlap.

In CMS, a simple way to determine the impact parameter on an event-by-event basis, is to use the transverse energy deposited in the calorimeters, $E_{\mathrm{T}}^{\mathrm{tot}}$, which decreases strongly from central to peripheral collisions [160]. Due to its relatively low initial parton density, the very forward rapidity region covered by the CMS Hadron Forward (HF) or CASTOR calorimeters, $|\eta| > 3$, is expected to be nearly free of final-state rescattering compared to the central rapidity region. Therefore the (transverse) energy deposition in the CMS forward calorimeters is determined mainly by the initial nuclear geometry of the collision rather than by final-state dynamics [160, 161].

The impact parameter dependence of the total transverse energy produced in the pseudorapidity interval $3 < |\eta| < 5$ (covered by the HF acceptance), as obtained at the generator-level with HIJING [54, 158], is presented in Fig. 2.3 for PbPb collisions at $\sqrt{s_{NN}}$ = 5.5 TeV and ArAr collisions at $\sqrt{s_{NN}}$ = 6.3 TeV. The E_{T}–b correlation is diffuse due to fluctuations in the nucleus-nucleus collision dynamics, including fluctuations in the number of nucleon-nucleon sub-collisions at a given b and fluctuations of transverse energy flow in each nucleon-nucleon interaction. Inclusion of the detector response obtained with a full GEANT3-based CMS simulation [161] has shown that the finite energy and spatial resolutions of the HF calorimeter do not substantially degrade the accuracy of the impact parameter determination. The correlation between the *total* energy and the impact parameter has a similar shape to the E_{T}–b correlation. The impact parameter distribution at fixed values of E_{T} is Gaussian-like with a width, σ_b, dependent on impact parameter. The estimated resolution σ_b is about $\sim$0.5 fm for PbPb and ArAr collisions, at impact parameter up to twice the nuclear radius, $b \sim 2R_A$. It is degraded by a factor of $\sim$2 for very peripheral collisions, $b > 2R_A$, due to the reduction of the produced energy in the HF pseudorapidity region. In order to improve the centrality determination for peripheral events, a correlation of the HF transverse energy with the total neutral energy deposited in the Zero Degree Calorimeters (ZDCs) is foreseen. Such a correlation technique has become *de facto* the standard for centrality determination by all experiments at RHIC.

Applying the method described here, any particle production rate, N_{X}, can be measured in bins of E_T^{tot}. The b and E_T^{tot} dependencies of N_{X} can be related by the $E_{\mathrm{T}}^{\mathrm{tot}}$–$b$ correlation functions C_{AA} with corresponding Gaussian widths $\sigma_{E_{\mathrm{T}}}$ and σ_b:

$$N^{\mathrm{X}}(E_{\mathrm{T}}^{\mathrm{tot}}) = \int \mathrm{d}^2 b N^{\mathrm{X}}(b) C_{AA}(E_{\mathrm{T}}^{\mathrm{tot}}, b) \quad , \tag{2.1}$$

$$C_{AA}(E_{\mathrm{T}}^{\mathrm{tot}}, b) = \frac{1}{\sqrt{2\pi}\sigma_{E_{\mathrm{T}}}(b)} \exp\left(-\frac{\left(E_{\mathrm{T}}^{\mathrm{tot}} - \overline{E_{\mathrm{T}}^{\mathrm{tot}}}(b)\right)^2}{2\sigma^2_{E_{\mathrm{T}}}(b)} \right),$$

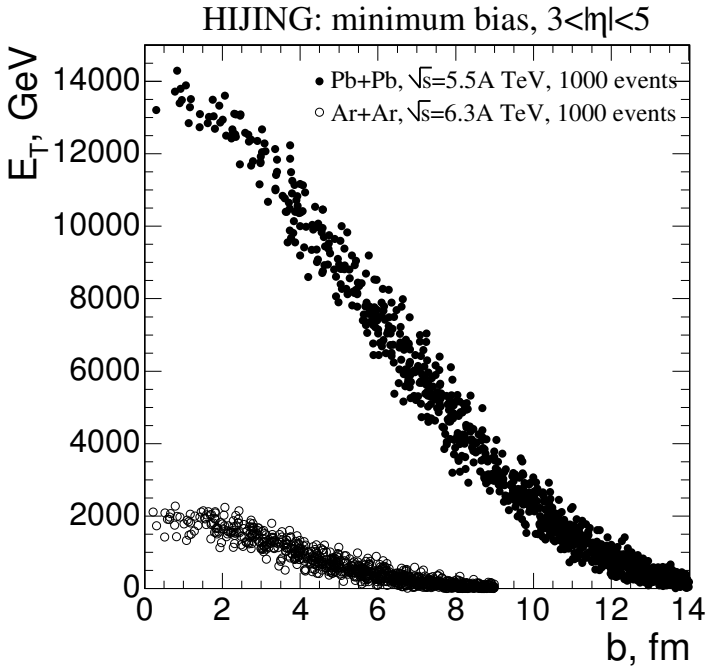

Figure 2.3: Correlation between the impact parameter b of the collision and the transverse energy, E_{T}, produced in the forward rapidities covered by HF, $3 < |\eta| < 5$, for 1000 minimum bias PbPb and ArAr collisions generated with HIJING [161].

$$N^{\mathrm{X}}(b) = \int \mathrm{d}E_{\mathrm{T}}^{\mathrm{tot}} N^{\mathrm{X}}(E_{\mathrm{T}}^{\mathrm{tot}}) C_{AA}(b, E_{\mathrm{T}}^{\mathrm{tot}}) \quad , \tag{2.2}$$

$$C_{AA}(b, E_{\mathrm{T}}^{\mathrm{tot}}) = \frac{1}{\sqrt{2\pi}\sigma_b(E_{\mathrm{T}}^{\mathrm{tot}})} \exp\left(-\frac{\left(b - \overline{b}(E_{\mathrm{T}}^{\mathrm{tot}})\right)^2}{2\sigma_b^2(E_{\mathrm{T}}^{\mathrm{tot}})} \right).$$

Similarly to what has just been described for the HF, also the CASTOR calorimeter can provide an estimate of the collision centrality, through the measurement of the transverse energy flux (or the total energy) emitted in the pseudo-rapidity windows $5.3 < |\eta| < 6.7$. Figure 2.4 shows again a monotonic correlation between the transverse energy produced in CASTOR pseudorapidity coverage and the impact parameter, b, of the nuclear collision, according to the HIJING event generator. From the width of this bidimensional correlation plot (or explicitly from the right plot of Fig. 2.4 obtained from the *total* energy deposited in CASTOR) we see that the resolution of the b variable, as extracted solely from CASTOR data, is around 0.6 fm.

By combining information from various independent measurements, such as the E_{T} measurements in both HF and in both CASTOR calorimeters (on each side of the interaction point), plus the forward energy of spectator forward neutrons measured in both ZDCs, we can certainly determine the impact parameter of the reaction with an improved experimental resolution of a few tenths of fm.

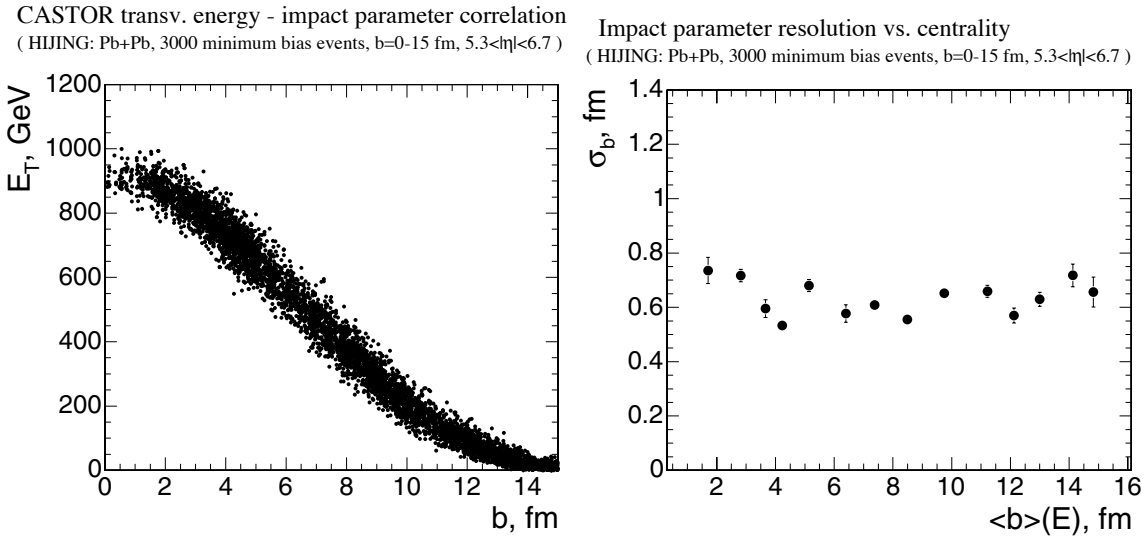

Figure 2.4: Left: Correlation between the impact parameter, b, and the transverse energy, E_{T}, deposited in the forward rapidities, $5.3 < |\eta| < 6.7$, covered by the CASTOR calorimeter, as simulated with HIJING for 3000 minimum bias PbPb collisions. Right: Impact parameter resolution in PbPb collisions using the total energy measured in CASTOR.

2.4 Minimum-bias trigger at Level 1

2.4.1 Introduction

The minimum bias trigger in both pp and heavy-ion collisions serves many purposes in terms of absolute (high-level-trigger) normalisation, detector performance and consistency determination, as well as evaluation of the event reconstruction quality. The resulting dataset will also provide valuable physics results to characterise the global properties of the (underlying) event in these collisions. In this section, sources of possible bias will be discussed in the context of good or bad triggering schemes for implementing a minimum bias trigger, where high efficiency and purity are desired. To better convey why this trigger is important for both proton and heavy-ion running conditions, a brief discussion of its most probable use, in each physics analysis context, follows.

In pp collisions, the design luminosity is expected to be so large that 20 collisions per beam crossing (or read-out event) are expected. In this large collection of data are both the event which gave the trigger (e.g. a jet event) plus 19 other pileup events which are effectively true minimum bias collisions (true means no bias is applied). To study the events of interest, one must first understand the "uninteresting" background events. Analysis of these partner events will begin with the low luminosity pp data, expected at the start-up of the LHC machine. This data will also be used to analyse global properties of hadron production — $\mathrm{d}N_{\mathrm{ch}}/\mathrm{d}\eta$, $\mathrm{d}E_{\mathrm{T}}/\mathrm{d}\eta$, charged particle spectra and others — as reference for the heavy-ion physics programme.

In the ion-ion running mode, the first measurements are likely to be based on the initial minimum bias dataset. The minimum bias dataset is a vital reference for the geometrical overlap of the colliding nuclei (centrality). Besides, there are also some direct physics measurements that can only be made from this data sample such as the charged particle multiplicity, azimuthal anisotropy (elliptic flow), and particle spectra.

2.4.2 Minimum bias in pp collisions at 14 TeV

In order to evaluate the most effective way to trigger on minimum bias events, one must first consider the total underlying particle distributions, $\mathrm{d}N/\mathrm{d}\eta$. To form the minimum bias sample studied here, PYTHIA subprocesses 92, 93 and 94 (diffractive events) as well as 95 (low p_{T} production) were enabled. Thus, for these simulations, the total inelastic cross section of minimum bias events is 79 mb, including a 55 mb hard core (non-diffractive), as well as 14 and 10 mb for single and double diffractive events, respectively. In Fig. 2.5, the expected primary and final hadron distributions predicted by PYTHIA [162] are presented. Primary hadrons are defined as those which are produced close to the initial collision vertex and are not decayed (for example, $\pi^0 \rightarrow \gamma\gamma$ decays are not considered). Final hadrons are those which reach the detectors. In these examples, particles produced from dead material are not included. Most neutral hadrons (in particular the π^0s) decay before reaching the detectors.

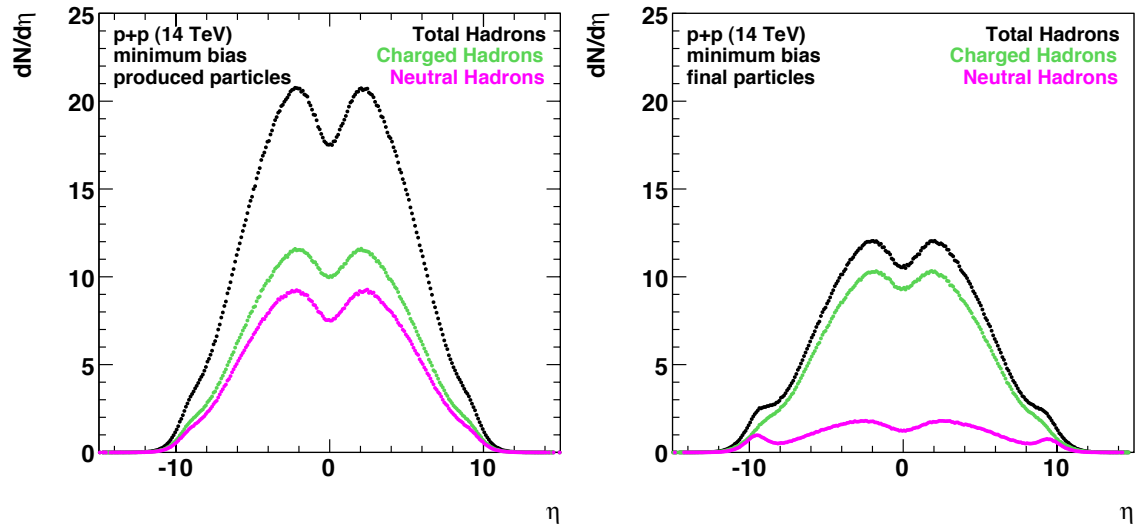

Figure 2.5: Hadron multiplicity as a function of pseudo-rapidity in pp minimum bias collisions at 14 TeV (PYTHIA 6.4, see text for details): Initially produced hadrons (left), and remaining hadrons after removing all particle decays (right).

Once the number of particles is known, restrictions on the data can be placed to mimic the detector response to the physical limitations that will be applied at the triggering level. Figure 2.6 shows the final particles (black markers; top curve) with two trigger conditions applied. First, a cut on total energy, $E > 1$ GeV, is applied to the final particles (blue markers; middle curve). This cut represents a realistic noise level for the tower read-out of the Level-1 trigger and results in a significantly reduced number of particles reaching the detectors in the central rapidity region ($|\eta| < 3.0$). The more forward region ($3.0 < |\eta| < 5.0$, corresponding to the coverage of the forward calorimeters, HF) is only mildly affected. Second, a cut of transverse energy $E_{\mathrm{T}} > 1$ GeV is applied to the final particles (red markers; bottom curve). In this case all regions are significantly affected. The integrated particle yields for the central and HF regions are given in Table 2.1.

The next step is to simulate the full response of the detectors in a more realistic environment. For these studies, full GEANT4-based CMS Monte Carlo (ORCA/OSCAR) simulations are used, where particles from dead material (e.g. secondary particles originating from the beam-pipe) are also included. These minimum bias events were generated from PYTHIA 6.2 with the same diffraction and low p_{T} subprocesses activated as for the prior generator level

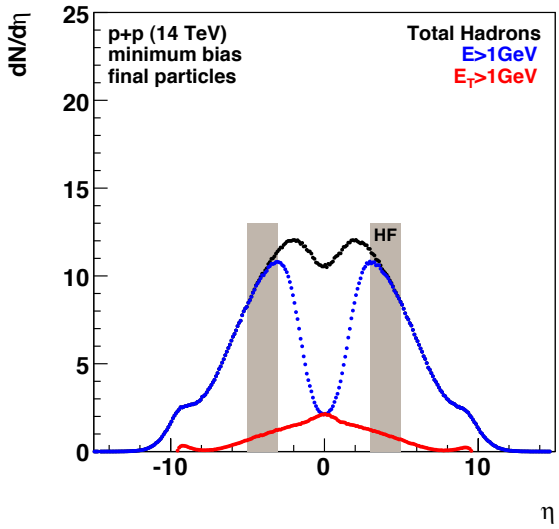

Figure 2.6: The same data as in Fig. 2.5-right, but with additional cuts to mimic hadronic calorimeter tower thresholds for total (E) and transverse (E_{T}) energy. The shaded regions show the HF pseudorapidity coverage.

Table 2.1: Final hadrons predicted by PYTHIA for minimum bias pp collisions at $\sqrt{s}$ = 14 TeV, integrated in the HF ($3.0 < |\eta| < 5.0$) and central calorimeter ($|\eta| < 3.0$) regions.

	Number of Hadrons	
Cut (GeV)	$3.0 < \|\eta\| < 5.0$	$\|\eta\| < 3.0$
No cut	44	70
$E > 1$	42	39
$E_{\mathrm{T}} > 1$	4	10

study. Figure 2.7 shows the number of simulated tracks hitting the detector. The histogram represents all initially generated particles (from the pp vertex), the dark-shaded region shows the particles that hit at least one of the hadronic calorimeter detectors, and the light-shaded region represents particles that do not originate from the initial vertex. In the forward region, additional hits from these secondary particles help provide a trigger for the minimum bias events.

Optimal design for pp minimum bias triggering

To maximise efficiency, it is desirable to trigger on regions with a large number of particles. Studies thus far show that by applying a total energy cut ($E > 1$ GeV), one should expect on average 21 hadrons in each HF, for a total of 42 (see Table 2.1). This number is significantly reduced after the transverse energy cut, when only 2 particles in each HF are expected, on average. In order to reject "non-collision" events, such as those due to beam-gas collisions, the interaction trigger should require a coincidence of signals from *both* HF calorimeters (at the expense of reducing the efficiency for single diffractive processes). The rejection of such spurious events would not be achievable using only the central calorimeter as a trigger.

The trigger read-out at Level-1 will utilise towers. For the central barrel and endcaps each hadronic cell is one tower, whereas in the forward calorimeter (HF) several cells are summed. An optimal minimum bias triggering scheme would be to count the number of towers in the

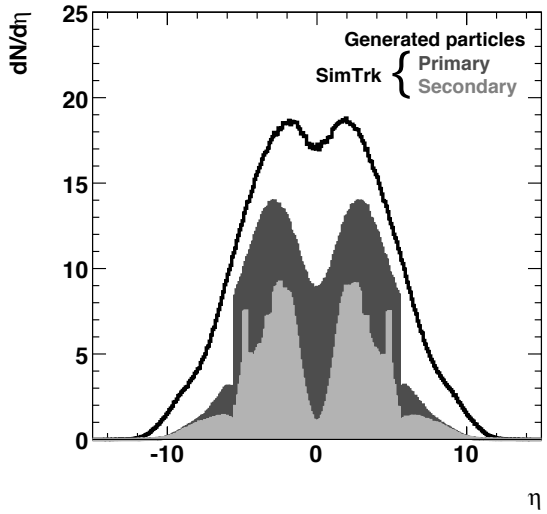

Figure 2.7: Pseudo-rapidity distribution of the generated tracks (upper curve), the tracks reaching the hadronic calorimeter detectors (dark-shaded area), and the tracks not originating from the primary vertex (light-shaded area) in fully simulated minimum bias pp collisions at 14 TeV.

HFs separately in the positive and negative η-regions. By requiring a specific number of towers, n, on both sides, a minimum bias trigger can be defined. As an example, Fig. 2.8-left shows the number of towers with energy above threshold in total energy E for positive (P) and negative (N) HF η-regions. By requiring more than 10 towers in both HF calorimeters, an efficiency of $> 90\%$ can be obtained. This threshold can be increased in the case of higher backgrounds, at the expense of efficiency, as illustrated in Fig. 2.8-right.

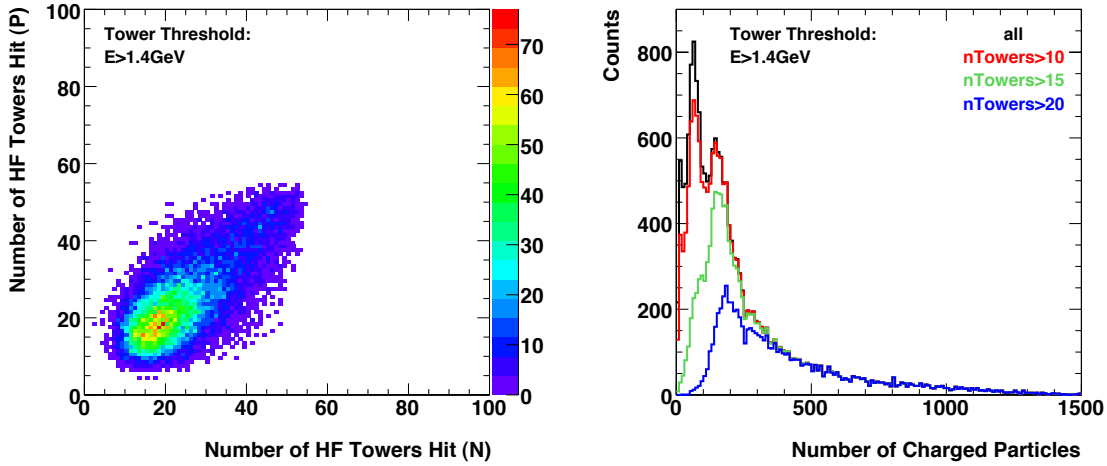

Figure 2.8: Left: Number of HF towers hit above threshold for towers cut on total energy, E. Right: Estimated loss of low multiplicity events due to triggering requirements on nTowers for cuts on E. See text for discussion.

Repeating the above logic with transverse energy (E_{T}) rather than total energy, we see that the efficiency is significantly reduced, as illustrated in Fig. 2.9. Requiring nTowers > 1 hit for this case gives only $\sim$60% efficiency. This extremely low threshold and correspondingly poor efficiency severely restricts options for handling unexpectedly high backgrounds.

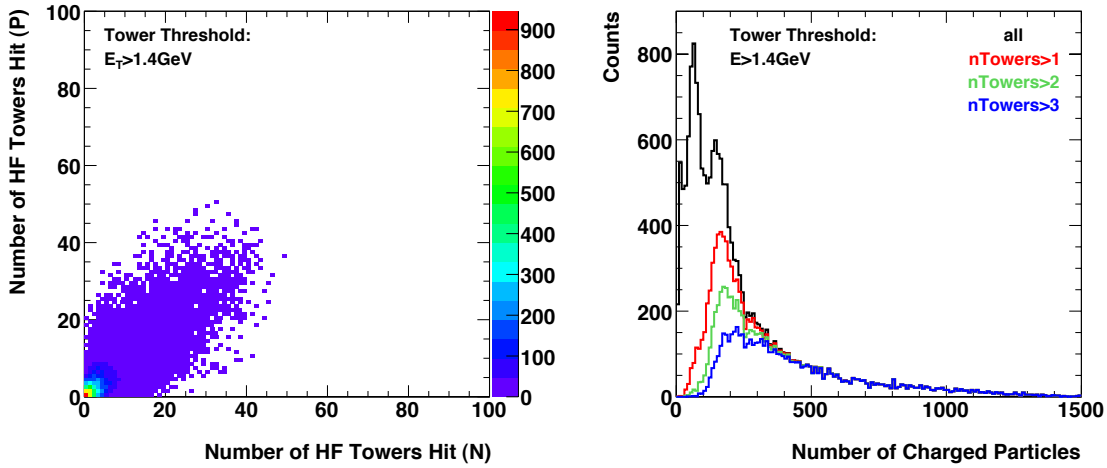

Figure 2.9: Left: Number of HF towers hit above threshold for towers cut on transverse energy, E_{T}. Right: Estimated loss of low multiplicity events due to triggering requirements on nTowers for cuts on E_{T}. See text for discussion.

2.4.3 Minimum bias in PbPb collisions at 5.5 TeV

To first order, one can classify minimum bias pp collisions (albeit at 14 TeV) as a very peripheral PbPb collision. From the studies already performed on the pp dataset, we concluded that it is possible to trigger with an efficiency greater than 90%. The purpose of the following studies is to check whether applying the same restrictions in heavy ions as for 14 TeV pp collisions will result in at least the same number of final particles and therefore a correspondingly good trigger efficiency. First, heavy-ion events are simulated with the HYDJET Monte Carlo [163] (see Appendix A) for various impact parameters ranging from $b = 0$ fm (central) to $b = 13.5$ fm (peripheral). Cuts in total and transverse energy have been applied to the generated data to check the total number of particles expected in HF. From this, the number of towers expected to be hit is known from full pp simulations.

Figure 2.10 illustrates the expected charged hadron multiplicity (black markers; top curve) from the HYDJET event generator. The maximum multiplicity considered is $\mathrm{d}N_{\mathrm{ch}}/\mathrm{d}\eta|_{\eta=0} \approx 3000$ (compared to about $\mathrm{d}N_{\mathrm{ch}}/\mathrm{d}\eta|_{\eta=0} \approx 8$ for pp at 14 TeV). The vastly increased number of particles represents a clear advantage in triggering. However, we find that although the number of particles is large, the same relative reduction is found from applying cuts on total (blue markers - middle curve) and transverse (red markers - bottom curve) energy. Although triggering will be possible for the most central collisions with transverse energy cuts, more peripheral collisions (with lower multiplicity) will suffer from inefficiency.

Following the proposed minimum bias triggering scheme for pp, Fig. 2.11 illustrates the expected number of particles in the HF pseudo-rapidity region versus impact parameter from the Monte Carlo simulation. Clearly, the number of particles hitting the detectors is expected to be large for very central collisions and decreases strongly for peripheral collisions. This large number of charged particles in the forward region is relatively insensitive to a small change in the total energy threshold of the trigger towers, as illustrated by the $E > 5$ GeV cut in Fig. 2.11-left. To estimate the loss of data in triggering due to the lower multiplicity peripheral events, Fig. 2.11-right gives the expected number of particles in the forward regions as a function of b on a log scale. The dashed line represents the equivalent multiplicity in the minimum bias pp collisions at the point where the efficiency will begin to fall. For total

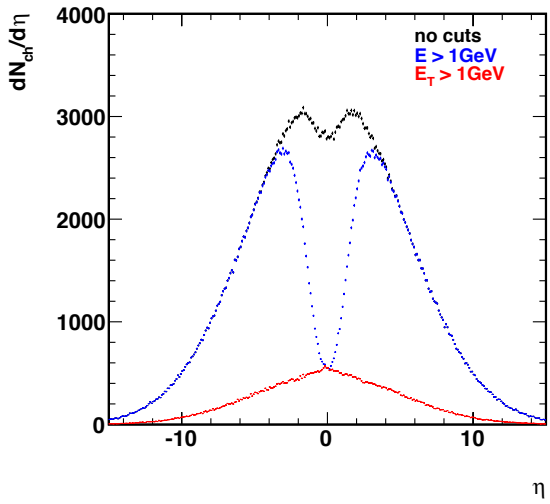

Figure 2.10: Pseudo-rapidity distribution of charged hadrons in central PbPb collisions at $\sqrt{s_{NN}}$ = 5.5 TeV as generated by the HYDJET Monte Carlo simulation. Particle selection to mimic the Level-1 trigger are applied for total (E) and transverse (E_{T}) energy.

energy cuts, only events with $b > 12$ fm suffer from inefficiency, relative to the pp baseline. A cut on transverse energy reduces the particle number and, thus, the trigger would become inefficient for smaller impact parameters, i.e. less peripheral collisions.

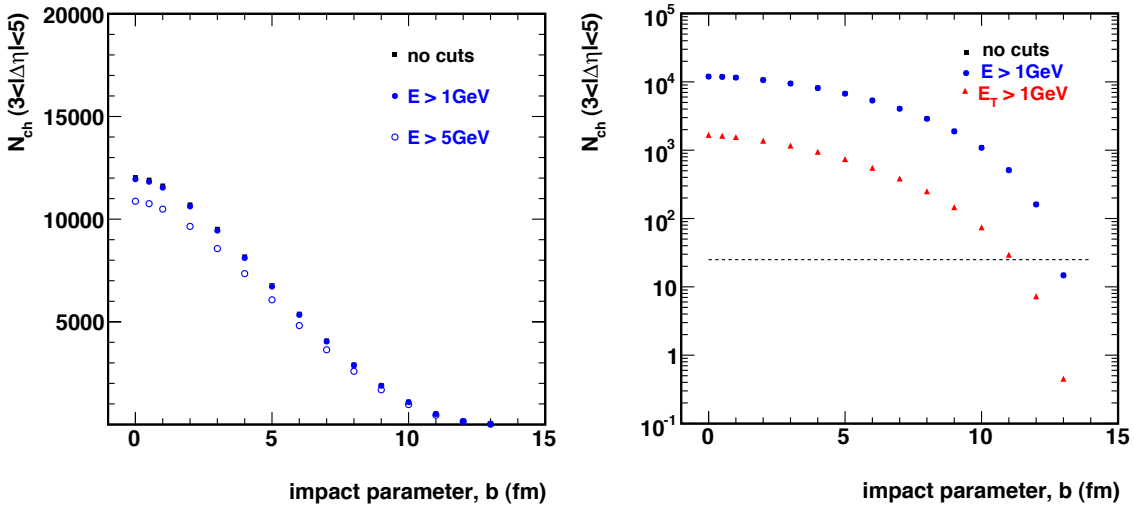

Figure 2.11: Total number of final particles produced in PbPb minimum bias collisions within the HF η windows, as a function of b, for cuts on total (left) and transverse (right) energies. The dashed line represents the equivalent minimum bias pp baseline.

One final, but important, point concerns the question of why a large efficiency is needed for heavy-ion collisions. In many pp analyses, knowing the cross section is not as important because many physics quantities can be compared with, or be classified by, the total measured multiplicity. In heavy ion studies, however, it is important to map the measured multiplicities to the number of participating nucleons (N_{part}), number of binary collisions (N_{coll}), impact parameter (b), and so on. This requires knowing the total inelastic cross section and the fractional cross section in a specific centrality bin. As these quantities are not directly available, the total number of minimum bias events, their efficiency (e.g. trigger-

ing efficiency) and the corresponding fractional cross section are needed. As the triggering efficiency directly enters this analysis, any inefficiency raises the relative uncertainty, and thus increases the uncertainty in modelled parameters such as N_{part}, which are necessary in any detailed analysis of the centrality dependences of physics signals, as well as in model comparisons. Thus, compromising the triggering efficiency in the minimum bias heavy-ion sample will increase the uncertainties of many physics analyses.

2.5 Transverse energy flow

The transverse energy rapidity density $\mathrm{d}E_{\mathrm{T}}/\mathrm{d}\eta$ is related, via the simple "Bjorken estimate", to the energy density attained in a nucleus-nucleus reaction (see Fig. 1.6-right). In several instances of this chapter as well as in chapter 4, the distribution of the transverse energy measured in different detectors has been presented in the context of discussions on reaction centrality and reaction plane determination. The measurement of $\mathrm{d}E_{\mathrm{T}}/\mathrm{d}\eta$ in CMS will be possible over the largest rapidity range at the LHC: within $|\eta| < 5$ for the ECAL and HCAL calorimeters; within $5.3 < |\eta| < 5.6$ for CASTOR; and for $|\eta| > 8.3$ in the ZDCs (neutrals only). Comparison of these measurements with the predictions of hydrodynamical models will provide valuable insights on the thermodynamical conditions as well as on the longitudinal extent of the produced strongly interacting system.

2.6 Summary

We have analysed the potential of CMS to study global observables in heavy-ion collisions, such as the event-by-event charged-particle multiplicities and the collision centrality, and we have presented the Level-1 trigger strategy for pp and PbPb collisions.

We have shown that the charged-particle multiplicity can be determined, on an event-by-event basis, using the innermost pixel layer of the silicon tracker, with an accuracy of $\sim 2\%$. Systematic uncertainties are estimated to be below 10%, based on experience with a similar analysis using the PHOBOS detector at RHIC.

The impact parameter can be estimated, also on an event-by-event basis, using the transverse energy deposited in the forward CMS calorimeters, which monotonically decreases from central to peripheral collisions. The resolution of this measurement is about 0.5 fm for impact parameter values up to two nuclear radii, for PbPb and ArAr collisions.

Finally, we have shown that requiring a similar number of calorimeter towers hit in both HF calorimeters (read out as total energy) should provide an optimal minimum bias Level-1 trigger for pp and PbPb collisions, besides providing useful information for further background rejection.

Chapter 3

Low p_{T} hadron spectra

3.1 Introduction

The reconstruction of low p_{T} charged and neutral hadrons (yields, spectra and correlations) is crucial to characterise the collective properties of the system produced in nucleus-nucleus collisions at the LHC (see Section 1.4.2). In pp collisions, the measurement of high p_{T} observables also requires good understanding of the characteristics of the underlying event and backgrounds which are dominated by soft p_{T} spectra [164].

In CMS, the measurement of charged particle trajectories is achieved primarily using the silicon tracker with both pixels and strips, embedded in the 4 T field, and with geometric coverage over $|\eta| < 2.5$. The highly segmented silicon pixel tracker consists of three barrel layers (with about 4, 7 and 11 cm radius) and two endcap disks, embedded in a 4 T magnetic field. There are about 66 million pixels with an area of 100×150 $\mu\mathrm{m}^2$ and a thickness of 300 μm. The strip part is a combination of single- and double-sided layers with ten barrel and nine forward layers on each side (9.3 million channels). The silicon tracker has excellent reconstruction performance for $p_{\mathrm{T}} > 1$ GeV/c: 95% efficiency for charged hadrons with high p_{T}, better than 98% for muons in pp and pA collisions and around 75% for central PbPb (with $\mathrm{d}N_{\mathrm{ch}}/\mathrm{d}y|_{y=0} = 3200$, see Section 7.3.2). The reconstruction capabilities at lower p_{T} are limited by the high magnetic field and effects of the detector material. In addition, in central AA collisions the high occupancy of the silicon strips (see Fig. 3.1) makes the inclusion of these strips in charged particle tracking difficult [165]. Using only silicon pixels allows the same analysis to be used for low multiplicity pp, pA and high multiplicity AA events. At the same time, it enables the reconstruction of very low p_{T} particles, even down to 0.1 GeV/c for pions, with low fake rate.

3.2 Track reconstruction

The default track reconstruction algorithm in the CMS tracker for charged particles above 1 GeV/c is based on seeded pattern recognition using a Kalman Filter formalism with four phases: (i) trajectory seed generation in the pixel detector, (ii) trajectory building (inside-out propagation), (iii) trajectory cleaning (resolution of ambiguities), and (iv) trajectory smoothing (final fit) [166, 167]. Several modifications are needed in the heavy-ion environment [165] to cope with the high occupancy in the Si-strip detectors (see Section 7.3.2). The alternative tracking algorithm described here allows one to reconstruct tracks down to 0.1 GeV/c using just the three Si pixel layers, with the modified hit triplet finding and cleaning procedures discussed below.

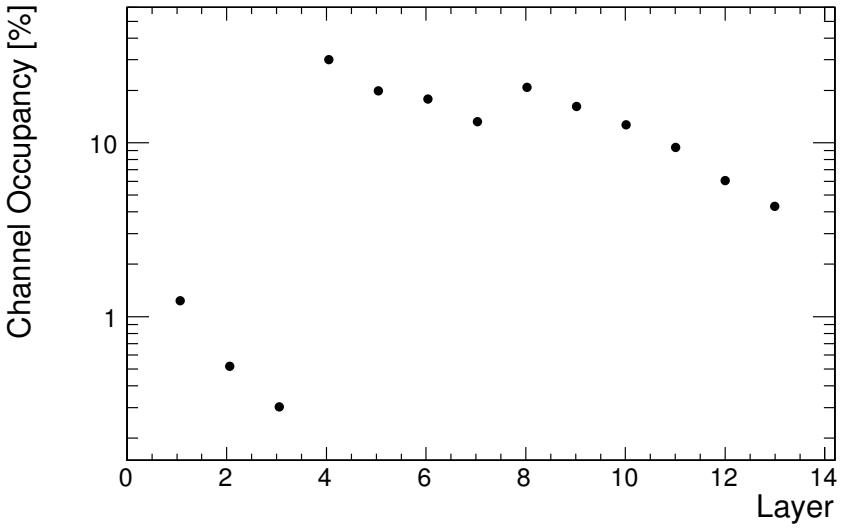

Figure 3.1: Channel occupancy in the barrel region as a function of tracker detector layer: 1–3 are pixel layers; 4–7 are inner strip layers; and 8–13 are outer strip layers [165].

3.2.1 Modified hit triplet finding

In our track finding procedure we start by pairing two hits from different layers (see Fig. 3.2). During the search for the third hit, the following requirements must be fulfilled: the track must come from the cylinder of origin (given by its radius, half-length and position along the beam-line); the p_{T} of the track must be above the minimal value $p_{\mathrm{T,min}}$; and the track must be able to reach the layer where the third hit may be located. In the small volume of the pixel detector the magnetic field is practically constant and the charged particles propagate on helices. The projection of a helix or a cylinder onto the transverse plane is a circle. Each requirement defines a region of allowed track trajectories. They are enclosed by a pair of limiting circles which can be constructed using simple geometrical transformations. A third hit candidate is accepted if its position is within the expected deviation from multiple scattering. The details are described in Ref. [168].

3.2.2 Triplet cleaning

While high p_{T} tracks are relatively clean, hits can often be combined to form fake low p_{T} tracks. Therefore, it is important to filter out this undesirable background. A hit contains much more information than merely its position. The geometrical shape of the hit cluster depends on the angle of incidence of the particle: bigger angles will result in longer clusters. This observation can be exploited in various ways. It can be used to check whether the measured shape of the cluster is compatible with the predicted angle of incidence of the track: if even one of the hits in the triplet is not compatible, the triplet is removed from the list of track candidates. The connection between the geometrical envelope and the angle can be obtained from simulation or from data [168].

3.2.3 Low p_{T} tracking results

The low-p_{T} reconstruction studies are based on 25 000 single minimum bias pp events (generated with PYTHIA [162], with the default *minimum bias* settings described in the previous chapter), reconstructed using the GEANT4 simulation package (ORCA 8_13_0) with the mod-

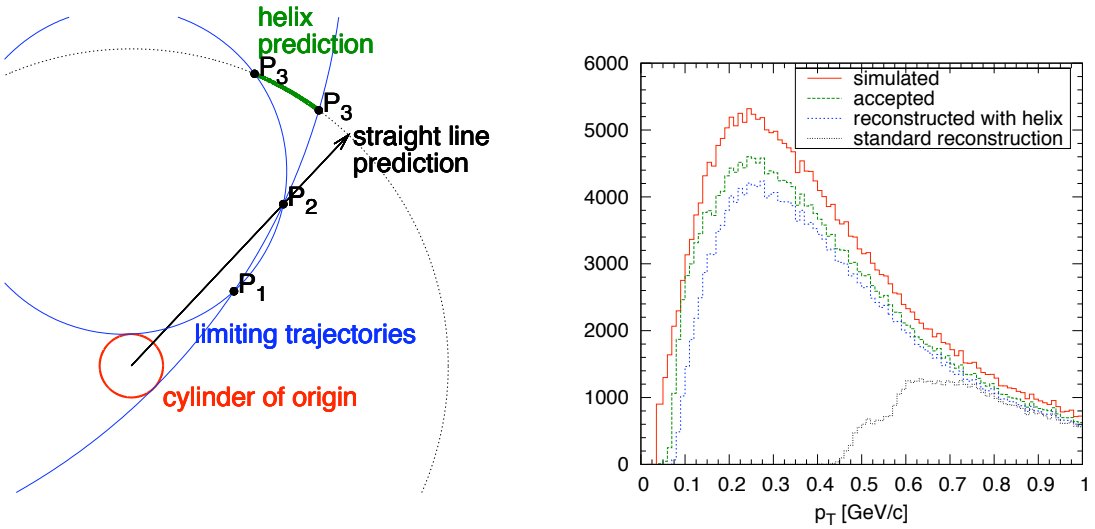

Figure 3.2: Left: Schematic comparison of the standard straight line prediction and the new helix prediction for finding the third hit. Limiting trajectories (solid blue) that touch the cylinder of origin cut out an arc (thick green) from the barrel layer of the third hit candidates. In the standard method, the azimuth of the outer hit, P_2, is used (solid black arrow). Right: Transverse momentum distributions of the charged particles: simulated (solid red), accepted (green dashed) and reconstructed, with the standard method (with a minimum p_{T} of 0.075 GeV/c, dotted black) or with the new helix method (dotted blue).

ified hit triplet finding. The algorithm uses standard settings, except for a much lower minimum p_{T} (0.075 GeV/c). Simulated and reconstructed tracks can be compared to each other by associating their hits using spatial distances. A simulated track is tagged as reconstructed if there is a reconstructed track such that all its hits are associated with hits of the simulated track. A reconstructed track is partially (fully) matched to a simulated one if at least one (all) of its hits are associated. With these notions the following properties can be defined:

- Acceptance: ratio between reconstructible and all generated tracks. A charged particle is reconstructible if its vertex is in the cylinder of origin and if it has hits in at least three different groups of pixel layers (out of: first, second and third barrel layers; closer and farther endcap layers).
- Efficiency: ratio of reconstructed to reconstructible tracks. This is the fraction of reconstructible tracks which are indeed found.
- Multiple counting: fraction of simulated tracks which are reconstructed more than once (have more than one full match). They are mostly loopers.
- Fake rate: fraction of reconstructed tracks which have one or two correctly matched hits to any of the simulated tracks, but not all the three. They are from combinatorial background.

Acceptance. The acceptance of the pixel detector is limited in both η and p_{T}. The limitation in η is a purely geometric effect, while in p_{T} it is due to the fact that a charged primary particle can reach the third pixel barrel only if its transverse momentum is $p_{\mathrm{T}} > 0.003 \cdot B \cdot R_3/2 \approx 60$ MeV$/c$ (with $B = 4$ T and $R_3 \approx 10$ cm). In reality, a higher momentum is needed because the particle loses energy (and momentum) in the beam-pipe, in the crossed pixel layers and in the supports. The specific energy loss is a function of $\beta\gamma = p/m$. Therefore, it is different

for particles having the same momentum but a different mass. This reduces the accepted $p_{\rm T}$ range of the protons and kaons with respect to the pions. The acceptance is also slightly influenced by the multiple scattering, which predominantly affects the heavier particles.

The acceptances rise sharply with $p_{\rm T}$ (see Fig. 3.3-left), and become approximately flat above $p_{\rm T}$ values around 0.1, 0.2 and 0.3 GeV/c, respectively for pions, kaons and protons. In the range $|\eta| < 2$, their averages are 0.88 (pions), 0.85 (kaons) and 0.84 (protons).

Efficiency. The reconstruction efficiencies rise sharply with $p_{\rm T}$ (see Fig. 3.3-right), and become nearly flat above $p_{\rm T}$ values around 0.2, 0.3 and 0.4 GeV/c, respectively for pions, kaons and protons. In the range $|\eta| < 1.5$, the average reconstruction efficiencies are 0.90, 0.90 and 0.86.

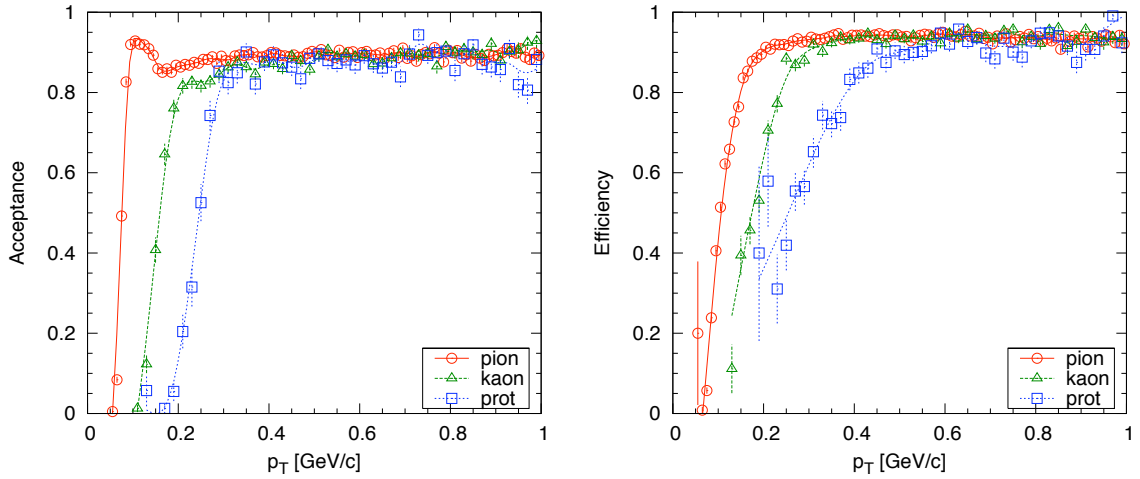

Figure 3.3: Acceptance (left) and efficiency (right) as a function of $p_{\rm T}$, for tracks in the range $|\eta| < 1$. Values are given separately for pions (circles), kaons (triangles) and (anti)protons (squares).

Multiple counting. The fraction of multiply-counted tracks is less than 1% near $\eta = 0$, and it decreases with η and $p_{\rm T}$: it is at the per mil level for $|\eta| > 0.5$ or $p_{\rm T} > 0.2$ GeV/c.

Fake rate. Without triplet cleaning, the fake rate is $\sim 4\%$ at $\eta \sim 0$ and reaches 20% at $|\eta| \sim 2$. With cleaning, the fake rate decreases very significantly (by a factor of 10), to around 0.5% and 2% at $\eta \sim 0$ and ~ 2, respectively. In the range $|\eta| < 1$, the fake rate decreases steeply with $p_{\rm T}$, being about 4% at 0.1 GeV/c, $\sim 1\%$ at 0.16 GeV/c and at the per mil level for higher $p_{\rm T}$ values.

Resolution. Figure 3.4-left shows, as a function of the generated $p_{\rm T}$ and separately for pions, kaons and protons, the ratio between the reconstructed and the simulated $p_{\rm T}$ (which we call "bias"). We see that the particles generated at low $p_{\rm T}$ tend to be reconstructed with a slightly lower $p_{\rm T}$ value, because of energy loss effects. This bias is negligible for high p/m values but is quite significant for low momentum protons (or antiprotons): a correction of almost 10% is needed for protons of $p_{\rm T} \sim 0.2$ GeV/c. In what concerns the pseudorapidity variable, the reconstructed value agrees very well with the generated value, with less than 1% bias.

Figure 3.4-right shows how the resolution of the reconstructed $p_{\rm T}$ depends on the generated $p_{\rm T}$. While at high $p_{\rm T}$ values (~ 1 GeV/c) the resolution is $\sim 6\%$ for all particles, at low $p_{\rm T}$ the multiple scattering and energy straggling effects are more important and lead to significantly degraded resolutions, in particular for protons.

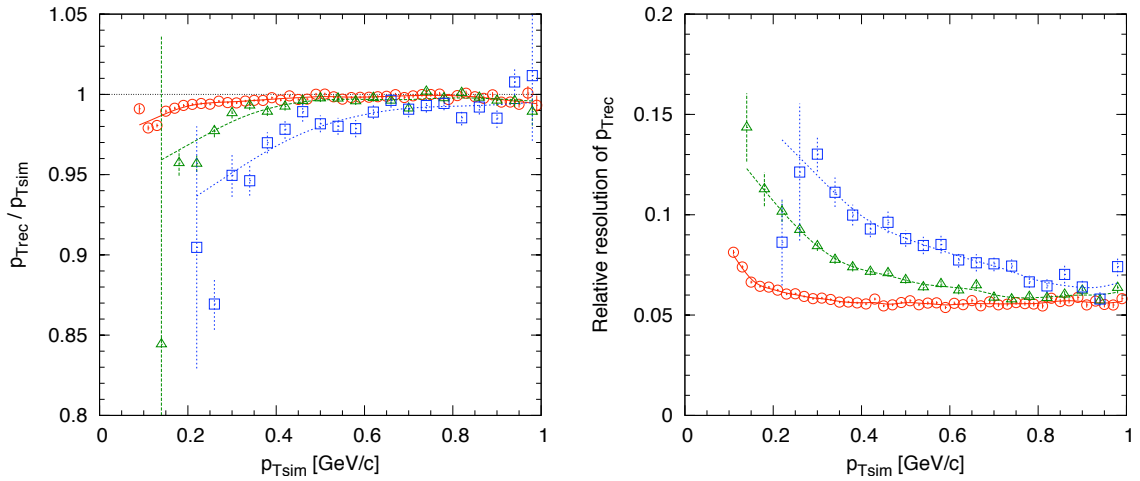

Figure 3.4: Degradation of the reconstructed p_{T} as a function of the simulated p_{T}, in terms of "bias" (left) and resolution (right), for pions (circles), kaons (triangles) and (anti)protons (squares), in the range $|\eta| < 1$.

Performance under various conditions. The performance of low p_{T} reconstruction was studied under several running conditions. These studies are based on 25 000 minimum bias pp events (PYTHIA generator) and on 25 central HYDJET PbPb events with two multiplicity settings: total particle multiplicities 30 000 ("central") and 15 000 ("mid-central"). In the pp case the single events have been superimposed according to a Poisson distribution, with an appropriate primary vertex distribution, in order to study the effect of pile-up at low-luminosity ($2 \cdot 10^{33}\mathrm{cm}^{-2}\mathrm{s}^{-1}$, 5 events per bunch-crossing on average) and at high-luminosity ($10^{34}\mathrm{cm}^{-2}\mathrm{s}^{-1}$, 25 events per bunch-crossing on average). Only in-time pile-up was considered. In the PbPb case, the primary vertex of the event was determined first, with good precision, using high p_{T} tracks. In a second step, the cylinder of origin was centred on this vertex, with a small half-length of 0.1 cm. In order to further reduce the reconstruction rate of fake tracks, the radius of the cylinder of origin was reduced to 0.1 cm. The reconstruction was made faster by increasing the minimum p_{T} cut to 0.175 GeV/c.

The reconstruction efficiency is shown in Fig. 3.5, for pions, as a function of η (left) and p_{T} (right). Above p_{T} around 0.4 GeV/c, the pion reconstruction efficiency in PbPb collisions is $\sim$ 90%, only 5% (or less) smaller than in pp collisions. Figure 3.6 shows that the reconstruction rate of fake tracks falls steeply with increasing p_{T}. It drops below 10% for $p_{\mathrm{T}} \sim 0.2$ GeV/c in high-luminosity pp collisions and for $p_{\mathrm{T}} \sim 0.4$ GeV/c in central PbPb collisions.

3.3 Neutral hadron (V0) and (converted) photon identification

We have seen in the previous sections that silicon detectors can detect charged particles with good position and momentum resolution. Some weakly-decaying neutral particles (V0s) such as $\mathrm{K}^0_{\mathrm{S}}$, Λ and $\overline{\Lambda}$, have a sizeable probability to decay far from the primary event vertex ($c\tau$ = 2.68 and 7.89 cm for $\mathrm{K}^0_{\mathrm{S}}$ and Λ, respectively). Their reconstruction is, thus, less challenging than that of other resonances decaying very close to the primary vertex. Such long-lived neutral particles can thus be reconstructed via their charged decay modes ($\mathrm{K}^0_{\mathrm{S}} \rightarrow \pi^+\pi^-$; $\Lambda \rightarrow \mathrm{p}\pi$).

Likewise, the silicon detectors can be used to reconstruct photons through their conversion to

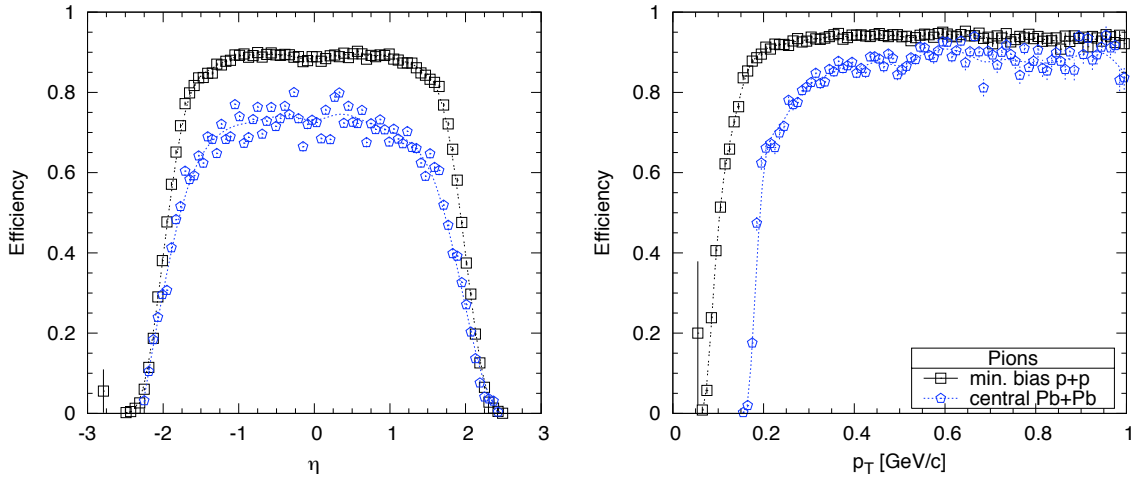

Figure 3.5: Pion reconstruction efficiency as a function of pseudo-rapidity η (left) and p_{T} (right, for tracks in the range $|\eta| < 1$), for minimum bias pp events (squares) and for central PbPb collisions ($\mathrm{d}N_{\mathrm{ch}}/\mathrm{d}y|_{y=0} = 3200$, circles). The difference in the η dependence for pp and PbPb is mostly due to the different $p_{\mathrm{T,min}}$ settings (0.075 and 0.175 GeV/c, respectively).

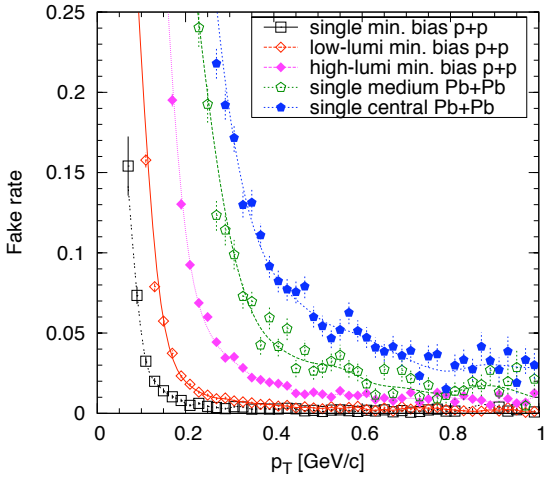

Figure 3.6: Reconstruction rate of fake tracks as a function of p_{T}, for tracks in the range $|\eta| < 1$, for single, low luminosity and high luminosity minimum bias pp events, and for central and mid-central PbPb collisions.

$\mathrm{e}^+\mathrm{e}^-$ pairs in the material of the beam-pipe, silicon pixels and supports. For a thin material, the probability of conversion is approximately $7/9\ x/X_0$, where x is the thickness of the material and X_0 is its radiation length. For a thickness of 0.1 cm this amounts to a conversion probability of 0.22% in beryllium and 0.83% in silicon. While the physics process is quite different, photon conversions are very similar to decays in most other aspects and will be treated together.

The analysis presented here only uses charged particles reconstructed from pixel hit triplets. Therefore, we can only find neutral particles which decay up to the first pixel barrel layer. Roughly half of the produced $\mathrm{K}^0_{\mathrm{S}}$ and Λ particles satisfy this condition. The probability that

a particle decays within a radius r is

$$P(r) = 1 - \exp\left(-\frac{r}{\tau}\frac{m}{p_{\mathrm{T}}}\right) \tag{3.1}$$

which is independent of pseudo-rapidity η.

These studies are based on 25 000 single minimum bias (PYTHIA) pp events, reconstructed with the modified hit triplet finding discussed in the previous Section, using the standard settings except for a much wider cylinder of origin (`originRadius` = 3.0 cm) and a minimum p_{T} of 0.075 GeV/c.

V0 finding. As already mentioned, in the small volume of the pixel detector the magnetic field is practically constant and the charged particles propagate on helices. The search for V0 candidates reduces to the determination of the closest point between two helices, as described in detail in Ref. [169].

Cuts. A neutral primary particle can only be formed if the two tracks have opposite electric charge. If there are n reconstructed tracks in an event, the number of such pairs is around $(n/2)^2$. For high multiplicity events, the number of combinations is enormous. Therefore, it is important to properly filter tracks and track-pairs in order to speed up the computations and reduce the background.

The distribution of the distance between the decay vertex and the beam-line (r) is shown in Fig. 3.7-left. The r distributions for V0s show an exponential behaviour, steeper for $\mathrm{K}^0_{\mathrm{S}}$ than for Λ, reflecting their different $c\tau$ values. The r distribution for photons is completely different. There are two peaks at $r \approx 4.2$ and 4.7 cm, due to conversions in the inner and outer silicon wafers of the first pixel barrel layer (the conversions in the 1-mm beryllium beam-pipe at 4 cm are hardly visible). The background distribution peaks near zero, as expected, and a cut at 0.5 cm rejects a big fraction of the background. A more detailed discussion is presented in Ref. [169].

Acceptance and efficiency. In the plateau region $|\eta| < 1.5$, about 30% of the produced $\mathrm{K}^0_{\mathrm{S}}$ and about 20% of Λ or $\overline{\Lambda}$ are reconstructed. Less photons are reconstructed, because they come mostly from π^0 decays and have low p_{T}.

Mass spectra. The invariant mass distribution of reconstructed $\mathrm{K}^0_{\mathrm{S}} \to \pi^+\pi^-$ decays is shown in Fig. 3.7-right. The $\mathrm{K}^0_{\mathrm{S}}$ is reconstructed with a resolution of 16 MeV/c^2, with an average mass of 0.496 GeV/c^2, in agreement with the nominal mass value. Figure 3.8 shows the Λ and $\overline{\Lambda}$ peaks, located at 1.114 GeV/c^2 and with a resolution of 6 MeV/c^2. The $\mathrm{d}E/\mathrm{d}x$ selection cut (see end of next section) removes almost all the background.

Performance. In the case of single collisions or low-luminosity pp running, the resonances can be exclusively identified. For high-luminosity pp running or PbPb collisions, the inclusive yield can still be extracted, with a reasonable background.

3.4 Further developments

Low p_{T} tracking. The study described above only used pixel hits. The reason for this limitation is the high occupancy in the strip layers, as already discussed in the introduction. Of course, even low p_{T} particles leave many hits in the strip layers. The pixel triplets should give good seeding for the inclusion of the strip layers of the tracker, which could be used

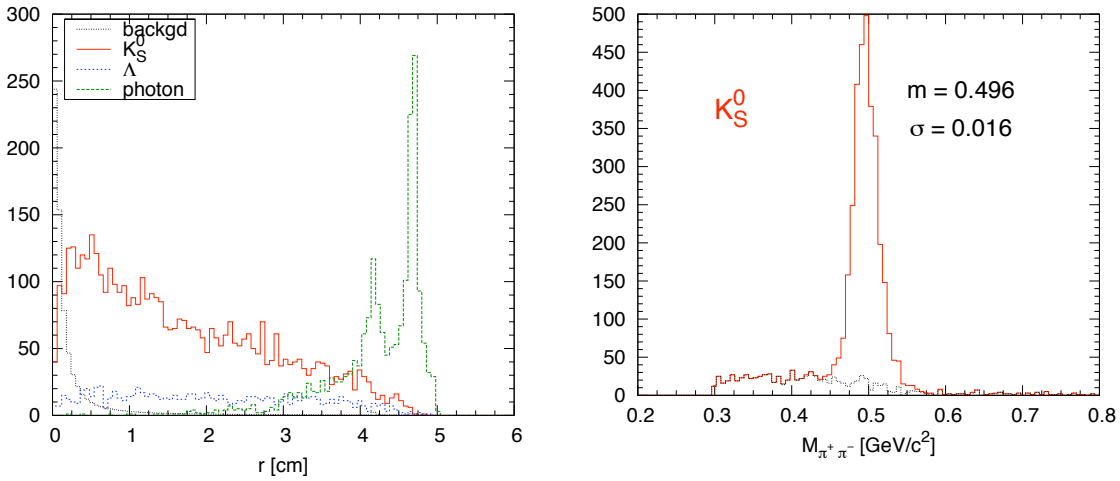

Figure 3.7: Left: Distribution of the distance (r) between the "decay vertex" and the beam-line for K^0_S, Λ and converted photons. The position of the inner and outer silicon wafers of the first pixel barrel layer are clearly visible in the r distribution of the photons. The scaled-down background is also shown. Right: Invariant mass distribution of reconstructed $\mathrm{K}^0_\mathrm{S} \rightarrow \pi^+\pi^-$ in single minimum bias pp collisions. The mass distribution of the background is indicated with a black dashed histogram. The results of a Gaussian fit to the signal are given in units of GeV/c^2.

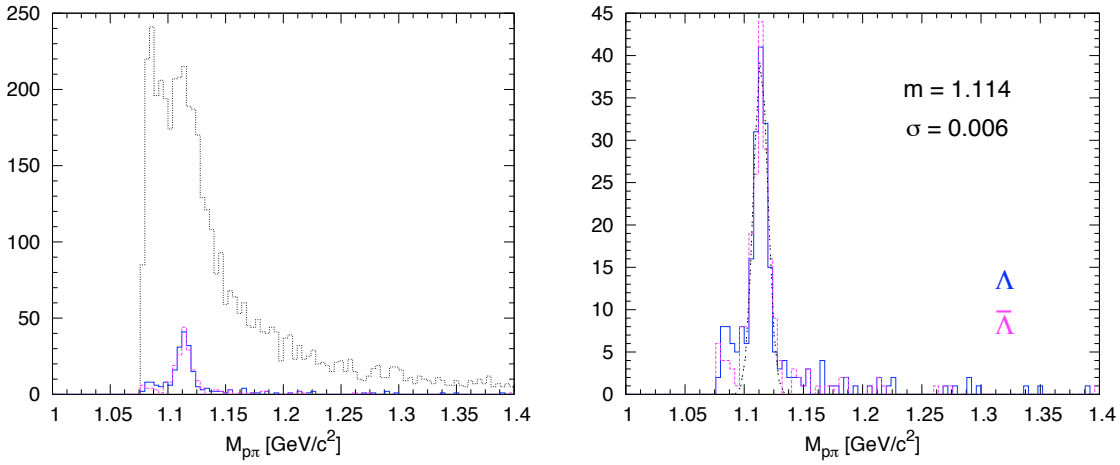

Figure 3.8: Invariant mass distribution of reconstructed Λ and $\overline{\Lambda}$ baryons in single minimum bias pp collisions. The dotted black line on the left shows the distribution before using $\mathrm{d}E/\mathrm{d}x$ to select the secondary proton or antiproton, while the solid histograms (plotted on the right with adjusted vertical scale) give the final result. The mass and resolution values extracted by a Gaussian fit are given in units of GeV/c^2.

for tracking (in low multiplicity pp collisions) or for vetoing (in high multiplicity nucleus-nucleus collisions). This extension should improve the momentum resolution for high p_{T} particles, where the curvature of the track is not sufficiently determined from the small volume of the pixel detector. Also in the case of the strip layers the analysis of the cluster shapes should provide useful information. In general, the use of the strip information should reduce the rate of fake tracks, although not many strip hits are expected for the lowest p_{T} tracks (up

to a few 100 MeV/c), where the fake tracks are most abundant.

V0 reconstruction. The found Λs can be used for the reconstruction of other weakly-decaying parent baryons, if the impact parameter cut is relaxed. By adding a π^-, we can reconstruct the doubly strange Ξ^-, through the decay $\Xi^- \rightarrow \Lambda\pi^-$ (100% branching ratio). The combination with a K^- gives the triple strange Ω^-, which decays via $\Omega^- \rightarrow \Lambda\mathrm{K}^-$ with 67.8% branching ratio. In these cases, the V0 finding corresponds to the analysis of the point of closest approach between the Λ line and the helix of the π^- or K^-.

Particle identification. The most probable energy loss of the charged particles can be estimated from the charge deposited in the individual pixels of the clusters [170], using a maximum likelihood analysis on the well known physical model of energy loss. Even with only three hits, it gives good relative $\mathrm{d}E/\mathrm{d}x$ resolution for minimum ionising pions. In the case of very low momenta, it enables the identification of pions, kaons and protons. Work in progress shows that inclusive yields can be extracted up to $p \approx 1$ GeV/c for pions and kaons, and up to about 2 GeV/c for protons. The expected p_T distributions of pions, kaons and protons, for pp and PbPb collisions, are shown in Fig. 3.9.

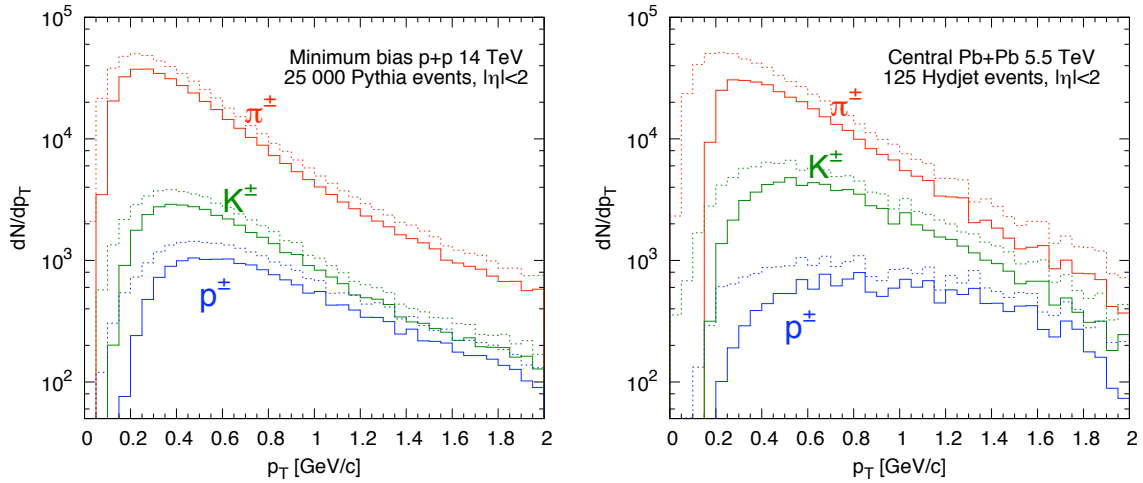

Figure 3.9: Reconstructed (solid lines) and generated (dotted lines) p_T distributions of the pions, kaons and protons produced in 25 000 minimum bias pp Pythia events at 14 TeV (left) and in 125 central PbPb HYDJET events at 5.5 TeV/nucleon (right).

3.5 Conclusions

With a modified hit triplet finding algorithm, the pixel detector can be employed for the reconstruction of low p_T charged hadrons in high luminosity pp collisions, as well as in PbPb reactions. The acceptance of the method extends down to 0.1, 0.2 and 0.3 GeV/c in p_T for pions, kaons and protons, respectively. The fake track rate can be greatly reduced by using the geometrical shape of the pixel clusters. Acceptances and efficiencies around 80–90% can be achieved, with $\sim 6\%$ p_T resolution in the midrapidity region. The fake track rate for single, low-luminosity and high-luminosity pp collisions is smaller than 2% above p_T values of 0.13, 0.2 and 0.35 GeV/c, respectively. In case of central (mid-central) PbPb events the fake rate is below 10% (5%) for $p_\mathrm{T} > 0.4$ GeV/c.

Although neutral particles do not create hits in the pixel detectors, they can be observed via their charged decay products. The combination of helices of secondary pions and/or protons

enables the reconstruction of low p_{T} weakly-decaying hadrons ($\mathrm{K}^0_{\mathrm{S}}$, Λ and $\overline{\Lambda}$) decaying before the first pixel layer. The observed mass widths are compatible with the resolution of the momentum reconstruction. Low p_{T} photons converting in the beam-pipe or in the first pixel barrel layer are also detectable.

In summary, the CMS detector is able to provide good quality data on low p_{T} charged and neutral particle spectra and yields, thus contributing to the soft hadronic physics program at the LHC.

Chapter 4

Elliptic flow

4.1 Introduction

Measurements of the azimuthal anisotropy of particle production with respect to the reaction plane are one of the important tools for studying the properties of the dense matter created in ultrarelativistic heavy-ion collisions (see Section 1.4.3). At RHIC, the elliptic flow parameter, v_2, defined as the second harmonic coefficient of the particle azimuthal distribution with respect to the reaction plane, Eq. (1.2), appears to grow monotonically with increasing p_{T} [171] and saturates for p_{T} above ~ 2 GeV/c, at $v_2 \approx 0.2$. Below $p_{\mathrm{T}} \approx 2$ GeV/c, the amount of anisotropic flow for all hadron species can be well described by hydrodynamical models, indicating that the produced matter develops a strong collective flow in the first ~ 5 fm/c of the collision and behaves as a "perfect fluid", with a viscosity near a conjectured lower bound [30]. Above $p_{\mathrm{T}} \approx 2$ GeV/c, particle production is dominated by the fragmentation of hard-scattered quarks and gluons. Azimuthal anisotropies arise from parton energy loss effects in the different medium path-lengths L traversed by the produced partons. Therefore, study of high-p_{T} particle production with respect to the reaction plane provides a quantitative cross-check of the expected L^2 dependence of non-Abelian (gluon bremsstrahlung) energy loss models [172, 173]. Since the initial gluon densities in PbPb reactions at $\sqrt{s_{NN}}$ = 5.5 TeV at the LHC are expected to be significantly higher than at RHIC, a stronger partonic energy loss and, correspondingly, larger high-p_{T} elliptic flow [44] is anticipated. In this chapter we analyse the capabilities of CMS calorimetric and tracker systems to study collective elliptic flow at low p_{T}, and parton energy loss induced azimuthal anisotropies at high p_{T}.

4.2 Reaction plane reconstruction

4.2.1 General method

Several methods have been proposed and used at the SPS and RHIC to determine the reaction plane. These can also be used at the LHC [174, 175]. The quantity under study in the most general case is the triple differential distribution with respect to the reaction plane, written as a Fourier series, Eq. (1.2). The reaction plane angle, Ψ_n, can then be determined from the measured n-th harmonic via the equation [176]

$$\tan n\Psi_n = \frac{\sum_i \omega_i \sin n\varphi_i}{\sum_i \omega_i \cos n\varphi_i} \quad , \tag{4.1}$$

where φ_i is the azimuthal angle of the i-th particle, ω_i is a weight, and the sum runs over all particles. A procedure to optimise the weights is usually needed in order to achieve the

best accuracy, e.g. using the particle transverse momentum, $\omega_i = p_{\mathrm{T}i}$, or (for calorimetric measurements) the energy deposition in the calorimetric sector i at azimuthal angle φ_i, $\omega_i = E_i(\varphi_i)$. The Ψ_n angle lies within $-\pi/n < \Psi_n < \pi/n$.

The distribution of the difference, $\Delta\Psi_n$, between the measured angle, Ψ_n, and the "true" angle, Ψ_0, is independent of Ψ_0 if non-flow particle correlations are neglected, and has the form [74, 176]

$$\frac{\mathrm{d}w}{\mathrm{d}(n\Delta\Psi_n)} = \frac{1}{2\pi}\left[e^{-\frac{\xi^2}{2}} + \xi\sqrt{\frac{\pi}{2}}\cos\left(n\Delta\Psi_n\right)\left[e^{-\frac{\xi^2\sin^2\left(n\Delta\Psi_n\right)}{2}}\left(1+\mathrm{erf}\left(\frac{\xi\cos\left(n\Delta\Psi_n\right)}{\sqrt{2}}\right)\right)\right]\right], \tag{4.2}$$

where w is the weighting variable. The dimensionless parameter ξ depends on particle multiplicity and strength of the anisotropy, and determines the resolution of the reaction plane: $\Psi_n(\xi \to \infty) = \Psi_0$.

When the azimuthal distribution of particles is described by an elliptic form, as is the case in non-central collisions where the initial state is characterised by an anisotropic distribution in coordinate-space given by the lens- or almond-like shape of the overlapping zone (Fig. 1.14-left), then

$$\frac{\mathrm{d}N}{\mathrm{d}\varphi} = \frac{N_0}{2\pi}\left[1 + 2v_2\cos 2(\varphi - \Psi_0)\right], \quad N_0 = \int_{-\pi}^{\pi}\mathrm{d}\varphi\,\frac{\mathrm{d}N}{\mathrm{d}\varphi}, \tag{4.3}$$

where N_0 is the total particle multiplicity in the event, and the reaction plane angle Ψ_0 can be determined via the second harmonic, $n = 2$ in Eq. (4.1). The elliptic flow coefficient v_2 is $\langle\cos 2(\varphi - \Psi_0)\rangle$.

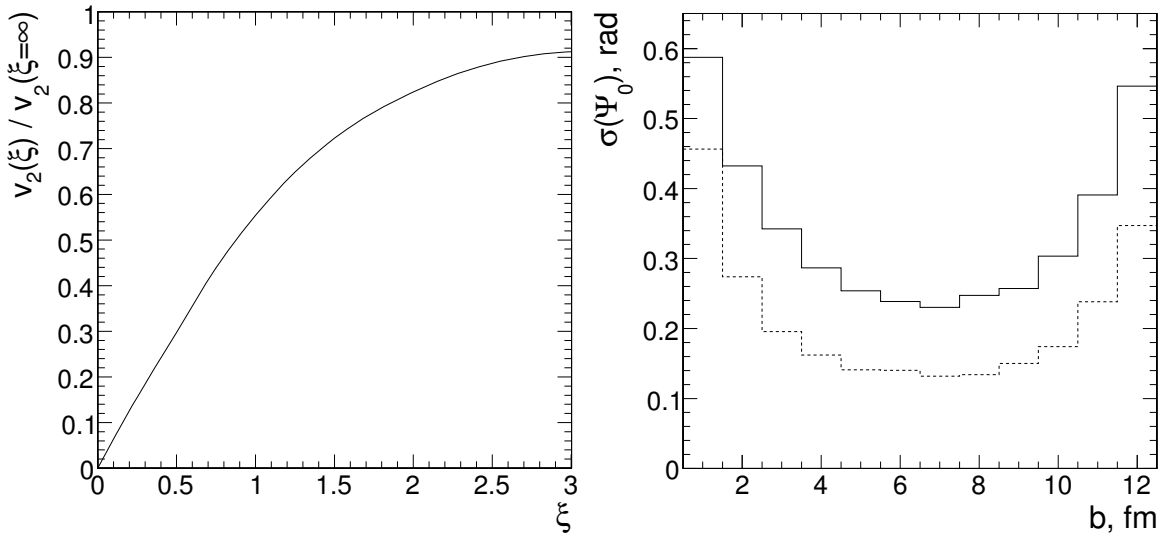

Figure 4.1: Left: The accuracy of the determination of the elliptic flow coefficient, $v_2(\xi)/v_2(\xi \to \infty)$, as a function of the parameter ξ. Right: Event plane resolution, $\sigma(\Psi_0)$, as a function of impact parameter in PbPb collisions with N_0 (b = 0 fm) = 58 000 (solid histogram) and 84 000 (dashed histogram) total particle multiplicities.

Figure 4.1-left shows the accuracy of the v_2 determination, defined as the ratio of the "measured" value, $v_2(\xi) = \langle\cos 2(\varphi - \Psi_2)\rangle$, to the "true" value, $v_2(\xi \to \infty) = \langle\cos 2(\varphi - \Psi_0)\rangle$ [74, 176]. This dependence has a universal form for different absolute values of v_2. For ex-

ample, Fig. 4.1-left shows that a value ξ = 2.5 (0.8) corresponds to an observed anisotropy parameter reduced by 10% (a factor of 2) compared to the true value.

Note that the procedure described above for the analysis of the azimuthal anisotropies relies on the assumption that collective elliptical flow is the dominant source of particle correlations. However, there exist other known physical sources of azimuthal correlations, such as (mini)jet production, global momentum conservation, resonance decays (where the decay products are correlated), final state Coulomb, strong or quantum interactions. The importance of these non-flow contributions can be assessed using different methods to determine v_2 and using detectors covering different ranges of pseudorapidity.

4.2.2 Generator level studies

In most of the available Monte Carlo heavy-ion event generators, azimuthal anisotropies with respect to the reaction plane are either ignored or inadequately implemented. The fast Monte Carlo event generator HYDJET (HYDrodynamics plus JETs, see Appendix A) [163, 177] has been developed to be able, among other things, to simulate flow effects in high-energy heavy ion collisions. The accuracy of event plane determination (ξ parameter) is mainly sensitive to two model factors: the strength of the elliptic flow signal, and the particle multiplicity of the event N_0. We used a set of 1000 HYDJET PbPb events, without jet quenching, for each centrality bin, covering the range of impact parameters from b = 0 fm to $b = 2R_A$ ($R_A^{Pb} \approx$ 6.7 fm). The mean total multiplicity of the soft part of central PbPb event was 26 000, that corresponds to a mean total multiplicity N_0 (b = 0 fm) $\approx$ 58 000 and a mean charged particle density at midrapidity of $\mathrm{d}N_{\mathrm{ch}}/\mathrm{d}\eta|_{\eta=0}(b = 0\ \mathrm{fm}) = 3000$. Stable particles (charged pions and kaons, protons, neutrons, photons and electrons), within the pseudorapidity window $|\eta| < 3$ (CMS barrel+endcap calorimetry acceptance), were considered for the event plane analysis using $n = 2$ and $\omega_i = p_{\mathrm{T}i}$ in Eq. (4.1). An additional cut $p_{\mathrm{T}} > 0.8$ GeV/c on the charged particle transverse momentum was applied in order to take into account the fact that charged particles with smaller p_{T} do not generally reach the calorimeter since they curl up in the 4 T magnetic field and are absorbed in the material in front of it.

Figure 4.1-right shows the calculated resolution $\sigma(\Psi_0)$ — defined as the width of a Gaussian fit to the distribution of the difference between the generated and the reconstructed azimuthal angles of the reaction plane — as a function of impact parameter in PbPb collisions. The interplay of multiplicity and anisotropic flow in opposite centrality directions results in the best resolution being obtained in semi-central collisions. Here, semi-central collisions have an impact parameter on the order of the nuclear radius, $b \approx R_A$. In order to demonstrate the influence of the multiplicity on the accuracy of the event plane determination, we also calculated the resolution for "high" multiplicity events (obtained by increasing mean multiplicity of the soft part of the event up to $\sim$ 52 000 particles in central PbPb collisions corresponding to a mean total event multiplicity N_0 (b = 0 fm) $\approx$ 84 000). Increasing the soft multiplicity by a factor of 2 results in an improvement of the resolution by a factor ~ 1.7 with no significant dependence on the event centrality.

Introducing jet quenching into the model results in a rise of the particle multiplicity in the event and the generation of some additional elliptic flow in the high-p_{T} region. The estimated improvement on the event plane resolution is around 20–25% for both lower and higher multiplicities.

4.2.3 Reaction plane via calorimetry

A detailed description of the CMS calorimetric system can be found in the Technical Design Reports [178, 179]. The electromagnetic (ECAL) and hadron (HCAL) calorimeters cover the pseudorapidity region $|\eta| < 3$ (i.e. $|\eta| < 1.5$ for the barrel part, and $1.5 < |\eta| < 3$ for the endcaps). A pair of quartz-fiber forward calorimeters (HF) cover the region $3 < |\eta| < 5$ and, together with the CASTOR and ZDC calorimeters, complement the energy measurement at very forward rapidities.

The capability of the CMS calorimetric system to study elliptic energy flow and jet azimuthal anisotropy in heavy-ion collisions was studied with the GEANT3-based CMS simulation package for the first time in Ref. [180], using a very high multiplicity value, $\mathrm{d}N_{\mathrm{ch}}/\mathrm{d}\eta|_{\eta=0} = 8000$ (corresponding to $N_0 \approx 100\,000$) in central PbPb collisions, and not including jet production. An update of this analysis has been performed for a more realistic value of HYDJET event multiplicity, $\mathrm{d}N_{\mathrm{ch}}/\mathrm{d}\eta|_{\eta=0} = 3000$ (corresponding to $N_0 \approx 58\,000$) in central PbPb collisions. The CMS calorimeter responses were obtained with the GEANT4-based CMS simulation code OSCAR_3_9_8 [181] and the package for signal digitisation and reconstruction ORCA_8_13_3 [182]. A sample of 10 000 HYDJET PbPb events (with jet quenching off) at $b = 9$ fm was used in the analysis.

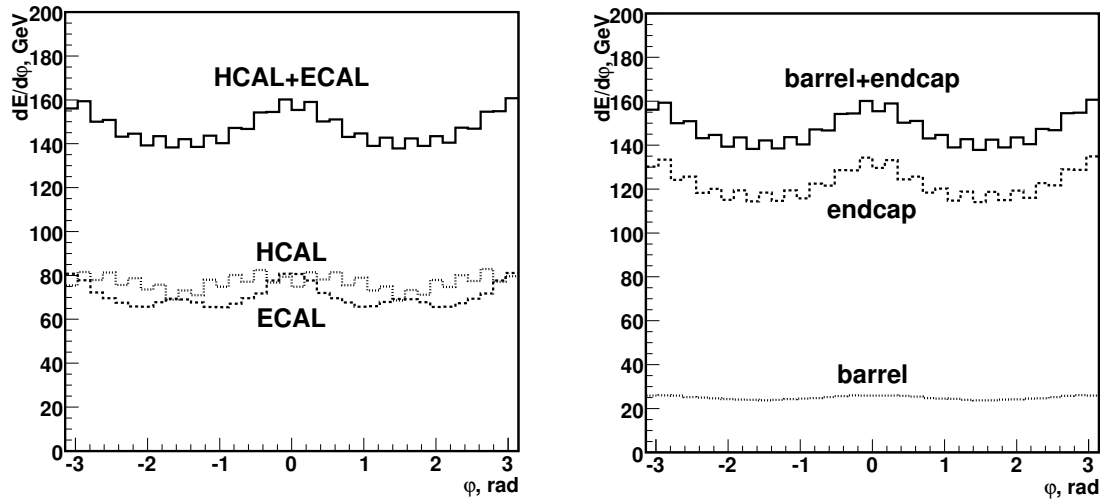

Figure 4.2: Azimuthal dependence of the total energy deposition in the CMS calorimeters in PbPb collisions at $b = 9$ fm (solid histogram) and how it is distributed between the HCAL and the ECAL (left), and between the barrel and the endcaps (right) regions. The $\cos(2\varphi)$ modulation due to the input HYDJET elliptic flow is clearly visible.

Figure 4.2 illustrates the energy deposited as a function of azimuthal angle for the HCAL and ECAL (barrel and endcap regions). The event plane resolutions obtained with $n = 2$ and $\omega_i = E_i(\varphi_i)$ in Eq. (4.1) are shown in Fig. 4.3 and are summarised in Table 4.1.

The best estimated resolution, $\sigma(\Psi_0) \approx 0.37$ rad for the ECAL (barrel+endcaps), allows the measurement of the v_2 elliptic flow coefficient with a $\sim 70\%$ accuracy. This accuracy is obtained from the ξ–dependence in Fig. 4.1-left. The corresponding value of ξ is determined by the Gaussian fit of the distribution Eq. (4.2) with $\sigma(\Psi_0)$. The "measured" $\sigma(\Psi_0)$ resolution with CMS calorimetry is about 40% worse than that obtained at the generator level (the value of the solid histogram in Figure 4.1 right, at $b = 9$ fm), before the smearing of the particle

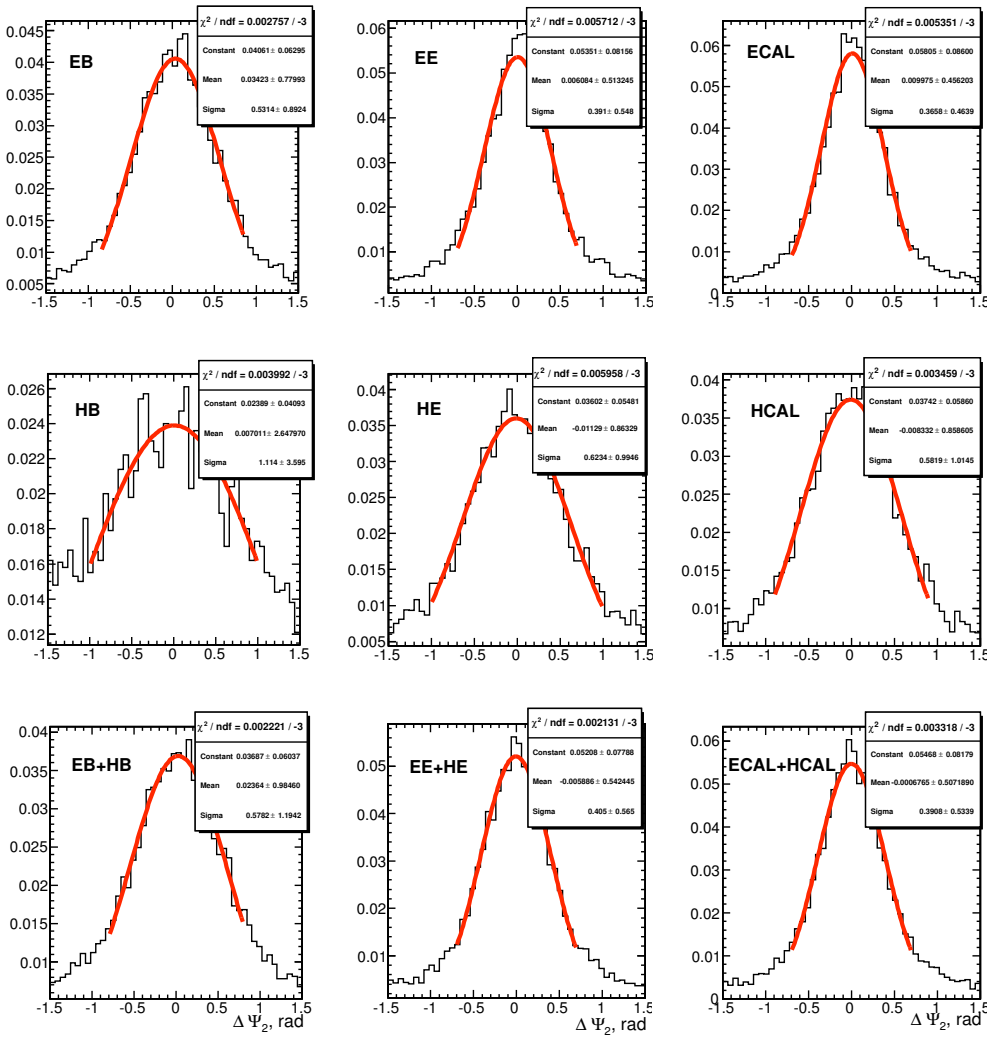

Figure 4.3: The *differences* between the generated and the reconstructed azimuthal angles of the reaction plane for PbPb collisions at $b = 9$ fm. From left to right: using only the barrel (HB, EB), only the endcaps (HE, EE), both barrel and endcaps. From top to bottom: only ECAL, only HCAL, ECAL+HCAL.

Table 4.1: Event plane resolutions, $\sigma(\Psi_0)$ in rad, for PbPb collisions at $b = 9$ fm.

Calorimeter	Barrel	Endcaps	Barrel + Endcaps
ECAL	0.53	0.39	0.37
HCAL	1.11	0.62	0.58
ECAL+HCAL	0.58	0.41	0.39

4-momenta by the detector effects (non linearity of calorimeter response, finite calorimetric energy resolution, magnetic field, etc.). The corresponding degradation in the accuracy of the v_2 determination is from $\sim 80\%$ at the generator level to $\sim 70\%$ at the calorimetric level.

The ECAL is more suitable than the HCAL for event plane determination. This is primarily due to the better energy resolution of the ECAL for low and moderate p_{T} particles, along with a larger distorting influence of the magnetic field on the HCAL energy flow. Another

important result is that, although the anisotropic flow is maximal at midrapidity, the much larger total energy deposition in the endcaps results in reducing the relative fluctuations and, accordingly, in a much better event plane resolution. Moreover, energy flow measurements in the endcaps are less sensitive to the magnetic field than in the barrel. We could even rely exclusively on the endcaps for the event plane determination. This would be particularly interesting for the study of jet azimuthal anisotropies. Indeed, we would perform a more robust measurement by only considering jets in the barrel (which would only reduce the dijet rate by a factor of 2, since the jet rapidity distribution peaks at midrapidity), in a rapidity window different from the one where the reaction plane would be determined.

An alternative method for calorimetric measurement of the jet azimuthal anisotropy, without direct event-by-event reconstruction of the reaction plane has been discussed in Ref. [183]. The technique is based on the correlation between the azimuthal position of a jet axis and the energy deposition in calorimetric sectors that are not incorporated in the jet. The accuracy of the $v_2^{\rm jet}$ determination achieved by such a method has been found to be similar to that derived from the direct reconstruction of the reaction plane [180].

4.2.4 Reaction plane determination with the tracker

The charged particle reconstruction capabilities in heavy-ion collisions using the CMS Silicon Tracking System [184] were evaluated in Ref. [165] using a full detector simulation. Even in the high-multiplicity environment of central PbPb events, a high algorithmic tracking efficiency of about 80% is achieved with less than a few percent fake track rate for $p_{\rm T} > 1$ GeV/c. Tracks are reconstructed with excellent momentum resolution, $\Delta p_{\rm T}/p_{\rm T} < 1.5\%$ (for $p_{\rm T}$ values up to 100 GeV/c). The resolution of the track offset at the event vertex is better than 50 μm, improving to 20 μm for $p_{\rm T}$ above 10 GeV/c. Thus, it seems feasible to use the CMS tracking system for elliptic flow measurements. A preliminary analysis, based on a full detector simulation of HYDJET PbPb events, shows that the event plane resolution achieved with the CMS tracker is close to the value obtained at the generator level and somewhat better than the value obtained with the CMS calorimetry. The transverse momentum and rapidity dependences of the elliptic flow coefficient can be reconstructed with the CMS tracker with high accuracy, using the event plane as well as the cumulant method. More detailed studies of this topic are currently in progress [185].

4.3 The cumulant method for flow studies

Anisotropic flow can also be measured without direct reconstruction of the reaction plane angle. Since all particles are correlated with the reaction plane, they are also indirectly correlated with each other [176, 186]. In the case when the particle distribution can be well described by an elliptic form, Eq. (4.3), and there are no other particle correlations besides those due to flow (or other correlations can be neglected), the azimuthal anisotropy coefficient can be determined using the two-particle azimuthal correlator without the event plane angle Ψ_0,

$$\begin{aligned}\langle\cos 2(\varphi_1-\varphi_2)\rangle &= \frac{1}{N_0^2}\int\limits_{-\pi}^{\pi}{\rm d}\varphi_1\int\limits_{-\pi}^{\pi}{\rm d}\varphi_2\ \cos 2(\varphi_1-\varphi_2)\,\frac{{\rm d}^2N}{{\rm d}\varphi_1{\rm d}\varphi_2}\\ &= \frac{1}{N_0^2}\int\limits_{-\pi}^{\pi}{\rm d}\varphi_1\int\limits_{-\pi}^{\pi}{\rm d}\varphi_2\ \cos 2((\varphi_1-\Psi_0)-(\varphi_2-\Psi_0))\,\frac{{\rm d}N}{{\rm d}\varphi_1}\,\frac{{\rm d}N}{{\rm d}\varphi_2} = v_2^2\,. \end{aligned} \tag{4.4}$$

The advantage of this method is that it automatically corrects for the detector anisotropies. Thus, the correlation-function method is more robust than the event-plane based approaches. On the other hand, in this procedure each harmonic of the azimuthal distribution is determined independently, without taking into account that the different harmonics are related to each other through the reaction plane. In the event-plane method these relations provide useful consistency checks which are absent here. The statistical uncertainties, and those arising from non-flow effects, are the same in the event-plane methods and in the correlation function approach, because all these methods rely on two-particle azimuthal correlations.

The sensitivity to non-flow effects in the two-particle azimuthal correlation methods motivated the development of new techniques which make use of the fact that anisotropic flow correlates *all* particles in the event. It was thus proposed to measure flow with multi-particle azimuthal correlations by performing a cumulant expansion where the collective source of correlations can be disentangled from other sources [186, 187]. The main advantage of the higher order cumulant analysis lies in the fact that, if the flow is larger than the non-flow correlations, the contribution of the latter to v_2, extracted from higher order correlators, is suppressed by powers of the particle multiplicity in the event, N_0.

Thus, for example, the fourth order cumulant for elliptic particle flow is defined as

$$\begin{aligned} c_2[4] \;\equiv\; & \langle \cos 2(\varphi_1 + \varphi_2 - \varphi_3 - \varphi_4) \rangle \\ - \langle \cos 2(\varphi_1 - \varphi_3) \rangle \, \langle \cos 2(\varphi_2 - \varphi_4) \rangle - \; & \langle \cos 2(\varphi_1 - \varphi_4) \rangle \, \langle \cos 2(\varphi_2 - \varphi_3) \rangle \; . \end{aligned} \tag{4.5}$$

If there are only correlations with the reaction plane (i.e. the multi-particle distributions factorise as in Eq. (4.4)), then

$$c_2[4] \;=\; -\, v_2^4 \quad . \tag{4.6}$$

If the coefficient v_2 is defined by the two-particle correlator,

$$v_2 \;=\; \sqrt{\langle \cos 2(\varphi_1 - \varphi_2) \rangle} \quad , \tag{4.7}$$

then the contribution of non-flow correlations is of order $1/\sqrt{N_0}$. Non-flow contributions to v_2, extracted from the fourth-order correlator,

$$v_2 \;=\; (-c_2[4])^{1/4} \quad , \tag{4.8}$$

scale as $1/N_0^{3/4}$, suppressed by an extra factor of $1/N_0^{1/4}$.

Ref. [188] has applied the two- and four-particle correlations technique with the HYDJET event generator to reproduce the elliptic flow observed at RHIC. Studies are ongoing [189] to apply the cumulant method with charged tracks measured in CMS.

4.4 Conclusions

Azimuthal correlation measurements in ultrarelativistic heavy ion collisions have recently generated a very strong interest. High-accuracy measurements of anisotropic flow provide important constraints on the viscosity (low p_{T}) and parton number density (high p_{T}) properties of the produced medium. The rescattering and energy loss of hard partons in an azimuthally anisotropic volume of dense matter can result in an observable azimuthal anisotropy of high-p_{T} particles and jets.

The reaction plane can be determined independently by different detector subsystems (in different pseudo-rapidity windows), and using different analysis methods. At central rapidities ($|\eta| < 2.5$), CMS will be able to determine the reaction plane for a very wide range of particle multiplicities and elliptic flow magnitudes, using the calorimeters and the tracker. The ECAL is found to be more suitable than the HCAL for event plane determination. Using the endcaps for the event plane reconstruction and reconstructing the jets in the barrel should provide a more robust analysis of elliptic flow. Use of the CMS tracking system for elliptic flow measurements. yields somewhat better values than those obtained with calorimetry at central rapidities.

In addition to the central rapidity region, measurements in the forward rapidity region covered by the HF and CASTOR calorimeters should allow us to study v_2 in a region almost free from non-flow contributions. Besides, the longitudinally segmented CASTOR calorimeter (and, to some extent, also the HF) has some capability for separating photons from hadrons, allowing us to compare photon and hadron flow.

At beam-rapidity, the ZDCs can provide an independent determination of the reaction plane from the directed flow signal (v_1). A systematic comparison between different methods and different detector subsystems in CMS will allow us to estimate non-flow contributions to the measured anisotropies and will be crucial for a quantitative interpretation of the results. The expected precision of the reaction-plane determination will allow for anisotropy measurements with a good accuracy for charged particles (identified or not) in a momentum range from a few hundred MeV/c up to a few hundred GeV/c.

Chapter 5

Triggering on hard probes

5.1 Introduction

The key component for exploiting the CMS capabilities in heavy-ion collisions is the trigger system, which is crucial for accessing the rare probes expected to yield the most direct insights into the properties of high-density strongly-interacting matter. Examples of such probes are high E_{T} jets and photons, Z^0 bosons, D and B mesons, and high-mass dileptons from quarkonia decays. The unique CMS trigger architecture employs only two trigger levels. The Level-1 trigger is implemented using custom electronics and inspects events at the full bunch crossing rate. All further online selection is performed in the High-Level Trigger (HLT) using a large cluster of commodity workstations (the "filter farm") with a vast computing power (equivalent to 12 000 1.8 GHz CPUs or $\sim$50 TFlops) running offline reconstruction algorithms on fully-assembled event information.

In this section, we will discuss the basic performance parameters of the trigger system in the context of heavy-ion collisions. We will define the overall trigger strategy and show examples of the CMS physics performance using event selection in the HLT. The studies are based on parametrisations of the performance of offline algorithms for jet and muon finding, described in previous CMS heavy-ion analysis notes [190, 191] and elsewhere in this volume. Using this information, we employ a simulation chain to translate production cross sections into rates to tape, making assumptions about the allocation of bandwidth to tape for various trigger channels (i.e. the trigger table). For the High Level Trigger (HLT), we follow the pp philosophy, assuming that the present offline reconstruction algorithms for the heavy-ion data will provide the baseline for the online HLT event selection algorithms.

The studies confirm that the design of the CMS trigger system is well suited to application in heavy-ion collisions. This is true even though the proposed basic trigger strategy is very different from that in pp: for PbPb running, it appears feasible and desirable to perform *all* event rejection for true PbPb collision events in the HLT, using the Level-1 hardware trigger mainly for rejection of background and beam-gas collision candidates. This may no longer be the case for runs with lighter nuclei, where luminosities should approach 10^{31} cm^{-2}s^{-1}.

5.2 Basic constraints for triggering in heavy-ion collisions

Experience from studies of heavy-ion collisions at the SPS and RHIC shows that there is no simple criterion for rejecting events based on global characteristics like multiplicity or total transverse energy. Rather, it was found that, for essentially all observables, studies as a function of collision centrality are critical for extracting the underlying physics. Therefore,

the basic trigger strategy for heavy-ion collisions has to be the efficient identification of any potentially interesting signature for a given input event. Experience also shows that the rejection of background events, such as those caused by beam-gas collisions, early on in the triggering chain is crucial for providing a sufficiently clean, low-rate environment for the high level trigger stages. In this section, we summarise the basic performance parameters of the CMS DAQ and trigger system that were used in our trigger studies, as well as the assumptions we made about PbPb luminosities and production rates for various physics processes.

The basic constraints for the CMS DAQ and trigger system follow from the pp running conditions. At LHC pp design luminosity, multiple collisions will occur at each bunch crossing with a frequency of 40 MHz. The effective pp event output rate to mass storage is limited to 150 Hz, for technology and cost reasons, corresponding to an output bandwidth of 225 MByte/s.

Consequently, the trigger system in pp running has to select less than 10^{-5} of all collision events for permanent storage while maximising the sensitivity to new physics. The Level-1 selection reduces the event rate by a factor of 400, to 100 kHz. In pp running, a reduction of the event rate by a factor of more than 600 in the HLT is required to achieve the design output rate. The fact that a typical pp "event" at design luminosity actually consists of ~ 20 superimposed pp collisions is also important for our discussion.

The PbPb design luminosity, $\mathcal{L} = 10^{27}$ cm^{-2}s^{-1} at the beginning of a store, is smaller than the pp design luminosity by 7 orders of magnitude. [1] Assuming collisions in three interaction regions, the instantaneous luminosity will drop quickly throughout the duration of a store, giving an average luminosity of $\langle\mathcal{L}\rangle = 4 \times 10^{26}$ cm^{-2}s^{-1}. Using a nucleon-nucleon inelastic cross section of 72 mb at 5.5 TeV, the corresponding PbPb collision rate at the beginning of a store is expected to be ~ 8 kHz, while the average collision rate over the duration of a store will be ~ 3 kHz.

Therefore, even the maximum rate for PbPb collisions is much smaller than the 100 kHz input rate for the HLT in pp collisions after Level-1 selection. This suggests that it will be possible to send all PbPb events to the HLT, provided that the average event size is less than a factor 10 larger than the average event size of the pp events sent to the HLT. To validate a possible trigger strategy in which *all event selection in PbPb running is done at the HLT level,* one therefore needs to verify two conditions:

1. The average PbPb event size is less than a factor of 10 larger than that of full luminosity pp running;
2. On average, the heavy-ion HLT algorithms are fast enough to process PbPb events at the full PbPb event rate.

If these conditions are fulfilled, PbPb event selection by algorithms using the full event information in the HLT will be feasible and, by definition, will provide the best possible selectivity for the physics of interest. Following this strategy, the main purpose of the Level-1 trigger in PbPb running will be to provide a clean discrimination of true heavy-ion collisions and to

[1] The "equivalent-pp luminosity" for hard processes — obtained scaling by the number of binary nucleon-nucleon collisions — is, however, a much larger value. For minimum bias PbPb, $\langle\mathcal{L}\rangle_{\mathrm{pp-equiv}} = A^2 \cdot \langle\mathcal{L}\rangle_{AA}$ = 20 μb^{-1}s^{-1}, corresponding to $\int \mathcal{L}\, dt$ = 20 pb^{-1} for the nominal 1 month and 50% efficiency.

provide seed objects, such as high p_{T} muon candidates, as input to the HLT algorithms. No significant rejection of PbPb collisions would be performed at Level-1.

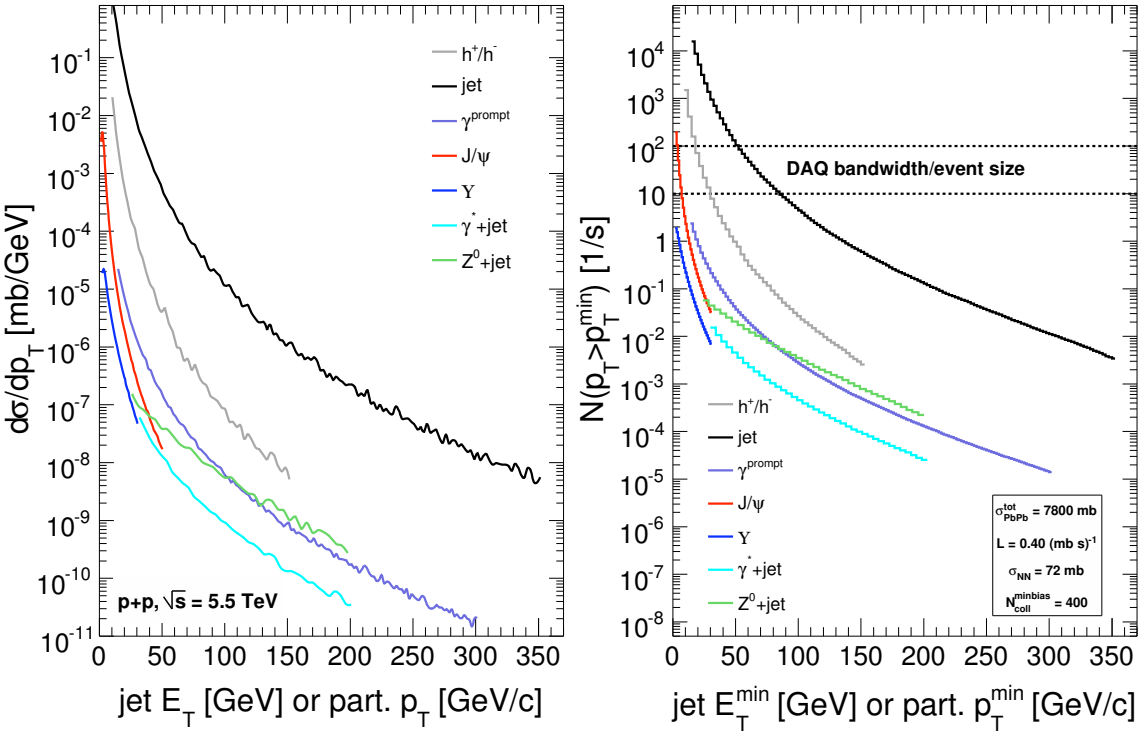

Figure 5.1: Left: Production cross sections of some of the relevant physics channels in pp collisions at $\sqrt{s_{NN}} = 5.5$ TeV, the nominal collision energy per nucleon in PbPb collisions at the LHC. The cross sections correspond to those used in the studies presented in Sections 6.1 (NLO pQCD for $Q\overline{Q}$) and 7.2 (PYTHIA for the other observables). Right: Production rates in minimum bias PbPb collisions at $\sqrt{s_{NN}} = 5.5$ TeV corresponding to the cross sections from the left plot scaled by $\langle N_{\mathrm{coll}} \rangle$ = 400 and for the average design luminosity.

The possible gain in physics reach by the HLT, relative to simply collecting minimum bias events, is determined by the ratio between the collision rate and the rate of events written to mass storage. The bandwidth to mass storage of 225 MByte/s translates into an event rate of 10-100 Hz, based on estimates of the heavy-ion event size that will be discussed below. This output rate is not only limited by the available mass storage technology but also by limits on the available offline analysis resources. It is more efficient to invest resources in a high quality online trigger scheme than in offline handling and storage of poorly-selected data.

Our calculations suggest a maximum average gain due to triggering of a factor 30–300 in the statistics of rare probes. Although this is far less than the gain in pp collisions, it is still crucial for the success of the CMS heavy-ion program. In practical terms, this gain in effective rate to tape will allow us to study rare processes as a function of impact parameter and reaction plane, for instance, instead of just measuring its overall yield. The flexibility of the HLT system will allow allocation of bandwidth not just to certain trigger channels, but differentially as a function of y and p_{T} of the trigger object, and as a function of collision centrality, thereby maximising the overall physics reach of our measurements.

The basic trigger strategy in PbPb running can be summarised as follows. Every PbPb collision in our interaction region, identified by the Level-1 trigger, will be sent to the HLT filter

farm. In the HLT, the full event information will be available for each event. All rejection of PbPb collisions will be based on the outcome of HLT trigger algorithms that are identical to the corresponding offline algorithms or optimised versions of the offline algorithms. This strategy relies on the fact that, in its final configuration, the HLT will provide sufficient input bandwidth to accept all collision events, even at the maximum PbPb collision rate. The strategy also requires that the algorithms can be executed fast enough. For comparison with the expected HLT CPU budget per event, we show the expected gain in physics reach for selected algorithms and present timing measurements of those algorithms. Overall, the selectivity that can be achieved by the trigger depends on the availability of sufficient CPU resources to execute the algorithms, possibly triggered by a Level-1 seed, and on the efficiency, acceptance, and background level of each particular algorithm. The output event rate is determined by the ratio between the "allowed" bandwidth to tape and the average size of the selected events. To validate this trigger strategy, studies of the PbPb event size and the timing of various algorithms will be presented in Section 5.3.

5.2.1 Trigger channels

The results from RHIC have clearly pointed out the importance of probes at intermediate and high p_{T}, such as leading hadrons, dihadron correlations and spectra, and azimuthal distributions of hadrons carrying charm. At the LHC, studies of high p_{T} hadron production can be extended from the present RHIC statistical limit of $p_{\mathrm{T}} < 20$ GeV/c to transverse energies of several hundred GeV/c. Similarly, studies of open and hidden heavy-flavour physics at the LHC will be extended to include b-quark production. Studies of vector bosons and fully formed jets in heavy-ion collisions will become possible for the first time. As is currently the case at RHIC, the corresponding studies at the LHC will ultimately be limited by the statistics given by production rates and integrated luminosity. The Level-1 and HLT triggers are essential for maximising the physics reach of CMS within these constraints.

The high granularity of the CMS silicon pixel tracker allows the reconstruction of a large fraction of the produced charged hadrons even in central PbPb collisions (see Section 7.3) [165]. The current execution time of the track reconstruction algorithm ($\sim$ 1200 s for a central event) prohibits running the full reconstruction on each event at the HLT level. While future studies will explore the possibility of running regional tracking to detect high p_{T} hadrons, including those from heavy flavour decays, the present trigger studies are focussed on channels related to calorimeter and muon chamber triggers. Figure 5.1-left summaries the production cross sections of some of the relevant physics channels, obtained using NLO pQCD (for the $Q\overline{Q}$, see Section 6.1) and version 6.326 of the PYTHIA event generator for the rest (Section 7.2). The range of cross sections of interest extends over 10 orders of magnitude, leading to the corresponding variation in production rates shown in Fig. 5.1-right. There, the production rates were calculated for an average luminosity of $\langle\mathcal{L}\rangle = 4 \times 10^{26}$ cm^{-2}s^{-1} and minimum bias (i.e. impact-parameter averaged) PbPb collisions with an average number of binary nucleon-nucleon collisions, $\langle N_{\mathrm{coll}}\rangle$, of 400 [102].

The corresponding average PbPb collision rate is 3 kHz, while the maximum event rate to tape is in the range 10–100 Hz, also indicated in Fig. 5.1. Table 5.1 shows the integrated production yields for the same channels, for one nominal CMS heavy-ion run with a total up-time of 10^6 s, and an ideal DAQ with infinite bandwidth. Yields are shown for the design average luminosity of $\langle\mathcal{L}\rangle = 4 \times 10^{26}$ cm^{-2}s^{-1} and for an initial "low-luminosity" run at 1/20 design luminosity. These yields form the input to our HLT simulation chain. Expected production rates after applying acceptance, efficiency and branching ratios will be discussed

in Section 5.4. Clearly, differential studies of Υ production and jets at high E_{T}, as well as measurements of γ+jet correlations, will require a highly-efficient trigger that selects a large fraction of the corresponding interesting events for storage on tape. This is particularly true for studies of these observables as a function of transverse momentum, rapidity, centrality and event plane. The purpose of the heavy-ion trigger is the allocation of the available output bandwidth to a selection of trigger channels such that we maximise the overall physics impact of the CMS heavy-ion program.

Table 5.1: Integrated yields of selected observables for a 10^6 s heavy-ion run, both at low-luminosity and at design luminosity (see text). The dilepton branching ratios and the muon p_{T} thresholds have not been applied to the quarkonia and vector boson channels.

Signal	Threshold	Yield/yr. (low lumi)	Yield/yr. (high lumi)
$h^{\pm}$	$p_{\mathrm{T}} > 25$ GeV/c	1.1×10^6	2.1×10^7
$h^{\pm}$	$p_{\mathrm{T}} > 50$ GeV/c	4.1×10^4	8.2×10^5
jet	$E_{\mathrm{T}} > 100$ GeV	2.2×10^5	4.4×10^6
jet	$E_{\mathrm{T}} > 200$ GeV	6.5×10^3	1.3×10^5
γ^{prompt}	$p_{\mathrm{T}} > 25$ GeV/c	2.2×10^4	4.3×10^5
J/ψ	–	1.3×10^7	2.6×10^8
Υ	–	1.0×10^5	2.1×10^6
γ^*	–	7.6×10^2	1.5×10^4
Z^0	–	6.5×10^3	1.3×10^5

5.3 Event size and timing measurements

As described in Section 5.2, the trigger strategy for PbPb collisions foresees running reconstruction algorithms on all PbPb collisions in the HLT filter farm, using the full event information. Detailed studies of the HLT performance in the dimuon and jet channels were discussed in Ref. [192] and are briefly summarised here. All event size and timing measurements are based on three sets of fully simulated HYDJET PbPb events corresponding to $b = 0$, 9 and 12 fm, processed with the CMS GEANT4 based OSCAR simulation package. The timing measurements were performed running the standard heavy-ion offline algorithms of the ORCA software package on standard PCs with 1.8 GHz Opteron CPUs and 4 GByte RAM.

5.3.1 Event size

The maximum gain in statistics for rare probes provided by the online trigger system is given by the ratio between the collision rate and the permanent storage event rate. The latter is given by the ratio between the bandwidth limit of 225 MByte/s and the average event size written to tape. The event size estimates were obtained by writing simulated raw data, including hits from background and secondary particles, in the form of CMS standard "Digis". The average midrapidity charged hadron densities for the three PbPb centrality cases considered are $\mathrm{d}N_{\mathrm{ch}}/\mathrm{d}\eta|_{\eta=0} = 3300$, 575, and 65, respectively for the $b = 0$, 9 and 12 fm. Pedestal subtraction and zero-suppression are performed for all hits. The output data were compressed using ROOT compression level 1, yielding a compression factor of

about 3.5. No additional compression or encoding of the hit information was attempted. The MC event size was found to increase approximately linearly with the charged hadron multiplicity, from 330 kByte for the $b = 12$ fm sample to 8.5 MByte for the $b = 0$ fm sample. From the impact parameter dependence of the event size and adjusting for additional noise, backgrounds and diagnostic information, we obtain 2.5 MByte per minimum bias event and up to $\sim$9.5 MByte for the most central events, when running at design luminosity [192]. With an average data rate to tape of 225 MByte/s, the corresponding average minimum bias event rate to tape is 90 Hz. Clearly, this estimate depends on the multiplicity of produced hadrons in PbPb collisions at the LHC. Predictions and extrapolations based on the present RHIC data suggest a range of $\mathrm{d}N_{\mathrm{ch}}/\mathrm{d}\eta|_{\eta=0} \approx 1300 - 4000$ for central PbPb collisions at the LHC (see Fig. 1.20). The value of $\mathrm{d}N/\mathrm{d}\eta|_{\eta=0} = 3300$ which we assumed for the most central collisions is, thus, quite conservative.

Including all the uncertainties, we expect that the bandwidth of 225 MByte/s will allow a rate of PbPb events to mass storage between 10 and 100 Hz. A large part of this uncertainty will only be resolved once the first LHC data are taken, emphasising the need for a flexible high-level trigger scheme.

The event sizes quoted above refer to the HLT output to tape, using ROOT compression. To validate the HLT input bandwidth, we note that the upper range of the expected midrapidity charged hadron densities in minimum bias PbPb collisions at the LHC is $\mathrm{d}N_{\mathrm{ch}}/\mathrm{d}\eta|_{\eta=0} \approx 1000$, to be compared to a density of $\mathrm{d}N_{\mathrm{ch}}/\mathrm{d}\eta|_{\eta=0} \approx 150$ for 20 superimposed minimum bias pp collisions at pp design luminosity. While PbPb collisions have a midrapidity multiplicity that is, at most, 7 times larger than for pp, the collision rate in PbPb is a factor of 12 smaller than the 100 kHz HLT input rate in pp. Furthermore, the rapidity distributions in 5.5 TeV PbPb collisions will be narrower than in 14 TeV pp collisions. Thus, safety factors in the data rate will be even larger away from midrapidity. Finally, the bandwidth requirements for low-luminosity PbPb running will be smaller by another order of magnitude, whereas the expected initial bandwidth should only be reduced by a factor of 2–4.

5.3.2 Trigger timing studies

The capabilities of the HLT are largely determined by the time required to process each event and are therefore strongly dependent on the CPU resources available in the filter farm. The online farm is expected to consist of about 1500 servers. Because of the expected increase in CPU performance/cost over the coming years, the detailed specifications of these servers are not yet precisely known. For the purpose of our present studies, we will assume that the servers purchased for 2008 running will have dual CPUs with quad cores, with a performance per core comparable to 1.5 times the performance of the 1.8 GHz Opteron CPUs used in our timing measurements. This estimate is conservative since the actual trigger PCs will be purchased no earlier than end of 2007. Timing measurements will be quoted in units of CPU seconds for the present CPUs. In these units the time budget per event for the full HLT filter farm will be $\sim$1.5 s at the beginning of each store (8 kHz collision rate), and $\sim$4 s averaged over the duration of the store (3 kHz collision rate).

The timing studies were performed using the full GEANT4-based simulations (ORCA) described above and the present offline algorithms for jet-finding and dimuon reconstruction. As of now, these algorithms have been optimised for reconstruction efficiency and background rejection, but not for timing performance. Work on optimising the timing of our trigger algorithms will begin once heavy-ion simulations and algorithms have been ported

to the new CMSSW software framework.

Based on generator-level studies with simplified geometries and comparisons to the optimised pp algorithms, we expect that significant gains relative to the timing performance shown below can still be achieved. However, these gains will be partially offset by the CPU resources needed for running the algorithms for additional trigger channels as shown in Table 5.3. These additional algorithms have so far only been tested in generator-level studies which do not allow detailed timing measurements.

Jet finder timing

The offline jet-finding algorithm used here is a modified iterative cone algorithm, with subtraction of the large underlying event energy in heavy-ion collisions, applied to the towers of the electromagnetic and hadronic calorimeters (ECAL+HCAL) in ORCA (see Section 7.2). The average execution times are found to be 820, 320, and 164 ms for $b = 0$, 9, and 12 fm, respectively. Averaging over the impact parameter distribution, the estimated average execution time is $\langle t \rangle = 250$ ms. Therefore, if it is executed for every event, the jet-finding algorithm is expected to use between 5 and 15% of the CPU budget for the average and for the maximum instantaneous (start of store) event rate. Although the present algorithm comfortably fits into the expected CPU budget, further optimisation is desirable. In the present implementation, a large fraction of the execution time is spent building the ECAL+HCAL objects. For the eventual online algorithm, significant time savings may be achieved by using the L1 trigger tower information embedded in the data stream.

Muon finder timing

The muon finder consists of three different algorithms. The first part, $L1$, is executed at Level-1 for every event, producing a list of muon candidates. The Level-1 muon selection is based on the corresponding selection for pp, although the cuts have been adjusted to increase acceptance at low p_{T}. The second part of the muon finder, $L2$, is also executed on all events, this time in the HLT. The average execution times for this algorithm are 710, 100, and 10 ms for $b = 0, 9$, and 12 fm, respectively. Parameterising the execution time as a function of the impact parameter and averaging over all centralities yields an estimated average execution time of $\langle t \rangle = 80 \pm 20$ ms. The error is dominated by the uncertainty in the functional form of the impact parameter dependence, due to the small number of points. Correspondingly, $L2$ execution uses 1 to 5% of the HLT CPU budget, depending on event rate.

The third part of the algorithm, $L3$, is run in the HLT on events with at least two muon candidates found by either $L1$ or $L2$. The $L3$ algorithm extends the tracks found in the muon system to the silicon tracker and provides a significant improvement in momentum resolution and background rejection. This is particularly important for low p_{T} dimuons, which are expected to take up the largest fraction of the output bandwidth to tape. Averaged over impact parameter, $L3$ will only be called for $2 \pm 1\%$ of all events. However, as $L3$ requires tracking in the silicon detector, its execution time is significantly longer than for the other algorithms studied here and shows a very steep dependence on multiplicity. The $L3$ execution time is found to be linear in the number of muon candidates from $L2$. Averaging over the impact parameter distribution of inputs selected by $L2$, we find an execution time for the $L3$ selection of 700 ± 200 s per $L2$ accepted event, corresponding to about 10 ± 3 s per minimum bias event.

The uncertainty in execution time results from the uncertainties in interpolation between

the three available impact parameter samples. Based on the total available CPU budget and the importance of the dimuon trigger, we estimate that an allocation of 0.5 s to 1 s per minimum bias event for the $L3$ algorithm is reasonable. Consequently, a further speed-up of the algorithm by about a factor of 10–20 is necessary. While this is a large factor, it should be attainable. The current $L3$ algorithm uses more than 10^3 CPU seconds for the determination of 2–4 muon candidates in central PbPb events, while the runtime for the full track reconstruction in the silicon tracker, yielding ~ 800 tracks with $p_{\mathrm{T}} > 1$ GeV/c [165], is less than 10^3 s on the same events. Further work on optimising or significantly modifying the present algorithm for use in the HLT event selection will proceed when the offline algorithms are ported to CMSSW.

5.4 HLT simulation procedure and results

A schematic description of the components of our HLT simulation chain is shown in Fig. 5.2. Below, we describe the individual elements of this chain and summarise the benefits of the HLT compared to a minimum bias trigger, for single jet and dimuon measurements, for two luminosity scenarios.

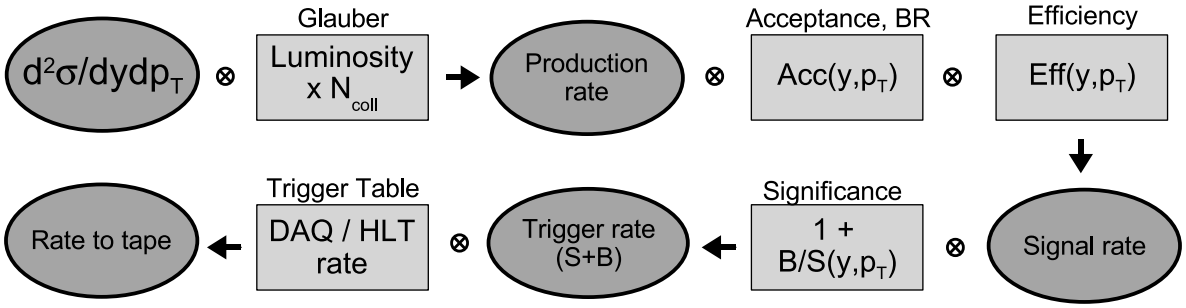

Figure 5.2: Schematic description of the HLT simulation chain. Input cross sections are obtained from PYTHIA 6.326 or NLO pQCD calculations. Acceptance, efficiency and background levels are parameterised from full GEANT4 based simulations. See the text for detailed descriptions of each of the steps.

5.4.1 Trigger signal rates

To evaluate the physics reach of the CMS detector, the production rates shown in Fig. 5.1 need to be translated into rates of observed events in the detector and finally into the rates to mass storage for the physics processes of interest. A straightforward measurement of the rates seen in full simulations is presently not feasible. Available CPU resources limit the sizes of typical MC data sets to about 100k, compared to a total integrated number of collisions of several times 10^9 for a nominal LHC heavy-ion run. As we are only interested in triggering on rare probes, we can instead use the approach shown schematically in Fig. 5.2 and described in the following sections. The production rates shown in Fig. 5.1 were scaled to minimum bias PbPb collisions ($\langle N_{\mathrm{coll}} \rangle$ = 400) and then multiplied by branching ratios, where appropriate, to obtain the rate of signal events as a function of (y, p_{T}). For the present rate studies, the yield of hard probes was taken to be proportional to N_{coll}, allowing us to use the rates for minimum bias PbPb collisions to estimate the average production rates, and no impact parameter selection except for the inherent bias from a trigger on hard probes was assumed.

The acceptance and efficiency of the offline algorithms for simulated events were also parameterised in as a function of (y, p_{T}).

Multiplication of the production rate histograms with acceptance and efficiency histograms yields the *trigger signal rate* for each channel. The rates for J/ψ and Υ production lie below the total output rate limit, while the expected rate of jet triggers exceeds this limit for minimum jet E_{T} trigger thresholds of around 40 GeV.

5.4.2 Trigger background rates

Offline studies show that the jet and dimuon triggers will include a substantial fraction of background events, depending on the chosen E_{T} and p_{T} thresholds. In addition, the dimuon analysis requires a certain number of events outside the J/ψ and Υ mass windows, to allow a reliable estimate of the dimuon continuum under the resonance peaks, mostly due to combinatorial background. To include these backgrounds in our rate estimate, we parameterised the fraction of background to signal events, B/S, from the full offline simulations (see Section 6.1), as a function of p_{T} or E_{T}. The trigger signal rates discussed previously were then multiplied by the factor $(1 + B/S)$, to obtain the actual trigger rates.

The possible trigger rates from the dimuon and jet channels alone far exceed the limit of 10–100 Hz if no minimum p_{T} or E_{T} threshold is applied to the triggers. Besides, additional bandwidth will be needed for composite channels such as γ+jet (see Section 7.4), for a trigger on ultraperipheral events in diffractive photoproduction processes (Section 8), and for minimum bias events (Section 2.4). The available output bandwidth needs to be allocated to the various trigger channels by applying trigger thresholds and pre-scales, such that the overall physics reach of the experiment is maximised. In allocating the bandwidth, it is important to take into account that the average event size satisfying each trigger condition will typically be significantly larger than that of minimum bias events. With the obvious exception of ultraperipheral triggers, the assumption that rates of the interesting processes scale with the number of nucleon-nucleon collisions heavily biases the accepted distributions towards more central collisions.

We have calculated the output signal rates using strawman trigger tables for two luminosity scenarios, corresponding to the conditions for an initial PbPb run in the Fall of 2008 and for runs at design luminosity in 2009. For each luminosity scenario, we defined a strawman trigger table to allocate output bandwidth to several trigger channels. The quoted signal rates to tape take into account that a fraction of the allocated bandwidth is taken up by background events for each particular channel.

Low luminosity scenario

For the initial PbPb run in 2008, we expect an average luminosity $\langle \mathcal{L} \rangle = 2 \times 10^{25}$ cm^{-2}s^{-1}, a factor of 20 below the design average luminosity. We calculated the trigger signal and background rates for this low luminosity. We assumed 10^6 s total run time and an event size 1 MByte larger than in later running periods, accounting for additional diagnostic information and less efficient data compression. For this initial run, we assumed that only 25% of the DAQ event builder CPUs and 25% of the HLT event filter will be installed. Even with the reduced DAQ capacity, the lower initial luminosity results in a more favourable CPU time budget per event than for a scenario with 100% of the DAQ capacity at design luminosity. This leaves the output bandwidth of 225 MByte/s as the main constraint. Figure 5.3-left shows the signal rates and statistical significance for jet and dimuon measurements for min-

imum bias running and for HLT running using the trigger allocations given in Table 5.2. Although the lower collision rate decreases the possible gain from using the HLT, the integrated yields are higher than for minimum bias triggering by a factor of 2 to 3 for jet and dimuon triggers, with the biggest gains seen for Υ measurements.

Table 5.2: Strawman trigger table for running at 1/20 of the design luminosity, assigning fractions of the total bandwidth (225 MByte/s) to individual trigger channels. The last column shows the average event size for each of the trigger streams.

Channel	Threshold	Pre-scale	Bandwidth [MByte/s]	Event size [MB]
Min. bias	–	1	146 (65%)	3.5
jet	50 GeV	1	45 (20%)	6.4
J/ψ	0 GeV/c	1	11 (5%)	5.9
Υ	0 GeV/c	1	2.5 (1%)	5.9
γ^{prompt}	10 GeV	1	18 (8%)	6.8
UPC/forward	–	1	2.5 (1%)	2

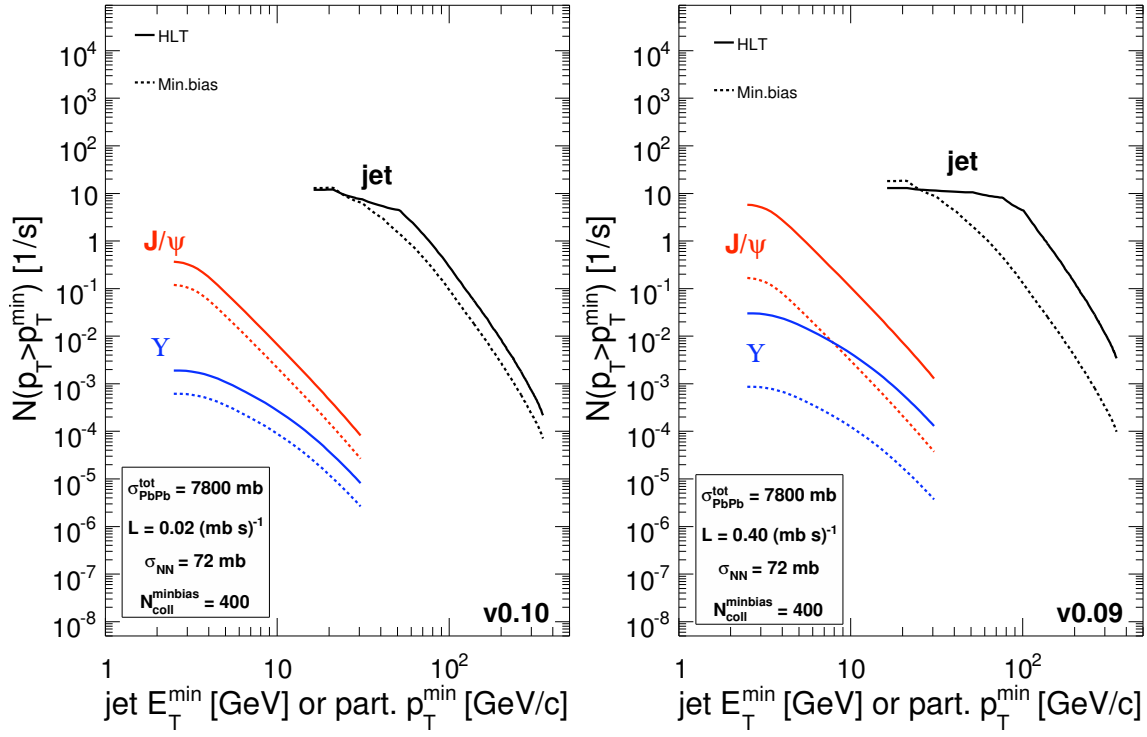

Figure 5.3: Minimum bias and HLT J/ψ, Υ, and jet trigger rates for the settings of Table 5.2, for low luminosity (left) and design luminosity (right).

Design luminosity scenario

In Fig. 5.3-right we compare the rates of signal events to tape for minimum bias running (no event selection in HLT) and for the HLT event selection conditions. The rates were calculated for the design average luminosity, $\langle\mathcal{L}\rangle = 4 \times 10^{26}$ cm^{-2}s^{-1}, with the bandwidth allocation given in Table 5.3. Clearly, this table will have to be optimised as further information becomes available.

Table 5.3: Strawman trigger table for running at design luminosity, assigning fractions of the total bandwidth (225 MByte/s) to individual trigger channels. The last column shows the average event size for each of the trigger streams.

Channel	Threshold	Pre-scale	Bandwidth [MByte/s]	Event size [MByte]
min. bias	–	1	33.75 (15%)	2.5
jet	100 GeV	1	24.75 (11%)	5.8
jet	75 GeV	3	27 (12%)	5.7
jet	50 GeV	25	27 (12%)	5.4
J/ψ	0 GeV/c	1	67.5 (30%)	4.9
Υ	0 GeV/c	1	2.25 (1%)	4.9
γ^{prompt}	10 GeV	1	40.5 (18%)	5.8
UPC/forward	–	1	2.25 (1%)	1

Using the HLT, a gain in statistics of more than an order of magnitude is achieved for large E_{T} jets and dimuons. Correspondingly, the usable range in E_{T} (p_{T}) for the jet and dimuon measurements is extended by more than factor of 2 and 3, respectively. Note that, for this comparison, the HLT rate for each process was only counted in the corresponding trigger stream, leading to rates below minimum bias for low E_{T} in the jet channel. In any case, at low E_{T} jet measurements will likely be limited by systematic errors.

5.4.3 Quarkonia and jet physics with the HLT

Two key examples of the physics benefit of the HLT for quarkonium and jet related measurements are shown below, with the measurements discussed in detail in detail in Sections 6.1 and 7.2. The first measurement, shown in Fig. 5.4, shows the ratio of Υ' to Υ yields as a function of transverse momentum. The projected statistical resolution is compared to model calculations of the p_{T} dependence of the Υ'/Υ ratio, for two different choices of initial conditions (parton gas and mini-jet cases) and two different assumptions of the temperature dependence of the screening mass [193]. This measurement, using the added statistics provided by the HLT selection, allows a clear distinction of the different scenarios, and may therefore serve as a sensitive probe of the initial QCD medium (see Section 6.1.4).

In Fig. 5.5 we show the nuclear modification factor, $R_{AA}(p_{\mathrm{T}})$, for charged hadrons measured in minimum bias data (left) and in events selected by an HLT trigger on high E_{T} jets (right). The triggered sample extends the useful range in p_{T} by more than a factor of two, to around 300 GeV/c. Predictions for R_{AA} in PbPb collisions at the LHC have been made using several models of parton energy loss in the QCD medium. The theoretical predictions differ most markedly in the high p_{T} region (Fig. 1.17), which can only be accurately measured in the jet-triggered event sample (see Section 7.3.3).

5.5 Summary

In summary, we have outlined a possible trigger strategy for heavy ion running of CMS which relies on event rejection solely in the HLT. We have validated the trigger strategy using event size and timing measurements on fully simulated HYDJET events, processed in the ORCA framework. By parameterising the performance of the offline algorithms, we have developed a trigger simulation chain that allows to compare the rate of signal events to tape for various trigger channels, luminosity scenarios and trigger tables. The simulation

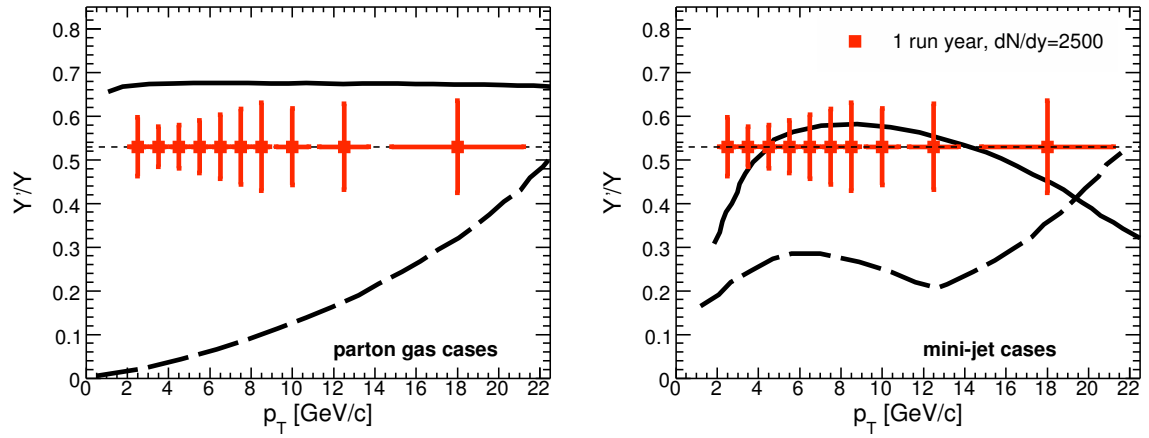

Figure 5.4: Υ' over Υ ratio as a function of their p_{T}. Statistics correspond to a 10^6 s heavy-ion run. The model calculations are for different choices of initial conditions and screening mass temperature assumptions [193] (see details in Section 6.1.4).

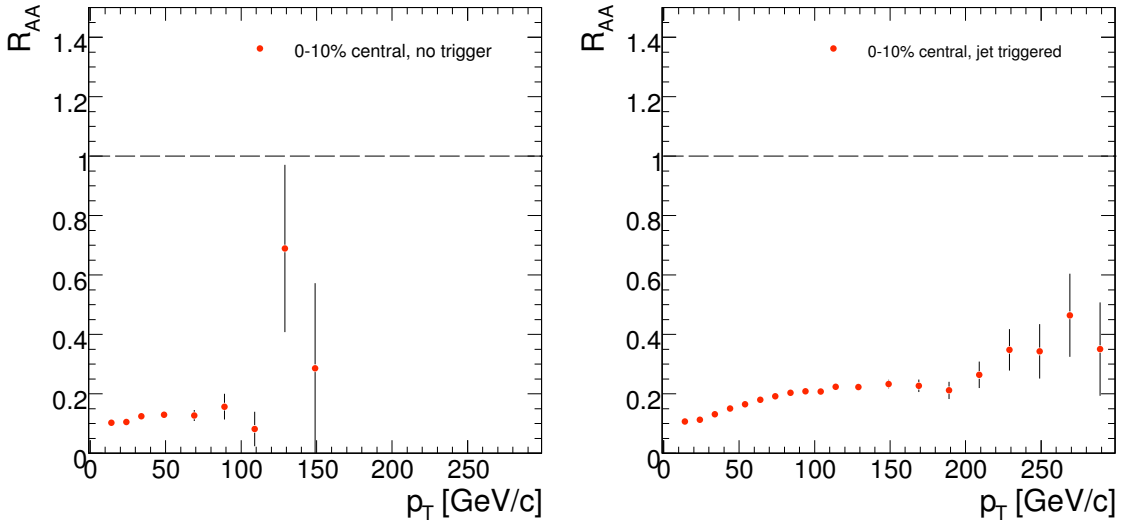

Figure 5.5: The nuclear modification factor, R_{AA}, as a function of p_{T}, for inclusive charged hadrons, for minimum bias data (left panel) and for data collected with a high-E_{T} jets trigger (right panel), in a 10^6 s heavy-ion run (see details in Section 7.3.3).

chain allows us to evaluate the impact of the HLT event selection on the physics reach of the experiment.

In terms of accessible physics, the benefits of the HLT can be summarised as follows.

- Without the HLT selection of dimuons in the Υ mass range, our simulations show less than 300 Υ recorded to tape per nominal year of data taking at design luminosity. With HLT selection, we expect a factor of 50 more Υ recorded. A study of the $\Upsilon^{'}$ and Υ relative yields, as a function of p_{T}, which is expected to provide information about the initial temperature of the medium produced in heavy ion collisions (Fig. 5.4) will only be possible using the HLT selection.
- The J/ψ statistics on tape, increased by about a factor 10 thanks to the HLT, will allow differential studies as a function of centrality, reaction plane (path length),

p_{T} and rapidity. These are important measurements to elucidate, in particular, the importance of recombination processes in the J/ψ yields.

- The statistics for high E_{T} jet measurements above 100 GeV are enhanced by a factor of 20 thanks to the HLT, extending the E_{T} reach by nearly a factor of two (up to $E_{\mathrm{T}} \approx 0.5$ TeV), using a yield of 10^4 jets as benchmark. These well-defined jets provide a qualitatively new tool for understanding the transport properties of QCD matter, giving the largest lever arm for testing different models of the interaction of a fast parton with the medium. Experience in pp collisions and our own model studies show that a large sample of jet events and highly differential studies will be necessary to calibrate these new experimental tools. Measurements of the nuclear modification factors of charged hadron spectra up to $p_{\mathrm{T}} = 300$ GeV/c will greatly benefit from the jet-triggered event sample. Predictions of current theoretical models of parton interactions with a strongly-coupled medium diverge in *shape* from each other in the region above $p_{\mathrm{T}} > 50$ GeV/c (see Fig. 1.17).
- Although studies are still ongoing, the rates for Z^0 production or for composite channels (such as Z^0+jet correlations) show that these measurements will only be feasible using an efficient trigger (see Section 7.4). Composite channels with a clear jet energy tag will be critical for calibrating the jet-finding performance in pp or peripheral PbPb events and for obtaining a qualitatively new handle on partonic energy loss in more central PbPb collisions.

Chapter 6

Quarkonia and heavy-quarks

6.1 Quarkonia

6.1.1 Introduction

The measurement of the charmonium (J/ψ, ψ') and bottomonium (Υ, Υ', Υ'') resonances in PbPb collisions at $\sqrt{s_{NN}}$ = 5.5 TeV will provide crucial information on the many-body dynamics of high-density QCD matter. First, the step-wise suppression of heavy quark-antiquark bound states with increasing energy density or temperature is generally agreed to be one of the most direct probes of Quark-Gluon-Plasma formation due to Debye screening of the colour potential in the plasma [115]. Lattice QCD calculations of the heavy-quark correlators indicate that the ground-state charmonium and bottomonium states, J/ψ and Υ, dissolve at $T_{\rm diss} \approx 2\ T_{\rm c}$ and $4\ T_{\rm c}$, respectively [116–119]. While the relevance of charmonia production studies in heavy-ion collisions is well established from measurements done at the SPS and at RHIC, where a factor of $\sim$2–3 *anomalous* suppression has been observed in PbPb and AuAu collisions at $\sqrt{s_{NN}}$ = 17.3 GeV [121, 194] and 200 GeV [123], respectively, the clarification of some important remaining questions requires equivalent studies at the LHC energies, where the Υ family becomes accessible to similar studies. Second, the production of heavy-quarks proceeds mainly via gluon-gluon processes and, as such, is sensitive to saturation of the gluon density at low-x in the nucleus (Colour Glass Condensate). Measured departures from the expected vacuum (proton-proton) quarkonia cross-sections in PbPb collisions at LHC will thus provide valuable information not only on the thermodynamical state of the produced partonic medium, but also on the initial-state modifications of the nuclear parton distribution functions, especially of the gluon.

In this chapter we present the expected capabilities of CMS to measure the heavy-quarkonia cross-sections versus centrality, rapidity y and transverse momentum $p_{\rm T}$, in PbPb collisions at $\sqrt{s_{NN}}$ = 5.5 TeV, via their dimuon decay channel. The generation of realistic signals and backgrounds, the dimuon reconstruction algorithm and the trigger, acceptance and efficiency corrections are discussed. The obtained dimuon mass resolutions, the signal over background ratio and the expected yields as a function of $p_{\rm T}$, y, and centrality in one-month PbPb running are also presented [191].

6.1.2 Simulation of physics and background processes

The relatively low Υ production rates ($\sim 10^{-4}$ per PbPb event) and the large number of particles to track in heavy-ion collisions make it very expensive computationally to use a full nucleus-nucleus event generator (such as HIJING [195]) with detailed detector simulation and reconstruction to obtain a statistically significant sample of signal events. Instead, a

combination of fast and slow simulations is used in this analysis. The input signal and backgrounds are obtained from realistic distributions: NLO pQCD for heavy-quark production processes and HIJING for the soft background, constrained by extrapolations from lower energy heavy-ion data. A full detector and trigger simulation plus reconstruction are carried out for a few 10^7 events with the embedded quarkonium states and the hadronic decays relevant to the muon background. The corresponding response functions (trigger acceptances, mass resolutions, reconstruction efficiencies, etc.) are parameterised, and implemented in a fast MC to obtain the final fully corrected yields. The response functions are cross-checked by comparing the final dimuon spectra obtained with the fast MC against 5×10^5 PbPb HIJING events fully simulated and reconstructed in the detector.

The quarkonium production cross sections per nucleon-nucleon collision are calculated to NLO in the total cross section at $\sqrt{s_{NN}}$ = 5.5 TeV using the colour evaporation model (CEM) [47] with the MRST parton densities weighted by the EKS98 parameterisation [196] of nuclear shadowing effects. The renormalisation and factorisation scales are $\mu_{\rm F} = \mu_{\rm R} = 2m_{\rm T}$ for charmonium and $\mu_{\rm F} = \mu_{\rm R} = m_{\rm T}$ for bottomonium, where $m_{\rm T} = (m_Q^2 + p_{\rm T}^2)^{1/2}$ with $m_c = 1.2$ GeV/c^2 and $m_b = 4.75$ GeV/c^2. The PbPb cross sections are obtained by scaling the per nucleon cross section with A^2, where $A = 208$ for Pb. The resulting PbPb (impact-parameter averaged) inclusive quarkonia production cross sections are quoted in Table 6.1, multiplied by the corresponding dimuon branching ratios, $B_{\mu^+\mu^-}$ (5.94%, 0.73%, 2.4%, 1.94% and 2.24%, for the J/ψ, ψ', Υ, Υ', and Υ'', respectively). The NLO J/ψ and Υ double-differential $\mathrm{d}^2\sigma/\mathrm{d}p_{\rm T}\mathrm{d}y$ distributions are also used for the other states within each quarkonium family, as prescribed by the CEM.

Table 6.1: The inclusive cross sections for quarkonium production, times the branching ratio into dimuons, in minimum bias PbPb collisions, at 5.5 TeV, calculated to NLO in the CEM.

$B_{\mu^+\mu^-} \times \sigma_{PbPb}$ (μb)				
J/ψ	ψ'	Υ	Υ'	Υ''
48 900	880	300	80	44

The two main sources of background in the dimuon invariant mass spectrum are:

1. Combinatorial muon pairs from the decays of **charged pions and kaons**. The production of $\pi^\pm$ and $K^\pm$, which represent about 90% of the total produced charged particles, was simulated using input $d^2N/dp_{\rm T}dy$ distributions from HIJING, normalised to give $\mathrm{d}N_{\rm ch}/\mathrm{d}\eta|_{\eta=0}$ = 2500 and 5000 in the 0–5% most central PbPb collisions. These multiplicities were selected as conservative lower and upper limits at $\eta = 0$. However, extrapolations from RHIC indicate that the LHC multiplicity may, in fact, be lower than our chosen lower limit, with $\mathrm{d}N_{\rm ch}/\mathrm{d}\eta|_{\eta=0}$ as low as 1300, see Section 1.4.2. The total relative yield of kaons over pions is ~11%, but since the kaons have a harder spectrum ($\langle p_{\rm T}\rangle$ = 0.6 GeV/c) than the pions ($\langle p_{\rm T}\rangle$ = 0.44 GeV/c) and a shorter lifetime, $c\tau$, they are responsible for ~ 80% of the background reaching the muon chambers [197]. Before decaying, a few metres away from the production point, many pions and kaons suffer nuclear interactions in the calorimeters (which have an effective thickness of 11–16 interaction lengths in the barrel and 11 in the endcaps) [51, 167]. Punchthrough in the muon chambers is less than 1.2×10^{-5} for hadrons with $p_{\rm T} < 10$ GeV/c [198]. About 0.3% (1%) of the produced pions (kaons) lead to tracks in the muon chambers, either

because they decay to muons or because of punchthrough. The proton punchthrough probability is more than two orders of magnitude lower and can safely be neglected.

2. Another source of background is due to muons from **open heavy flavour** (D,B) meson decays. The probability to produce at least one muon at the end of the decay chain of charm (bottom) quarks is ∼18% (38%) according to PYTHIA 6.025. The corresponding double differential $(p_{\rm T}, y)$ cross sections are obtained from pp NLO calculations (with CTEQ5M1 PDFs and scales $\mu_{\rm F} = \mu_{\rm R} = 2\,m_{\rm T}$ for charm and $m_{\rm T}$ for bottom), which give $\sigma_{c\bar{c}}$ = 7.5 mb and $\sigma_{b\bar{b}}$ = 0.2 mb [47]. Including shadowing on the PDFs reduces the cross sections by 35% and 15%, respectively [199]. The number of heavy-quark pairs produced in AA collisions, as a function of impact parameter b, is

$$N_{AA}(Q\overline{Q}) = \sigma(Q\overline{Q})\; T_{AA}(b)\;, \tag{6.1}$$

where $T_{AA}(b)$ is the nuclear overlap function (30.4 mb^{-1} for head-on PbPb collisions). The D and B meson decays give similar contributions to the dimuon background since the higher average $p_{\rm T}$ of the b quark ($\langle p_{\rm T}^{\mu}\rangle_b = 1.45$ GeV/c versus $\langle p_{\rm T}^{\mu}\rangle_c = 0.55$ GeV/c) is compensated by the much larger number of $c\bar{c}$ pairs produced.

Note that in all input MC distributions for either the signal or the background we have not considered any nuclear modification other than a mild shadowing effect of the PDFs. Possible yield suppressions in the hot and dense medium due to colour screening and/or strong gluon saturation effects (for the quarkonia) or due to parton energy loss (for the light and heavy quarks background) have not been taken into account. We consider this approach to be the least biased possible since although the total quarkonia cross-sections will obviously be reduced if medium effects are present — the final goal of the analysis is exactly to use those reductions of the yields to infer the QCD matter properties — the reconstruction efficiencies and signal-over-background ratios should not be significantly changed.

Table 6.2 shows the average particle multiplicities for the heavy-quark background as expected in three PbPb centrality classes: head-on (b = 0 fm), 0–5% most central, and minimum bias (0–100%) collisions. The charged hadron multiplicity quoted corresponds to the *high-multiplicity* setting ($\mathrm{d}N_{\rm ch}/\mathrm{d}\eta|_{\eta=0}$ = 5000) used in the fast MC simulations.

A fast MC simulation equivalent to $5 \cdot 10^7$ PbPb events was then carried out superimposing the decay dimuons from the five quarkonium resonances on top of the background from the π, K and open heavy flavour combinatorial decays. Each muon track (with a given momentum, pseudorapidity, charge and origin) is weighted by a factor that takes into account the corresponding detector acceptance, as well as the trigger and reconstruction efficiencies for the two event multiplicities considered (see next section).

6.1.3 Reconstruction and analysis

Dimuon trigger efficiency and acceptance

The response of the CMS detector to muons (or long-lived punchthrough pions and kaons reaching the muon chambers) is parameterised by 2-dimensional (p, η) acceptance and trigger tables. The particles are fully tracked using GEANT4 (OSCAR 3_4_0 and ORCA 8_7_1) from the vertex to the chambers. Each track is accepted or rejected according to the Level-1 and Level-2 heavy-ion dimuon trigger criteria (i.e. the standard L1 pp muon trigger, with a low-quality μ condition and without $p_{\rm T}$-cut, and the standard pp L2 muon trigger, see Ref. [51]).

Table 6.2: Expected average multiplicities per PbPb collision at 5.5 TeV for the quarkonia signals and for the heavy-quark background.

	$b \approx 0$ fm	0–5% central	min. bias
$\mathrm{d}N_{\mathrm{ch}}/\mathrm{d}\eta\|_{\eta=0}$	5000	4600	1380
$N_{PbPb}(\mathrm{J}/\psi \to \mu^+\mu^-)$	0.034	0.026	6.3×10^{-3}
$N_{PbPb}(\psi' \to \mu^+\mu^-)$	6.2×10^{-4}	4.7×10^{-4}	1.3×10^{-4}
$N_{PbPb}(\Upsilon \to \mu^+\mu^-)$	2.1×10^{-4}	1.6×10^{-4}	3.8×10^{-5}
$N_{PbPb}(\Upsilon' \to \mu^+\mu^-)$	5.6×10^{-5}	4.3×10^{-5}	1.0×10^{-5}
$N_{PbPb}(\Upsilon'' \to \mu^+\mu^-)$	3.0×10^{-5}	2.3×10^{-5}	5.7×10^{-6}
$N_{PbPb}(c\bar{c})$ no shadowing	220	180	41
$N_{PbPb}(c\bar{c})$ with shadowing	150	120	26
$N_{PbPb}(b\bar{b})$ no shadowing	6	4.9	1.1
$N_{PbPb}(b\bar{b})$ with shadowing	5	4.1	1.0

The corresponding efficiencies, $\epsilon^{L1}_{\mathrm{trig}}(p,\eta)$ and $\epsilon^{L2}_{\mathrm{trig}}(p,\eta)$, are then computed. The trigger efficiencies are of the order of 90% for the muons reaching the muon chambers.

The J/ψ and Υ acceptances are shown as a function of p_{T} in Fig. 6.1 for two η ranges: full detector ($|\eta| < 2.4$) and central barrel ($|\eta| < 0.8$). Because of their relatively small mass, low momentum J/ψ's ($p \lesssim 4\,\mathrm{GeV/c}$) are mostly not accepted: their decay muons do not have enough energy to traverse the calorimeters and coil, and are absorbed before reaching the muon chambers, curling in the 4 T magnetic field. At more forward rapidities the extra longitudinal Lorentz boost improves the acceptance, as can be seen in Fig. 6.2. The J/ψ acceptance increases with p_{T}, flattening out at $\sim 15\%$ for $p_{\mathrm{T}} \gtrsim 12\,\mathrm{GeV/c}$. The Υ acceptance starts at $\sim 40\%$ at $p_{\mathrm{T}} = 0\,\mathrm{GeV/c}$ and remains constant at $\sim 15\%$ (full detector) or 5% (barrel only) for $p_{\mathrm{T}} > 4$ GeV/c. The p_{T}-integrated acceptance is about 1.2% for the J/ψ and 26% for the Υ, assuming our input theoretical distributions [197, 200].

Dimuon reconstruction efficiency and purity

The dimuon reconstruction algorithm used in the heavy-ion analysis follows the regional track finder, based on the muons seeded by the muon stations and on the knowledge of the primary vertex [191, 197]. It is adapted to deal with the high hit occupancy of the silicon tracker in PbPb collisions. The muon track segments found by the Level 1 and Level 2 trigger algorithms (the same as used for pp running [51]), with the lowest quality requirement on the muon candidates at Level 1 [51], are extrapolated inwards to identify hits in the outermost silicon strip layer, and form the starting points (seeds) for the matching between the muons and the tracks in the silicon tracker. The propagation in the tracker is performed from the outer silicon strip layer towards the primary vertex [197, 200]. The final fit of the full trajectories is performed with a Kalman-fitter. The efficiency of a given muon pair is $\epsilon_{\mathrm{pair}}(p,\eta) = \epsilon_{\mathrm{track1}} \times \epsilon_{\mathrm{track2}} \times \epsilon_{\mathrm{vertex}}$. The dependence of the Υ reconstruction efficiency on the event charged-particle multiplicity was obtained from a full GEANT simulation using the Υ signal dimuons embedded in HIJING PbPb events. Figure 6.3 shows the Υ efficiency and

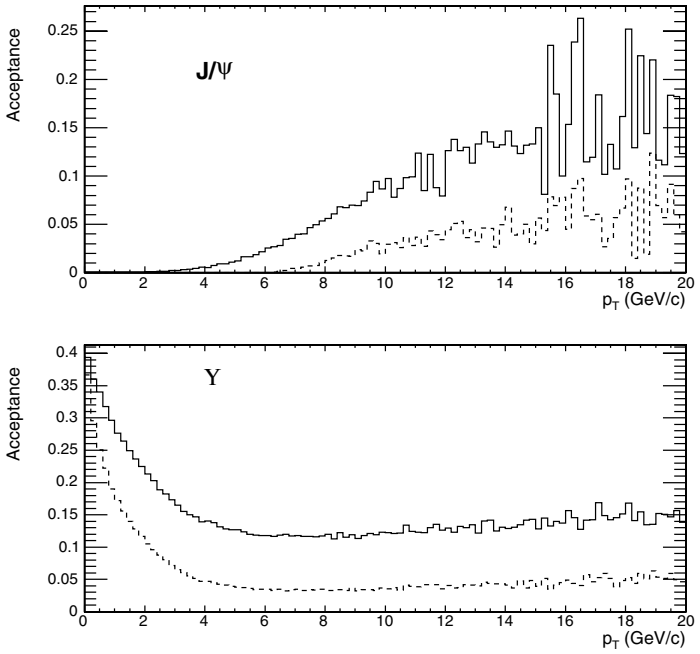

Figure 6.1: J/ψ (top) and Υ (bottom) acceptances (convoluted with trigger efficiencies) as a function of p_{T}, in the full detector (barrel and endcap, $|\eta| < 2.4$, full line) and only in the barrel ($|\eta| < 0.8$, dashed line).

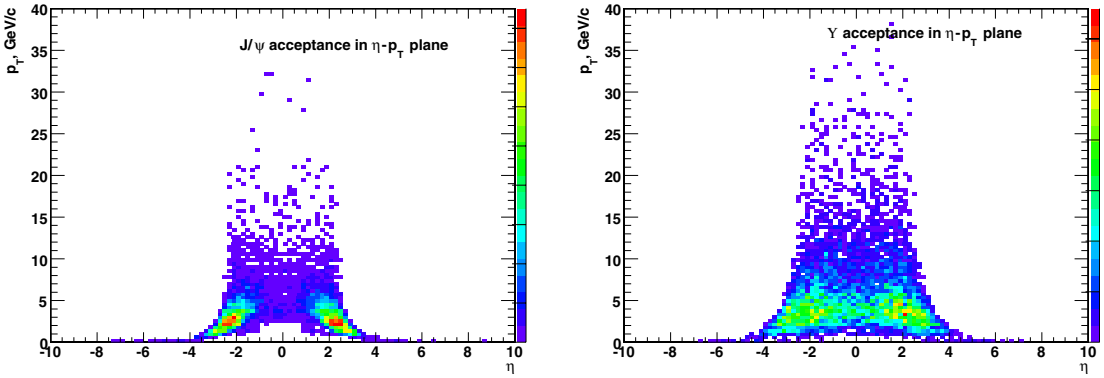

Figure 6.2: Geometrical acceptances (no trigger efficiency included) as a function of p_{T} and pseudorapidity for J/ψ (top) and Υ (bottom) when requiring that both decay muons reach the muon chambers and penetrate through at least one muon chamber.

purity (where purity is defined as the fraction of correctly reconstructed Υ) as a function of charged-particle multiplicity. Note that particle multiplicities are given here in terms of *rapidity* densities: due to the $\eta \rightarrow y$ Jacobian transformation, $\mathrm{d}N_{\mathrm{ch}}/\mathrm{d}y|_{y=0} \approx 6500$ is equivalent to $\mathrm{d}N_{\mathrm{ch}}/\mathrm{d}\eta|_{\eta=0} = 5000$. In the central barrel, the dimuon reconstruction efficiency remains above 80% for all multiplicities whereas the purity decreases slightly with increasing $\mathrm{d}N_{\mathrm{ch}}/\mathrm{d}y|_{y=0}$ but also stays above 80% even at multiplicities as high as $\mathrm{d}N_{\mathrm{ch}}/\mathrm{d}y|_{y=0} = 6500$. If (at least) one of the muons is detected in the endcaps, the efficiency and purity drop due to stronger reconstruction cuts. Nevertheless, for the $\mathrm{d}N_{\mathrm{ch}}/\mathrm{d}\eta|_{\eta=0} \approx 2000$ multiplicity realistically expected in central PbPb at LHC, the efficiency (purity) remains above 65% (90%) even including the endcaps.

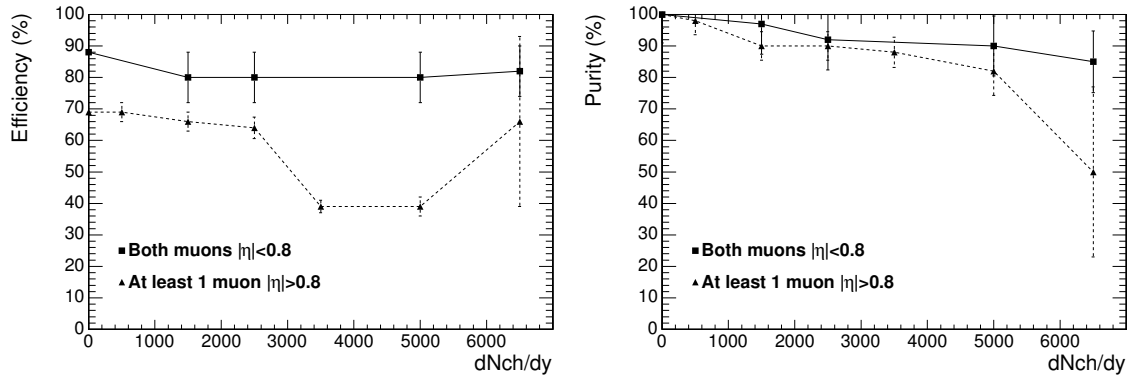

Figure 6.3: Υ reconstruction efficiency (left) and purity (right) as a function of the PbPb charged particle rapidity density, $\mathrm{d}N_{\mathrm{ch}}/\mathrm{d}y|_{y=0}$.

J/ψ and Υ mass resolutions

At the Υ mass, the dimuon mass resolution for muon pairs in the central barrel, $|\eta| < 0.8$, is 54 MeV/c^2, as obtained from a Gaussian fit of the reconstructed $M_{\mu^+\mu^-}$ distribution (using a detailed MC simulation without background). In the full pseudorapidity range, the dimuon mass resolution is about 1% of the quarkonium mass: 35 MeV/c^2 at the J/ψ mass and 86 MeV/c^2 at the Υ mass (Fig. 6.4). These dimuon mass resolutions (the best among the LHC experiments) provide a clean separation of the different quarkonia states. These values are used to smear the dimuon mass distribution in the fast MC studies.

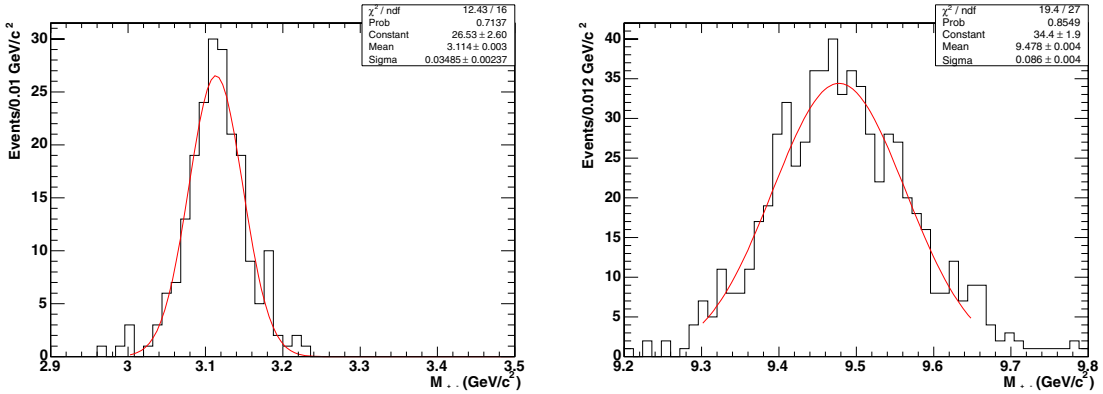

Figure 6.4: Reconstructed J/ψ (left) and Υ (right) dimuon decays in the full simulation, for events without background. Both muons are in $|\eta| < 2.4$.

There is a slight dependence of the mass resolution on the event multiplicity. Increasing the multiplicity from $\mathrm{d}N_{\mathrm{ch}}/\mathrm{d}y|_{y=0}$ = 0 to 2500 degrades the mass resolution of the reconstructed Υ from 86 to 90 MeV/c^2. For larger particle densities, the resolution goes down more significantly because the endcap muons are then treated in a stricter way: a stronger cut is applied to the muons that intersect the endcap tracker disks to keep the purity of the reconstructed dimuon sample. This is done because the tracks in the endcap have up to two times worse momentum resolution than barrel tracks [51]. The efficiency of the forward muons is reduced but the purity is kept above 80% (Fig. 6.3). Alternatively, applying the same stringent cuts for all multiplicities would result in a degradation of the mass resolution to 58, 63 and 66 MeV/c^2 for $\mathrm{d}N_{\mathrm{ch}}/\mathrm{d}y|_{y=0}$ = 0, 2500 and 5000, respectively. The residual dependence of the mass resolution on the event multiplicity reflects the ratio between events with both muons in the barrel part of the tracker and events with at least one muon intersecting the endcap tracker disks. This ratio amounts to 0.25, 0.28 and 0.34 for $\mathrm{d}N_{\mathrm{ch}}/\mathrm{d}y|_{y=0}$ = 0, 2500 and 5000, respectively.

Two different approximations were studied to parameterise the mass resolution in the fast Monte Carlo. In the first method, a fixed value (37 MeV/c^2 for the J/ψ and 86 MeV/c^2 for the Υ mass ranges) was used to smear the dimuons for all pseudorapidity and multiplicity ranges. In the second method, the mass resolution was taken to be $0.009 \times M_{\mu^+\mu^-}$, where $M_{\mu^+\mu^-}$ is the invariant mass of the muon pair. The two methods were used with both the fast and the full (HIJING) simulations [200]. No significant differences were observed and, thus, the first method was used to produce the final figures.

6.1.4 Results

About 5×10^7 PbPb collisions were generated with the fast MC, as described previously. Muons passing the acceptance tables are combined to form pairs and each pair is weighted according to the trigger and reconstruction efficiencies (dependent on the momentum, pseudorapidity, purity and event multiplicity) determined with the full simulation. Their invariant mass is calculated and smeared as described in the previous section. The obtained dimuon mass distributions are then scaled to 0.5 nb^{-1}, corresponding to the PbPb luminosity integrated in one month with average luminosity $\mathcal{L} = 4 \times 10^{26}$ cm^{-2}s^{-1} and 50% machine operation efficiency. Figure 6.5 shows the resulting opposite-sign dimuon mass distributions, for the high and low multiplicity cases and full acceptance ($|\eta| < 2.4$). The different quarkonia resonances appear on top of a continuum due to the various sources of decay muons: $\pi + K$, charm and bottom decays.

The background of uncorrelated muon pairs should also contribute to the like-sign muon pairs mass distribution. Figure 6.6 shows the like-sign and the opposite-sign distributions around the J/ψ and Υ signals for the two multiplicity scenarios considered in the central barrel ($|\eta| < 0.8$). Assuming that the CMS trigger and acceptance conditions treat opposite-sign and like-sign muon pairs on equal footing, the combinatorial like-sign background can be subtracted from the opposite-sign dimuon mass distribution, giving us a better access to the quarkonia decay signals. Applying such a background subtraction technique, in each mass bin, the signal is given by [121]:

$$N^{\mathrm{Sig}} = N^{+-} - 2\sqrt{N^{++}\,N^{--}} \quad . \tag{6.2}$$

Figure 6.7 shows the *signal* dimuon mass distributions, after background subtraction, for two different scenarios: $\mathrm{d}N_{\mathrm{ch}}/\mathrm{d}\eta|_{\eta=0} = 5000$ and $|\eta| < 2.4$ (worst case scenario); $\mathrm{d}N_{\mathrm{ch}}/\mathrm{d}\eta|_{\eta=0} =$

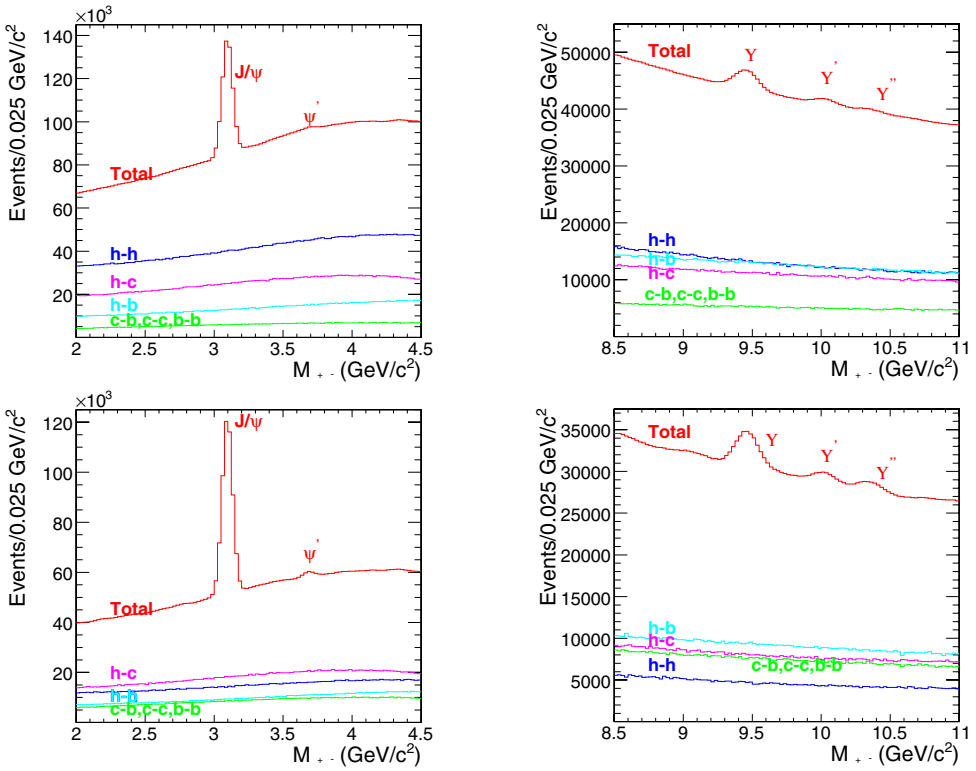

Figure 6.5: Dimuon mass distributions measured within $|\eta| < 2.4$ for PbPb events with $\mathrm{d}N_{\mathrm{ch}}/\mathrm{d}\eta|_{\eta=0}$ = 5000 (top) and 2500 (bottom) in the J/ψ (left) and Υ (right) mass regions. The main background contributions are also shown: h, c and b stand for $\pi + K$, charm, and bottom decay muons, respectively.

2500 and $|\eta| < 0.8$ (best case scenario). The track reconstruction has a better momentum resolution in the barrel ($|\eta| < 0.8$) than in the endcaps, providing a better dimuon mass resolution. Except for the ψ', all quarkonia states are clearly visible.

Signal/Background ratio and statistics

Table 6.3 shows the J/ψ and Υ statistics expected in one month of data taking. The Signal/Background ratios are also indicated: S/B = 1.2 (0.6) in the low (high) multiplicity settings for the J/ψ and ten times lower for the Υ. As mentioned above, these quantities have been calculated for an integrated luminosity of 0.5 nb^{-1}, corresponding to an average luminosity $\mathcal{L} = 4 \times 10^{26}$ cm^{-2}s^{-1} and a 50% machine efficiency. In the tables, the background and reconstructed resonance yields are given for a mass interval $\pm\sigma$, where σ is the mass resolution. Since the reconstruction efficiencies depend on the multiplicity of tracks, it is not surprising to have a higher number of reconstructed resonances at the lower $\mathrm{d}N_{\mathrm{ch}}/\mathrm{d}\eta|_{\eta=0}$. The total expected statistics should be enough to allow for differential analyses of the yields as a function of the centrality of the collision, or of the transverse momentum or rapidity of the resonances.

The signal-to-background ratios and number of events tabulated in Table 6.3 correspond to an average over the impact parameter distribution. The corresponding signal-to-background ratios and number of reconstructed resonances in three different centrality bins (0–10% "central", 15–50% "semicentral" and 60–100% "peripheral") are shown in Table 6.4 for the two charged-particle multiplicity scenarios.

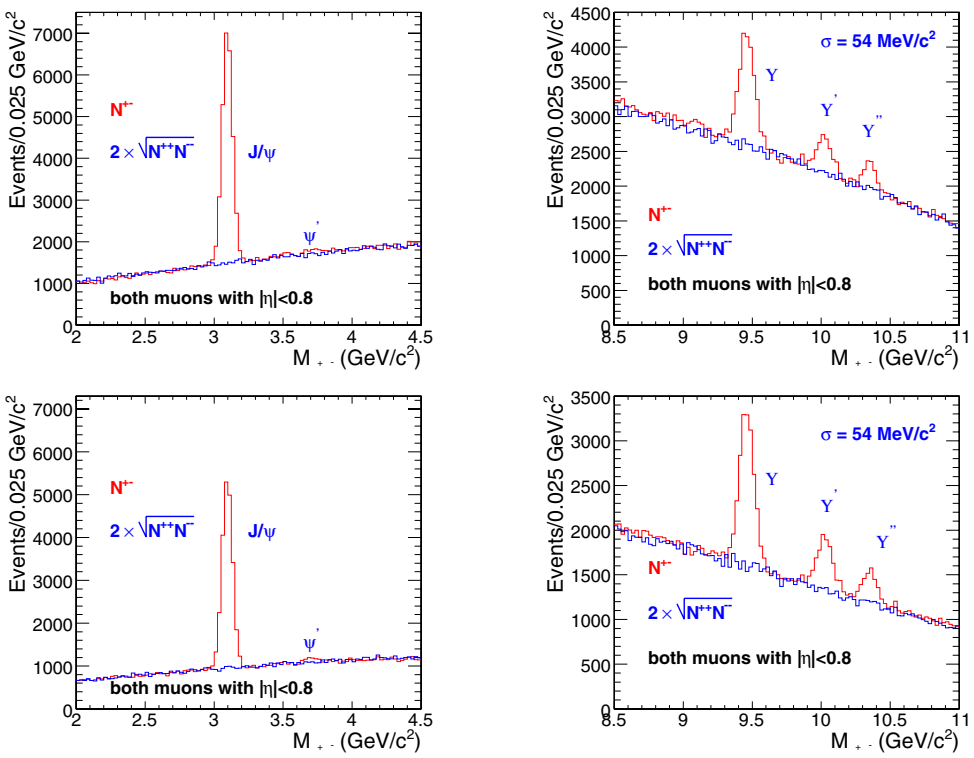

Figure 6.6: Invariant mass spectra of opposite-sign and like-sign muon pairs with $\mathrm{d}N_{\mathrm{ch}}/\mathrm{d}\eta|_{\eta=0} = 5000$ (top) and 2500 (bottom), in the J/ψ (left) and Υ (right) mass regions. Both muons have $|\eta| < 0.8$.

Table 6.3: Signal-to-background ratios and integrated quarkonia yields expected in one month of PbPb running (0.5 nb^{-1} integrated luminosity) for two charged-particle multiplicity scenarios and two pseudorapidity windows, assuming no quarkonia suppression.

$\mathrm{d}N_{\mathrm{ch}}/\mathrm{d}\eta\|_{\eta=0}$, $\Delta\eta$	S/B	N(J/ψ)	S/B	N(Υ)	N(Υ')	N(Υ'')
2500, $\|\eta\| < 2.4$	1.2	184 000	0.12	26 000	7300	4400
2500, $\|\eta\| < 0.8$	4.5	11 600	0.97	6400	2000	1200
5000, $\|\eta\| < 2.4$	0.6	146 000	0.07	20 300	5900	3500
5000, $\|\eta\| < 0.8$	2.8	12 600	0.52	6000	1800	1100

If we assume that, at the LHC, we will see a J/ψ suppression of the same order of magnitude as seen at RHIC, the J/ψ is not likely to be more suppressed than the muon background from light and heavy quark decays due to the foreseeable parton energy loss in the accepted phase space window ($p > 3$ GeV/c, $|\eta| < 2.4$) [107, 201]. Thus the signal-to-background ratio at the J/ψ mass should not change significantly from the values quoted here.

Transverse momentum and rapidity spectra

The J/ψ transverse momentum and rapidity distributions are shown in Fig. 6.8, at the generated and reconstructed levels, for the two different multiplicity scenarios. The corresponding

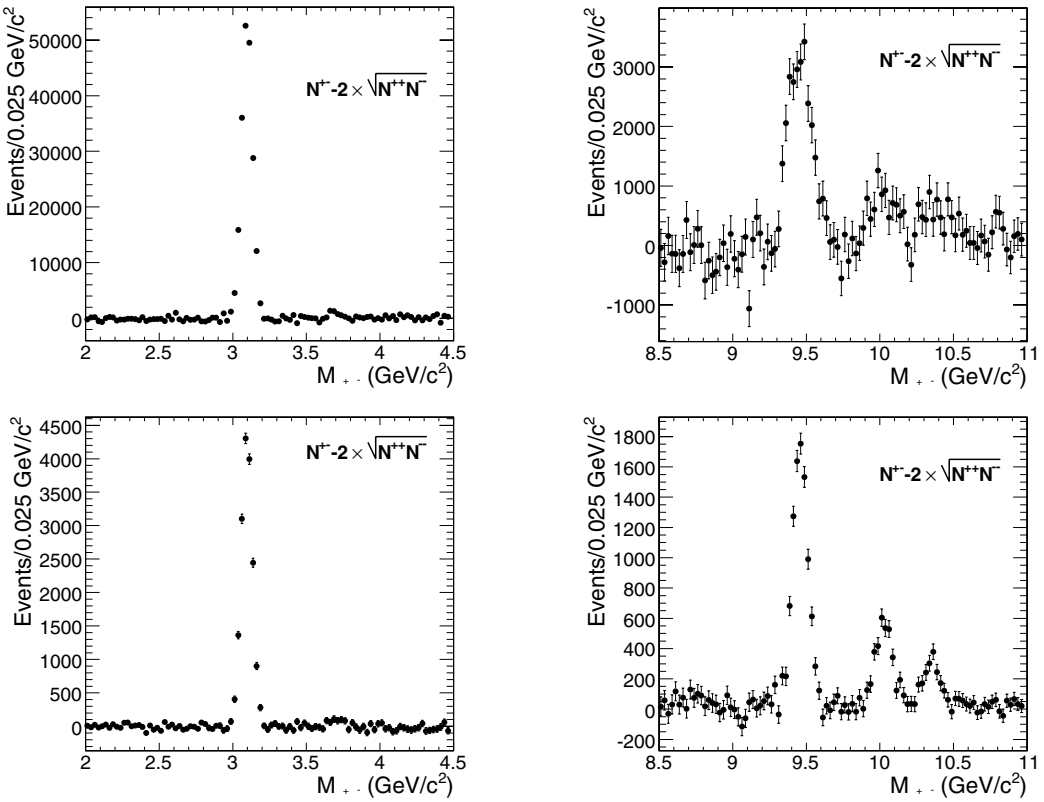

Figure 6.7: Signal dimuon mass distributions in the J/ψ (left) and Υ (right) mass regions, as expected after one month of PbPb running (0.5 nb^{-1}). Top panels for $\mathrm{d}N_{\mathrm{ch}}/\mathrm{d}\eta|_{\eta=0} = 5000$ and $|\eta| < 2.4$ (worst case scenario), bottom panels for $\mathrm{d}N_{\mathrm{ch}}/\mathrm{d}\eta|_{\eta=0} = 2500$ and $|\eta| < 0.8$ (best case scenario); assuming no quarkonia suppression.

Table 6.4: Signal-to-background ratios and quarkonia yields expected in central, semi-central and peripheral PbPb collisions (0.5 nb^{-1} integrated luminosity, full muon acceptance $|\eta| < 2.4$), for two charged-particle multiplicity scenarios.

$\mathrm{d}N_{\mathrm{ch}}/\mathrm{d}\eta|_{\eta=0}$, PbPb centrality	S/B	N(J/ψ)	S/B	N(Υ)
2500, 0–10% (central)	0.9	72 000	0.1	9200
2500, 15–50% (semicentral)	1.5	100 000	0.2	15 000
2500, 60–100% (peripheral)	6.7	10 400	0.9	1600
5000, 0–10% (central)	0.5	50 000	0.04	6200
5000, 15–50% (semicentral)	0.6	85 000	0.08	12 000
5000, 60–100% (peripheral)	2.5	11 000	0.4	1600

distributions for the Υ are shown in Fig. 6.9.

While the reconstructed Υ transverse momentum distributions have a shape quite similar to the generated one, we see a pronounced acceptance effect on the J/ψ spectrum up to about 4 GeV/c, reflecting the J/ψ p_{T} acceptance curve (see Fig. 6.1). With regard to the rapidity

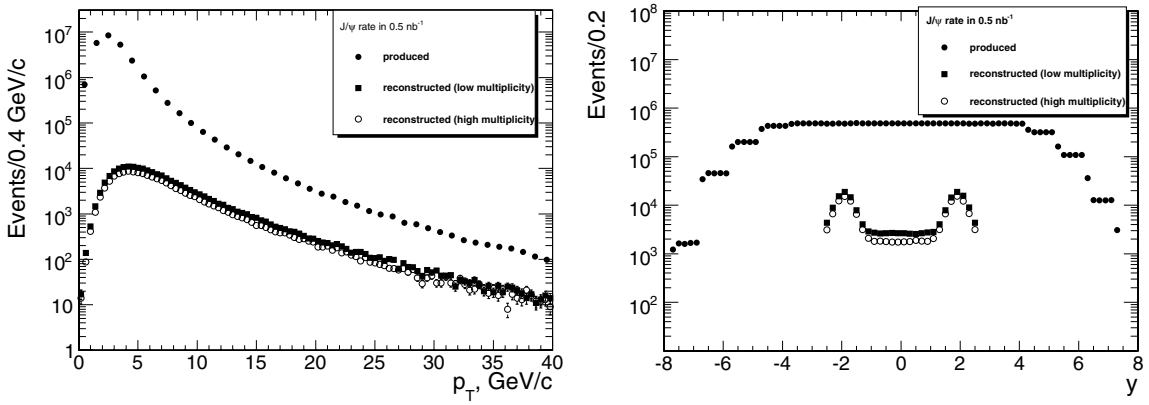

Figure 6.8: p_{T} (left) and rapidity (right) distributions of the muon pairs in the J/ψ mass peak for PbPb at 5.5 TeV assuming no quarkonia suppression. The three distributions are the J/ψ's produced in 0.5 nb^{-1} (solid circles), and the reconstructed ones with either $\mathrm{d}N_{\mathrm{ch}}/\mathrm{d}\eta|_{\eta=0} = 2500$ (squares) or $\mathrm{d}N_{\mathrm{ch}}/\mathrm{d}\eta|_{\eta=0} = 5000$ (open circles).

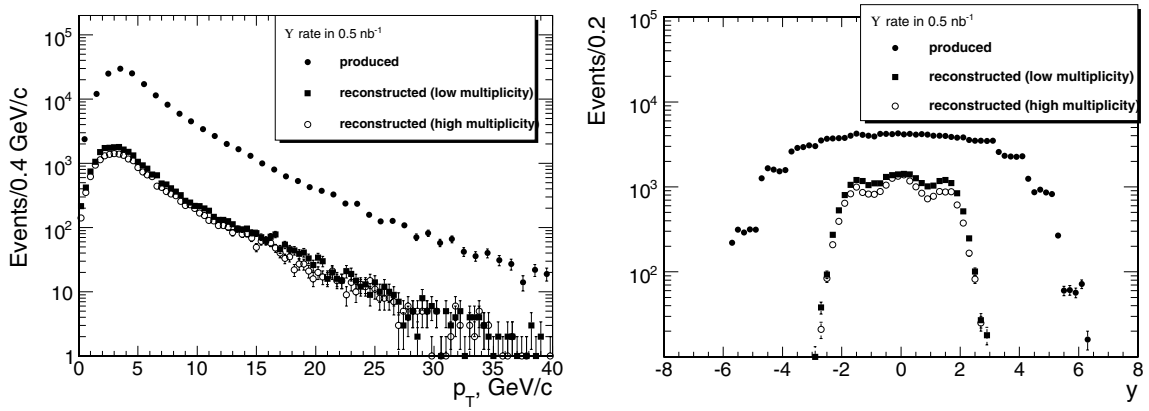

Figure 6.9: p_{T} (left) and rapidity (right) distributions of the muon pairs in the Υ mass peak for PbPb at 5.5 TeV assuming no quarkonia suppression. The three sets of points correspond to: Υ's produced in 0.5 nb^{-1} (solid circles), reconstructed Υ's with $\mathrm{d}N_{\mathrm{ch}}/\mathrm{d}\eta|_{\eta=0}$ =2500 (squares), and reconstructed Υ's with $\mathrm{d}N_{\mathrm{ch}}/\mathrm{d}\eta|_{\eta=0}$ = 5000 (open circles).

distributions, we see that the J/ψ acceptance is smaller at midrapidity than at $|y| \approx 2$, because of the lower *total* momentum of the midrapidity muons, not large enough to traverse the calorimeters and the magnet coil. The reconstructed Υ rapidity distribution has a shape similar to the generated one. The reconstructed spectra are almost insensitive to the difference between the two considered multiplicity scenarios. The amount of statistics collected for the Υ resonance family in one nominal heavy-ion run with the high-level-trigger (HLT) settings discussed in chapter 5 would allow one to study the p_{T}-dependence of the Υ' over Υ ratio (Fig. 6.10), which is a very sensitive probe of the thermodynamical properties of the produced QGP [193].

6.1.5 Conclusions

With its very broad muon acceptance and precise tracking, CMS will provide significant contributions to heavy ion physics at the LHC. Studies of quarkonium production in PbPb reactions at $\sqrt{s_{NN}}$ = 5.5 TeV (and their comparison to the corresponding N_{coll}-scaled proton-

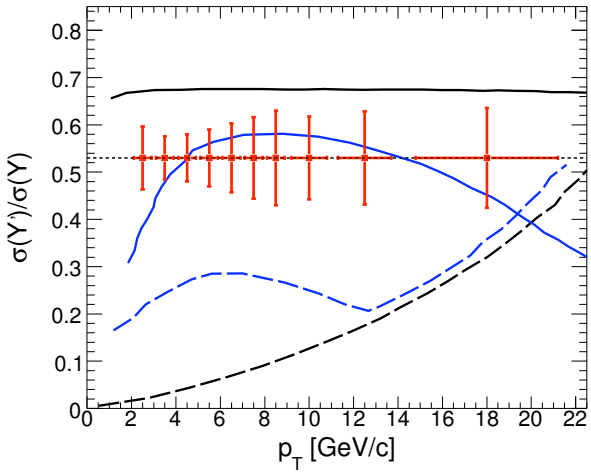

Figure 6.10: Υ' over Υ ratio as a function of p_{T}. Statistical errors correspond to a 10^6 s heavy-ion run with the HLT settings tabulated in Table 5.3. The curves are model calculations for different choices of the plasma initial conditions and for various assumptions on the screening mass temperature [193].

proton cross sections at the same energy) will provide crucial information on the thermodynamical state of the QCD medium formed in these reactions, through the expected step-wise "melting" pattern of the different $Q\overline{Q}$ states due to colour screening. These results will also be sensitive to modifications of the low-x nuclear parton distribution functions, as expected in the case of gluon saturation.

CMS can reconstruct the charmonium and bottomonium resonances, via their dimuon decay channel, with large acceptances (26% for the Υ and 1.2% for the J/ψ), high efficiencies ($\sim$80%), good purity ($\sim$90%) and a very good dimuon mass resolution (54 MeV/c^2 at the Υ mass), when both muons are detected in the central barrel ($|\eta| < 0.8$), even in the case of exceptionally high multiplicities ($\mathrm{d}N_{\mathrm{ch}}/\mathrm{d}\eta|_{\eta=0} \approx 5000$). When considering the full pseudo-rapidity region ($|\eta| < 2.4$), the mass resolution becomes 86 MeV/c^2 at the Υ and 35 MeV/c^2 at the J/ψ, with 50% dimuon reconstruction efficiencies. The Υ states can be measured all the way down to p_{T} = 0 GeV/c with acceptances as large as 40%, while the lower rest mass of the J/ψ state and the large amount of material in the calorimeters prevent us from measuring J/ψ's below $p_{\mathrm{T}} \approx 4$ GeV/c at mid-rapidity. At high p_{T} (above 12 GeV/c for the J/ψ and 4 GeV/c for the Υ) the dimuon acceptance flattens out at 15%.

The large aperture of the muon detectors and the precise tracking result in a very good separation between the $Q\overline{Q}$ states in the dimuon mass distributions, with relatively high statistics and good signal to background ratios. After one month of PbPb running (0.5 nb^{-1}) we should collect 180 000 J/ψ and 25 000 Υ dimuons, enough to compare central and peripheral PbPb collisions, and to carry out differential studies ($\mathrm{d}N/\mathrm{d}y$, $\mathrm{d}N/\mathrm{d}p_{\mathrm{T}}$), which will contribute significantly to clarify the physics mechanisms behind the production (and destruction) of quarkonia states in high-energy nucleus-nucleus collisions.

6.2 Heavy Quarks

6.2.1 Introduction

While the study of inclusive high-p_{T} jet production provides information on the differential response of a hot and dense quark-gluon environment to gluons and light quarks, the study of open heavy flavour production gives corresponding information on massive colour charges, providing a complementary view of the thermodynamical and transport properties of QCD matter. Recent RHIC results show a significant suppression of the yields of heavy-quark decay electrons at high p_{T}, comparable to that observed for light-quark hadrons [202]. This observation was surprising since heavy quarks, especially bottom quarks, expected to dominate the single electron spectra at RHIC for $p_{\mathrm{T}} > 5$ GeV/c, were predicted to lose less energy than the light quarks [203]. The RHIC results suggest that either charm production dominates the single electron spectra over all p_{T} or that bottom quarks lose as much energy as the charm quarks. Neither option was anticipated. At the LHC, the charm and bottom production cross sections are much larger than at RHIC [47] and systematic studies of heavy flavour (especially B) production can be performed for the first time. Such studies, particularly of high mass dimuons, can test the effects of energy loss on bottom quarks to greater precision than at RHIC and in a mass region where other contributions to the continuum are small. In this section we present a first exploratory (mostly generator-level) study of the CMS capabilities to indirectly measure heavy quarks via three channels: (i) high mass dimuons from open heavy-quark decays [204–206]; (ii) secondary J/ψ's from B decays [205, 206]; and (iii) muon tagged b-jet production [207].

6.2.2 High-mass dimuons

The open charm and bottom semileptonic decays are the main sources of muon pairs in the resonance-free high invariant mass region, $20 < M_{\mu^+\mu^-} < 50$ GeV/c^2, between the Υ and Z^0 peaks. Heavy quark pairs are primarily produced at the very beginning of the nuclear collisions, in gluon-gluon processes. The quarks propagate through the dense medium before forming B and D mesons by capturing u, d or s quarks during the hadronization stage. Heavy mesons decay subsequently with mean lifetimes $c\tau$ = 496, 464, 315 and 124 μm, respectively for $\mathrm{B}^{\pm}$, B^0, $\mathrm{D}^{\pm}$ and D^0, with muon branching ratios of about 20% (12%) for B (D) mesons. However, not all the produced muons are expected to pass the CMS acceptance cuts $p_{\mathrm{T}}^{\mu} \gtrsim 4$ GeV/c and $|\eta^{\mu}| < 2.4$. Firstly, about half of the muons from B decays are produced through an intermediate D [208] and populate the softer part of the muon p_{T} spectrum. Secondly, dimuon production from single B decays, $\mathrm{B} \rightarrow \overline{\mathrm{D}}\mu^+\mathrm{X} \rightarrow \mu^+\mu^-\mathrm{Y}$ (which have comparable yields to $b\bar{b}$ pair decays), are concentrated at masses below the B meson mass and, therefore, outside of the region under consideration here.

Figure 6.11 shows the expected dimuon mass spectra within the CMS acceptance corresponding to one month of PbPb running at a luminosity $\mathcal{L}$ = 10^{27} cm^{-2}s^{-1} with 50% efficiency [160]. The PbPb production cross sections of all processes contributing to the high-mass dimuon yield (heavy flavours, Drell-Yan, Z^0, W, WW, WZ^0 and Z^0Z^0) were obtained from the PYTHIA [162] values for pp interactions at $\sqrt{s} = 5.5$ TeV, scaling them with $\sigma_{AA} = A^2\sigma_{pp}$. Uncorrelated muon pairs from hadronic π and K decays were obtained from PbPb events generated with HIJING [158], as described in Section 6.1.2. The dimuon detection efficiencies have been taken into account. In the mass range $10 < M_{\mu^+\mu^-} < 70$ GeV/c^2, the dominant contribution comes from $b\bar{b}$ fragmentation. Hence, the dimuon yield in this mass region should be sensitive to the in-medium bottom quark energy loss. The combina-

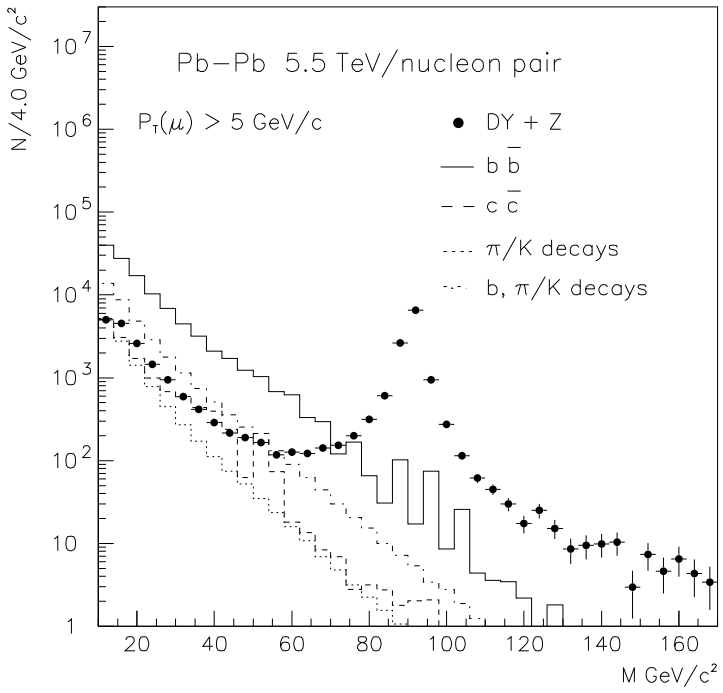

Figure 6.11: Expected contributions to the dimuon mass distribution, for $p_{\mathrm{T}}^{\mu} > 5$ GeV/c and $|\eta^{\mu}| < 2.4$, after one month of PbPb running.

torial background contribution, where one muon is from beauty decays and the other from π/K decays, is about 16%. The contributions from π/K and charm decays are 5–6%. In addition, a clear signal from $Z^0 \rightarrow \mu^+\mu^-$ decays is seen, about 11 000 events within $M_Z \pm 10$ GeV/c^2, with less than 5% background. While Z^0 production is sensitive to the proton and neutron content of the colliding nuclei as well as to modifications of the quark densities in the nucleus at high Q^2, it is unaffected by final-state interactions in the medium. Thus, the Z^0 could be used as a reference process to normalise the jet, quarkonium and heavy flavour rates in AA relative to pp collisions. The dimuon rates from other massive sources ($t\bar{t}$, WW, WZ^0, Z^0Z^0) are negligible.

It is important to isolate the (possibly suppressed) *signal* dimuons from $b\bar{b}$ and $c\bar{c}$ decays with respect to other sources. The uncorrelated background from decays of pions and kaons, and the muon pairs of mixed origin, can be estimated from the like-sign $\mu^+\mu^+$ and $\mu^-\mu^-$ mass spectra and subtracted from the total $\mu^+\mu^-$ distribution, as discussed in the previous Section. Out of the remaining correlated background, the Drell-Yan dimuons (which are unaffected by medium-induced final state interactions) can be rejected with a secondary vertex cut: Drell-Yan muons come from the primary vertex while those from B and D meson decays appear at some distance from the interaction point. The path length between the primary and secondary vertices depends on the meson lifetime and its momentum (Lorentz boost). Thus, an efficient way to select the dimuons from B decays is to require a minimum transverse distance, δr. If P_{min} is the track point with minimal distance to the beam axis, z, then δr is the distance in the x–y plane between the points $P_{1,\mathrm{min}}$ and $P_{2,\mathrm{min}}$, of two different muon

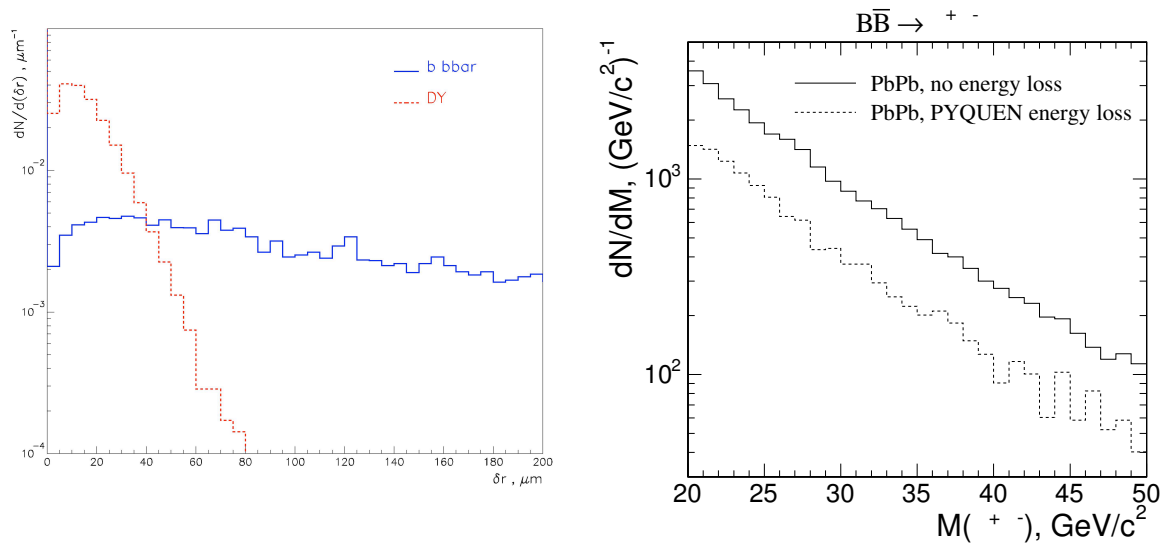

Figure 6.12: Left: Transverse distance, δr, distribution for muon pairs from beauty decays (solid histogram) and for Drell-Yan dimuons (dashed histogram). Right: Invariant mass distribution of $\mu^+\mu^-$ pairs from $b\bar{b}$ decays with $p_{\mathrm{T}}^{\mu} > 5$ GeV/c and $|\eta^{\mu}| < 2.4$ in minimum bias PbPb collisions, with (dashed histogram) and without (solid histogram) bottom quark energy loss.

tracks. Muon pairs from $b\bar{b}$ decays show a rather flat distribution while those from Drell-Yan production are concentrated at small δr values, vanishing at $\delta r \approx 70$ μm (see Fig. 6.12-left). Fast simulation studies, including the track and vertex resolutions, indicate that a cut $\delta r > 50$ μm suppresses the Drell-Yan rate by two orders of magnitude while the signal is only reduced by 30% [206].

Figure 6.12-right shows the PYTHIA spectra (scaled by A^2) of high-mass $\mu^+\mu^-$ pairs (with $p_{\mathrm{T}}^{\mu} > 5$ GeV/c and $|\eta^{\mu}| < 2.4$) for minimum bias PbPb collisions, with and without medium-induced energy loss of bottom quarks, according to the PYQUEN energy loss model [177, 209]. A factor of around 3 suppression for $b\bar{b} \rightarrow \mu^+\mu^-$ would be clearly observed over the 15% initial state nuclear shadowing expected in this kinematic region. Note that the open bottom yield integrated over all phase space is always conserved: the suppression in the rate becomes apparent only when the kinematic cuts are applied.

6.2.3 Secondary J/ψ production

Another process which also carries information about medium-induced rescattering and bottom energy loss is secondary J/ψ production from the $\mathrm{B} \rightarrow \mathrm{J}/\psi$ X decay (1.15% branching ratio). The J/ψ subsequently decays to dimuons with a 5.9% branching ratio so that the whole process reads $gg \rightarrow b\bar{b} \rightarrow \mathrm{B\bar{B}}$ X $\rightarrow \mathrm{J}/\psi$ Y $\rightarrow \mu^+\mu^-$ Y. A leading order pQCD calculation with muon kinematical cuts imposed to take into account the region where CMS is efficient ($p_{\mathrm{T}}^{\mu} > 5$ GeV/c and $|\eta^{\mu}| < 2.4$) yields 13 000 dimuons from secondary J/ψ decays in a nominal one month PbPb run. Primary J/ψ's produced at the nucleus-nucleus interaction point can be rejected using the secondary vertex information (see Fig. 6.13-left), as previously discussed. Figure 6.13-right shows the p_{T} distribution of the J/ψ mesons resulting from B meson decays in two cases: as generated by PYTHIA and after including energy loss effects (according to the PYQUEN [177, 209] model). It is clear that the measured secondary J/ψ

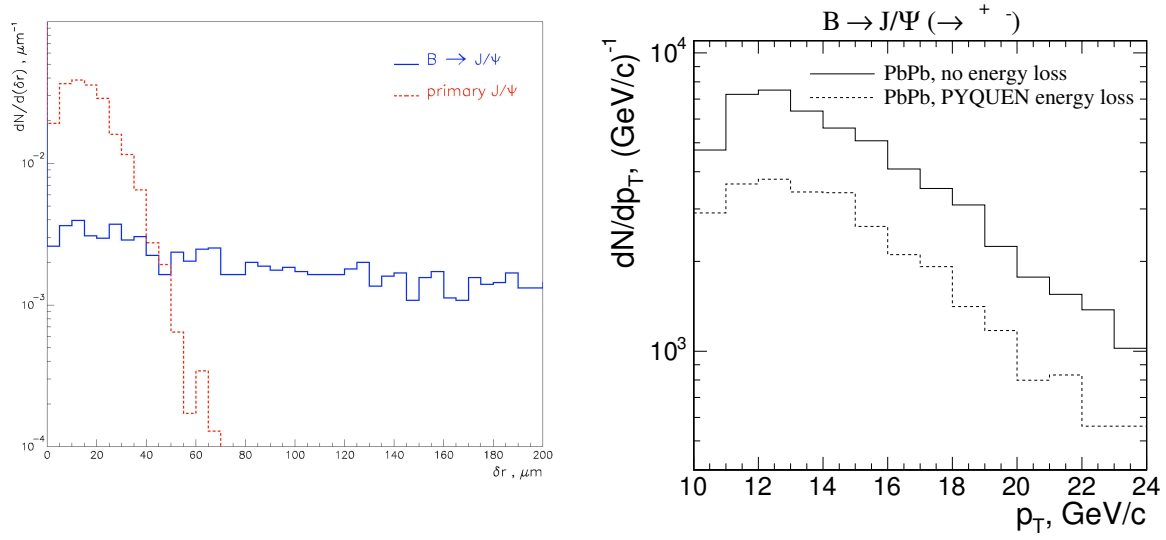

Figure 6.13: Left: Transverse distance, δr, distribution of $\mu^+\mu^-$ pairs from secondary (solid histogram) and primary (dashed histogram) J/ψ decays. Right: Transverse momentum distribution of secondary J/ψ dimuons, with $p_{\mathrm{T}}^{\mu} > 5$ GeV/c and $|\eta^{\mu}| < 2.4$, in minimum bias PbPb collisions, with (dashed histogram) and without (solid histogram) bottom energy loss [177].

yields will be very sensitive to the suppression of open bottom yields.

6.2.4 B-jet tagging via energetic muons

The possibility to observe the medium-modified fragmentation of hard b quarks tagged by a leading muon in ultrarelativistic heavy ion collisions has been analysed in Ref. [207], using PYTHIA 6.2 [162] with CTEQ5L PDFs to calculate the cross section of b-jet production at $\sqrt{s_{NN}}$ = 5.5 TeV, scaled by A^2 to obtain the corresponding PbPb spectra. The event rate has been estimated for the central CMS acceptance, $|\eta^{\mathrm{jet}}| < 3$ and $|\eta^{\mu}| < 2.4$, where the muon is considered as a leading particle if it belongs to a hard jet and carries at least 20% of the jet transverse momentum. More specifically, the jet energy is determined as the total transverse energy of the final particles collected around the direction of a leading particle inside a cone $R = \sqrt{\Delta\eta^2 + \Delta\varphi^2} = 0.5$, where η and φ are the pseudorapidity and the azimuthal angle, respectively. The pp cross section to have a leading muon from a B meson is ~ 0.7 pb, with the kinematical cuts $p_{\mathrm{T}}^{\mu} > 5$ GeV/c and $E_{\mathrm{T}}^{\mathrm{jet}} > 50$ GeV. This gives a $0.7\ \mathrm{pb} \times (208)^2 \approx 0.03$ mb PbPb cross section. The corresponding event sample collected in one month of PbPb running is high enough, 2×10^4, for detailed B-jet energy loss studies. Naturally, increasing the minimal jet energy threshold reduces the measured rates; but even for $E_{\mathrm{T}}^{\mathrm{jet}} > 100$ GeV we still expect around 10^3 events.

Chapter 7

Jets and high-p_{T} hadrons

7.1 Introduction

The abundance of high Q^2 processes at LHC energies will provide large samples of high E_{T} jets, large p_{T} hadrons, and jets produced back-to-back to gauge bosons (γ, Z^0). The strong interest in these observables in heavy-ion collisions stems from the fact that high E_{T} quarks and gluons can be used as tomographic probes of the hot and dense medium produced in the collision as they propagate (and, potentially, attenuate) through it (see discussion in Section 1.4.5). Their hard momentum ensures that their production cross sections and medium modifications are perturbatively calculable, making them quantitative tomographic tools of QCD matter.

Experimentally, one can study jet quenching phenomena in several channels. In jet+jet events, the energy of the jets can be asymmetrically reduced by the medium, leading to the appearance of monojet topologies [91]. Comparisons of jets with their weakly interacting counterparts in γ-jet or Z-jet events allow one to directly estimate the amount of medium-induced energy loss. The process by which the high-p_{T} partons become final state hadrons is characterised by fragmentation functions, that are also expected to be modified in the medium. Medium-induced parton energy loss is expected to change the multiplicity inside the jet cone and the p_{T} distribution relative to the jet axis [44, 210]. The jet quenching can also manifest itself by a reduced yield of inclusive (leading) hadrons at high p_{T} compared to pp collisions. The corresponding nuclear modification factors, $R_{AA}(p_{\mathrm{T}})$, and the central-to-peripheral ratios, $R_{CP}(p_{\mathrm{T}})$, of charged particle p_{T} spectra are important observables characterising energy loss in the created medium, and have been extensively studied at RHIC [211–214]. The p_{T} reach of these measurements will be dramatically increased at LHC energies.

CMS is, by design, an experiment extremely well suited to measure hard scattering processes. With high quality electromagnetic and hadronic calorimeters covering a wide pseudorapidity range and with excellent trigger capabilities, CMS will undoubtedly provide better measurements than the dedicated heavy-ion ALICE experiment in the perturbative sector. In particular, CMS will be able to adequately reconstruct jets in the high multiplicity environment of PbPb collisions, using full calorimetric measurements [44, 160, 215, 216], as well as precise charged particle tracking and momentum reconstruction in its 4 T field up to momenta of hundreds of GeV/c [165]. This is particularly interesting given the fact that heavy-ion collisions at LHC energies will provide, for the first time, fully formed high E_{T} jets, at a rate of more than 10 jet pairs per second. Systematic studies will, hence, be possible in a clean kinematic regime, far beyond the limits of RHIC, and with high statistics.

This chapter starts with the methodology and performance of the jet reconstruction in heavy-ion collisions, followed by a description of the jet triggering strategy and the trigger rates expected using the calorimeters. We will then present the expected reach in jet E_{T}, up to 0.5 TeV in central PbPb using the triggered event sample. We will then introduce the reconstruction performances of the CMS tracker in heavy ion collisions for high-p_{T} hadrons, the statistical reach of the inclusive charged particle p_{T} spectra (up to 300 GeV/c), the nuclear modification factors and the central-to-peripheral ratios of these spectra, discussing the benefits of triggering on jets with respect to the option of simply using minimum bias data. The combination of the large reach of the inclusive jet and hadron measurements allows for a detailed study of the in-medium jet fragmentation function. The chapter closes with a discussion of the physics interest and experimental capabilities of studies of jet production tagged with gauge bosons (γ, $\gamma^{\star}$, Z^0).

7.2 Jets

7.2.1 Introduction

In this section we present a realistic estimate of the expected statistical reach of the inclusive jet spectra measurement in different PbPb centralities in one month at design luminosity (0.5 nb^{-1}). We review the full jet reconstruction capabilities of CMS, including a description of the algorithm to deal with the high particle multiplicities and the detector performance. We discuss the expected trigger rates for the HLT strategy and thresholds discussed in the previous HLT chapter, and we present the results obtained with a fast simulation, with parameterised jet energy resolutions obtained from full GEANT4 studies.

7.2.2 Jet measurement

The reconstruction of full jets in PbPb collisions at the LHC faces two experimental challenges. First, the randomness of the fragmentation/hadronization process leads to fluctuations of the fraction of jet energy going into final state charged and neutral particles (see Fig. 7.1-left) [217] which require an efficient measurement of the jet hadronic as well as electromagnetic energy, using fully hermetic and highly segmented calorimeters. Given the steep falloff of the jet cross section as a function of energy, a precise calibration of the jet energy scale is also essential in order to perform an unbiased comparison between data and theoretical predictions. The second experimental challenge in a heavy-ion environment — where the amount of soft hadronic activity (the "underlying event") is much larger than in pp collisions — is the separation of the particles associated with the jet from the background of soft remnants in the underlying event. The right panel of Fig. 7.1 shows the jet "fragmentation function", $\mathrm{d}N/\mathrm{d}z$, i.e. the transverse momentum distribution of hadrons resulting from the fragmentation of a jet (z is the fraction of parton energy carried by the hadron). Even for very high energy partons, most of the energy goes into rather soft particles. To separate the particles belonging to the jet from the underlying collision background a minimum momentum must be required (say, well above 4 GeV/c), resulting in a severe bias in the fragmentation function of low energy jets ($E_{\mathrm{T}} < 50$ GeV). This emphasizes the advantage of studying highly energetic jets ($E_{\mathrm{T}} > 50$ GeV), to reduce such bias in the cross sections and fragmentation functions. Furthermore, such studies give access to the low-z region of the fragmentation functions.

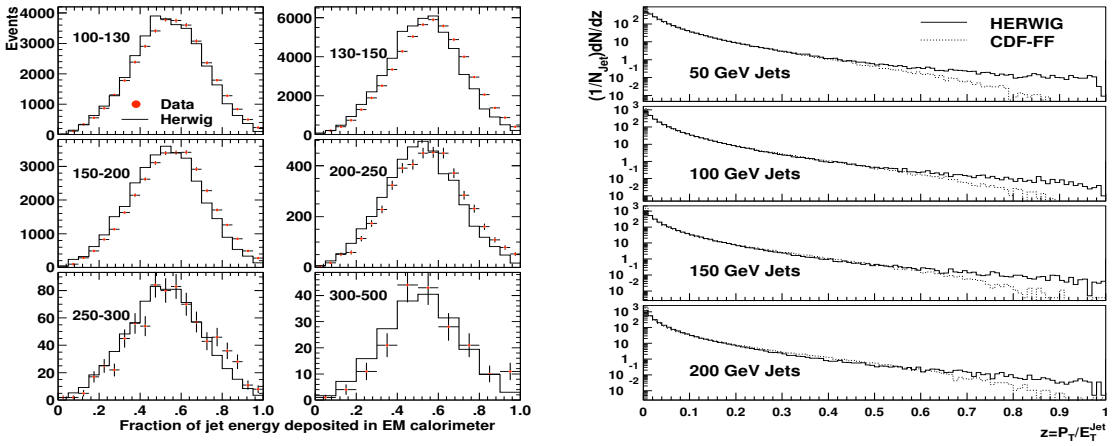

Figure 7.1: Jet properties measured by CDF in $\mathrm{p\bar{p}}$ collisions at $\sqrt{s}$ = 1.8 TeV [217]. Left: Fraction of electromagnetic energy in jets with different ranges of E_{T} (dots) compared to the HERWIG Monte Carlo predictions (histogram). Right: Fragmentation function for jets of different E_{T} obtained by CDF compared to HERWIG predictions.

7.2.3 Reconstruction algorithm

Jet reconstruction in heavy-ion collisions in CMS is performed with an iterative cone algorithm modified to subtract the underlying soft background on an event-by-event basis [160]. The algorithm is a variant of an iterative "noise/pedestal subtraction" technique. Initially, the mean value and dispersion of the energies recorded in the calorimeter cells are calculated for all rings of cells at constant pseudorapidity, η. The value of this pedestal function, P(η), is then subtracted from all cells and the jets are reconstructed, using a standard iterative cone algorithm, from the remaining non-empty cells. In a second iteration, the pedestal function is recalculated using only calorimeter cells outside the area covered by reconstructed high E_{T} jets ($E_{\mathrm{T}} > 30$ GeV). The cell energies are updated with the new pedestal function and the jets are reconstructed again, using the updated calorimeter cells. This method fully exploits the large η and full azimuthal coverage of the CMS calorimetry (6 units of pseudorapidity in the barrel and endcap sections; and about 10 units in total including the HF).

7.2.4 Reconstruction performance

The capability of CMS to reconstruct hard QCD jets in PbPb events has been extensively studied using full GEANT4 (OSCAR) detector simulations with realistic assumptions concerning jet and hadron spectra, and particle multiplicities. To evaluate the reconstruction performance, event samples of (signal) QCD dijet events were generated as pp collisions with PYTHIA 6.158 [162], in several intervals of the initial parton transverse momentum ($\hat{p}_{\mathrm{T}}$ = 50–60, 70–80, 90–105, 120–130, 200–210, and 300–310 GeV/c), and embedded into central PbPb background events at $\sqrt{s_{NN}}$ = 5.5 TeV. The PbPb background was simulated with the HIJING Monte-Carlo generator [158] (default settings, quenching on) scaling the charged particle multiplicity to a value $\mathrm{d}N_{\mathrm{ch}}/\mathrm{d}y|_{y=0}$ = 5000 and only generating events *without* hard collisions. The energy flow, $\left\langle E_{\mathrm{T}}^{\mathrm{tower}}(\eta)\right\rangle$, defined as the transverse energy per calorimeter tower averaged over the full azimuthal angle at a given η^{tower}, is shown in the left panel of Fig. 7.2, separately for the ECAL and HCAL calorimeters. The transverse energy flow shows a strong η dependence; at mid-rapidity, most of the energy is reconstructed in the ECAL. The right

panel of Fig. 7.2 shows the background fluctuations in the (ECAL + HCAL) calorimeter towers, $\left\langle \sigma_{\mathrm{T}}^{\mathrm{tower}}(\eta) \right\rangle = \sqrt{\left\langle D_{\mathrm{T}}^{\mathrm{tower}}(\eta) \right\rangle}$, where $D_{\mathrm{T}}^{\mathrm{tower}}(\eta)$ is the variance of the transverse energy per tower, $D_{\mathrm{T}}^{\mathrm{tower}}(\eta) = \overline{(E_{\mathrm{T}}^{\mathrm{tower}}(\eta))^2} - (\overline{E_{\mathrm{T}}^{\mathrm{tower}}(\eta)})^2$, summed over all towers at a given η^{tower}. The average values of E_{T} per tower (ECAL + HCAL) for central PbPb collisions are 1.7 GeV in the barrel and 4.8 GeV in the endcap (excluding the last tower in the endcap), with dispersions of 0.9 and 1.5 GeV, respectively.

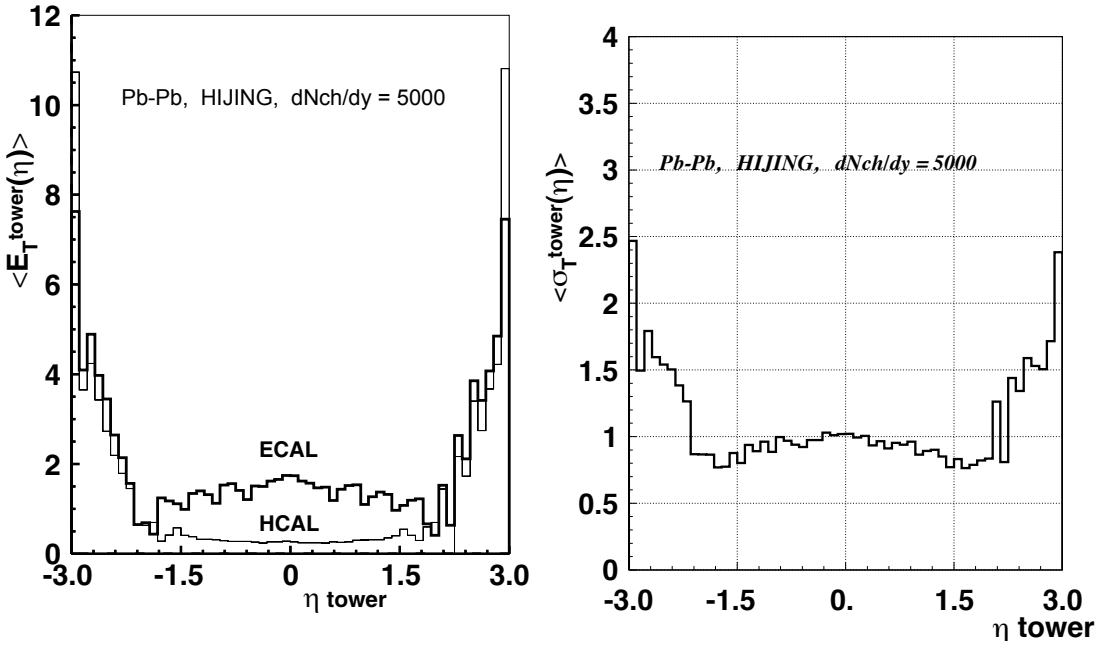

Figure 7.2: Left: η^{tower} dependence of the transverse energy flow averaged over φ, $\left\langle E_{\mathrm{T}}^{tower}(\eta) \right\rangle$, in GeV, as reconstructed in the ECAL (open histogram) and in the HCAL (closed histogram). Right: η^{tower} dependence of the dispersion of the transverse energy distribution in the calorimeter towers (ECAL + HCAL), $\left\langle \sigma_{\mathrm{T}}^{\mathrm{tower}}(\eta) \right\rangle$, in GeV.

The jet reconstruction performance is studied in events with and without addition of the background from central PbPb collisions. Jets are reconstructed using the modified iterative cone jet finder (cone radius of $R = 0.5$) with event-by-event background subtraction and a threshold of 30 GeV on the reconstructed jet energy. Only one jet per event, the jet with the largest transverse energy, is used for further analysis. The quality of the jet reconstruction is evaluated by matching the jets reconstructed in the full detector simulation to jets reconstructed from the generator level particles in the corresponding signal events.

The influence of the background subtraction algorithm on the jet energy scale is evaluated by studying the correlation between the reconstructed, $E_{\mathrm{T}}^{\mathrm{reco}}$, and the generated, $E_{\mathrm{T}}^{\mathrm{MC}}$, transverse energies of jets in a cone of R = 0.5, both in central PbPb events and in jet events without background. Such correlations are shown in Fig. 7.3, for the barrel (left panel) and endcap (right panel) regions. The points represent the mean transverse energy of the reconstructed jets and the error bars show the dispersion of the corresponding distributions. On average, the reconstructed jet energy in central PbPb collisions corresponds very well to the energy reconstructed without background. In events with background, with respect to the events without background, the mean values of the reconstructed jet transverse energy are slightly lower for $E_{\mathrm{T}}^{\mathrm{MC}} > 200$ GeV and slightly higher for $E_{\mathrm{T}}^{\mathrm{MC}} < 100$ GeV. Although the values with

and without background are compatible with each other within their error bars, the $E_{\mathrm{T}}^{\mathrm{reco}}$ vs. $E_{\mathrm{T}}^{\mathrm{MC}}$ correlation seems to have a slightly different "slope".

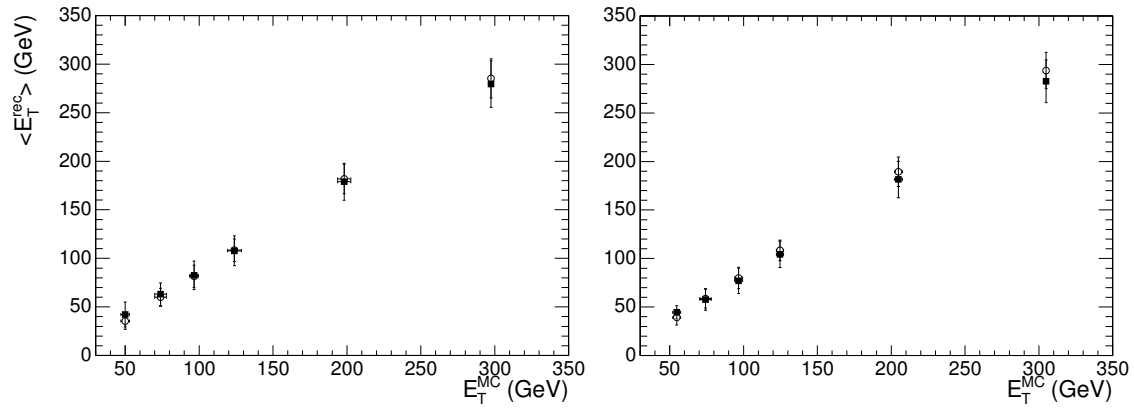

Figure 7.3: Correlation between the reconstructed and the generated jet transverse energies, in PbPb (full squares) and in jet events without background (open circles), in the central barrel ($|\eta| < 0.3$, left panel) and endcap ($1.6 < |\eta| < 1.9$, right panel) regions.

The jet energy resolution, defined as $\sigma(E_{\mathrm{T}}^{\mathrm{reco}}/E_{\mathrm{T}}^{\mathrm{MC}})/\langle E_{\mathrm{T}}^{\mathrm{reco}}/E_{\mathrm{T}}^{\mathrm{MC}}\rangle$, is shown in Fig. 7.4 for the central barrel (left panel) and endcap (right panel) regions. For jets above E_{T} = 75 GeV, the jet energy resolution is degraded by a factor ~ 1.3 in high multiplicity central PbPb collisions compared to jets without background.

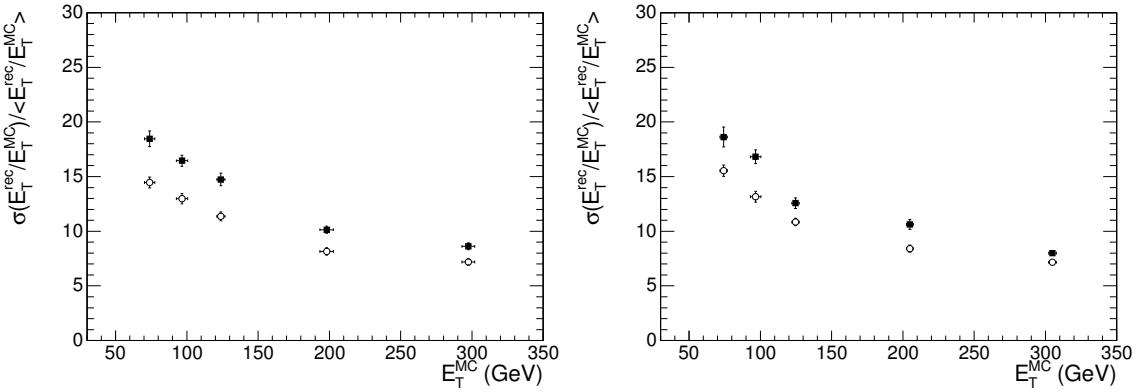

Figure 7.4: Jet energy resolution, in percent, in central PbPb collisions (full squares) and in jet events without background (open circles), in the central barrel ($|\eta| < 0.3$, left panel) and endcap ($1.6 < |\eta| < 1.9$, right panel) regions.

Since the azimuthal angle and the rapidity distributions of jets are of particular interest for jet quenching observables in heavy-ion collisions, spatial resolution is important. Figure 7.5 shows the differences in pseudorapidity ($\Delta\eta$, left panel) and in azimuthal angle ($\Delta\varphi$, right panel) between reconstructed and generated jets in events without and with PbPb background for different generated jet energies in the barrel. For 100 GeV jets, the η and φ resolutions are 2.8% and 3.2%, respectively. They are slightly better in the endcap region than in the barrel. The jet spatial resolution is degraded in central PbPb collisions in comparison with the event sample without background, but is still better than the η, φ size of one calorimeter tower (0.087×0.087). Thus, the spatial position of a hard jet can be reconstructed in heavy-ion collisions in CMS with sufficient accuracy for the analysis of jet production as a function of azimuthal angle and of pseudorapidity.

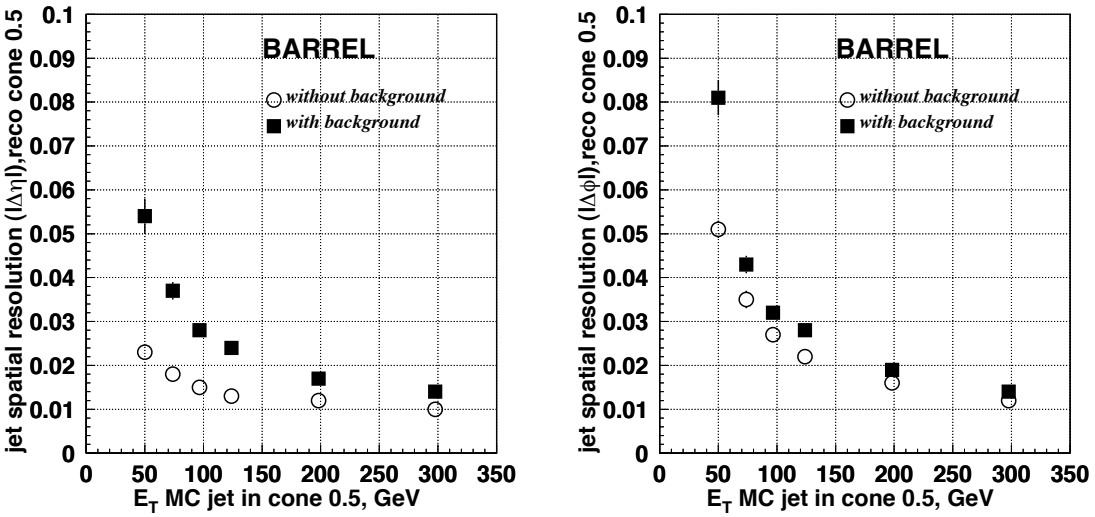

Figure 7.5: Jet pseudorapidity (left) and azimuthal angle (right) resolutions as a function of jet transverse energy, in central PbPb collisions (full squares) and in jet events without background (open circles) in the central barrel ($|\eta| < 0.3$) region.

Figure 7.6 shows the efficiency and purity of the calorimetric jet reconstruction in the barrel (left panel) and endcap regions (right panel) as a function of the MC jet energy. The efficiency of the jet reconstruction is defined as the fraction of events with a true QCD jet matched to the reconstructed jet among all the generated events. It is essentially 100% for E_{T} above 75 GeV (100 GeV) jets in the barrel (endcap) region. The purity of the reconstructed jet sample is defined as the number of events with a matched true QCD jet divided by the number of events with at least one reconstructed jet (fake or real) with transverse energy above 30 GeV. For jets in the barrel (endcap) with E_{T} above 50 GeV (75 GeV), the purity of the reconstructed jet sample is essentially 100%. More detailed descriptions of the jet reconstruction algorithm and performance can be found in Refs. [215, 216, 218, 219].

7.2.5 Jet studies with fast simulation

The aim of this study is to estimate the statistical reach of the expected inclusive jet (and corresponding inclusive high-p_{T} charged hadron) spectra in different PbPb collision centralities, corresponding to one month of LHC heavy-ion running at design luminosity (0.5 nb^{-1}). Given the large statistics (millions of heavy-ion events) necessary to complete the study, a full detector simulation is, computationally, too expensive. Alternatively, we have employed a *fast* simulation technique including the basic geometrical coverage of the CMS calorimeter system, magnetic field and segmentation, adjusting the most important detector response features, like the energy resolution of the jet reconstruction algorithm, to agree with the performance obtained using detailed detector simulations [215, 216, 218, 219]. A summary of the procedure is described below. More detailed information can be found in Ref. [190].

Jet reconstruction is carried out within the HIROOT framework (see Appendix B). The same modified iterative cone algorithm is used as in the full simulations, with a seed threshold of E_{seed} = 10 GeV and a minimum E_{T} cut of 30 GeV. The particles in the PbPb final state, generated by HYDJET, are sorted into $\eta - \phi$ bins corresponding to the CMS hadronic calorimeter segmentation. Charged tracks with p_{T} smaller than 0.8 GeV/c are not considered (since they

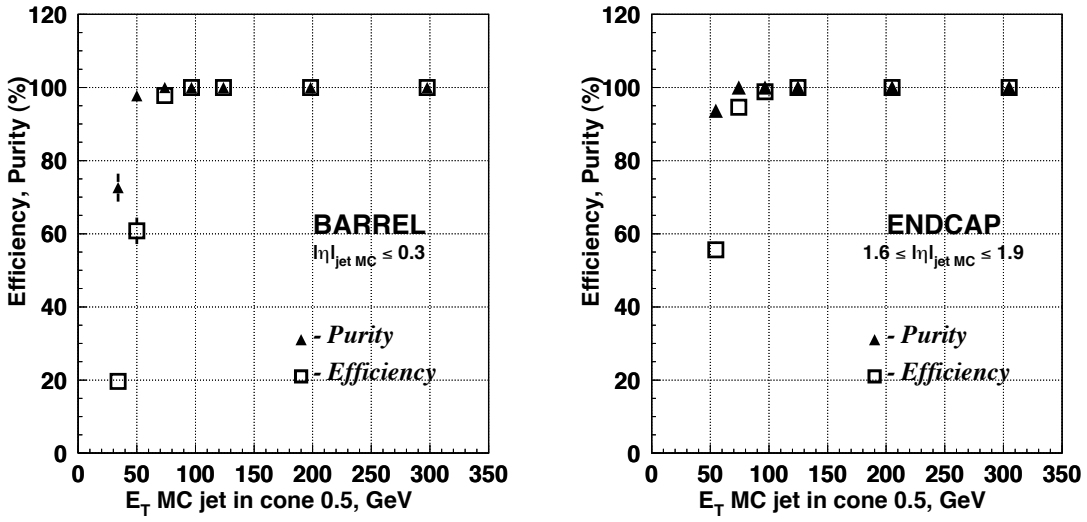

Figure 7.6: Transverse energy dependence of the reconstruction efficiency (open squares) and purity (closed triangles) of the jet reconstruction, in central PbPb events in the central barrel ($|\eta| < 0.3$, left panel) and in the endcap ($1.6 < |\eta| < 1.9$, right panel).

cannot reach the calorimeter surface in the 4 T magnetic field), but for all other purposes the magnetic field is neglected (trajectories are approximated as straight lines). The deposited energy in all calorimeter towers is collected (without including a specific detailed calorimeter response) and a "jet component" object is created for all calorimeter towers. The energy of such a jet component will simply be the sum of energies of the particles hitting the given calorimeter tower. The iterative cone algorithm and the background subtraction is run on these jet components. The first step is to find all jet candidates using a $R = 0.5$ cone radius, iteratively, starting from jet component seeds in decreasing order of transverse energy. The second step is to calculate the average energy and the RMS of the tower energies for all η-rings excluding the cones of the jet candidates. The sum of the average and the dispersion of the energies in each η-ring are subtracted from all towers in that η-ring. The third step is to find the jets on the jet towers with the newly corrected energies.

The resolution of the jet energy obtained by this procedure, includes the smearing induced by the fluctuating soft particle underlying heavy-ion background. However, the resolution obtained in this way does not take into account the intrinsic energy resolution of the calorimeter, or any kind of detector response. To approach reality more closely, the jet energy resolutions were adjusted ("smeared") to match the full GEANT4 (OSCAR) detector simulations discussed in the previous section.

Figure 7.7 compares the resolutions from the fast (HIROOT) and full (OSCAR) detector simulations. In the case of central PbPb collisions, the E_{T} dependence of the resolution given by the full detector simulation (closed black squares) is well reproduced by the fast simulation results (closed blue triangles). A very good agreement is obtained when the jet energy reconstructed is convoluted with an additional Gaussian smearing function of 3–15%, depending on multiplicity and E_{T} (closed red circles).

In pp collisions the difference between the generator level and OSCAR resolutions is much larger, because of the lack of background fluctuations and any other detector effects in the fast simulation. Therefore, a larger jet energy smearing is added in the pp case to adjust

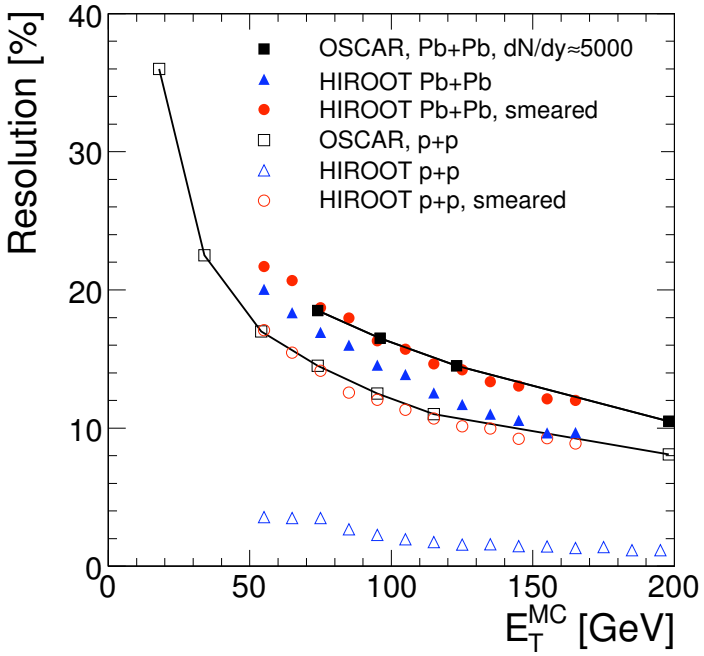

Figure 7.7: Jet E_{T} resolutions (in percent), as a function of E_{T}, as obtained in the fast (HIROOT) and full (OSCAR) detector simulations. After additional smearing, the HIROOT resolutions are in good agreement with those from the full simulations, both for pp and for PbPb collisions.

the fast Monte Carlo resolutions to the OSCAR results. The extra smearing is slightly E_{T} dependent in both the pp and PbPb cases. The good agreement seen in Fig. 7.7 between the red circles (smeared fast MC) and the black squares (OSCAR) is precise enough to justify doing the large statistics simulations and the trigger studies only using the fast simulation tool. After the extra necessary smearing has been determined for pp and central PbPb collisions, the amount of smearing in non-central PbPb collisions is interpolated between these two cases, for each generated event, assuming that the smearing scales like the square root of the multiplicity density at midrapidity, $\sqrt{\mathrm{d}N_{\mathrm{ch}}/\mathrm{d}y|_{y=0}}$. Although a multiplicity density of $\mathrm{d}N_{\mathrm{ch}}/\mathrm{d}y|_{y=0}$ = 5000 was used in these comparisons and adjustments, a smaller multiplicity density, $\mathrm{d}N_{\mathrm{ch}}/\mathrm{d}y|_{y=0}$ = 3200, is assumed for central PbPb collisions for all other results presented here.

7.2.6 Trigger rates

The expected number of jet pairs produced with $E_{\mathrm{T}}^{\mathrm{jet}} > 100$ GeV in the CMS acceptance is as high as 4.3×10^6 in one month of PbPb running at the LHC [44]. As discussed in detail in Chapter 5, the high readout rate of the CMS data acquisition system allows inspection of all minimum bias PbPb events by the high level trigger farm. The jet reconstruction algorithm fits into the foreseen HLT time budget and can thus be used to derive a trigger decision using fully reconstructed jets in each inspected PbPb event.

Table 7.1 collects the bandwidth allocations for the various trigger channels relevant for jet studies (see Table 5.3 for more details). The average event size depends on the trigger condition, because a high energy jet trigger tends to select slightly more central collisions. The maximum logging rate in each channel (last column) is the ratio between the allocated bandwidth and the average event size. Since the jet quenching effect introduces a centrality-

dependent modification of the shape of the jet E_T distribution, it is not a priori possible to calculate the corresponding HLT pre-scale factor, which will have to be determined from real data once data taking starts.

Table 7.1: Part of the strawman trigger table (Table 5.3) relevant for jet-related studies at design PbPb luminosity. For each channel we quote the allocated bandwidth, the average size of the events satisfying the trigger condition and the average data logging rate.

Channel	E_{T} threshold	Bandwidth [MByte/s]	event size [MByte]	rate to tape [Hz]
min. bias	-	33.75 (15%)	2.5	13.50
jet	100 GeV	24.75 (11%)	5.8	4.27
jet	75 GeV	27 (12%)	5.7	4.74
jet	50 GeV	27 (12%)	5.4	5.00

The CMS High Level Trigger will have a large buffer storage that ensures data taking with almost no dead time. The channels with large input rate will be appropriately prescaled so that the rate to tape will be $\min\{r_i, R_i\}$, where r_i is the input rate and R_i is the maximum rate to tape in the i^{th} channel. The jet rates were obtained using the standard integrated luminosity of 0.5 nb^{-1} and a 7.8 b inelastic PbPb cross section, giving a total of 3.9×10^9 PbPb collisions. The impact parameter distribution was sliced into bins corresponding to 10% of the total inelastic cross section, from most central (0–10%) to most peripheral (80–90%). A few million minimum bias HYDJET events were used to count the number of jets in each centrality bin, with axis within $|\eta| < 2$, including jet quenching and the extra smearing that makes the resolution in the fast simulation similar to the one of OSCAR. The number of jets with E_{T} above 50, 75, and 100 GeV are listed in the "Infinite bandwidth" rows of Table 7.2.

The second row for each centrality bin lists the number of jets in the minimum bias trigger channel, which has 15% of the allocated bandwidth. The trigger efficiency was estimated to be 0.35%, assuming a 2.5 MByte average event size [192], 10^6 seconds of data taking per month and a constant luminosity during each store. The third row, labelled "Triggered", contains the number of jets to be collected using the jet trigger.

The values in Table 7.2, which reflect the jet quenching model of the HYDJET event generator, show that the production rate of $E_{\mathrm{T}} > 100$ GeV jets is below the bandwidth limit (hence, all those events will be stored), while the events with less energetic jets will have to be pre-scaled, by factors around 10 and 2 for the 50 and 75 GeV jet trigger channels, respectively. We can also see that the gain in the number of jets at high E_{T} due to the jet trigger, compared to the minimum bias rates, will be more than two orders of magnitude. We will now present the benefit of the high-E_{T} trigger on the expected E_{T} reach of the jet spectra, for different PbPb centralities.

7.2.7 Jet E_{T} spectra reach

The left panel of Fig. 7.8 shows the simulated leading jet E_{T} distribution as collected after one month of PbPb running at the LHC (0.5 nb^{-1}), taking into account High Level Trigger bandwidths and jet quenching effects implemented in HYDJET. There are four different data sets contributing to this figure, collected with the minimum bias trigger and with the three different triggered samples, requiring jet E_{T} values above 50, 75 and 100 GeV. The relative integrals of these different contributions reflect the HLT bandwidth allocations. In particular,

Table 7.2: Number of jets (with axis within $|\eta| < 2$) above three different E_{T} thresholds, assuming 7.8 b inelastic PbPb cross-section and 0.5 nb^{-1} integrated luminosity. 15% of the total bandwidth was allocated to the minimum bias trigger and 11–12% to the individual triggered channels.

		Number of jets above:		
Centrality bin	Data taking mode	50 GeV	75 GeV	100 GeV
0–10%	Infinite bandwidth	2.27×10^7	3.71×10^6	9.67×10^5
	Minimum bias	7.86×10^4	1.28×10^4	3.35×10^3
	Triggered	2.02×10^6	1.79×10^6	9.67×10^5
10–20%	Infinite bandwidth	1.40×10^7	2.51×10^6	6.74×10^5
	Minimum bias	4.85×10^4	8.69×10^3	2.33×10^3
	Triggered	1.23×10^6	1.21×10^6	6.74×10^5
20–30%	Infinite bandwidth	1.03×10^7	1.98×10^6	6.29×10^5
	Minimum bias	3.57×10^4	6.85×10^3	2.18×10^3
	Triggered	9.22×10^5	9.54×10^5	6.29×10^5
30–40%	Infinite bandwidth	7.06×10^6	1.25×10^6	3.17×10^5
	Minimum bias	2.44×10^4	4.33×10^3	1.10×10^3
	Triggered	6.33×10^5	6.01×10^5	3.17×10^5
40–50%	Infinite bandwidth	4.84×10^6	9.30×10^5	2.78×10^5
	Minimum bias	1.68×10^4	3.22×10^3	9.62×10^2
	Triggered	4.34×10^5	4.48×10^5	2.78×10^5
50–60%	Infinite bandwidth	3.28×10^6	5.89×10^5	1.72×10^5
	Minimum bias	1.14×10^4	2.04×10^3	5.95×10^2
	Triggered	2.94×10^5	2.84×10^5	1.72×10^5
60–70%	Infinite bandwidth	1.87×10^6	3.68×10^5	9.92×10^4
	Minimum bias	6.47×10^3	1.27×10^3	3.43×10^2
	Triggered	1.68×10^5	1.78×10^5	9.92×10^4
70–80%	Infinite bandwidth	9.23×10^5	1.80×10^5	4.98×10^4
	Minimum bias	3.12×10^3	6.23×10^2	1.72×10^2
	Triggered	8.26×10^4	8.67×10^4	4.98×10^4
80–90%	Infinite bandwidth	3.96×10^5	7.24×10^4	1.82×10^4
	Minimum bias	1.37×10^3	2.52×10^2	6.29×10^1
	Triggered	3.55×10^4	3.49×10^4	1.82×10^4
Total	Infinite bandwidth	6.54×10^7	1.16×10^7	3.20×10^6
	Minimum bias	2.26×10^5	4.02×10^4	1.11×10^4
	Triggered	5.82×10^6	5.59×10^6	3.20×10^6

assigning 15% of the total bandwidth to minimum bias triggers, we should collect 13.5 million minimum bias events in one month. The original shape of the non-triggered distribution can be recovered by scaling the relative yields of the four data sets so that a smooth distribution is obtained. The scaling factors are determined by considering each pair of consecutive data sets and fitting the combined leading jet E_T spectrum with a power law in the joining region (see Fig. 7.8). It is worth noting that the optimal scaling factors can be determined

from the data distribution without any prior knowledge of the spectrum, simply minimising the χ^2 of the power-law fit.

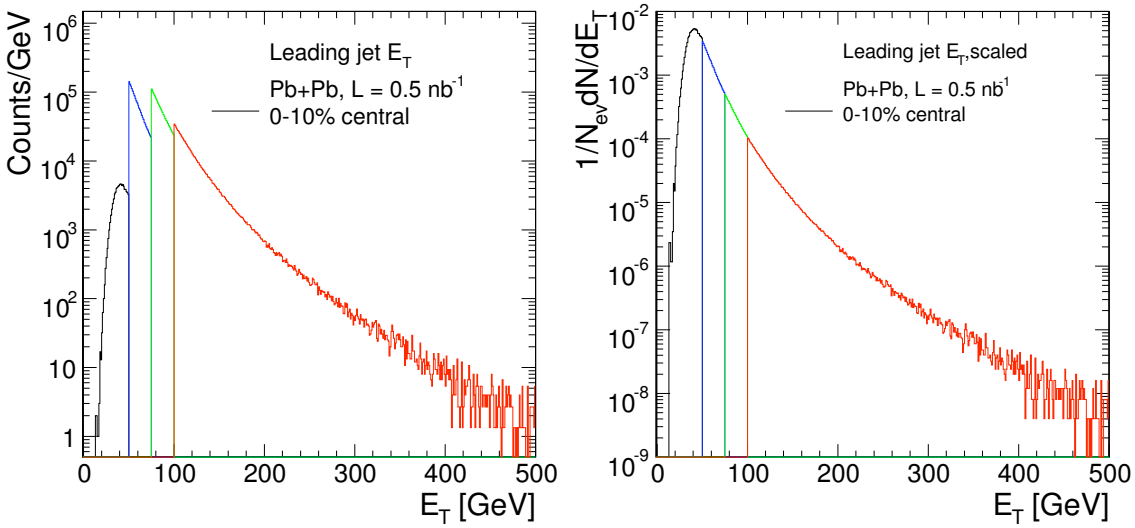

Figure 7.8: Left panel: Leading jet E_{T} distributions for one month PbPb running (0.5 nb^{-1}) taking into account the HLT bandwidth allocations: untriggered dataset (black) and triggered samples with E_{T} thresholds of 50, 75 and 100 GeV (blue, green and red, respectively). Right panel: The same distributions but normalised per event and scaled by appropriate factors to recover the shape of the non-triggered distribution, with much higher statistics.

This way, the shape of the minimum bias E_{T} spectrum is recovered, but with much larger statistics. The right panel of Fig. 7.8 shows these datasets scaled by the appropriate factors, and sliced into the intervals between trigger thresholds. Here, only the events generated for the dataset with 50 GeV threshold contribute to the histogram in the zone of leading jet transverse energies between 50 and 75 GeV, and so on. Figure 7.9 shows the corresponding inclusive jet E_T distributions.

With the effective integrated luminosity sampled by our HLT trigger settings, CMS can measure inclusive jet production up to $E_{\mathrm{T}} \approx 0.5$ TeV in central PbPb collisions at 5.5 TeV. Such a large E_{T} reach and statistics allow one to carry out detailed differential studies of jet quenching phenomena. A few examples are shown in the next sections.

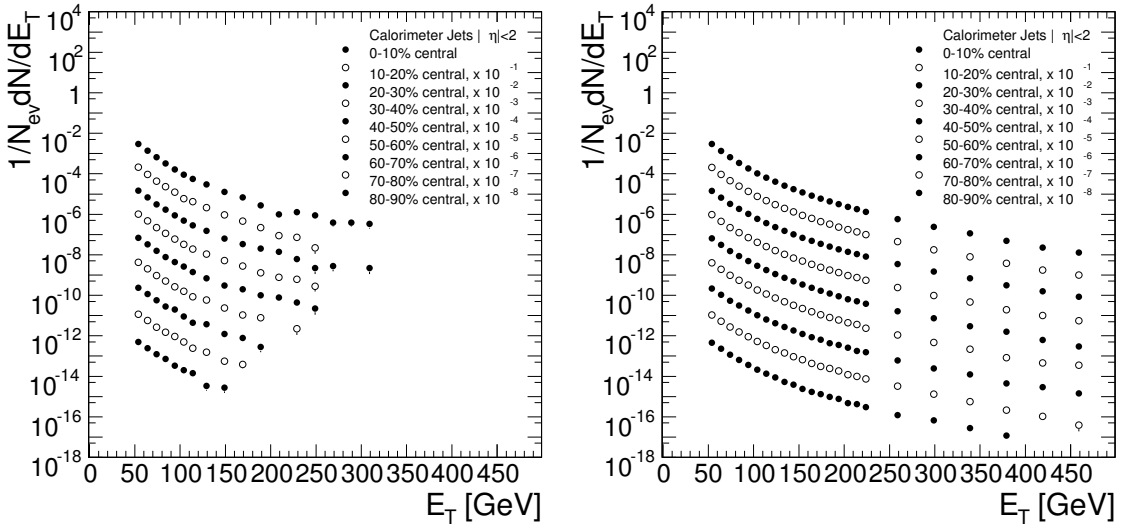

Figure 7.9: Inclusive jet E_T distributions in 10 centrality bins expected for PbPb (5.5 TeV) collisions with nominal integrated luminosity 0.5 nb^{-1}. The distributions for different centrality bins are offset by factors of 10 for illustration purposes. Left panel: Minimum bias. Right panel: Triggered data sets merged by the scaling procedure.

7.3 High-p_{T} hadrons

7.3.1 Introduction

Above $p_{\mathrm{T}} \approx 5$ GeV/c, hadron production is dominated by the fragmentation products of (semi)hard partons. In high-energy AA collisions, the momentum of the *leading* hadrons of the jets carry information on the amount of energy lost by the fragmenting parent parton. At RHIC, in central AuAu collisions, the suppression of hadron production at high transverse momenta (up to p_{T} = 20 GeV/c) has been one of the most important observables to study medium-induced parton energy loss (see Section 1.4.5). The measured suppression factor provides information on the initial gluon density and on the diffusion properties of the medium (quantified by the transport coefficient, $\langle\hat{q}\rangle$) [96, 220]. CMS can extend the transverse momentum reach of this measurement up to p_{T} = 300 GeV/c, in PbPb collisions, thanks to the large hard scattering cross sections at $\sqrt{s_{NN}}$ = 5.5 TeV, the high luminosity, the large acceptance of the CMS tracking system ($|\eta| < 2.5$) and the triggering capability on jets. The trigger is necessary to enhance particle yields at the highest transverse momenta reachable at LHC energies. In this section, we present the statistical reach expected for the measurement of inclusive charged hadron spectra in different PbPb centrality classes as well as in the nuclear modification factors, by making use of the powerful tracking capabilities of the CMS silicon tracker and the high-E_{T} jet trigger scheme discussed in the previous section.

7.3.2 Charged particle tracking efficiency

The reconstruction capabilities of the CMS Silicon Tracking System for charged particles with $p_{\mathrm{T}} > 0.8$ GeV/c have been studied in detail [165] using a full detector simulation, with the GEANT4-based detector simulation package OSCAR and the reconstruction package ORCA. Figure 7.10 shows the transverse momentum dependence of the obtained algorithmic tracking efficiency (left panel) and of the fake rate (right panel) in central (b = 0 fm, closed symbols) and peripheral (b = 9 fm, open symbols) PbPb collisions. A charged particle multiplicity

density of $\mathrm{d}N_{\mathrm{ch}}/\mathrm{d}y|_{y=0} = 3200$ is assumed for central reactions. In this high-multiplicity environment, an algorithmic *tracking* efficiency of at least 75% is achieved for all centralities, keeping the fake track rate for $p_{\mathrm{T}} > 1$ GeV/c below the 5% level. The charged particle reconstruction code developed for treating PbPb events requires, for particles to be reconstructible, that they deposit hits in all the three pixel layers, for trajectory seeding, and have a minimum of 8 hits in the full silicon tracker (pixel plus strip layers).

These geometrical requirements, convoluted with the probability that particles suffer nuclear interactions in the tracker material and, hence, fail to deposit the minimum number of hits in the silicon tracking system, give an efficiency of about 80% for charged particles in the tracker volume ($|\eta| < 2.5$). Folding in the algorithmic reconstruction efficiency, high p_{T} charged tracks have a global probability of $75\% \times 80\% = 60\%$ to be reconstructed.

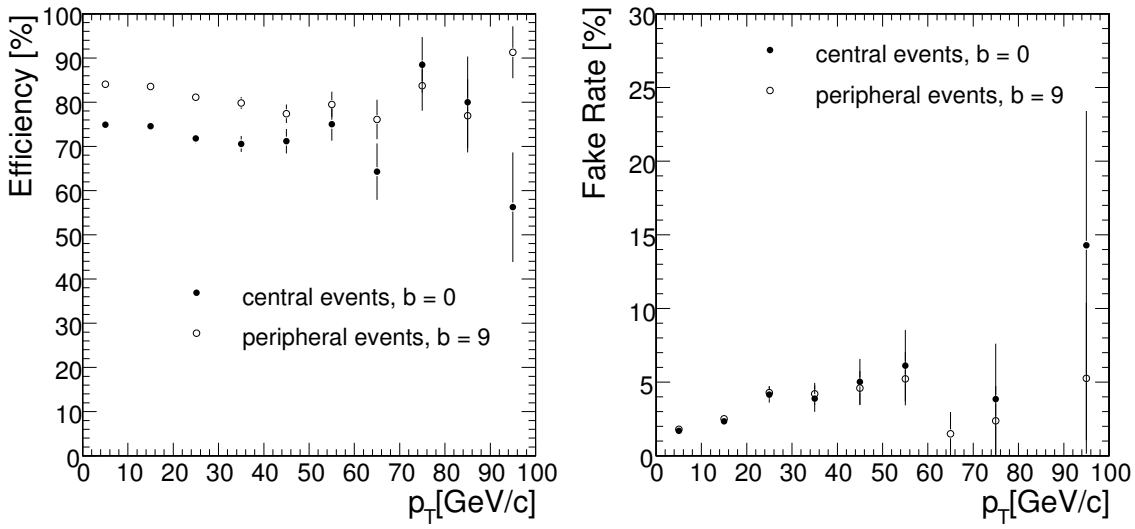

Figure 7.10: Algorithmic charged particle tracking efficiency (left panel) and fake rate (right panel), obtained from detailed OSCAR simulation and ORCA reconstruction for central (b=0, closed symbols) and peripheral (b=9 fm, open symbols) PbPb collisions [165].

In addition, as shown in Fig. 7.11, high-p_{T} tracks are reconstructed with excellent momentum resolution, $\Delta p_{\mathrm{T}}/p_{\mathrm{T}} < 1.5\%$ (for $p_{\mathrm{T}} < 100$ GeV/c), and with a track impact parameter resolution better than 50 μm at high p_{T}.

7.3.3 Results

The HYDJET model gives a factor of 4–5 suppression of the hadron yields at high p_{T} in central PbPb collisions at $\sqrt{s_{NN}}$ = 5.5 TeV, due to parton energy loss in the produced medium, with a decreasing amount of suppression with increasing impact parameter (i.e. when going from central to peripheral collisions). In order to determine the expected inclusive charged particle spectra and nuclear modification factors for different PbPb centrality classes, we use the HIROOT fast MC complemented with realistic parametrisations of the efficiencies, as obtained from full simulations. The total reconstruction efficiency for high-p_{T} charged tracks in the CMS silicon tracker is $\sim 60\%$, independently of p_{T}. The effect of this efficiency loss is simulated in our generator level study by randomly removing 40% of the generated tracks (in a p_{T}-independent way) and by applying a $1/0.6$ correction factor when getting the charged particle p_{T} spectrum. In addition, we also correct for the trigger efficiencies, by applying

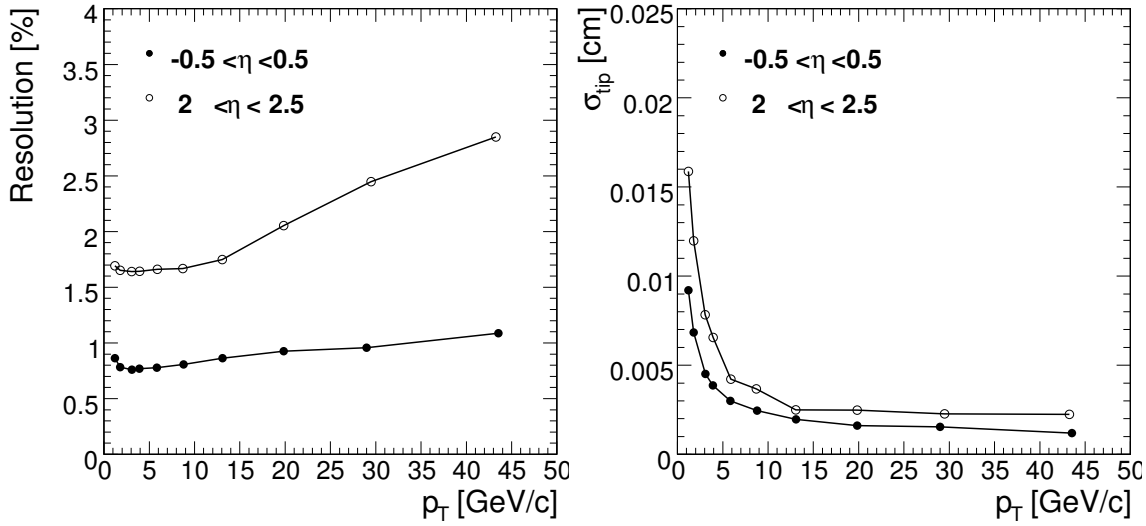

Figure 7.11: p_{T} dependence of the track transverse momentum resolution (left) and of the transverse impact parameter resolution (right) achieved in heavy ion events (with $\mathrm{d}N_{\mathrm{ch}}/\mathrm{d}y|_{y=0}$ = 3200) in the barrel (full symbols) and in the forward (open symbols) regions.

scaling factors obtained for each HLT trigger class. Data sets have been generated following the trigger requirements and containing the amount of jets (with E_{T} above the specific threshold of each class) expected for one month of PbPb data taking at design luminosity. The data sets are then combined in the way explained in the previous section, so that the statistical errors on the charged particle p_{T} spectrum realistically reflect the expected experimental situation after one month of data taking with the four different trigger conditions. In total, 7.2 million minimum bias events and 6.2 million triggered events were generated. The resulting spectra, as well as the $R_{AA}(p_{\mathrm{T}})$ and $R_{CP}(p_{\mathrm{T}})$ ratios are presented in the next sections.

Inclusive high-p_{T} spectra

Figure 7.12 shows the charged particle transverse momentum spectra in the four event classes discussed in the previous section (Section 7.2):

A) minimum bias events where the E_{T} of the leading jet is below 50 GeV;

B) triggered events where $50 < E_{\mathrm{T}}^{\mathrm{lead}} < 75$ GeV;

C) triggered events where $75 < E_{\mathrm{T}}^{\mathrm{lead}} < 100$ GeV;

D) triggered events where $E_{\mathrm{T}}^{\mathrm{lead}} > 100$ GeV.

Each histogram is corrected by the appropriate trigger scaling factor. Since the four (scaled) sets of simulated data, together, give the minimum bias set (as was shown for the leading jet distributions), the sum of the four histograms (represented by the closed black circles) gives the minimum bias charged particle distribution. The shape of this merged charged particle p_{T} spectrum is identical to the spectrum that would be obtained without the jet triggers from a data set of much larger statistics. Figure 7.13 shows the expected charged particle p_{T} spectra for the minimum bias (left) and merged triggered (right) data samples, in several

centrality bins. Using the jet-triggered data samples, CMS can measure with good efficiency the inclusive charged spectra up to $p_{\mathrm{T}} \approx 300$ GeV/c, in central PbPb collisions.

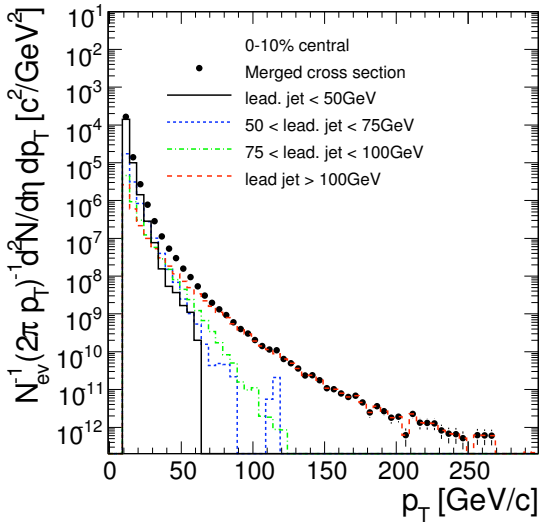

Figure 7.12: Charged particle transverse momentum distributions in the $|\eta| < 2.5$ window for the four event categories, selected according to the transverse energy of the highest E_{T} (leading) jet. The merged spectrum (closed black circles) has the same shape as the minimum bias spectrum but much larger statistics.

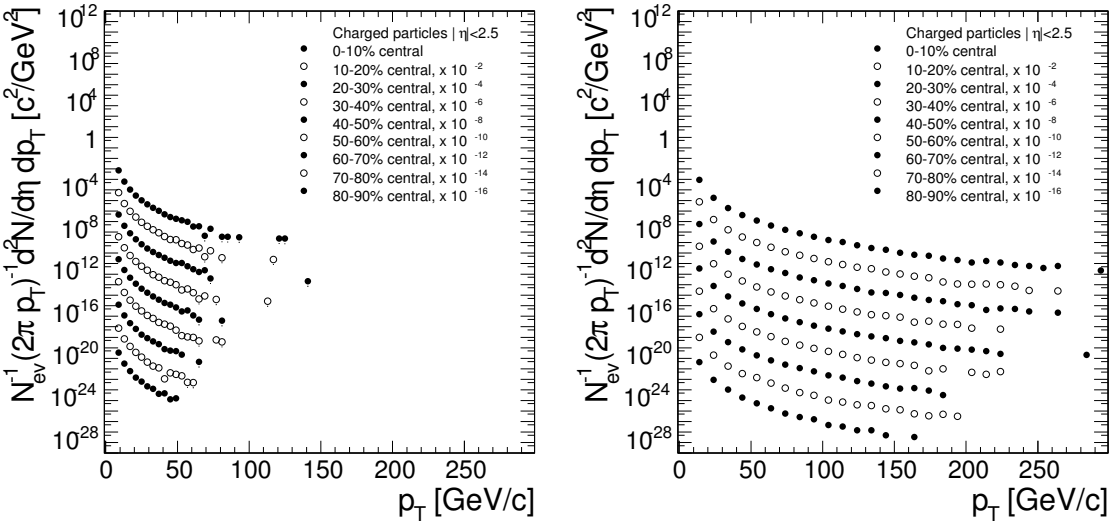

Figure 7.13: Charged particle p_{T} spectra expected for PbPb collisions at 5.5 TeV with nominal integrated luminosity (0.5 nb^{-1}), in 9 centrality bins, offset by factors of 100 for illustration purposes, only using the minimum bias triggered sample (left) and using also the jet-triggered data sets (right) merged following the procedure described in the text.

Nuclear modification factors

The nuclear modification factor, $R_{AA}(p_{\mathrm{T}}, \eta)$, and the central to peripheral ratio, $R_{CP}(p_{\mathrm{T}}, \eta)$, provide quantitative information on the level of the energy lost by hard scattered partons, and on its p_{T} and η dependence, as they traverse the high density QCD medium. The study

of $R_{AA}(p_{\rm T},\eta)$ and $R_{CP}(p_{\rm T},\eta)$ for leading hadrons provides important information on the (thermo)dynamical properties of the created plasma, namely the initial gluon rapidity density, $\mathrm{d}N_g/\mathrm{d}y$, and the transport coefficient, $\langle\hat{q}\rangle$ (see Section 1.4.5). These nuclear modification factors are defined as:

$$R_{AA}(p_{\rm T},\eta;b) = \frac{\sigma_{pp}^{\rm inel}}{\langle N_{\rm coll}\rangle}\frac{\mathrm{d}^2N_{AA}/\mathrm{d}p_{\rm T}\mathrm{d}\eta}{\mathrm{d}^2\sigma_{pp}/\mathrm{d}p_{\rm T}\mathrm{d}\eta}$$

$$R_{CP}(p_{\rm T},\eta;b) = \frac{\langle N_{\rm coll}^{\rm periph}\rangle}{\langle N_{\rm coll}^{\rm central}\rangle}\frac{\mathrm{d}^2N_{AA}^{\rm central}/\mathrm{d}p_{\rm T}\mathrm{d}\eta}{\mathrm{d}^2N_{AA}^{\rm periph}/\mathrm{d}p_{\rm T}\mathrm{d}\eta}$$

where $\langle N_{\rm coll}\rangle = \langle T_{PbPb}(b)\rangle \times \sigma_{pp}^{\rm inel}$ is the average number of binary nucleon-nucleon collisions in a given centrality class (with nucleus overlap function $\langle T_{PbPb}(b)\rangle$ at impact parameter b) obtained with a standard Glauber MC (see Ref. [52]).

R_{AA} quantifies the suppression (or enhancement) of hadron production with respect to pp collisions, which are considered as a baseline for the QCD vacuum. If there are no nuclear effects, the value of R_{AA} at high $p_{\rm T}$ should be unity. At LHC, no pp data will be available at $\sqrt{s_{NN}}$ = 5.5 TeV at the time of the first PbPb data taking and analysis. Thus, transverse momentum spectra of charged particles in pp collisions will be interpolated to this energy using next-to-leading-order (NLO) predictions constrained by the existing Tevatron data at 2 TeV and by the LHC results at 14 TeV [221]. The R_{CP} ratio, on the other hand, does not require a pp reference, as it compares central to peripheral heavy ion collisions. It is not equivalent to R_{AA}, since even the most peripheral heavy ion collisions are influenced by nuclear effects. Experimentally, the $p_{\rm T}$ reach of the R_{CP} ratio will be limited by the peripheral data set (denominator), where only relatively few jets are produced as they scale with the number of underlying nucleon-nucleon collisions and $\langle N_{\rm coll}^{\rm periph}\rangle \approx 23 \ll \langle N_{\rm coll}^{\rm cent}\rangle \approx 1556$. This is a practical limitation to the $p_{\rm T}$ range of the R_{CP} measurement.[1]

Figure 7.14 shows the final result for one month of PbPb running (0.5 nb^{-1}). The PYTHIA proton-proton spectrum, obtained with the same settings as the PYTHIA/PYQUEN part of the HYDJET generator (except, obviously, for the quenching part) has been consistently used here as reference (denominator) for the R_{AA} ratio. The R_{AA} nuclear modification factor is shown as a function of $p_{\rm T}$ for minimum bias (left panel) and for triggered data (right panel). The statistical errors limit the reach of the minimum bias data sample to $p_{\rm T} \approx 90$ GeV/c while values of $p_{\rm T} \approx 200$ GeV/c can be measured by applying the jet trigger with three different thresholds. This shows that the application of the jet trigger is clearly very useful for high statistics measurements of large transverse momentum charged particles. The actual suppression factor, $R_{AA} \approx 0.3$, shown in Fig. 7.14 reflects the specific implementation of the jet energy loss model in our HYDJET event generator, which is in the ballpark of other existing theoretical predictions (see Fig. 1.17).

Figure 7.15 shows our result for the $p_{\rm T}$ reach of the R_{CP} ratio for one month of data taking at nominal luminosity. Comparing the minimum bias sample (left panel) to the jet triggered sample (right panel), we conclude that triggering on jets extends the $p_{\rm T}$ range where R_{CP} is measurable very significantly, from $\sim$50 to $\sim$150 GeV/c.

It is important to note that the procedure to match and merge data from different data streams is not sensitive to details of the physics model chosen for jet quenching. It is also insensitive to the precise knowledge of the jet energy resolution (by construction, the scale

[1] A possible extension of the present work is the study of a triggering scheme combining centrality and jet energy, to enhance the yield of peripheral events with produced jets.

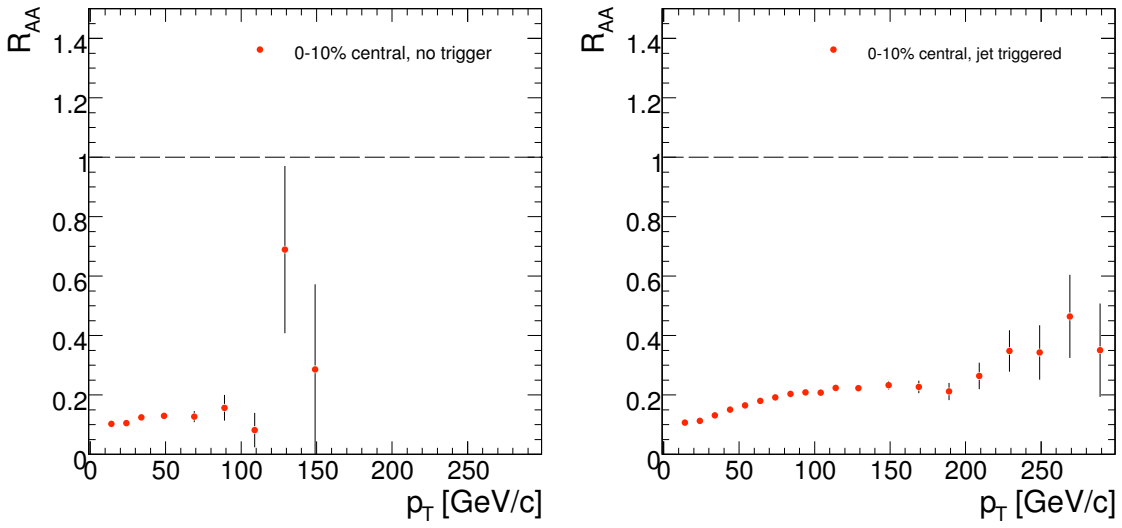

Figure 7.14: Expected statistical reach for the nuclear modification factor, $R_{AA}(p_{\mathrm{T}})$, for inclusive charged hadrons in central PbPb collisions generated with HYDJET for a nominal integrated luminosity of 0.5 nb^{-1}, for minimum bias data (left panel) and for data triggered on high-E_{T} jets (right panel).

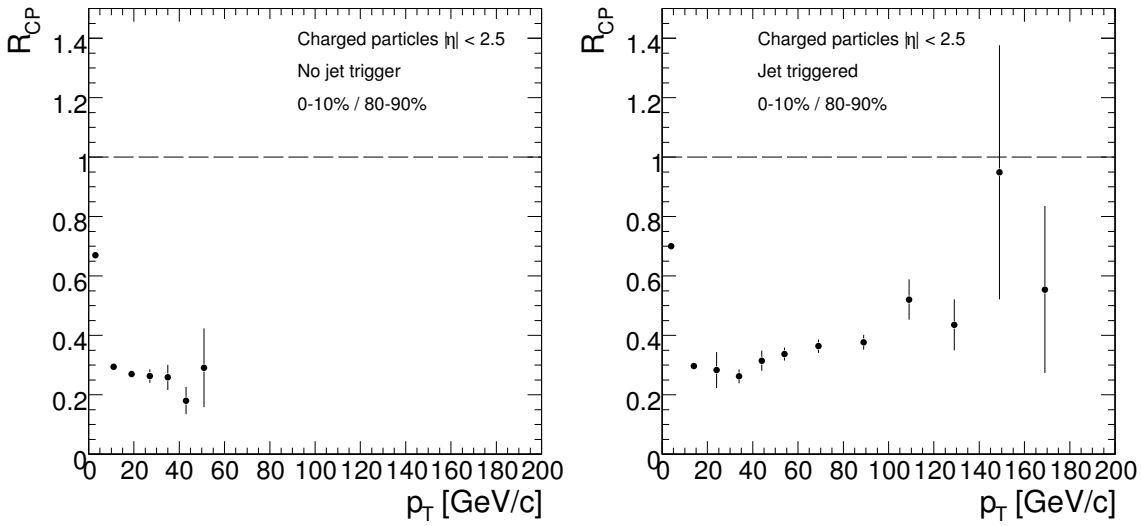

Figure 7.15: Same as previous figure but for the central-to-peripheral ratio, $R_{CP}(p_{\mathrm{T}})$.

factors do not depend on the jet energy resolution), as long as the jet energy resolution is not extremely poor. Other observables, like the jet E_{T} spectra and the jet fragmentation functions, are much less robust against poor knowledge of the jet reconstruction performance. Because of their robustness, the measurements presented here are likely to be the first ones to emerge from the PbPb data analyses, related to jet quenching phenomena.

7.3.4 Jet fragmentation function

We have seen in previous sections that CMS can measure jets up to $E_{\mathrm{T}} \approx 500$ GeV and leading hadrons up to $p_{\mathrm{T}} \approx 300$ GeV/c. We can exploit such large 'dynamical range' to study in detail the properties of the effects of parton energy loss on the "jet fragmentation function"

(JFF), $D(z)$, defined as the probability for a given product of the jet fragmentation to carry a fraction z of the jet transverse energy, E_{T}. In nuclear (AA) interactions, the JFF for *leading* hadrons (i.e. the hadron carrying the largest fraction of the jet momentum) can be written as [222]:

$$D(z) = \int\limits_{z\cdot p_{\mathrm{T}\,\mathrm{min}}^{\mathrm{jet}}} d(p_{\mathrm{T}}^{h})^2 \mathrm{d}y \mathrm{d}z' \frac{\mathrm{d}N_{\mathrm{AA}}^{\mathrm{h(k)}}}{\mathrm{d}(p_{\mathrm{T}}^{h})^2 \mathrm{d}y \mathrm{d}z'} \delta\left(z - \frac{p_{\mathrm{T}}^{h}}{p_{\mathrm{T}}^{\mathrm{jet}}}\right) \Bigg/ \int\limits_{p_{\mathrm{T}\,\mathrm{min}}^{\mathrm{jet}}} \mathrm{d}(p_{\mathrm{T}}^{\mathrm{jet}})^2 \mathrm{d}y \frac{dN_{\mathrm{AA}}^{\mathrm{jet(k)}}}{\mathrm{d}(p_{\mathrm{T}}^{\mathrm{jet}})^2 \mathrm{d}y}\,, \quad (7.1)$$

where $p_T^h \equiv z p_{\mathrm{T}}^{\mathrm{jet}} = z' p_{\mathrm{T}}$ is the transverse momentum of a leading hadron, z' is the hadron momentum fraction relative to the p_{T} of the parent parton (i.e. without energy loss $z = z'$ in leading order pQCD), $p_{T\,\mathrm{min}}^{\mathrm{jet}}$ is the minimum momentum threshold of observable jets, and $(\mathrm{d}N_{\mathrm{AA}}^{\mathrm{jet(k)}})/(\mathrm{d}(p_{\mathrm{T}}^{\mathrm{jet}})^2\mathrm{d}y)$ and $(\mathrm{d}N_{\mathrm{AA}}^{\mathrm{h(k)}})/(\mathrm{d}(p_{\mathrm{T}}^{\mathrm{h}})^2\mathrm{d}y\mathrm{d}z')$ are the yields of k-type jets ($k = q, g$) and "jet-induced" hadrons, respectively. Comparison of the JFF in nuclear and pp collisions (or in central and peripheral nuclear interactions) yields information about the in-medium modification of the JFF.

The leading hadron in a jet can be a charged hadron or a neutral pion. As described previously, the CMS tracking system can measure with high efficiency the high-p_{T} (leading) charged hadrons. Detecting energetic neutral pions in jets is more challenging since at high enough transverse momentum (above ≈ 15 GeV/c), the two photons from the π^0 decay fall into a single crystal of the CMS electromagnetic calorimeter, and traditional techniques for reconstructing the π^0's using $\gamma\,\gamma$ invariant mass analysis fail. However, such merged electromagnetic clusters can still be identified as a leading π^0 with relatively large efficiency [223] using cluster-shape analysis in the central barrel and using the preshower in the endcaps.

A significant softening of the JFF, determined by the absolute value of medium-induced partonic energy loss and the angular radiation spectrum, has been predicted for heavy-ion collisions at the LHC [222, 224]. Figure 7.16 shows JFF's with and without partonic energy loss simulated with PYTHIA [162]. The one with energy loss has been computed for central PbPb collisions using the PYQUEN energy loss model [177, 209]. The jet energy was determined as the total transverse energy of the final particles collected around the direction of the leading particle inside the cone of radius $R = \sqrt{\Delta\eta^2 + \Delta\varphi^2} = 0.5$, where η and φ are the pseudorapidity and the azimuthal angle, respectively. Extra cuts of $|\eta^{\mathrm{h}}| < 2.4$, $|\eta^{\mathrm{jet}}| < 3$ and $E_{\mathrm{T}}^{\mathrm{jet}} > 100$ GeV were applied. The number of entries and the statistical errors correspond to the estimated jet rate in central PbPb collisions for one month of LHC running (first row in Table 7.2). A concurrent study of the possible softening of the JFF and suppression of the absolute jet rates due to in-medium gluon bremsstrahlung out of jet cone can be carried out in order to differentiate between various energy loss mechanisms (small-angle radiation versus wide-angle radiation and collisional loss) [222]. Significant softening of the JFF without substantial jet rate suppression would be an indication of small-angle gluon radiation dominating the medium-induced partonic energy loss. Increasing the contribution from wide-angle gluon radiation and collisional energy loss leads to jet rate suppression with less pronounced softening of the JFF. If, instead, the contribution of the "out-of-cone" jet energy loss is large enough, the jet rate suppression may be even more significant than the JFF softening.

Note that, in the real experimental situation, the jet observables will be sensitive to the accuracy of the jet energy reconstruction, in particular to the systematic jet energy loss. However, since the average reconstructed jet energy in PbPb collisions is expected to be about the same as in pp interactions [215, 216], the reduced jet energy measurement will be a well-controlled

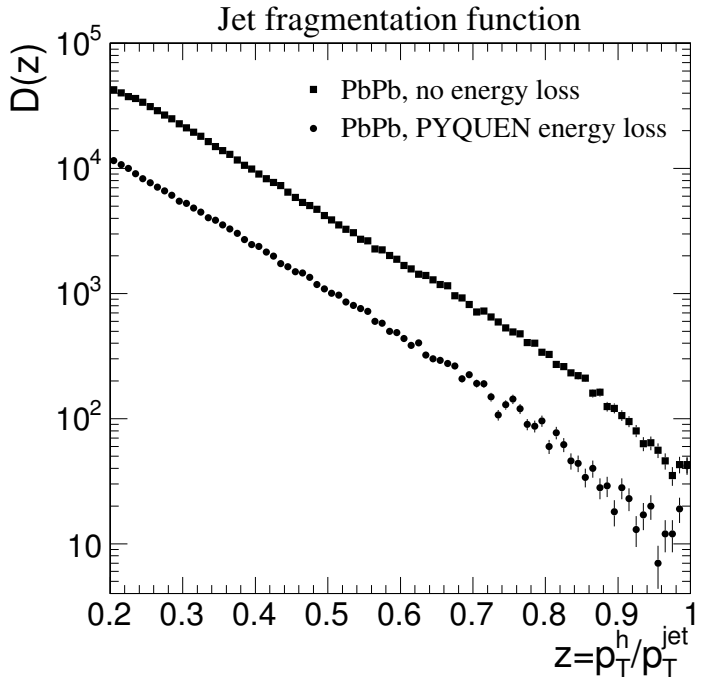

Figure 7.16: Jet fragmentation function for leading hadrons with $|\eta^{\mathrm{h}}| < 2.4$, $|\eta^{\mathrm{jet}}| < 3$ and $E_{\mathrm{T}} > 100$ GeV in central PbPb collisions for the cases without (squares) and with (circles) partonic energy loss. The number of histogram entries and statistical errors correspond to the estimated jet rate in most central PbPb collision for one month of LHC run.

systematic error, for heavy-ion data as well as for pp collisions, and it can be taken into account using the standard calibration procedure.

7.3.5 Summary

The high-p_{T} charged particle reconstruction capabilities using the CMS Silicon Tracking System have been evaluated using a full detector simulation, assuming a charged particle density in central PbPb collisions of $\mathrm{d}N_{\mathrm{ch}}/\mathrm{d}y|_{y=0}$ = 3200. In this high-multiplicity environment, a p_{T}-independent algorithmic tracking efficiency of about 75% is achieved with only a few percent fake track rate for $p_{\mathrm{T}} > 1$ GeV/c. Tracks are reconstructed with excellent momentum resolution, $\Delta p_{\mathrm{T}}/p_{\mathrm{T}} < 1.5\%$ (for $p_{\mathrm{T}} < 100$ GeV/c). The proposed high level jet trigger enhances the statistics of high-p_{T} particle spectra significantly. The p_{T} reach of the measured inclusive spectra and nuclear modification factors can be extended from about p_{T} = 90 GeV/c to about 300 GeV/c in central PbPb collisions, allowing precise differential studies of the expected high-p_{T} suppression pattern due to parton energy loss in the hot and dense medium produced in the reaction (such as medium-modified JFFs), and providing crucial information on the thermodynamical and transport properties of the system.

7.4 Jet tagging

An ideal direct probe of in-medium parton energy loss in high-energy nucleus-nucleus collisions is provided by hard processes where a high-p_{T} jet is tagged by an "unquenched" (i.e. not strongly interacting) particle such as a prompt γ or a $\gamma^{\star}/Z^0$ decaying into dileptons (see Fig. 7.17). The advantage of such processes is that the initial transverse momentum of the hard jet can be determined since at LO $p_{\mathrm{T}}^{\mathrm{jet}} \approx p_{\mathrm{T}}^{\gamma,Z^0}$, and the energy lost by the parton in the QCD medium can be directly estimated. The dependence of the energy loss per unit length, dE/dx, on the initial jet energy or on the distance traversed through the medium can then be measured by varying the energy of the tagged (virtual) photon or Z^0 in collisions of different nuclei or as a function of centrality.

The production of high-mass virtual photons, γ^*, and Z^0 bosons in association with hadronic jets is, for the first time, energetically feasible in heavy-ion collisions at the LHC [114, 225], with reasonable cross sections (see Fig. 7.20, below). In this section, we present a generator-level study with basic CMS acceptance cuts on the expected signal and backgrounds for different observables related to jets (or high-p_{T} hadrons) produced opposite a gauge boson decaying into a muon pair.

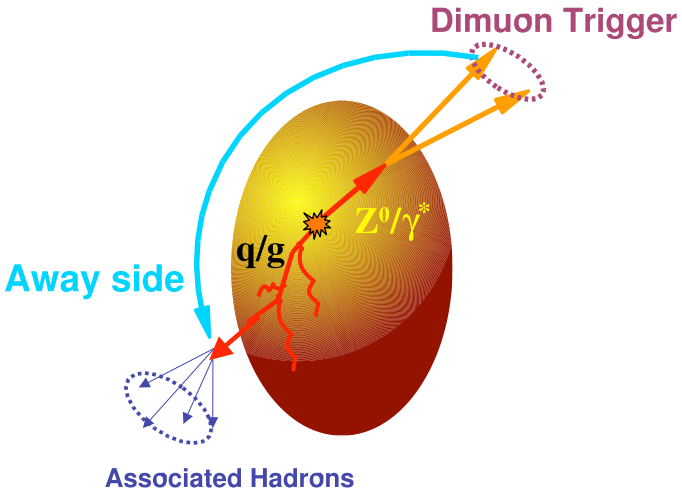

Figure 7.17: Cartoon illustrating the $Z^0/\gamma^*(\rightarrow \mu^+\mu^-)+$ (quenched) jet azimuthal geometry.

7.4.1 γ + jet studies

Obtaining precise information on parton energy loss via the study of jet-jet correlations (or leading hadron-hadron correlations, as done at RHIC [226]) is not trivial because both hard scattered partons can potentially be affected by the medium and the *initial* energy of both jets is, in principle, unknown. An alternative measurement suggested by Wang and collaborators [227, 228] was to study the hadron momentum fraction distribution, $z = p_{\mathrm{T}}^{\mathrm{hadron}}/p_{\mathrm{T}}^{\gamma}$, in γ+jet processes. Replacing the hadronic probe on one side by an electromagnetic probe, it is possible to measure the p_{T} of the initial hard scattering since $\vec{p}_{\mathrm{T}}^{\,\mathrm{jet}} \approx -\vec{p}_{\mathrm{T}}^{\,\gamma}$. The relation is valid at leading order up to k_{T} effects, where k_{T} is the intrinsic transverse momentum of the initial partons. The jet is then considered to be tagged (γ-tag). The direct photon couples weakly with the medium and conserves its initial kinematics while, on the other side, the parton loses energy (by collisions, gluon radiation) and will be attenuated. Precise studies of the medium-modified leading hadron fragmentation functions are thus accessible in the γ+

jet channel [113, 229]. In addition, since the dominant channel for high p_{T} γ + jet production is $qg \rightarrow q\gamma$, the bulk of the jets detected in this channel originate from *quarks*. Therefore, at variance with the dominant *gluon* scattering in dijet production below $E_{\mathrm{T}} \approx 100$ GeV, the $\gamma+$ jet process makes it possible to directly study quark energy loss and thus test the expected colour Casimir-factor dependence of QCD bremsstrahlung, see Eqs. (1.3) and (1.4).

An example of the expected E_{T} "imbalance" between a γ and a quenched jet in PbPb collisions at the LHC is shown in Fig. 7.18, from Refs. [230, 231]. Both the γ and the jet have $E_{\mathrm{T}}^{\gamma/\mathrm{jet}} > 120$ GeV and are produced at central rapidities ($|y_{\gamma}, y_{\mathrm{jet}}| < 1.5$) for three different "jet quenching" scenarios, depending on the average parton energy losses at $y = 0$: (i) $\langle \Delta E_g \rangle \simeq 0$ (no quenching); (ii) $\langle \Delta E_g \rangle \simeq 9$ GeV; (iii) $\langle \Delta E_g \rangle \simeq 18$ GeV. Initial state gluon radiation and finite jet energy resolution have been taken into account. Without parton energy loss, the difference $E_{\mathrm{T}}^{\gamma} - E_{\mathrm{T}}^{\mathrm{jet}}$ is relatively broad but symmetric. With increasing energy loss, the distribution becomes more skewed as $E_{\mathrm{T}}^{\gamma} - E_{\mathrm{T}}^{\mathrm{jet}}$ grows larger.

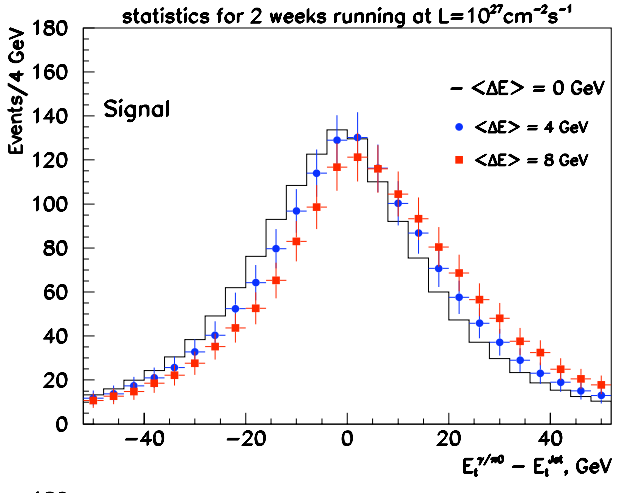

Figure 7.18: Distribution of E_{T} "imbalance" between the γ and jet with $E_{\mathrm{T}}^{\gamma}, E_{\mathrm{T}}^{\mathrm{jet}} > 120$ GeV, at mid-rapidity ($|y| < 1.5$), for different values of the leading parton energy loss [230, 231]. The statistical errors correspond to those expected for a two week run at $\mathcal{L} = 10^{27}\mathrm{cm}^{-2}\mathrm{s}^{-1}$ with HLT triggering.

7.4.2 Z^0- and γ^*-tagged jet studies

A drawback of the $\gamma+$ jet measurement presented in the previous section, is the difficulty of prompt photon identification. At variance with the proton-proton case, and due to the large particle multiplicities in AA interactions, in general no isolation criteria can be applied to identify prompt photons from the underlying event. Several instrumental and analysis factors conspire to make this measurement relatively challenging: random pairing of a direct photon with a decay γ to give an invariant mass consistent with a π^0; two photons from a high-p_{T} π^0 merging into a single cluster in the ECAL; and others. In addition, direct photons can also be produced by the collinear fragmentation of a hard quark or gluon [232]. Thus their inclusive cross section can also (potentially) be affected by medium-induced attenuation [233], blurring their use as a clean calibration of the opposing jet.

Alternatively, the processes $qq \rightarrow q\gamma^*$ or $qq \rightarrow qZ^0$ with *dilepton+jet* as the experimental signature, overcome all the drawbacks of the $\gamma+$ jet analysis while keeping the 'golden channel'

characteristic of an unbiased measure of the original energy of the hard-scattered parton. The only disadvantage is the significantly lower cross section relative to γ+jet (see Fig. 7.20, below). While the reaction $gq \rightarrow qZ^0$ is a small contribution to the total Z^0 yield [46], it is a more distinctive signature than the $gq \rightarrow q\gamma$ channel since the Z^0 is free from the high background of hadronic decays contributing to the direct photon spectrum [160]. The transverse momentum imbalance in γ^*/Z^0+ jet production due to interactions of the parent parton in the medium has been studied [114] for $\mu^+\mu^-+$ jet, as has the correlation between the $\mu^+\mu^-$ pair and the leading particle in a jet. The average fraction of the parent parton energy carried by a leading hadron at these energies is $z \approx 0.2$. Figure 7.19 shows the difference between the transverse momentum of a $\mu^+\mu^-$ pair, $p_{\mathrm{T}}^{\mu^+\mu^-}$, and five times the transverse energy of the leading particle in a jet (since $z \approx 0.2$) for minimum bias PbPb collisions at 5.5 TeV. The process was simulated with COMPHEP /PYTHIA [162, 234] with and without partonic energy loss as parameterised in the PYQUEN model [177, 209]. The CMS acceptance cuts, $|\eta^{\mu}| < 2.4$, $|\eta^{\mathrm{jet}}| < 3$, $p_{\mathrm{T}}^{\mu} > 5$ GeV/c, $p_{\mathrm{T}}^{\mu^+\mu^-} > 50$ GeV/c and $E_{\mathrm{T}}^{\mathrm{jet}} > 50$ GeV, have been applied. The jet energy was determined as the total transverse energy of the final particles collected around the direction of a leading particle inside a cone $R = \sqrt{\Delta\eta^2 + \Delta\varphi^2} = 0.5$, where η and φ are the pseudorapidity and azimuthal angle, respectively. Despite the fact that the initial distribution is smeared and asymmetric due to initial-state gluon radiation, hadronization effects, etc., we can clearly see the additional smearing and the displaced mean and maximum values of the p_{T} imbalance due to partonic energy loss. The p_{T}-imbalance between the $\mu^+\mu^-$ pair and a leading particle in a jet is directly related to the absolute value of partonic energy loss, and almost insensitive to the form of the angular spectrum of the emitted gluons or to the experimental jet energy resolution.

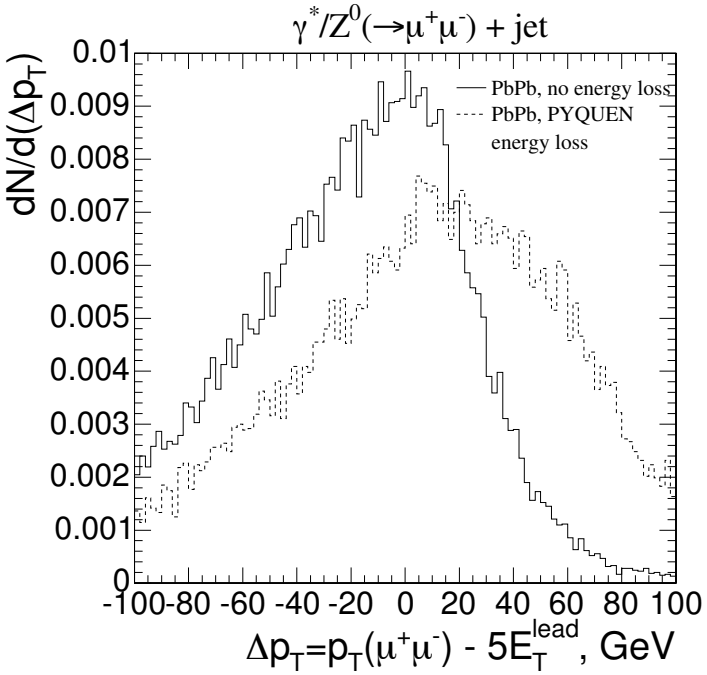

Figure 7.19: The distribution of the difference between the transverse momentum of a $Z^0/\gamma^* \rightarrow \mu^+\mu^-$ pair, $p_{\mathrm{T}}^{\mu^+\mu^-}$, and five times the transverse energy of the leading particle in a jet, $5\,E_{\mathrm{T}}^{\mathrm{lead}}$, in minimum bias PbPb collisions at 5.5 TeV with (dashed histogram) and without (solid histogram) parton energy loss [114]. See text for the kinematic cuts.

Medium-modified jet "fragmentation functions"

The production channels $q\overline{q} \rightarrow \gamma^*/Z^0 g$ (annihilation) and $gq \rightarrow \gamma^*/Z^0 q$ (Compton scattering) with the subsequent decay $\gamma^*/Z^0 \rightarrow l^- l^+$ ($l = e, \mu$) and the fragmentation of the parton $q/g \rightarrow$ jet (Fig. 7.17) are useful tools for determining the jet "fragmentation function" constructed from the normalised yields of associated hadrons produced opposite (in the "away-side" azimuthal hemisphere) the Z^0/γ^* as a function of the variable $z = p_T^{\rm assoc}/p_T^{\rm trigger}$,

$$D(z) = \frac{1}{N_{\rm trigger}} \frac{{\rm d}N_{\rm away}}{{\rm d}z}\bigg|_{p_{\rm T}^{\rm trigger}{}_{\rm fixed}} \tag{7.2}$$

where the variables are described below. On an event-by-event basis, dileptons (*trigger*) coming from Z^0/γ^* decays are identified and paired with all *associated hadrons* within different momentum ranges from the same event. The overall azimuthal distribution per trigger particle is defined as

$$N(\Delta\phi) = \frac{\sum_{\rm event} N_{\rm pairs}(\Delta\phi)}{\sum_{\rm event} N_{\rm trigger}} \ , \tag{7.3}$$

where $\Delta\phi = \phi^{\rm trigger} - \phi^{\rm assoc}$. The $N(\Delta\phi)$ distributions are generated for a fixed $p_{\rm T}^{\rm trigger}$ interval and several $p_{\rm T}^{\rm assoc}$ intervals. After identifying the away-side ($\Delta\phi \sim \pi$) jet component, the dependence of the $N_{\rm away}$ yield can be computed for a fixed $p_{\rm T}^{\rm trigger}$ interval, as in Eq. (7.2). This distribution contains all the hadronic fragments of the initial parton, including the hadrons from the fragmentation of medium-induced gluon radiation of the parton. Thus $D(z)$ is not the same as the vacuum fragmentation function measured in e^+e^- collisions, though this identification is typically assumed.

The analysis can be performed in azimuth (in the plane perpendicular to the beam axis) and in rapidity (along the beam axis), but only the principles of the azimuthal analysis are discussed here. Only muons are considered with cuts, where mentioned, imposed by the CMS muon detector ($p > 3.5$ GeV/c and $|\eta| < 2.4$). Dielectrons can also be used to increase the signal statistics as well as to reduce the systematic uncertainties of the measurement (the branching ratios for both signal and background decays into electrons and muons are equal). However, the capabilities of the CMS electromagnetic calorimeter for dielectron measurements in the high multiplicity heavy-ion environment have not yet been investigated.

Expected signal yields

The following discussion considers PbPb collisions at $\sqrt{s_{NN}}$ = 5.5 TeV with nominal luminosity, $\mathcal{L} = 5 \times 10^{26}$ cm^{-2}s^{-1}. A runtime of 10^6 s is used, corresponding to one month of collisions at 50% efficiency, giving an integrated luminosity of 0.5 nb^{-1}. The Z^0/γ^*+ jet rates in PbPb collisions are obtained from the pp cross sections, evaluated with the PYTHIA 6.32 event generator [235] (default parameters and CTEQ5M PDFs), via $\sigma_{AA} = A^2\sigma_{pp}$. In order to reduce the MC generation time, all PYTHIA processes were turned off (`MSEL=0`) except $q\overline{q} \rightarrow Z^0/\gamma^* g$ (`ISUB=15`) and $qg \rightarrow Z^0/\gamma^* q$ (`ISUB=30`). The Z^0 (`MSTP(43)=2`) and $\gamma*$ (`MSTP(43)=1`) contributions were separated. To obtain good statistics at high transverse momentum, 10 000 events were simulated in 10 GeV/c wide $\widehat{p}_{\rm T}$ bins between 10 and 300 GeV/c. Each bin was afterwards scaled by its corresponding cross section and added to the rest of the bins to give the final signal spectra. Only dimuon decays were selected, BR($Z^0/\gamma^* \rightarrow \mu^+\mu^-$) = 3.36%, and only dimuons with individual muon $p_{\rm T}$ high enough to pass the CMS acceptance momentum and pseudorapidity cuts were kept ($p >$3.5 GeV/c and $|\eta| < 2.4$).

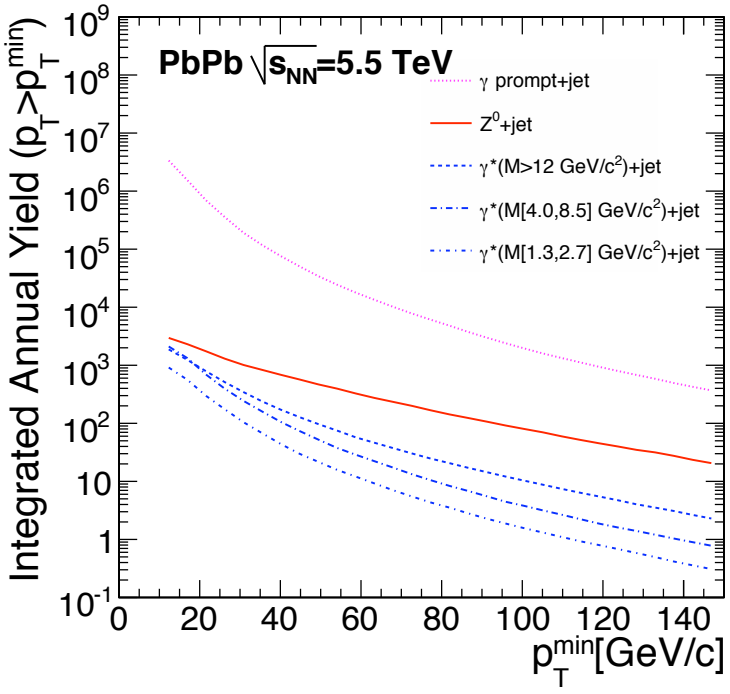

Figure 7.20: Integrated annual yield of tagged jets in PbPb at $\sqrt{s_{NN}}$ =5.5 TeV for 0.5 nb^{-1} integrated luminosity, as a function of the lower bound $p_{\mathrm{T}}^{\mathrm{min}}$. The lines depict γ tags and dimuon tags from Z^0 and γ^* for different dilepton invariant mass, M, intervals.

The results of the PYTHIA simulations are presented in Fig. 7.20, which shows the total integrated yield above the corresponding $p_{\mathrm{T}}^{\mathrm{min}}$ for Z^0+ jet and γ^*+ jet (three different mass windows). The γ+jet yield is also shown, for comparison. The highest mass interval, above 12 GeV/c^2, is PYTHIA's default. As reference, we also show two lower mass windows: between the light-quark resonances (η, ϕ) and the J/ψ mass; and between the ψ' and Υ masses.

In Table 7.3 we list the integrated dimuon+jet yields expected with the nominal integrated PbPb luminosity for four values of p_T^{min}, from Fig. 7.20. The lower limit on the dimuon p_T is the value for which we can reasonably well reconstruct the back-to-back leading hadron, knowing that, on average, the leading hadrons carry $\approx 20\%$ of the initial parton p_T.

Dimuon backgrounds

The main source of dimuon background is the combinatorial background from decays of D and $\overline{\mathrm{D}}$ (charm) and B and $\overline{\mathrm{B}}$ (bottom) mesons. Dijets can also contribute through hadrons

Table 7.3: Integrated annual yield of dimuon tags from Z^0 and γ^* for different invariant mass, $M_{\mu^+\mu^-}$, intervals in PbPb at $\sqrt{s_{NN}}$ = 5.5 TeV and 0.5 nb^{-1} integrated luminosity, for four minimum p_{T} values, $p_{\mathrm{T}}^{\mathrm{min}}$.

p_T^{min}(GeV/c)	10	20	30	50
$Z^0 \rightarrow \mu^+\mu^-$	3000	1800	900	500
γ^* ($M_{\mu^+\mu^-}$ >12 GeV/c^2)	1900	750	300	90
γ^* ($M_{\mu^+\mu^-}$[4.0,8.5] GeV/c^2)	2100	750	200	40
γ^* ($M_{\mu^+\mu^-}$[1.3,2.7] GeV/c^2)	900	300	100	20

that are not stopped in the hadron absorber and are misidentified as muons in the muon chambers, as well as through kaon and pion decays to muons (see Section 6.1). The semileptonic decays $D\overline{D}/B\overline{B} \rightarrow l^+l^- + X$ produce dileptons with branching ratios $\sim 10.5\%$ [236], that overlap with the real dilepton signal from Z^0/γ^* decays. In order to estimate the effect of this background, we have used, as in previous studies [47], the HVQMNR [237] code (with the CTEQ6M parton distribution functions [238]) which calculates heavy quark production at next-to-leading order (NLO). The azimuthal distributions of the heavy quark pairs (and corresponding decay dileptons) are peaked closer to $\phi = \pi$ for the more massive bottom quarks than for charm. The HVQMNR input parameters are listed in Table 7.4. The parameters ξ_F and ξ_R determine the proportionality of the factorisation and the renormalisation scales, respectively, to a default scale μ_0: $\mu_F = \xi_F \mu_0$ and $\mu_R = \xi_R \mu_0$. For double differential distributions, $\mu_0 = (m_Q^2 + \langle p_T^2 \rangle)^{1/2}$, where m_Q is the quark mass and $\langle p_T^2 \rangle$ is the average of the Q and $\overline{Q}$ squared transverse momentum. For single inclusive distributions, $\mu_0 = (m_Q^2 + p_T^2)^{1/2}$.

Table 7.4: Parameters used in HVQMNR: $\langle k_T \rangle$ is the mean intrinsic momentum, ϵ is the parameter in the Peterson fragmentation function [239], and ξ_F and ξ_R are factorisation and the renormalisation scale factors respectively.

	m_Q (GeV/c^2)	$\langle k_T \rangle$ (GeV/c)	ϵ	ξ_F	ξ_R
charm	1.5	1.0	0.06	1.0	1.0
bottom	4.75	1.0	0.006	1.0	1.0

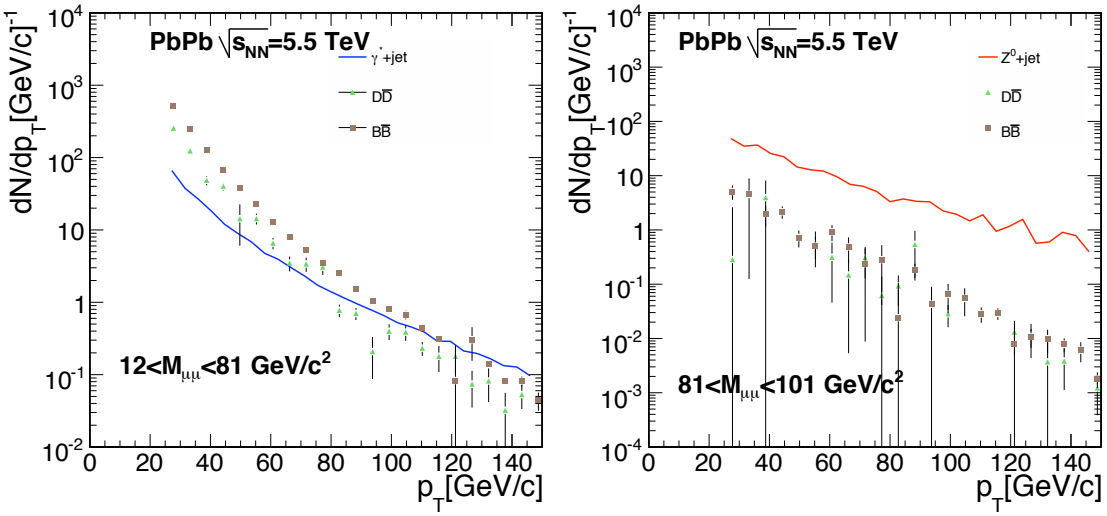

Figure 7.21: Annual dimuon yield for signal and background dimuons in two mass windows: from 12 to 81 GeV/c^2 (left) and from 81 to 101 GeV/c^2 (right) in minimum bias PbPb collisions at 5.5 TeV with integrated luminosity 0.5 nb^{-1}. The error bars are only statistical.

The D and B background combined with the Z^0/γ^* signal dimuons are shown in Fig. 7.21, as a function of $p_T^{\mu^+\mu^-}$, for two different invariant mass cuts: $12 < M_{\mu^+\mu^-} < 81$ GeV/c^2 (left panel) and $81 < M_{\mu^+\mu^-} < 101$ GeV/c^2 (in the Z^0 mass region, right panel).

Figure 7.22 shows the dimuon invariant mass distribution for the Z/γ^*−jet signal on top of the heavy-quark decay muon background. At low invariant mass the continuum dimuons are overwhelmed by the heavy-meson decays but in the Z^0 mass region the Z^0 peak is well

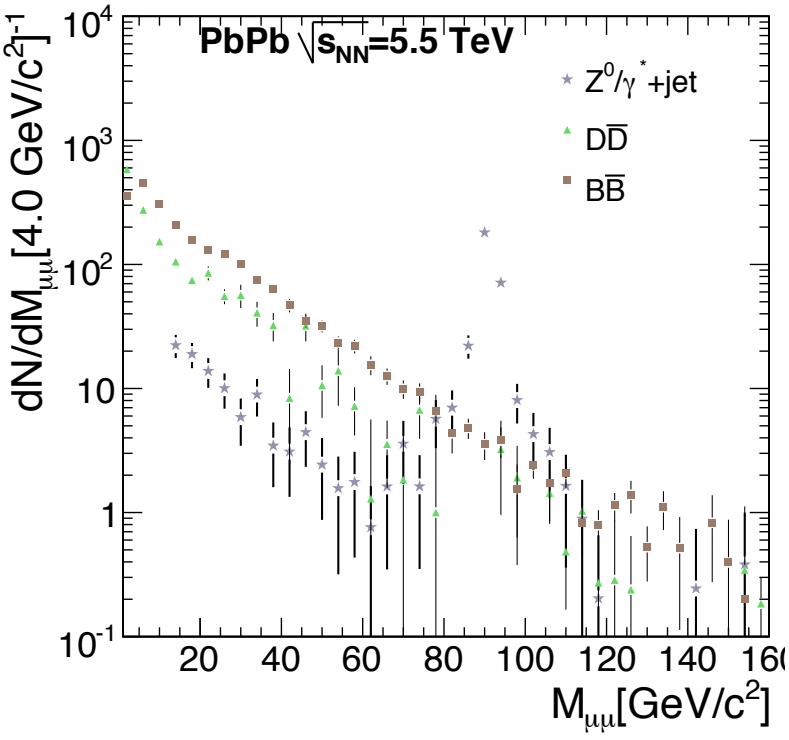

Figure 7.22: The invariant mass distribution for Z^0/γ^*+jet and $D\overline{D}/B\overline{B}$ dimuons with $p_T^{\mu^+\mu^-} > 25\,\mathrm{GeV}/c$, $p^{\mu} > 3.5\,\mathrm{GeV}/c$ and $|\eta^{\mu}| < 2.4$ in PbPb collisions at 5.5 TeV. An integrated luminosity of $0.5\,\mathrm{nb}^{-1}$ is assumed.

above the background. A few thousand Z^0/γ^*+ jet signal events can be collected, sufficient for detailed studies of the medium modification of jet fragmentation functions (Eq. 7.2).

DD, BB background rejection

The signal dileptons from γ^* and Z^0 decays come directly from the collision vertex whereas the background muons from D and B decays issue from a secondary vertex a few hundreds of μm away. The distance of closest approach (DCA) between the primary vertex and the lepton trajectory can then be used to reject this background. The DCA cut consists of two separate "point-to-line" DCA cuts, used together (one *or* the other). The dilepton rejection factor for heavy meson decays has been estimated with a typical DCA cut for the CMS silicon vertex tracker. The DCA resolution in a heavy-ion environment [165] is $\sigma_{r\phi} \approx 20\,\mu$m in the transverse plane and $\sigma_{rz} \approx 50\,\mu$m in the longitudinal plane (see Section 7.3.2). Figure 7.23 shows the rejection factor achieved with a 3σ cut (DCA($r\phi$)$> 60\,\mu$m or DCA(rz)$> 150\,\mu$m). The vertical bars are statistical errors corresponding to 50M events with $\hat{p}_T^{\rm hard} > 15$ GeV/c. Hence, a rejection factor of about 5 can be obtained by two simple DCA cuts between each lepton trajectory and the primary vertex, OR'ed together. Note that, even though an ideal decay geometry was simulated in our event-generator studies (straight trajectories for zero magnetic field and perfect primary vertex position), the DCA resolution has been estimated with the full detector simulation in a heavy-ion environment (bent tracks, high multiplicity, realistic resolutions) [165].

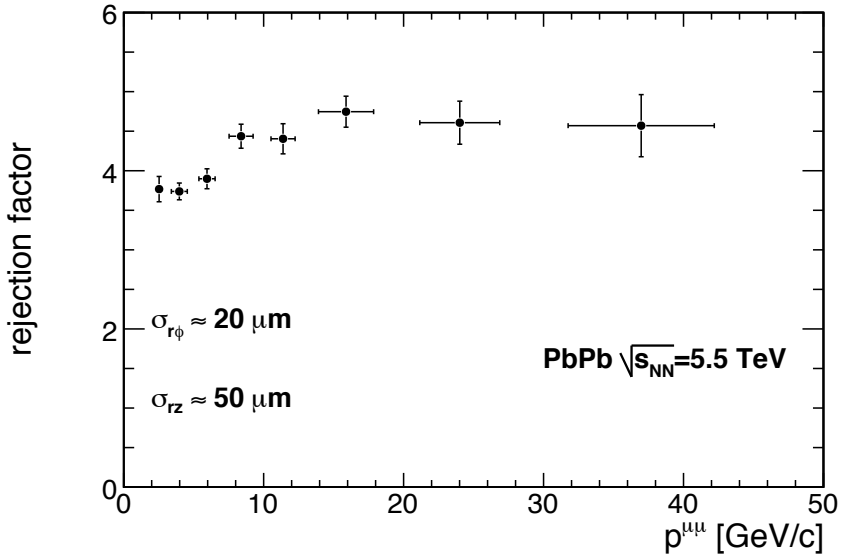

Figure 7.23: The rejection factor of D and B decay dimuons obtained applying a 3σ DCA cut in the CMS silicon vertex tracker. The vertical bars are statistical errors while the horizontal ones are the r.m.s. of the momentum distribution within the bin.

Chapter 8

Ultraperipheral collisions

8.1 Introduction

Ultra-peripheral collisions (UPCs) of heavy-ions involve long range electromagnetic interactions at impact parameters larger than twice the nuclear radius where no nucleon-nucleon collisions occur. At the LHC, the strong electromagnetic field due to the coherent action of the $Z = 82$ proton charges of the lead nucleus accelerated at TeV energies generates an equivalent flux of photons which can be used for high-energy photoproduction studies (see e.g. [127, 128]). The equivalent (Weiszäcker-Williams) photon spectrum of UPCs has a $\propto Z^2/E_\gamma$ dependence and, thus, for a Pb beam, a $Z^2 \approx 7000$ flux enhancement factor is expected compared to electron or proton beams. The upper limit in the photon energies is of the order of the inverse Lorentz contracted radius R_A of the nucleus: $\omega_{max} \approx \gamma/R_A$. The requirement that all the charges act coherently in the generation of the equivalent photon imposes very small virtualities for the photoproduction process. Therefore, the emitted photons are quasi-real ($Q^2 \approx 0$), the beam charges are barely deflected in the process and any produced particles have very low transverse momenta, of the order $p_{\rm T} < 2/R_A \approx 50$ MeV/c or $p_{\rm T} \approx M_X/\gamma \approx 30$ MeV/c. At the LHC, lead beams at 2.75 TeV/nucleon have Lorentz factors γ = 2930 leading to maximum (equivalent) photon energies $\omega_{max} \approx 80$ GeV. These photons can then collide either with the other incoming Pb ion at maximum c.m. energies of $W^{max}_{\gamma\,\rm Pb} \approx 1$ TeV/nucleon (3–4 times larger than those of equivalent ep collisions at HERA), or they can interact with another similarly radiated photon leading to two-photon collisions at $W^{max}_{\gamma\gamma} \approx 160$ GeV, comparable to those studied at LEP.

The physics interest of ultraperipheral PbPb collisions at the LHC is two-fold. On the one hand, γ A collisions open up the possibility to carry out precision QCD studies (e.g. of the gluon distribution function in the nucleus [130]) with a low background and a much simpler initial state than in pA or AA collisions. On the other hand, photon-photon collisions allow one to study QED in a non-perturbative regime (where $\alpha_{\rm em}Z \approx 0.6$) as well as, for example, quartic gauge couplings (such as $\gamma\gamma W^+W^-$, see Ref. [131] and references therein).

We present in this chapter the CMS capabilities to measure diffractive photoproduction of light (ρ) and heavy (Υ) vector mesons, as well as photon-photon production of high-mass ($M_{l+l-} > 5$ GeV/c^2) dileptons (considered here as a background of the photoproduced Υ). The lowest-order diagrams of these processes are shown in Fig. 8.1. Diffractive vector meson production can be viewed in the "target" nucleus rest frame, as a sequence of three processes well separated in time: the intermediate photon fluctuates into a $q\bar{q}$ pair; the $q\bar{q}$ pair participates in a hard interaction with the nucleus via the exchange of a colour singlet state (a Pomeron or two-gluons); and then recombines again to form a vector meson. On the one hand, the study of ρ meson photoproduction extends the measurements performed

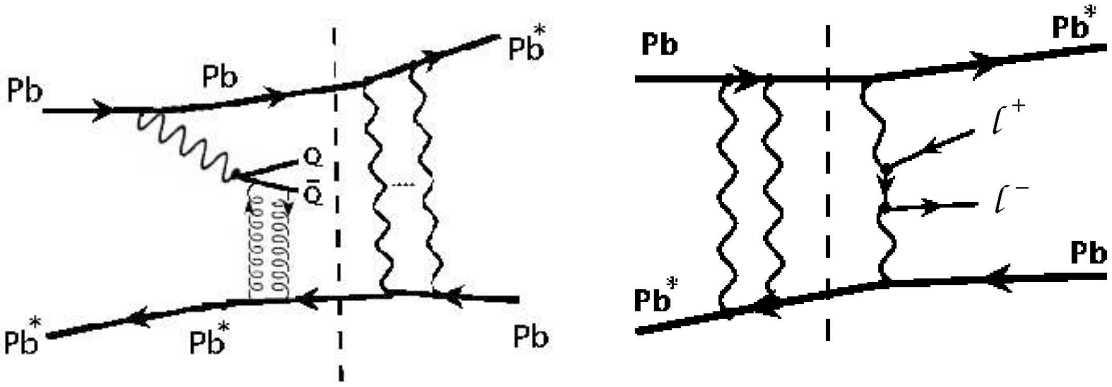

Figure 8.1: Lowest order Feynman diagrams for Υ (left) and lepton pair (right) production in $\gamma\,\mathrm{A}$ and $\gamma\,\gamma$ processes accompanied by Pb Coulomb excitation in ultra-peripheral PbPb collisions. The dashed lines indicate factorisation.

at HERA [240] and provides new information on the interplay of soft and hard physics in diffraction [241, 242]. A clean signature with a low background in the $\pi^+\pi^-$ invariant mass makes this measurement relatively straightforward in UPCs, as demonstrated in AuAu collisions at RHIC [132]. On the other hand, the production of heavier quarkonia states ($\mathrm{J}/\psi, \Upsilon$) provide valuable information on the gluon density in the nucleus $xG(x, Q^2)$ [130], and extends previous studies at RHIC energies [133] in a (x, Q^2) range completely unexplored so far (see Fig. 8.4).

Table 8.1 lists the expected cross sections for ρ, J/ψ and Υ photoproduction in PbPb UPCs at the LHC, as given by the STARLIGHT model [243–246]. STARLIGHT satisfactorily reproduces the existing UPC ρ [132], J/ψ [133] and low- [134] and high-mass [133] dielectron data at RHIC energies. It is worth noting, for comparison, that the theoretical Υ cross section in inelastic pp collisions at 5.5 TeV is $\sim$600 times smaller: $\sigma_{pp\to\Upsilon+X} \approx 0.3$ μb [247], and the inelastic minimum bias PbPb Υ cross section (discussed in Section 6.1) is $\sim$100 times larger: $\sigma_{\mathrm{PbPb}\to\Upsilon+\mathrm{X}} = A^2 \cdot \sigma_{pp\to\Upsilon+X} \approx 13$ mb.

Table 8.1: Cross sections predicted by the STARLIGHT model [243] for exclusive vector meson photoproduction in ultraperipheral PbPb interactions at 5.5 TeV accompanied with neutron emission in single (Xn) or double ($Xn|Xn$) Pb breakup (left diagram in Fig. 8.1). (σ_{Xn} includes $\sigma_{Xn|Xn}$).

Process	σ_{tot}	σ_{Xn}	$\sigma_{Xn\|Xn}$
$\mathrm{PbPb} \to \gamma\,\mathrm{Pb} \to \rho + \mathrm{X}$	5200 mb	790 mb	210 mb
$\mathrm{PbPb} \to \gamma\,\mathrm{Pb} \to \mathrm{J}/\psi + \mathrm{X}$	32 mb	8.7 mb	2.5 mb
$\mathrm{PbPb} \to \gamma\,\mathrm{Pb} \to \Upsilon(1\mathrm{S}) + \mathrm{X}$	173 μb	78 μb	25 μb

The most significant source of physical background for these measurements is the coherent production of lepton pairs in two-photon processes (Fig. 8.1, right). Table 8.2 lists the expected cross sections for the dilepton continuum in the mass ranges of relevance for the quarkonia measurements. The fraction of the continuum cross sections accompanied by nuclear breakup with neutron emission is expected to be the same as in the case of quarkonia photoproduction, i.e. of the order of $\sim$50% for the high-mass dileptons.

Table 8.2: Cross sections for dilepton production in two-photon collisions from ultraperipheral PbPb interactions at 5.5 TeV (right diagram in Fig. 8.1) according to the STARLIGHT model [243], in the mass regions of relevance for J/ψ and Υ measurements.

Process	$\gamma\gamma \to e^+e^-$	$\gamma\gamma \to \mu^+\mu^-$
$\sigma(M > 1.5$ GeV/c$^2)$	139 mb	45 mb
$\sigma(M > 6.0$ GeV/c$^2)$	2.8 mb	1.2 mb

8.2 Trigger considerations

Ultraperipheral collisions are (i) mediated by the exchange of a colour-singlet object (the photon) with a small momentum transfer, (ii) characterised by a large rapidity gap between the produced system and the beam rapidity, and (iii) the nuclei remain basically intact or in a low excited state after the interaction. Thus UPCs can be considered "photonic-diffractive" processes sharing many characteristics with hadronic-diffractive (Pomeron-mediated) collisions. An optimum UPC trigger is usually defined based on these typical signatures:

(1) A large rapidity gap between the produced state and the interacting nuclei.

(2) Forward emission of neutron(s) from the deexcitation of one or both nuclei: (mutual) Coulomb excitation — indicated by the soft γ exchanged in the diagrams of Fig. 8.1 — occurs in about 50% of the UPCs and generates a Giant-Dipole-Resonance (GDR) oscillation of the nucleus which subsequently decays via neutron emission.

(3) Very low global multiplicities: the central detector is virtually empty apart from the few tracks/clusters originating from the photo-produced system.

(4) Relatively narrow $\mathrm{d}\sigma/\mathrm{d}y$ centered[1] at mid-rapidity (narrower for larger M_X).

Given these general properties of UPC events and based upon our previous experience on the J/ψ photoproduction studies in AuAu UPCs at RHIC [133], we will use the following CMS L1 primitives as part of the UltraPeripheral Trigger:

- To ensure a large rapidity gap in one or in both hemispheres, we reject events with signals in the forward hadron calorimeters towers ($3 < |\eta| < 5$) above the default energy threshold for triggering on minimum-bias nuclear interactions ($\overline{HF^+}$ .OR. $\overline{HF^-}$). Pure $\gamma\,\mathrm{Pb}$ coherent events have rapidity gaps in both hemispheres but we are also interested in triggering in the "incoherent" $\gamma\,N$ photoproduction, which usually breaks the target nucleus and lead to particles partially filling one of the hemispheres.
- To tag Pb* Coulomb breakup (via GDR neutron deexcitation), we require energy deposition in ZDC$^+$ or ZDC$^-$ above the default threshold in normal PbPb running. It is worth noting that having the ZDC signals in the L1 trigger decision gives CMS an advantage with respect to the ALICE experiment [199].

[1] Though the energies of the γ and "receiver" nucleus are very different and the produced final-state is boosted in the direction of the latter, each one of the nuclei can act as "emitter" or "target" and the sum of their $d\sigma/dy$ distribution is symmetric with respect to $y = 0$.

8.3 ρ photoproduction in γPb collisions

This section presents a preliminary feasibility study for the measurement in CMS of low mass objects, like the ρ, produced in UPCs (Fig. 8.2). At RHIC energies, ρ photoproduction has been measured by the STAR collaboration [132] in the process AuAu $\rightarrow$ Au*Au$^{(*)}\rho$ at 200 GeV, where the ρ decays into two pions and one or both nuclei deexcite by emitting at least one forward neutron which is detected in the ZDC. Those events have been collected with a back-to-back multiplicity trigger, requiring a signal in the ZDCs and low multiplicity in the tracking detector. In CMS, the measurement of photoproduced ρ is, in principle, not straightforward since the detector is designed to trigger on large transverse energies, and objects with masses below a few GeV/c^2 decay into low p_{T} particles which will not reach the calorimeters. However, even for low mass objects, it should be feasible to trigger on low-multiplicity reactions with Pb* Coulomb breakup tagged with a neutron signal in the ZDCs.

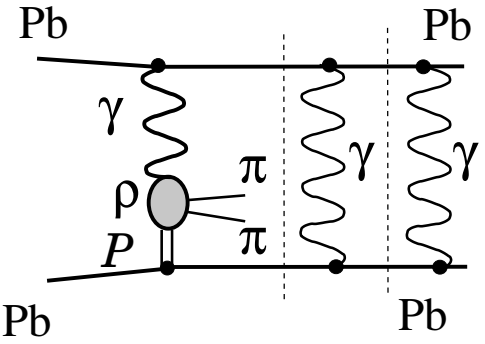

Figure 8.2: Lowest order Feynman diagram for ρ photoproduction accompanied by Pb Coulomb excitation in ultra-peripheral PbPb collisions. The dashed lines indicate factorisation.

A set of 1000 ρ particles produced in PbPb UPCs at LHC energies was generated with STARLIGHT and run through the detailed CMS detector simulation (CMSIM package [248]). Events were passed through the digitisation packages using the standard reconstruction program ORCA 7.1.1. The ρ decays into two pions, with transverse momentum of the order of a few hundred MeV/c, which are detected in the three layers of the silicon pixel detector. The hits reconstructed by ORCA were then used as input for a fast simulation tracking programme. Only the information of the three silicon pixel layers was used. The information from the strip layers was not taken into account because the low p_{T} tracks of interest in this study only cross one or two strip layers, not resulting in a significant improvement of the tracking performance. The ρ candidates are reconstructed by combining tracks of opposite sign. The background from same sign tracks in UPC events was found to be negligible at RHIC [132] and should be also minimal at the LHC. Charged pion identification via $\mathrm{d}E/\mathrm{d}x$ in the pixel detectors, as described in Chapter 3, was not included in the present analysis, but can easily be used to further clean the signal. The mass, transverse momentum and rapidity distributions of the generated and reconstructed ρ's are shown in Fig. 8.3. Assuming that all unlike-sign pairs in the range 0.6–0.9 MeV/c^2 are ρ mesons, an overall reconstruction efficiency of 35% is obtained.

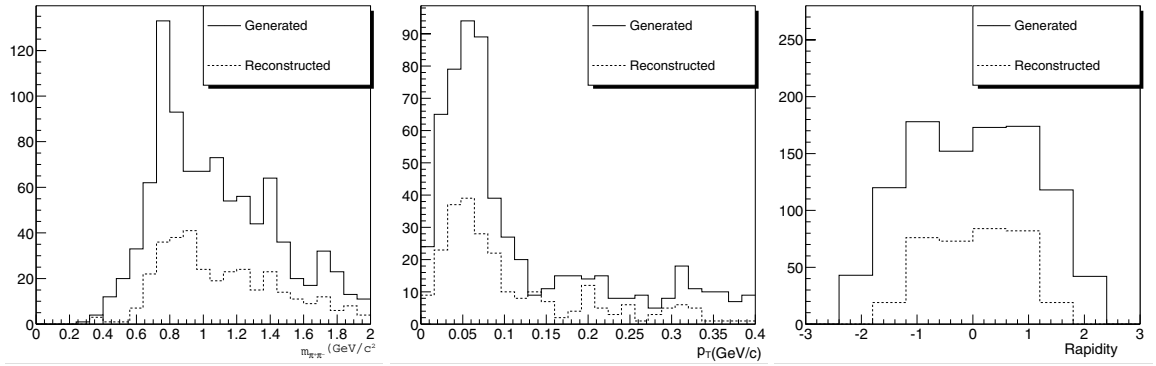

Figure 8.3: The mass, transverse momentum and rapidity distributions of the generated and reconstructed ρ mesons in PbPb UPCs at 5.5 TeV [248].

8.4 Quarkonia photoproduction in γ Pb collisions

At leading order, diffractive $\gamma\,\mathrm{A}$ photoproduction of heavy vector mesons ($\mathrm{J}/\psi, \Upsilon$) proceeds through a colourless two-gluon (Pomeron) exchange (Fig. 8.1-left). After the scattering, both nuclei remain intact (or in a low excited level) and separated by a rapidity gap from the produced state. Such hard diffractive processes are thus a valuable probe of the gluon density since their cross sections are proportional to the *square* of the gluon density, $xG(x,Q^2)$ [249, 250]:

$$\left.\frac{\mathrm{d}\sigma_{\gamma\,\mathrm{p,A}\to\mathrm{V\,p,A}}}{\mathrm{d}t}\right|_{t=0} = \frac{\alpha_s^2\Gamma_{ee}}{3\alpha M_V^5}16\pi^3\left[xG(x,Q^2)\right]^2\,, \quad \text{with } Q^2 = M_V^2/4 \quad \text{and } x = M_V^2/W^2_{\gamma\,\mathrm{p,A}}.$$

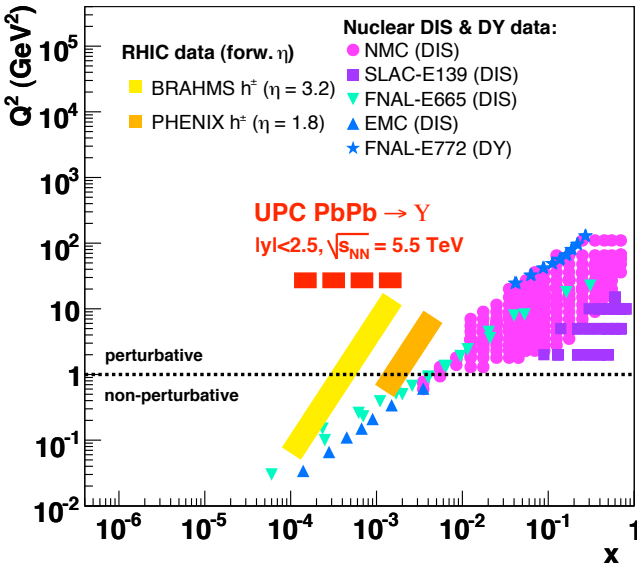

Figure 8.4: Available measurements in the (x,Q^2) plane used to constrain the nuclear PDFs [251]. The approximate (x,Q^2) range covered by Υ photoproduction in PbPb UPCs at the LHC is indicated.

The x values probed in $\gamma\,\mathrm{A} \to \Upsilon\ \mathrm{A}$ processes at $y = 0$ are of the order of $x \approx 2\cdot 10^{-3}$ (but can be a factor ~ 10 lower/higher at rapidities $-2.5 < y < 2.5$) therefore probing the nucleus PDFs in a (x,Q^2) range unexplored so far in nuclear DIS and/or in lower energy nucleus-nucleus collisions (Fig. 8.4). Photoproduction measurements help thus to constrain the low-x

behaviour of xG in the nucleus in a regime where gluon-saturation effects due to non-linear QCD parton evolution are expected to set in [27, 252].

The expected cross sections for ρ, J/ψ and Υ photoproduction in PbPb UPCs at the LHC, as given by the STARLIGHT model, are listed in Table 8.1. They do not include feed-down contributions (at the $\sim$10–20% level) from excited S states (Υ',Υ''), nor do they include contributions from incoherent γ-nucleon ($\gamma\, N$) processes, which should produce $\sim$50% more J/ψ, Υ yields [253] (the latter can be separated experimentally as the produced Υ have larger $p_{\rm T}$ and the "target" nucleus breaks up with a high probability). Other $\gamma\,{\rm Pb}$ theoretical predictions for LHC [254] give comparable results (σ_Υ = 135 μb). Inclusion of *leading-twist* shadowing effects in the nuclear PDFs reduces the yield by up to a factor of two, σ_Υ(LT-shadowing) = 78 μb [254]. Even larger reductions are expected in calculations including gluon-saturation (Colour Glass Condensate) effects [255]. The motivation of our measurement is precisely to pin-down the amount of low-x suppression in the Pb PDF compared to the (known) proton PDF in the studied (x, Q^2) range.

The coherence condition results in very low transverse momenta and the decay electrons or muons from the J/ψ, produced basically at rest, have lower energies ($E_{e^\pm} \approx M_{{\rm J}/\psi}/2 \approx 1.6$ GeV) than those needed to reach the ECAL or muon chambers without significant energy losses in the intermediate material. We will therefore concentrate our efforts in the measurement of the Υ, whose decay leptons have larger energies close to 5 GeV and can, in principle, reach both detectors. We consider, in particular, the CMS barrel+endcap regions ($|\eta| < 2.5$) in the dielectron and dimuon decay channels, to search for diffractive photo-production of the Υ (Fig. 8.1-left) [256]:

(1) PbPb ($\rightarrow \gamma\,{\rm Pb}$) $\rightarrow$ Υ + Pb* Pb$^{(*)}$, with $\Upsilon \rightarrow e^+e^-$ measured in the ECAL;

(2) PbPb ($\rightarrow \gamma\,{\rm Pb}$) $\rightarrow$ Υ + Pb* Pb$^{(*)}$, with $\Upsilon \rightarrow \mu^+\mu^-$ measured in the muon chambers.

The most significant source of physical background for these measurements is the coherent production of (high-mass) lepton pairs in two-photon processes (Fig. 8.1-right):

(1) PbPb ($\rightarrow \gamma\,\gamma$) $\rightarrow$ Pb* Pb$^{(*)}$ + e^+e^- measured in the ECAL;

(2) PbPb ($\rightarrow \gamma\,\gamma$) $\rightarrow$ Pb* Pb$^{(*)}$ + $\mu^+\mu^-$ measured in the muon chambers.

Table 8.2 lists the expected cross sections for the dilepton continuum in the mass ranges of relevance for the quarkonia measurements. Those are actually interesting pure QED processes proposed as a luminometer in pp and ion-ion collisions at the LHC [257, 258], and will likely be used to get the absolute cross-section normalisation of this and other heavy-ion measurements.

8.4.1 Trigger rates

As briefly discussed in Section 8.2, we propose to use the following CMS L1 primitives as part of the quarkonium UltraPeripheral Trigger:

- Veto on signals in the forward hadron calorimeters ($3 < |\eta| < 5$), $\overline{HF^+}$ .OR. $\overline{HF^-}$ (requirement of a large rapidity gap in one or both hemispheres);
- One or more neutrons in at least one ZDC (Xn), in order to tag Pb* Coulomb breakup (via GDR neutron deexcitation);

- Isolated ECAL tower with $E_T^{\rm thresh} \gtrsim 3$ GeV in order to select $e^{\pm}$ from the Υ decay ($E_{e^{\pm}} \approx M_{\Upsilon}/2 \approx 4.6$ GeV) depositing at least $E_{\rm T}$ = 3 GeV in a 5×5 ECAL trigger tower (the ECAL towers are defined at L1 in terms of *transverse* energy $E_{\rm T}$);
- Hit(s) in the muon RPCs ($|\eta| < 2.1$) or CSCs ($0.8 < |\eta| < 2.4$); no track momentum threshold is required since the material budget in front of the chambers effectively reduces any muon background below ∼4 GeV, whereas the Υ decay muons have $E_{\mu} \gtrsim M_{\Upsilon}/2 \approx 4.6$ GeV.

Schematically, the following two dedicated L1 UPC triggers are proposed:

$$\texttt{UPC-mu-L1=(ZDC+ .OR. ZDC-).AND.(}\overline{HF+}\texttt{.OR.}\overline{HF-}\texttt{).AND.(muonRPC.OR.muonCSC)}$$

$$\texttt{UPC-elec-L1=(ZDC+ .OR. ZDC-).AND.(}\overline{HF+}\texttt{.OR.}\overline{HF-}\texttt{).AND.ECALtower(E}_{\rm T} > 2.5\ \texttt{GeV)}$$

The genuine $\gamma\,\mathrm{Pb} \rightarrow \mathrm{Pb}^{*}\,\Upsilon \rightarrow l^{+}\,l^{-}$ counting rate (assuming perfect trigger, full acceptance, no efficiency losses) for the nominal PbPb luminosity of $\langle\mathcal{L}\rangle = 5{\cdot}10^{26}$ cm^{-2}s^{-1} = 0.5 mb^{-1}s^{-1}, yielding $\int \mathcal{L}\,\mathrm{dt}$ = 0.5 nb^{-1} for 1 month (10^6 s) of PbPb running and 50% efficiency, is

$$N_{UPC-\Upsilon} = \langle\mathcal{L}\rangle\ \sigma_{\mathrm{PbPb}\rightarrow\gamma\,\mathrm{Pb}\rightarrow\Upsilon}\ BR(\Upsilon \rightarrow l^{+}\,l^{-}) = 0.5\ \mathrm{mb}^{-1}\mathrm{s}^{-1} \times 0.078\ \mathrm{mb} \times 0.024 = 0.001\ \mathrm{Hz}$$

Obviously, not only the signal but several backgrounds which share a few characteristics with UPC events, will generate an *accept* of the UPC-L1 triggers defined above:

1. *Beam-gas* and *beam-halo* collisions: no good vertex, (comparatively) large particle multiplicity, asymmetric $\mathrm{d}N/\mathrm{d}y$, ZDC signal, low $E_{\rm T}$.

2. *Accidental* coincidence of *cosmic* muon(s) with (mutual) *Pb electromagnetic dissociation*, $\gamma\,\mathrm{A} \rightarrow \mathrm{Pb}^{*}{+}\mathrm{Pb}^{(*)} \rightarrow Xn$ (ZDC): no vertex, track(s) only in muon chambers with large net $p_{\rm T}$, ZDC signal from Pb dissociation.

3. *Peripheral nuclear* collisions (A A $\rightarrow$ X): (comparatively) large particle multiplicities, mainly pions, large total $p_{\rm T}$, ZDC signal.

4. *Two-photon electromagnetic* collisions ($\gamma\,\gamma \rightarrow l^{+}\,l^{-}$) are virtually indistinguishable from our signal at the level-1 trigger as defined above. Still such a background can be significantly removed with an asymmetry cut in the pair decay, and any final residual contribution below the Υ invariant mass peak can be statistically subtracted in the final offline analysis (see Section 8.4.4).

5. *Hadronic diffractive* collisions ($I\!P$ Pb, $I\!P\,I\!P \rightarrow X$): larger multiplicities than e.m. diffractive ($\gamma\,\mathrm{Pb}$) collisions, $p_{\rm T}(I\!P\,I\!P) > p_{\rm T}(\gamma I\!P) > p_{\rm T}(\gamma\,\gamma)$, like-sign pairs, ZDC signal.

6. Other hard diffractive *photoproduction* processes ($\gamma\,\mathrm{Pb} \rightarrow \mathrm{X}$, with X=dijets, open heavy-flavour, ...), interesting in their own right as they address the same physics topics as the $Q\bar{Q}$ measurement discussed here [129, 259], are characterised by: (comparatively) larger multiplicities, ZDC signal, removable offline with $e^{\pm}$ and $\mu^{\pm}$ PID cuts and standard invariant mass subtraction techniques.

7. *Two-photon hadronic* collisions ($\gamma\,\gamma \rightarrow X$): mainly pions (removable with $e^{\pm}$ and $\mu^{\pm}$ PID cuts), ZDC signal.

Among the backgrounds mentioned above, # 1 will be significantly suppressed by the ($\overline{HF+}$ .OR. $\overline{HF-}$) rapidity-gap requirement and will not be discussed further. Backgrounds # 2 and # 3, however, are likely to generate high L1 background rates. Backgrounds # 4 – # 7 are, on the other hand, interesting low-counting rates diffractive and photonic physics processes that can be studied offline as a "by-product" of the UPC trigger. An example of a process that can trigger UPC-L1 is exclusive χ_c production ($I\!P I\!P \rightarrow \chi_c \rightarrow \mathrm{J}/\psi\gamma$) [260], of which candidate events have been measured in CDF at the Tevatron [131].

The cross section for EM dissociation of Pb nuclei at the crossing point of the two beams at LHC energies is huge, $\sigma_{\mathrm{PbPb-ED}}$ = 215 b [261], becoming *de facto* the main limiting factor for the luminosities reachable at the LHC in the ion-ion mode. Such large cross sections translate into very large counting rates: $N_{\mathrm{PbPb-ED}} = \langle\mathcal{L}\rangle \times \sigma_{\mathrm{PbPb-ED}} = 10^5$ Hz, and thus accidental coincidences with cosmic muons traversing the muon chambers and activating the `UPC-mu-L1` trigger are possible. The typical rate of cosmic muons on the ground level is about 60 Hz/m^2 with $\langle E_\mu\rangle \approx 4$ GeV [262]. At the IP5 cavern level (∼80 m underground) this rate is reduced by a factor 100, down to approximately 0.6 Hz/m^2. Since the total muon chambers area is roughly 20×15 m^2, the total rate of cosmic muons above 4 GeV crossing is $N_{\mu-\mathrm{cosmic}} \approx 180$ Hz. The accidental coincidence rate of two detectors with counting rates N_1 and N_2 and trigger time window Δt is $N_{\mathrm{fake}} = 2N_1\,N_2\,\Delta t$. For a time window of Δt_{trig} = 10 ns around the nominal bunch crossings of 25 ns, this translates into:

$$N^{\mathrm{backgd}}_{\mathrm{PbPb-ED}+\mu-\mathrm{cosmic}} = 2\,N_{\mathrm{PbPb-ED}}\,N_{\mu-\mathrm{cosmic}}\,\Delta t_{\mathrm{trig}} \approx 10^5\ \mathrm{Hz} \times 180\ \mathrm{Hz} \times 10^{-8}\ \mathrm{s} \approx 0.2\ \mathrm{Hz}$$

Only very few of the cosmic muons will have a chance to give a trigger if we require the tracks to be pointing to the vertex: the reduction factor is 40 when requiring $z_{hit} < 60$ cm, $R_{hit} < 20$ cm [263]. At higher trigger levels this background can be thus reduced by requiring vertex reconstruction.

At RHIC energies, usually a fraction $\epsilon_{\mathrm{periph}} \approx 5\%$ of the most peripheral (grazing) nuclear AA collisions (i.e. the centrality class corresponding to 95–100% of the total AA cross section) do not generate activity within $3 < |\eta| < 4$ but still produce a signal in the ZDC [264]. Assuming that at the LHC the same fraction of PbPb collisions will be accepted by the '`(ZDC+ .OR. ZDC-) .AND.` ($\overline{HF+}$ `.OR.` $\overline{HF-}$)' L1 condition, such grazing PbPb collisions will fire `UPC-elec-L1` (and/or `UPC-mu-L1`) provided that these reactions produce also an electron (and/or a muon) above $E^{\mathrm{thr}}_{\mathrm{T,ECAL}}$ = 3 GeV (E^{thr}_{μ} = 4 GeV). According to PYTHIA 6.4 about $\epsilon_{\mathrm{high-p_T}\ \mu/\mathrm{e}} \approx 1\%$ of the pp events at 5.5 TeV produce at least one electron (muon) within $|\eta| < 2.5$ with energy above the UPC-L1 threshold. We will assume that the same relative fraction will hold for the peripheral PbPb reactions. The corresponding counting rate for the type # 3. background is, therefore:

$$N^{\mathrm{backgd}}_{\mathrm{PbPb-periph}} = \langle\mathcal{L}\rangle\ \sigma_{\mathrm{tot\ PbPb}}\,\epsilon_{\mathrm{periph}}\,\epsilon_{\mathrm{high-p_T}\ \mu/\mathrm{e}} = 0.5\ \mathrm{mb}^{-1}\mathrm{s}^{-1} \times 7800\ \mathrm{mb} \times 0.05 \times 10^{-2} \approx 2\ \mathrm{Hz}$$

If the zero-activity in both HFs is not sufficient to reduce these background rates at level-1 we may consider in addition an extra L1 primitive such as the total energy in ECAL-HCAL, requiring only a few GeV's above the noise in the calorimeters. This will suppress peripheral nuclear events which have (much) larger multiplicity than UPCs.

Out of the # 4 – # 7 "interesting" physics backgrounds that will likely trigger our UPC-L1 trigger, we will consider in more detail # 4 in the following. The known QED cross sections

for two-photon processes leading to lepton pair production are quoted in Table 8.2. We have determined from the Monte Carlo generated $\gamma\gamma \rightarrow l^+ l^-$ data (see Section 8.4.2), that the fraction of those two-photon events producing an electron above the ECAL trigger threshold of $E_{\mathrm{T,ECAL}}^{\mathrm{thr}}$ = 3 GeV and within $|\eta| < 2.5$, and thus potentially triggering `UPC-elec-L1`, is only of the order $\epsilon_{\mathrm{high-p_T\,e}} \approx 5\%$ (the corresponding fraction, and cross-section, for muons triggering the `UPC-mu-L1` is even lower and we do not discuss it in our counting rates estimates here). Thus, the expected counting rate for the type # 4. background for the design average PbPb luminosity is:

$$N_{\gamma\gamma-\mathrm{em-backgd}} = \langle\mathcal{L}\rangle\ \sigma_{\gamma\gamma\rightarrow e^+e^-}\ P_{Xn}\ \epsilon_{\mathrm{high-p_T\,e}} = 0.5\ \mathrm{mb}^{-1}\mathrm{s}^{-1} \times 139\ \mathrm{mb} \times 0.5 \times 0.05 = 1.7\ \mathrm{Hz}$$

To summarise, the sum of all backgrounds considered here, N_{L1} = (2)+(3)+(4)+N_{others} is in the 5 Hz ballpark range, whereas the Υ physics signal given in expression (1), is $\sim$5000 smaller. It is therefore important not to have any significant trigger dead-time and not to remove good events while further reducing the L1 rates at the high-level-trigger (HLT).

At the PbPb running mode luminosities, the CMS L1 can consider *all* triggered events ($\sim$ 3 kHz in average) and send them without reduction to the HLT (see Chapter 5). The allocated UPC-trigger bandwidth in the HLT for the PbPb running is 2.25 MBytes/s (1% of the total logging rate) i.e. $\sim$ 1–2 Hz for an UPC event size of 1–2 MBytes (see Tables 5.2,5.3). The estimated event size of a very peripheral PbPb *nuclear* event (with impact parameter $b > 12$ fm) is 0.3 MBytes plus a conservative 1 MByte "noise" overhead. Since events triggering the UPC-L1 trigger have, by design, very low multiplicities they will certainly be below the 2 MBytes size already at L1. Logging UPC-HLT rates at the allocated 1–2 Hz rate, implies that we need a reduction factor of up to 5 from the expected UPC-L1 rates. In order to do so we will need to apply (one or more of) the following simple algorithms at the HLT level, until the HLT-output rate matches the allocated bandwidth:

1. Verification of the L1 electron/muon candidates.
2. Event vertex within e.g. $|z| < 15$ cm of (0,0,0) (note that the intrinsic low tracks/clusters multiplicity of UPC events results in a rather wide vertex distribution).
3. Low total transverse momentum of all particles in the event (performing a rough determination of the net transverse momentum of all muons/electrons HLT candidates).
4. Back-to-back dimuons/dielectrons (both objects exist as part of the Global Calo and Global Muon Triggers)

Condition 1. is just an improved software cross-check of the level-1 accepts which will remove part of the fake signals. Condition 2. with an even looser cut, $|z| < 60$ cm, is expected to reduce by a factor of 40 the cosmic-muon triggers, as well as any remaining accepts generated by beam-gas or beam-halo collisions. The hadrons emitted in peripheral nuclear events at 5.5 TeV, have an average transverse momentum of order $\langle p_{\mathrm{T}}\rangle \approx 600$ MeV/c which is much larger than the $\langle p_{\mathrm{T}}\rangle \approx 70$ MeV/c expected for coherent photoproduction events. Thus, applying Condition 3. should significantly reduce the # 2 background. However, we may want to look at other hard photo-produced processes with larger p_{T} which can trigger the UPC-L1, so Condition 4. is probably more appropriate. Again, all these considerations can be taken when setting the final L1 thresholds and HLT algorithms and do not affect the quantitative conclusions of the Υ measurement described here.

8.4.2 Input Monte Carlo

Event samples for the physical signal ($\Upsilon \rightarrow e^+e^-, \mu^+\mu^-$) and the dilepton continuum are generated with the STARLIGHT Monte Carlo [243], which computes the equivalent photon flux of the interacting ions and determines the corresponding QCD (for quarkonia) and QED (for the dilepton continuum) cross sections (Tables 8.1 and 8.2). The coherence condition results in Υ mesons and lepton pairs produced almost at rest. The Υ p_{T} distribution is even sensitive to the form factor of the nuclear charge distribution in the colliding ion and shows a diffractive-like pattern with several local maxima (Fig. 8.5, left). The mass spectrum of the dilepton continuum decreases in a exponential or power-law way. The rapidity distributions of signal and background are both peaked at y = 0, but the continuum has a wider shape. The rapidity spectrum of the *decay* single leptons is much narrower for the Υ than for the $l^+ l^-$ continuum (Fig. 8.5, right). Events with one or both leptons emitted outside of the CMS rapidity coverage will not affect the Υ invariant mass reconstruction.

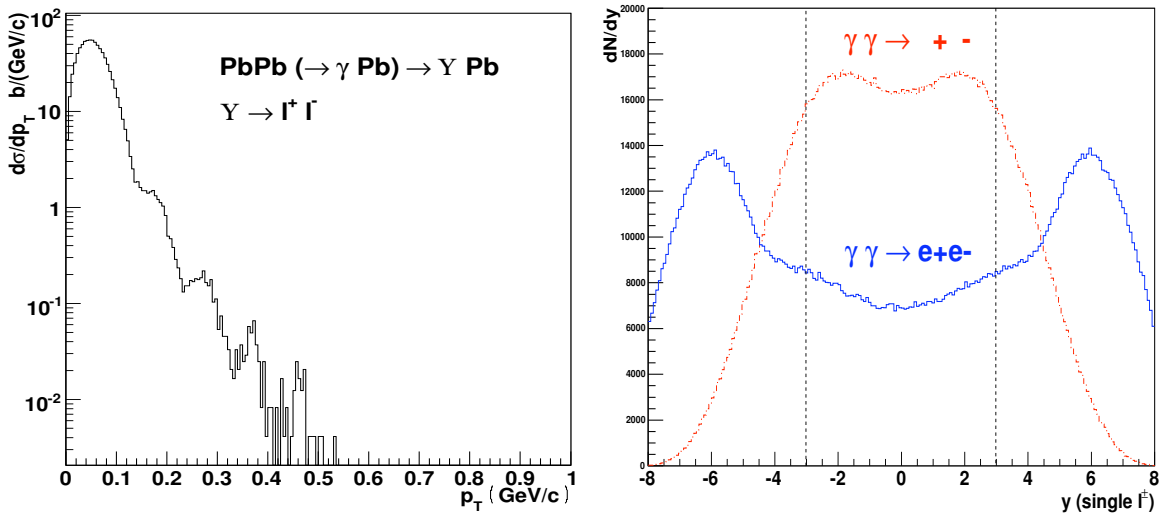

Figure 8.5: Typical STARLIGHT distributions for photo-produced Υ and dilepton continuum in PbPb UPCs at 5.5 TeV. Left: p_{T} spectrum of the photoproduced Υ (note the diffractive-like peaks). Right: Rapidity distributions of the single leptons $\mu^{\pm}$ (red, dashed line) and $e^{\pm}$ (blue, solid line) from the continuum. The dashed lines indicate approximately the CMS acceptance.

8.4.3 Acceptance, trigger and reconstruction efficiencies

The total number of STARLIGHT UPC events generated was 10^6 for the dilepton continuum and 50 000 for the Υ, in each (dielectron and dimuon) decay channel. They were used as input for the CMS simulation package (CMSSW 1.1.0 sim+digi+hit+reco chain) [256]. The yields were chosen to match their relative total production cross-sections. The input vertex of the simulated events was smeared with a σ_z = 5.3 cm resolution. The simulation of the detector response was invoked with the default configuration with nominal magnetic field, CMS geometry, and without any kinematics or geometry cuts. Digitisation was activated for all relevant detectors in this analysis (tracker, calorimeters and muons) in the zero-pileup mode and with ECAL zero suppression. The reconstructed global-muons are a combination of stand-alone muons measured in the muon chambers and tracker tracks obtained with a stepping-helix propagator, and have a final ∼2% momentum resolution. Isolated electron objects combine tracking and electromagnetic (clustering) calorimetry information for efficient

energy reconstruction (collecting and/or correcting for the pre-showering in the tracker) and electron identification [265]. The electron objects are created by combining the tracks measured in the three pixel layers (using a Kalman filter method) with the ECAL information, properly correcting for the energy lost by the $e^{\pm}$ and γ's while crossing the tracker material, before reaching the ECAL.

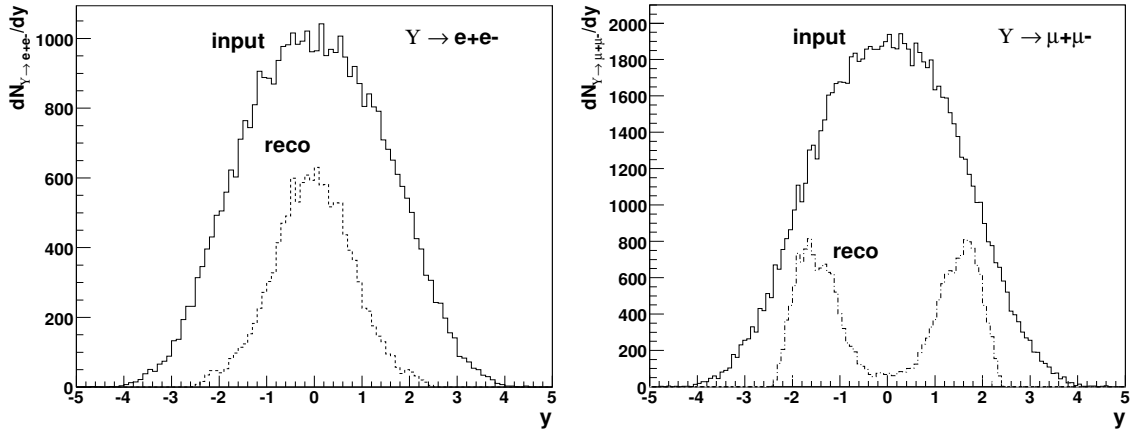

Figure 8.6: Generated and reconstructed rapidity spectra of the Υ measured in the e^+e^- (left) and $\mu^+\mu^-$ (right) channels.

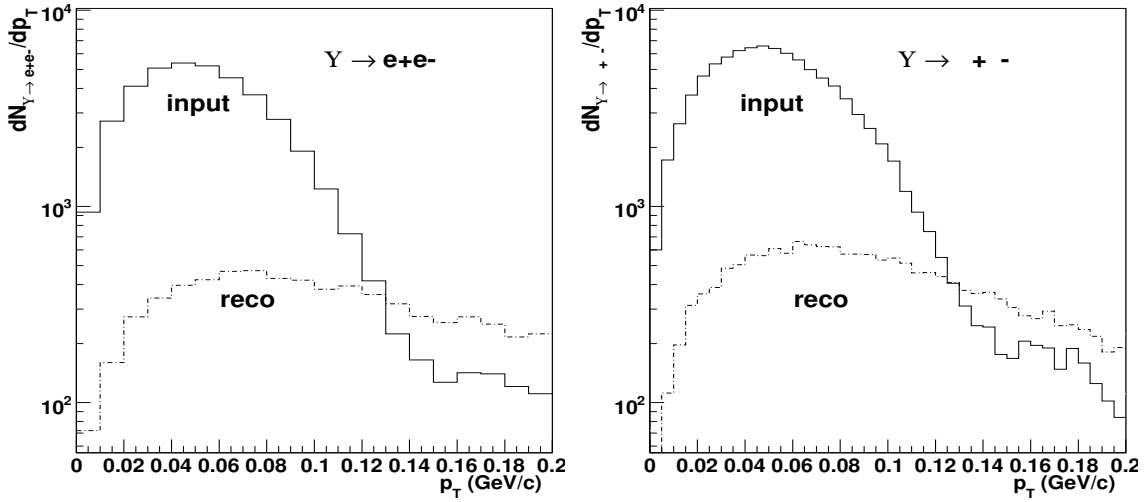

Figure 8.7: Generated and reconstructed p_{T} spectra of the Υ measurement in the e^+e^- (left) and $\mu^+\mu^-$ (right) channels.

Figures 8.6 and 8.7 show, respectively, the rapidity and transverse momentum spectra of the $\Upsilon \rightarrow e^+e^-$ (left) and $\mu^+\mu^-$ (right). The differences between the generated and reconstructed spectra are basically due to geometric acceptance and detector responses, since the only kinematics cut applied in both analyses is the requirement that *both* reconstructed leptons have energy (or momentum) above 3 GeV. This cut, which automatically includes the L1 trigger condition, does not have a very important effect on the reconstruction efficiencies of the Υ ($\epsilon_{\mathrm{loss}} \approx 8\%$) but reduces considerably the contributions from the dilepton continuum ($\epsilon_{\mathrm{loss}} \approx 95\%$ of the yield) or other backgrounds present in the real data. Interestingly, although the rapidity acceptances of both analyses are different and complementary — the

muon events are peaked around $|y| = 2$ and the electrons at $|y| < 1$ — the measured p_{T} efficiencies are quite similar. The reconstructed spectrum is higher than the generated one for p_{T} values above $\sim$130 MeV/c. This "artifact" is due to the combination of a steeply falling spectrum and a reconstruction which yields p_{T} values for the Υ larger than the input ones. Figure 8.8 shows the obtained efficiency times acceptance as a function of the Υ rapidity and transverse momentum, in the $\mu^+\mu^-$ (red, dashed line) and e^+e^- (blue, solid line) analyses.

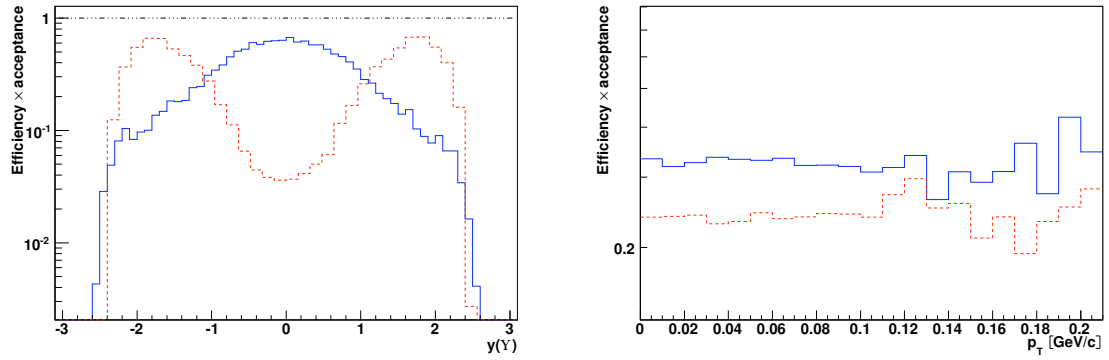

Figure 8.8: Efficiency $\times$ acceptance for the UPCs Υ measurement in the $\mu^+\mu^-$ (red, dashed line) and e^+e^- (blue, solid line) decay modes obtained from a full CMS simulation (CMSSW 1.1.0) of the input STARLIGHT Monte Carlo as a function of the Υ rapidity (left) and p_{T} (right) [256].

The overall *integrated* geometric-acceptance and reconstruction efficiencies of both analyses are: $\epsilon \times \mathcal{A}|_{e^+e^-} = 26\%$ for the e^+e^- analysis; and $\epsilon \times \mathcal{A}|_{\mu^+\mu^-} = 21\%$ for the $\mu^+\mu^-$ one.

8.4.4 Mass distributions ($\Upsilon \rightarrow e^+e^-, \mu^+\mu^-$) and expected rates

In order to determine a realistic invariant mass distribution for the Υ measurement it is necessary to include the lepton pair continuum. The residual combinatorial background can be removed by directly subtracting the like-sign (l^+l^+ or l^-l^-) from the unlike-sign pairs. The generated input signal and continuum background events are mixed according to their relative theoretical cross section ratio (Tables 8.1 and 8.2) and taking into account the corresponding Υ branching-ratio into dileptons ($BR \approx 2.4\%$). The signal-to-background ratio integrated over all phase-space is rather low,

$$\frac{N_{\mathrm{signal}}}{N_{\mathrm{continuum}}} = \frac{\sigma(\gamma\,\mathrm{Pb} \rightarrow \Upsilon) \times BR(\Upsilon \rightarrow l^+\,l^-)}{\sigma(\gamma\,\gamma \rightarrow l^+\,l^-)(6 < M < 12\ \mathrm{GeV/c^2})} \approx 0.35\%\ \ (0.15)\% \quad \text{for } \mu^+\mu^-\ (e^+e^-)\,, \tag{8.1}$$

but, as aforementioned, coherent lepton pairs are emitted more forward than the Υ, and the corresponding single leptons fall often outside the CMS $|\eta| < 2.5$ acceptance.

Figure 8.9 shows the combined signal plus background mass spectra in the dielectron and dimuon channels. The signal over background is roughly 1 (0.67) for the $\mu^+\mu^-$ (e^+e^-) analysis. The combined reconstructed mass spectra are fitted to a Gaussian (for the Υ peak) plus an exponential (to account for the underlying lepton pair contribution). The exponential fit to the continuum is then subtracted from the signal+background distribution. The resulting background-subtracted Υ mass plots are shown in Fig. 8.10 fitted to a Gaussian alone. The final peak positions and widths are: $M_{\mu^+\mu^-} = 9.52$ GeV/c^2 ($\sigma_{\mu^+\mu^-} = 0.090$ GeV/c^2) and $M_{e^+e^-} = 9.34$ GeV/c^2 ($\sigma_{e^+e^-} = 0.154$ GeV/c^2), very close to the nominal $M_\Upsilon = 9.46$ GeV/c^2

mass [262]. In the dimuon channel, the good mass resolution of our measurement would allow for a clean separation of the Υ' (10.02 GeV/c^2) and Υ'' (10.36 GeV/c^2) which are also vector mesons and can be photoproduced (but were not included in the current simulation).

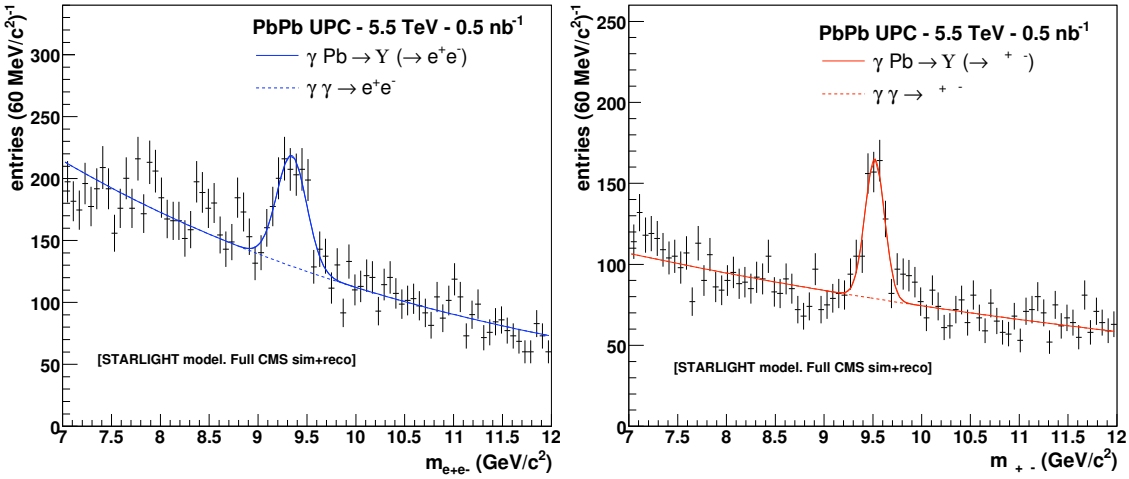

Figure 8.9: Invariant mass e^+e^- (left) and $\mu^+\mu^-$ (right) distributions in CMS for photoproduced Υ and dilepton continuum, as expected in PbPb UPCs at 5.5 TeV, for a nominal integrated luminosity of 0.5 nb^{-1}.

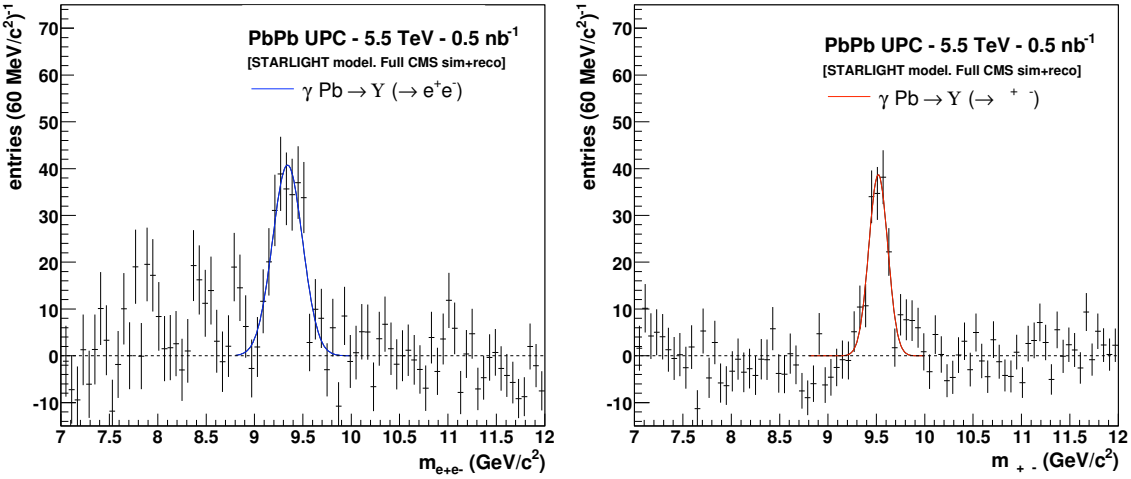

Figure 8.10: Invariant mass e^+e^- (left) and $\mu^+\mu^-$ (right) distributions in CMS for photoproduced Υ (after subtraction of the dilepton continuum background) expected in PbPb UPCs at 5.5 TeV, for a nominal integrated luminosity of 0.5 nb^{-1}.

The extracted yields, integrating the counts within 3σ around the Υ peak after subtracting the continuum background, are computed for both decay modes. The efficiency of the yield extraction procedure is $\epsilon_{\mathrm{yield-extract}}$ = 85%, 90% for the e^+e^- and $\mu^+\mu^-$ analyses (lower in the dielectron channel due to the larger background). The total Υ production yields expected with the design PbPb integrated luminosity of $\int \mathcal{L}\ \mathrm{dt}$ = 0.5 nb^{-1} are $N_{\Upsilon\to e^+e^-} \approx 220 \pm 15$ (stat) and $N_{\Upsilon\to\mu^+\mu^-} \approx 180 \pm 14$ (stat) in the e^+e^- and $\mu^+\mu^-$ channels, respectively. Systematic uncertainties related to the continuum background subtraction and yield extraction procedure have been estimated to be of the order of 10%, using different continuum functional forms (exponential and power law) and extracting the yield by directly counting the number

of entries or by integrating the Gaussian fit within $\pm 3\sigma$. Conservatively, the luminosity normalisation uncertainty will be of the order of $\pm 5\%$ since the concurrent measurement of the lepton pair continuum provides a direct calibrated cross-section to compare against the QED theoretical expectations [257, 258]. Combining the statistics of both channels, the Υ y and p_{T} spectra will test different theoretical model predictions for the amount of low-x saturation in the nuclear PDFs. Even reducing the Υ yields by a factor of 4, as predicted by different gluon saturation (Colour-Glass-Condensate) calculations [255] of the non-linear parton evolution at small x, would not prevent us from having a statistically significant data sample to compare with the theoretical expectations.

8.5 Summary

We have presented the possibilities of carrying out the measurement of $\rho \rightarrow \pi^+\pi^-$ and $\Upsilon \rightarrow e^+e^-, \mu^+\mu^-$ produced in ultra-peripheral PbPb collisions at $\sqrt{s_{NN}}$ = 5.5 TeV in CMS, tagged with forward neutron detection in the Zero Degree Calorimeters. In both analyses, signals and backgrounds are generated with the STARLIGHT Monte Carlo which reproduces satisfactorily lower-energy UPC data. The fast simulation study of ρ photoproduction, based on similar analyses done at RHIC, confirms the feasibility of the measurement in the silicon pixel detector with a 30% efficiency. This analysis extends the measurements performed at HERA and provides new information on the interplay of soft and hard physics in diffraction. The Υ study is based on a full Monte Carlo simulation for the signal and lepton pair background. Two dedicated level-1 triggers have been defined and their expected (signal and background) counting rates have been estimated. A high-level trigger configuration strategy has been discussed in order to adjust the L1 counting rates to the available HLT PbPb bandwidth. The input MC files have been analysed with the full CMSSW 1.1.0. chain. The geometrical acceptance, detector response and resolutions, and reconstruction efficiency losses, have been determined for the dimuon and dielectron decay modes. The rapidity distributions in both analyses are complementary, with the dimuons peaked around $|y|$ = 2 and the dielectrons at $|y| < 1$. The final invariant mass plots, including appropriately scaled contributions from the dilepton continuum, have been obtained. The signal over background is around unity for the $\mu^+\mu^-$ mode and around 0.67 for the e^+e^- mode. After subtracting the continuum background, the reconstructed Υ peak positions are $M_{\mu^+\mu^-}$ = 9.5 GeV/c^2 and $M_{e^+e^-}$ = 9.3 GeV/c^2, with resolutions of 13% and 24%, respectively. The total Υ production yields are obtained from an integration within 3σ of the corresponding peak maxima. The final acceptance and efficiencies are $\epsilon_{\mathrm{rec}} \times \mathcal{A}\epsilon_{\mathrm{yield-extract}}$ = 21% for the e^+e^- analysis and 19% for the $\mu^+\mu^-$ one. The total expected number of Υ events, normalised to the nominal PbPb integrated luminosity of 0.5 nb^{-1}, are 220 $\pm$ 15 (stat) and 180 $\pm$ 14 (stat) in the e^+e^- and $\mu^+\mu^-$ channels, respectively, with a $\sim$10% systematic uncertainty. With a total yield of $\sim$400 Υ, detailed studies of p_{T} and rapidity dependences can be carried out, which will significantly constrain the gluon density at small values of parton fractional momentum in the Pb nucleus.

Chapter 9

Other heavy-ion observables

In this last chapter of the report we summarise a few heavy-ion observables whose measurement is feasible in CMS but for which a final analysis result is lacking (or a detailed simulation is not available) at the time of closing this report. The following topics are under consideration:

- **Hard probes at forward rapidities:** Exploratory studies of the measurement of perturbative probes at very forward rapidities (such as Drell-Yan and jets in the CASTOR-TOTEM and HF acceptances) have been presented in Ref. [145] for proton-proton collisions. Those measurements provide valuable information on the parton distribution functions in a regime of very low x, where non-linear QCD evolution should appear. Extension of these studies (including other hard probes such as e.g. inclusive high-p_{T} hadrons or photons) could be tried in PbPb and, certainly, pPb reactions, where the gluon saturation effects are expected to be much stronger.
- **Detailed Z^0 studies:** CMS has very strong capabilities to reconstruct the Z^0 in the dimuon and dielectron channels. The large p_{T} of its decay leptons allows for a clean identification of the gauge boson over the underlying heavy-ion event background. Apart from the jet-tagging discussion in Section 7.4, the inclusive measurement of the Z^0 provides very valuable information on the nuclear PDFs at intermediate and moderately large values of parton momentum fraction, x [46, 266]. In this kinematic regime, nuclear modifications (anti-shadowing and EMC effect) have been observed at much lower Q^2 scales [267].
- **Study of jet algorithms in heavy-ion collisions** Tests of the performance of the FASTJET algorithm [268] for full jet reconstruction are currently ongoing in CMS. Such a k_{T}-based jet finder uses a new geometrical algorithm that reduces the computational time from a typical N^3 law (N being the number of particles in the event) to a $N \ln N$ form. FASTJET is a very promising substitute of the standard jet-finder codes in the high multiplicity events found in PbPb collisions at the LHC [269].
- **High-p_{T} D,B meson identification:** The measurement of heavy-quark jets via secondary vertex tagging has been discussed in several sections of this document. Such an observable provides a stringent test of jet quenching models based on parton energy loss. The possibility to measure the high-p_{T} suppression and elliptic flow parameter of *leading* heavy mesons (D,B) is an interesting complementary measurement that has yielded precise insights on the nature of the strongly interacting plasma at RHIC energies (see Sections 1.4.3 and 1.4.5). Studies of the

identification in CMS of open charm and beauty mesons (e.g. via their $K\,\pi$ and $\mathrm{J}/\psi\,K$ decays) produced in heavy-ion collisions are a priority.

- **Single inclusive prompt photons:** Direct photons provide a handle on the temperature of the produced plasma as well as an unbiased reference for jet-tagging studies. The identification of hard photons in a heavy-ion environment has always been very challenging [270] due to the impossibility of applying isolation criteria (there is always hadronic activity surrounding any photon) and due to the large background of photons from π^0 and η decays (the observed large suppression of high-p_T mesons at RHIC [271] has somehow reduced this problem). Nonetheless, the standard *statistical* measurement of prompt γ's in AA collisions [272] should be possible in CMS.
- **Strangelets and cosmic-ray-related studies:** In Section 1.4.8 we have presented several intriguing observations related to the hadronic composition of ultra-high-energy (UHE) cosmic-ray events. One of the main physics motivations behind the conception of the CASTOR calorimeter is precisely to carry out detailed studies of the QCD interactions that dominate the hadronic and electromagnetic cascade development of the forward particles produced in ultrarelativistic nucleus-nucleus and proton-nucleus collisions [155]. Full GEANT simulations are currently being carried out to carefully assess the experimental capabilities of the CMS CASTOR detector for such measurements.

Appendix A

HYDJET event generator

A fast Monte Carlo event generator, HYDJET (HYDrodynamics plus JETs) [163, 177] has been developed to, among other things, simulate jet quenching and flow effects in high-energy nucleus-nucleus collisions. The final state in nuclear collisions from HYDJET is obtained as a combination of soft hydro-type particle production and hard (mini)jets fragmentation. The *"soft"* component in HYDJET is parameterised so as to reproduce known collective effects (elliptic flow) and bulk features of the data (charged particle density, $\mathrm{d}N_{\mathrm{ch}}/\mathrm{d}\eta$) at RHIC energies [177]. The shape of the $\mathrm{d}N_{\mathrm{ch}}/\mathrm{d}\eta$ distribution for charged particles is extrapolated from the highest RHIC energy to the LHC energy using the longitudinal scaling behaviour observed at RHIC (see e.g. Fig. 1.20 left) [138]. A value $\mathrm{d}N/\mathrm{d}\eta = 3000$ was used as charged particle density at $\eta = 0$ in central PbPb events, corresponding to a total multiplicity of $\sim$26 000 hadrons. The bulk transverse momentum spectra and the mean transverse momentum are also consistently extrapolated from lower energies. For different centrality classes, the number of produced particles is generated proportionally to the average number of nucleons participating in the collision, $\langle N_{\mathrm{part}} \rangle$, in agreement with RHIC data [273]. $\langle N_{\mathrm{part}} \rangle$ and the number of binary nucleon-nucleon sub-collisions, $\langle N_{\mathrm{coll}} \rangle$, are connected to the impact parameter, b, through a standard Glauber model calculation.

"Hard" particle production in the HYDJET model is generated according to the PYTHIA Monte Carlo event generator [162, 274]. The mean number of jets produced in AA events at a given impact parameter b is calculated as a product of the number of binary nucleon-nucleon sub-collisions and the integral cross section of 2→2 parton scattering in pp collisions with momentum transfer $\hat{p}_{\mathrm{T}} > p_{\mathrm{T}}^{\mathrm{min}}$ ($p_{\mathrm{T}}^{\mathrm{min}} \approx 7$ GeV/c was used). In the HYDJET framework, partons produced in (semi)hard processes with momentum transfer less than $p_{\mathrm{T}}^{\mathrm{min}}$ are considered thermalized in the medium, so their hadronization products are "automatically" included in the soft part of the event. The probability that a randomly generated minimum bias PYTHIA event will fall in this hard category is $p(p_{\mathrm{T}}^{\mathrm{min}})$. Thus, the generation of the hard component of the heavy ion event consists in producing $p \times \langle N_{\mathrm{coll}} \rangle$ proton-proton collisions according to a binomial distribution. Parton energy loss as described in the BDMPS approach [94], leading to the quenching of the generated jet energy can also be turned on via the PYQUEN model [177, 209]. The approach is based on an accumulated energy loss. The gluon radiation is associated with each parton scattering in the expanding medium and includes the interference effect of the modified radiation spectrum as a function of decreasing temperature as the medium expands. The simulation procedure includes the event-by-event generation of the initial parton spectra with PYTHIA, convoluted with production vertices according to a realistic nuclear geometry, the simulation of the parton path length in a dense volume, radiative and collisional energy loss in each rescattering, momentum and angular fluctuations of medium-induced gluon radiation. Final hadronization is carried out with the Lund

string model [275] for hard partons and for in-medium radiated gluons. This model is capable of reproducing the inclusive hadron momentum spectra and the main features of the jet quenching phenomena observed in heavy ion collisions at RHIC energies such as the p_{T} dependence of the nuclear modification factor, $R_{AA}(p_{\mathrm{T}})$, and the suppression of azimuthal back-to-back jet-like correlations [177].

HYDJET was implemented in the CMKIN generator package in order to obtain the detector responses within the OSCAR/ORCA framework, and is about to be included in the new CMS software framework, CMSSW. HYDJET and PYQUEN are also part of the GENSER 2.0 (Generator Services) subproject of the LGG (LHC Computing Grid Project) [276].

Appendix B

HIROOT framework

The HIROOT [277] framework, developed by some of the authors of this report, provides a convenient environment to study and compare event generators and to benchmark reconstruction and analysis algorithms at the generator level.

HIROOT is written in C++ and based on the powerful ROOT analysis framework [278]. It incorporates (interfaces) various FORTRAN-based event generators, among them the PYTHIA [162] and HYDJET [163] generators used in the studies presented in this report. It provides a convenient way to generate, store and read back events, using a flexible and extendable event data model layered on top of the highly efficient ROOT `TTree` mechanism. It maintains the full information about generator parameters, tracks, vertices and decay history. The mixing module provides a flexible way to mix events on the fly and/or using pre-generated samples, while giving the user access to the full event information.

The user-defined analysis makes use of TAM [279], the Tree Analysis Modules facility, an extension of the ROOT analysis tool that allows a sequence or hierarchy of `TSelector`-like modules to be created and executed in a pre-defined order. This way, modules can be used to trigger on certain events, filter data in the event, produce derived data for downstream modules, etc. TAM provides a simple interface to select data (branches) from the Tree, decoupling the modules from the exact tree structure.

Examples of simple usage of the HIROOT tool include generating single PYTHIA events (high E_{T} dijets, etc.) and mixing them into unbiased full heavy-ion events; generating heavy-ion events with user-defined multiplicity and scaling properties; generating heavy-ion events with one pp subevent that is restricted to have a predefined minimum $\hat{p}_{\mathrm{T}}$ value; etc.

References

Notes:

a) CMS Notes are available at `http://cms.cern.ch/iCMS/` unless otherwise noted.

b) References marked **doi** should be prefixed with `http://dx.doi.org/`.

---

[1] T. Schäfer, "Phases of QCD," `arXiv:hep-ph/0509068`.

[2] F. Karsch and E. Laermann, "Thermodynamics and in-medium hadron properties from lattice QCD," `arXiv:hep-lat/0305025`.

[3] Y. Aoki, Z. Fodor, S. D. Katz, and K. K. Szabo, "The QCD transition temperature: Results with physical masses in the continuum limit," *Phys. Lett.* **B643** (2006) 46–54, `arXiv:hep-lat/0609068`.

[4] M. Cheng et al., "The transition temperature in QCD," *Phys. Rev.* **D74** (2006) 054507, `arXiv:hep-lat/0608013`.

[5] E. V. Shuryak, "Theory of hadronic plasma," *Sov. Phys. JETP* **47** (1978) 212–219.

[6] J. C. Collins and M. J. Perry, "Superdense matter: neutrons or asymptotically free quarks ?," *Phys. Rev. Lett.* **34** (1975) 1353.

[7] **MILC** Collaboration, C. Bernard et al., "QCD thermodynamics with three flavors of improved staggered quarks," *Phys. Rev.* **D71** (2005) 034504, `arXiv:hep-lat/0405029`.

[8] A. M. Jaffe and E. Witten, "Quantum Yang-Mills theory." `http://www.claymath.org/millennium/Yang-Mills_Theory/`. Clay Maths Inst. Millennium Prize.

[9] D. Gross et al., "Ten Problems in Fundamental Physics." `http://feynman.physics.lsa.umich.edu/strings2000/millennium.html`.

[10] D. J. Schwarz, "The first second of the universe," *Annalen Phys.* **12** (2003) 220–270, `arXiv:astro-ph/0303574`.

[11] M. Hindmarsh and O. Philipsen, "WIMP dark matter and the QCD equation of state," *Phys. Rev.* **D71** (2005) 087302, `arXiv:hep-ph/0501232`.

[12] M. Laine, "Hot QCD and warm dark matter," `arXiv:hep-lat/0612023`.

[13] **H1** Collaboration, C. Adloff et al., "Deep-inelastic inclusive e p scattering at low x and a determination of α_s," *Eur. Phys. J.* **C21** (2001) 33–61, arXiv:hep-ex/0012053.

[14] **ZEUS** Collaboration, J. Breitweg et al., "ZEUS results on the measurement and phenomenology of F_2 at low x and low Q^2," *Eur. Phys. J.* **C7** (1999) 609–630, arXiv:hep-ex/9809005.

[15] V. N. Gribov and L. N. Lipatov, "Deep inelastic e p scattering in perturbation theory," *Sov. J. Nucl. Phys.* **15** (1972) 438–450.

[16] G. Altarelli and G. Parisi, "Asymptotic freedom in parton language," *Nucl. Phys.* **B126** (1977) 298.

[17] Y. L. Dokshitzer, "Calculation of the structure functions for DIS and e^+e^- annihilation by perturbation theory in QCD (in Russian)," *Sov. Phys. JETP* **46** (1977) 641–653.

[18] L. N. Lipatov, "Reggeization of the vector meson and the vacuum singularity in non-Abelian gauge theories," *Sov. J. Nucl. Phys.* **23** (1976) 338–345.

[19] E. A. Kuraev, L. N. Lipatov, and V. S. Fadin, "The Pomeranchuk singularity in non-Abelian gauge theories," *Sov. Phys. JETP* **45** (1977) 199–204.

[20] I. I. Balitsky and L. N. Lipatov, "The Pomeranchuk singularity in Quantum Chromodynamics," *Sov. J. Nucl. Phys.* **28** (1978) 822–829.

[21] E. Iancu and R. Venugopalan, "The color glass condensate and high energy scattering in QCD," arXiv:hep-ph/0303204.

[22] J. Jalilian-Marian, A. Kovner, A. Leonidov, and H. Weigert, "The BFKL equation from the Wilson renormalization group," *Nucl. Phys.* **B504** (1997) 415–431, arXiv:hep-ph/9701284.

[23] J. Jalilian-Marian, A. Kovner, A. Leonidov, and H. Weigert, "The Wilson renormalization group for low x physics: Towards the high density regime," *Phys. Rev.* **D59** (1999) 014014, arXiv:hep-ph/9706377.

[24] E. Iancu, A. Leonidov, and L. D. McLerran, "Nonlinear gluon evolution in the color glass condensate. I," *Nucl. Phys.* **A692** (2001) 583–645, arXiv:hep-ph/0011241.

[25] Y. V. Kovchegov, "Small-x F_2 structure function of a nucleus including multiple pomeron exchanges," *Phys. Rev.* **D60** (1999) 034008, arXiv:hep-ph/9901281.

[26] E. Iancu, "In the shadow of the color glass," arXiv:hep-ph/0608086.

[27] D. d'Enterria, "Low-x QCD physics from RHIC and HERA to the LHC," *Eur. Phys. J.* **A (to appear)** (2006) arXiv:hep-ex/0610061.

[28] J. M. Maldacena, "The large N limit of superconformal field theories and supergravity," *Adv. Theor. Math. Phys.* **2** (1998) 231–252, arXiv:hep-th/9711200.

[29] E. Witten, "Anti-de Sitter space, thermal phase transition, and confinement in gauge theories," *Adv. Theor. Math. Phys.* **2** (1998) 505–532, arXiv:hep-th/9803131.

[30] P. Kovtun, D. T. Son, and A. O. Starinets, "Viscosity in strongly interacting quantum field theories from black hole physics," *Phys. Rev. Lett.* **94** (2005) 111601, arXiv:hep-th/0405231.

[31] H. Liu, K. Rajagopal, and U. A. Wiedemann, "Calculating the jet quenching parameter from AdS/CFT," *Phys. Rev. Lett.* **97** (2006) 182301, arXiv:hep-ph/0605178.

[32] C. P. Herzog, A. Karch, P. Kovtun, C. Kozcaz, and L. G. Yaffe, "Energy loss of a heavy quark moving through N = 4 supersymmetric Yang-Mills plasma," *JHEP* **07** (2006) 013, arXiv:hep-th/0605158.

[33] S. S. Gubser, "Drag force in AdS/CFT," arXiv:hep-th/0605182.

[34] J. Casalderrey-Solana and D. Teaney, "Heavy quark diffusion in strongly coupled N = 4 Yang Mills," *Phys. Rev.* **D74** (2006) 085012, arXiv:hep-ph/0605199.

[35] M. G. Alford, K. Rajagopal, and F. Wilczek, "QCD at finite baryon density: Nucleon droplets and color superconductivity," *Phys. Lett.* **B422** (1998) 247–256, arXiv:hep-ph/9711395.

[36] J. Cleymans, H. Oeschler, K. Redlich, and S. Wheaton, "Status of chemical freeze-out," *J. Phys.* **G32** (2006) S165–S170, arXiv:hep-ph/0607164.

[37] Z. Fodor and S. D. Katz, "Critical point of QCD at finite T and mu, lattice results for physical quark masses," *JHEP* **04** (2004) 050, arXiv:hep-lat/0402006.

[38] J. Schukraft, "The future of high energy nuclear physics in Europe," arXiv:nucl-ex/0602014.

[39] J. D. Bjorken, "Highly relativistic nucleus-nucleus collisions: the central rapidity region," *Phys. Rev.* **D27** (1983) 140–151.

[40] **PHENIX** Collaboration, S. S. Adler et al., "Systematic studies of the centrality and $\sqrt{s_{NN}}$ dependence of dE(T)/deta and d N(ch)/deta in heavy ion collisions at mid-rapidity," *Phys. Rev.* **C71** (2005) 034908, arXiv:nucl-ex/0409015.

[41] R. Sahoo, S. Chattopadhaya, A. A. P. Suaide, M. M. de Moura, and D. P. Mahapatra, "Transverse energy measurement in $\sqrt{s_{NN}}$ = 62.4 GeV Au + Au collisions at RHIC," *Rom. Rep. Phys.* **58** (2006) 055–062, arXiv:nucl-ex/0510059.

[42] P. F. Kolb and U. W. Heinz, "Hydrodynamic description of ultrarelativistic heavy-ion collisions," arXiv:nucl-th/0305084.

[43] R. Vogt, "Heavy ion physics at the LHC," *Nucl. Phys.* **A752** (2005) 447–456, arXiv:hep-ph/0412301.

[44] A. Accardi et al., "Hard probes in heavy ion collisions at the LHC: Jet physics," arXiv:hep-ph/0310274.

[45] A. Accardi et al., "Hard probes in heavy ion collisions at the LHC: PDFs, shadowing and p A collisions," arXiv:hep-ph/0308248.

[46] R. Vogt, "Shadowing effects on vector boson production," *Phys. Rev.* **C64** (2001) 044901, arXiv:hep-ph/0011242.

[47] M. Bedjidian et al., "Hard probes in heavy ion collisions at the LHC: Heavy flavour physics," arXiv:hep-ph/0311048.

[48] D. Kharzeev, E. Levin, and M. Nardi, "Color glass condensate at the LHC: Hadron multiplicities in p p, p A and A A collisions," *Nucl. Phys.* **A747** (2005) 609–629, arXiv:hep-ph/0408050.

[49] CMS Collaboration, "The Compact Muon Solenoid Letter of Intent," *CERN/LHCC* **1992-3** (1992). LHCC/I 1.

[50] CMS Collaboration, "The Compact Muon Solenoid Technical Proposal," *CERN/LHCC* **94-38** (1994). LHCC/P1.

[51] CMS Collaboration, "The CMS Physics Technical Design Report, Volume 1," *CERN/LHCC* **2006-001** (2006). CMS TDR 8.1.

[52] D. d'Enterria, "Quark-gluon matter," arXiv:nucl-ex/0611012.

[53] K. J. Eskola, "On predictions of the first results from RHIC," *Nucl. Phys.* **A698** (2002) 78–87, arXiv:hep-ph/0104058.

[54] M. Gyulassy and X.-N. Wang, "HIJING 1.0: A Monte Carlo program for parton and particle production in high-energy hadronic and nuclear collisions," *Comput. Phys. Commun.* **83** (1994) 307, arXiv:nucl-th/9502021.

[55] A. Capella, U. Sukhatme, C.-I. Tan, and J. Tran Thanh Van, "Dual parton model," *Phys. Rept.* **236** (1994) 225–329.

[56] N. Armesto and C. Pajares, "Central rapidity densities of charged particles at RHIC and LHC," *Int. J. Mod. Phys.* **A15** (2000) 2019–2052, arXiv:hep-ph/0002163.

[57] D. Kharzeev and M. Nardi, "Hadron production in nuclear collisions at RHIC and high density QCD," *Phys. Lett.* **B507** (2001) 121–128, arXiv:nucl-th/0012025.

[58] N. Armesto, C. A. Salgado, and U. A. Wiedemann, "Relating high-energy lepton hadron, proton nucleus and nucleus nucleus collisions through geometric scaling," *Phys. Rev. Lett.* **94** (2005) 022002, arXiv:hep-ph/0407018.

[59] L. V. Gribov, E. M. Levin, and M. G. Ryskin, "Semihard processes in QCD," *Phys. Rept.* **100** (1983) 1–150.

[60] A. H. Mueller and J.-w. Qiu, "Gluon recombination and shadowing at small values of x," *Nucl. Phys.* **B268** (1986) 427.

[61] B. B. Back et al., "The PHOBOS perspective on discoveries at RHIC," *Nucl. Phys.* **A757** (2005) 28–101, arXiv:nucl-ex/0410022.

[62] D. d'Enterria and D. Peressounko, "Probing the QCD equation of state with thermal photons in nucleus nucleus collisions at RHIC," *Eur. Phys. J.* **C46** (2006) 451–464, arXiv:nucl-th/0503054.

[63] B. Jäger, A. Schäfer, M. Stratmann, and W. Vogelsang, "Next-to-leading order QCD corrections to high-p_{T} pion production in longitudinally polarized p p collisions," *Phys. Rev.* **D67** (2003) 054005, arXiv:hep-ph/0211007.

[64] W. Vogelsang. private communication.

[65] **PHENIX** Collaboration, K. Adcox et al., "Formation of dense partonic matter in relativistic nucleus nucleus collisions at RHIC: Experimental evaluation by the PHENIX collaboration," *Nucl. Phys.* **A757** (2005) 184–283, arXiv:nucl-ex/0410003.

[66] **PHOBOS** Collaboration, B. Alver et al., "System size, energy, pseudorapidity, and centrality dependence of elliptic flow," arXiv:nucl-ex/0610037.

[67] **NA49** Collaboration, C. Alt et al., "Directed and elliptic flow of charged pions and protons in Pb + Pb collisions at 40 AGeV and 158 AGeV," *Phys. Rev.* **C68** (2003) 034903, arXiv:nucl-ex/0303001.

[68] **PHOBOS** Collaboration, S. Manly et al., "System size, energy and pseudorapidity dependence of directed and elliptic flow at RHIC," *Nucl. Phys.* **A774** (2006) 523–526, arXiv:nucl-ex/0510031.

[69] **STAR** Collaboration, S. A. Voloshin, "Energy and system size dependence of elliptic flow: Using rapidity gaps to suppress non-flow contribution," *AIP Conf. Proc.* **870** (2006) 691–694, arXiv:nucl-ex/0610038.

[70] S. A. Voloshin and A. M. Poskanzer, "The physics of the centrality dependence of elliptic flow," *Phys. Lett.* **B474** (2000) 27–32, arXiv:nucl-th/9906075.

[71] P. F. Kolb, J. Sollfrank, and U. W. Heinz, "Anisotropic transverse flow and the quark-hadron phase transition," *Phys. Rev.* **C62** (2000) 054909, arXiv:hep-ph/0006129.

[72] D. Teaney, J. Lauret, and E. V. Shuryak, "A hydrodynamic description of heavy ion collisions at the SPS and RHIC," arXiv:nucl-th/0110037.

[73] J.-Y. Ollitrault, "Anisotropy as a signature of transverse collective flow," *Phys. Rev.* **D46** (1992) 229–245.

[74] S. Voloshin and Y. Zhang, "Flow study in relativistic nuclear collisions by Fourier expansion of Azimuthal particle distributions," *Z. Phys.* **C70** (1996) 665–672, arXiv:hep-ph/9407282.

[75] X.-l. Zhu, M. Bleicher, and H. Stoecker, "Elliptic flow analysis at RHIC: Fluctuations vs. non-flow effects," *Phys. Rev.* **C72** (2005) 064911, arXiv:nucl-th/0509081.

[76] D. Molnar and M. Gyulassy, "Saturation of elliptic flow at RHIC: Results from the covariant elastic parton cascade model MPC," *Nucl. Phys.* **A697** (2002) 495–520, arXiv:nucl-th/0104073.

[77] P. Huovinen and P. V. Ruuskanen, "Hydrodynamic models for heavy ion collisions," arXiv:nucl-th/0605008.

[78] T. Hirano and K. Tsuda, "Collective flow and two pion correlations from a relativistic hydrodynamic model with early chemical freeze out," *Phys. Rev.* **C66** (2002) 054905, arXiv:nucl-th/0205043.

[79] **PHENIX** Collaboration, S. S. Adler et al., "Saturation of azimuthal anisotropy in Au + Au collisions at $\sqrt{s_{NN}}$ = 62 GeV – 200 GeV," *Phys. Rev. Lett.* **94** (2005) 232302, arXiv:nucl-ex/0411040.

[80] E. Shuryak, "Why does the quark gluon plasma at RHIC behave as a nearly ideal fluid?," *Prog. Part. Nucl. Phys.* **53** (2004) 273–303, arXiv:hep-ph/0312227.

[81] T. D. Lee, "The strongly interacting quark-gluon plasma and future physics," *Nucl. Phys.* **A750** (2005) 1–8.

[82] M. Gyulassy and L. McLerran, "New forms of QCD matter discovered at RHIC," *Nucl. Phys.* **A750** (2005) 30–63, arXiv:nucl-th/0405013.

[83] A. Peshier and W. Cassing, "The hot non-perturbative gluon plasma is an almost ideal colored liquid," *Phys. Rev. Lett.* **94** (2005) 172301, arXiv:hep-ph/0502138.

[84] U. W. Heinz, "'RHIC serves the perfect fluid' - Hydrodynamic flow of the QGP," arXiv:nucl-th/0512051.

[85] C. Bernard et al., "QCD equation of state with 2+1 flavors of improved staggered quarks," arXiv:hep-lat/0611031.

[86] M. H. Thoma, "The quark-gluon plasma liquid," *J. Phys.* **G31** (2005) L7, arXiv:hep-ph/0409213.

[87] T. Hirano and M. Gyulassy, "Perfect fluidity of the quark gluon plasma core as seen through its dissipative hadronic corona," *Nucl. Phys.* **A769** (2006) 71–94, arXiv:nucl-th/0506049.

[88] M. Mangano, H. Satz, and U. Wiedemann, eds., "Hard probes in heavy-ion collisions at the LHC". 2004. CERN-2004-009.

[89] **PHENIX** Collaboration, K. Adcox et al., "Suppression of hadrons with large transverse momentum in central Au + Au collisions at $\sqrt{s_{NN}}$ = 130 GeV," *Phys. Rev. Lett.* **88** (2002) 022301, arXiv:nucl-ex/0109003.

[90] J. D. Bjorken, "Energy loss of energetic partons in quark-gluon-plasma: possible extinction of high p_{T} jets in hadron-hadron collisions,". FERMILAB-PUB-82-059-THY.

[91] M. Gyulassy and M. Plumer, "Jet quenching in dense matter," *Phys. Lett.* **B243** (1990) 432–438.

[92] M. Gyulassy, P. Levai, and I. Vitev, "Reaction operator approach to non-Abelian energy loss," *Nucl. Phys.* **B594** (2001) 371–419, arXiv:nucl-th/0006010.

[93] I. Vitev and M. Gyulassy, "High-p_{T} tomography of d + Au and Au + Au at SPS, RHIC, and LHC," *Phys. Rev. Lett.* **89** (2002) 252301, arXiv:hep-ph/0209161.

[94] R. Baier, Y. L. Dokshitzer, A. H. Mueller, S. Peigne, and D. Schiff, "Radiative energy loss and p_{T}-broadening of high energy partons in nuclei," *Nucl. Phys.* **B484** (1997) 265–282, arXiv:hep-ph/9608322.

[95] R. Baier, D. Schiff, and B. G. Zakharov, "Energy loss in perturbative QCD," *Ann. Rev. Nucl. Part. Sci.* **50** (2000) 37–69, arXiv:hep-ph/0002198.

[96] U. A. Wiedemann, "Gluon radiation off hard quarks in a nuclear environment: Opacity expansion," *Nucl. Phys.* **B588** (2000) 303–344, arXiv:hep-ph/0005129.

[97] C. A. Salgado and U. A. Wiedemann, "Calculating quenching weights," *Phys. Rev.* **D68** (2003) 014008, arXiv:hep-ph/0302184.

[98] A. Dainese, C. Loizides, and G. Paic, "Leading-particle suppression in high energy nucleus nucleus collisions," *Eur. Phys. J.* **C38** (2005) 461–474, arXiv:hep-ph/0406201.

[99] K. J. Eskola, H. Honkanen, C. A. Salgado, and U. A. Wiedemann, "The fragility of high-p_{T} hadron spectra as a hard probe," *Nucl. Phys.* **A747** (2005) 511–529, arXiv:hep-ph/0406319.

[100] N. Armesto, A. Dainese, C. A. Salgado, and U. A. Wiedemann, "Testing the color charge and mass dependence of parton energy loss with heavy-to-light ratios at RHIC and LHC," *Phys. Rev.* **D71** (2005) 054027, arXiv:hep-ph/0501225.

[101] C. Loizides, "High transverse momentum suppression and surface effects in nucleus nucleus collisions within the parton quenching model," arXiv:hep-ph/0608133.

[102] D. d'Enterria, "Hard scattering cross sections at LHC in the Glauber approach: From pp to pA and AA collisions," arXiv:nucl-ex/0302016.

[103] **WA98** Collaboration, M. M. Aggarwal et al., "Transverse mass distributions of neutral pions from Pb-208 induced reactions at 158 AGeV," *Eur. Phys. J.* **C23** (2002) 225–236, arXiv:nucl-ex/0108006.

[104] D. d'Enterria, "Indications of suppressed high p_{T} hadron production in nucleus nucleus collisions at CERN-SPS," *Phys. Lett.* **B596** (2004) 32–43, arXiv:nucl-ex/0403055.

[105] **PHENIX** Collaboration, M. Shimomura, "High-p_{T} π^0, η, identified and inclusive charged hadron spectra from PHENIX," *Nucl. Phys.* **A774** (2006) 457–460, arXiv:nucl-ex/0510023.

[106] D. d'Enterria, "High p_{T} leading hadron suppression in nuclear collisions at $\sqrt{s_{NN}}$ = 20 GeV - 200 GeV: Data versus parton energy loss models," *Eur. Phys. J.* **C43** (2005) 295–302, arXiv:nucl-ex/0504001.

[107] **PHENIX** Collaboration, A. Adare, "Energy loss and flow of heavy quarks in Au + Au collisions at $\sqrt{s_{NN}}$ = 200 GeV," arXiv:nucl-ex/0611018.

[108] **STAR** Collaboration, B. I. Abelev et al., "Transverse momentum and centrality dependence of high-p_{T} non-photonic electron suppression in Au + Au collisions at $\sqrt{s_{NN}}$ = 200 GeV," arXiv:nucl-ex/0607012.

[109] M. Djordjevic, M. Gyulassy, and S. Wicks, "The charm and beauty of RHIC and LHC," *Phys. Rev. Lett.* **94** (2005) 112301, arXiv:hep-ph/0410372.

[110] M. G. Mustafa and M. H. Thoma, "Quenching of hadron spectra due to the collisional energy loss of partons in the quark gluon plasma," *Acta Phys. Hung.* **A22** (2005) 93–102, arXiv:hep-ph/0311168.

[111] A. Peshier, "Rethinking the QCD collisional energy loss," arXiv:hep-ph/0607275.

[112] S. Wicks, W. Horowitz, M. Djordjevic, and M. Gyulassy, "Heavy quark tomography of A + A including elastic and inelastic energy loss," arXiv:nucl-th/0512076.

[113] F. Arleo, P. Aurenche, Z. Belghobsi, and J.-P. Guillet, "Photon tagged correlations in heavy ion collisions," *JHEP* **11** (2004) 009, arXiv:hep-ph/0410088.

[114] I. P. Lokhtin, A. V. Sherstnev, and A. M. Snigirev, "p_{T}-imbalance in dimuon + jet production as a signal of partonic energy loss in heavy ion collisions at LHC," *Phys. Lett.* **B599** (2004) 260–268, arXiv:hep-ph/0405049.

[115] T. Matsui and H. Satz, "J/ψ suppression by Quark-Gluon Plasma formation," *Phys. Lett.* **B178** (1986) 416.

[116] T. Umeda, K. Nomura, and H. Matsufuru, "Charmonium at finite temperature in quenched lattice QCD," *Eur. Phys. J.* **C39S1** (2005) 9–26, arXiv:hep-lat/0211003.

[117] M. Asakawa and T. Hatsuda, "J/ψ and η_c in the deconfined plasma from lattice QCD," *Phys. Rev. Lett.* **92** (2004) 012001, arXiv:hep-lat/0308034.

[118] S. Datta, F. Karsch, P. Petreczky, and I. Wetzorke, "Behavior of charmonium systems after deconfinement," *Phys. Rev.* **D69** (2004) 094507, arXiv:hep-lat/0312037.

[119] A. Mocsy and P. Petreczky, "Heavy quarkonia survival in potential model," *Eur. Phys. J.* **C43** (2005) 77–80, arXiv:hep-ph/0411262.

[120] **NA38** Collaboration, C. Baglin et al., "ψ' and J/ψ production in p W, p U and S U interactions at 200-GeV/nucleon," *Phys. Lett.* **B345** (1995) 617–621.

[121] **NA50** Collaboration, M. C. Abreu et al., "Evidence for deconfinement of quarks and gluons from the J/ψ suppression pattern measured in Pb Pb collisions at the CERN-SPS," *Phys. Lett.* **B477** (2000) 28–36.

[122] **NA60** Collaboration, R. Arnaldi et al., "Anomalous J/ψ suppression in In-In collisions at 158- GeV/nucleon," *Nucl. Phys.* **A774** (2006) 711–714.

[123] **PHENIX** Collaboration, A. Adare, "J/ψ production vs centrality, transverse momentum, and rapidity in Au + Au collisions at $\sqrt{s_{NN}}$ = 200 GeV," arXiv:nucl-ex/0611020.

[124] C. Lourenço, "Open questions in quarkonium and electromagnetic probes," arXiv:nucl-ex/0612014.

[125] F. Karsch, D. Kharzeev, and H. Satz, "Sequential charmonium dissociation," *Phys. Lett.* **B637** (2006) 75–80, arXiv:hep-ph/0512239.

[126] R. L. Thews, M. Schroedter, and J. Rafelski, "Enhanced J/ψ production in deconfined quark matter," *Phys. Rev.* **C63** (2001) 054905, arXiv:hep-ph/0007323.

[127] G. Baur, K. Hencken, D. Trautmann, S. Sadovsky, and Y. Kharlov, "Coherent $\gamma\,\gamma$ and γ A interactions in very peripheral collisions at relativistic ion colliders," *Phys. Rept.* **364** (2002) 359–450, arXiv:hep-ph/0112211.

[128] C. A. Bertulani, S. R. Klein, and J. Nystrand, "Physics of ultra-peripheral nuclear collisions," *Ann. Rev. Nucl. Part. Sci.* **55** (2005) 271–310, arXiv:nucl-ex/0502005.

[129] A. Baltz et al., "The physics of ultra-peripheral collisions at the LHC," *Yellow Report* (2007).

[130] L. Frankfurt, M. Strikman, and C. Weiss, "Small-x physics: From HERA to LHC and beyond," *Ann. Rev. Nucl. Part. Sci.* **55** (2005) 403–465, arXiv:hep-ph/0507286.

[131] A. Baltz et al., "Photoproduction at collider energies: from RHIC and HERA to the LHC," *ECT* Workshop Miniproceedings* (2007) arXiv:hep-ph/0702212.

[132] **STAR** Collaboration, C. Adler et al., "Coherent ρ^0 production in ultra-peripheral heavy ion collisions," *Phys. Rev. Lett.* **89** (2002) 272302, arXiv:nucl-ex/0206004.

[133] D. d'Enterria, "Coherent photoproduction of J/ψ and high-mass e^+e^- pairs in ultra-peripheral Au + Au collisions at $\sqrt{s_{NN}}$ = 200-GeV," arXiv:nucl-ex/0601001.

[134] **STAR** Collaboration, J. Adams et al., "Production of e^+e^- pairs accompanied by nuclear dissociation in ultra-peripheral heavy ion collision," *Phys. Rev.* **C70** (2004) 031902, arXiv:nucl-ex/0404012.

[135] V. Guzey, M. Strikman, and W. Vogelsang, "Observations on d A scattering at forward rapidities," *Phys. Lett.* **B603** (2004) 173–183, arXiv:hep-ph/0407201.

[136] W. Busza, "Structure and fine structure in multiparticle production data at high energies," *Acta Phys. Polon.* **B35** (2004) 2873–2894, arXiv:nucl-ex/0410035.

[137] G. I. Veres, "Bulk hadron production at high rapidities," *Nucl. Phys.* **A774** (2006) 287–296, arXiv:nucl-ex/0511037.

[138] B. B. Back et al., "The significance of the fragmentation region in ultrarelativistic heavy ion collisions," *Phys. Rev. Lett.* **91** (2003) 052303, arXiv:nucl-ex/0210015.

[139] **BRAHMS** Collaboration, I. Arsene et al., "Centrality dependence of charged-particle pseudorapidity distributions from d+Au collisions at $\sqrt{s_{NN}}$ = 200 GeV," *Phys. Rev. Lett.* **94** (2005) 032301, arXiv:nucl-ex/0401025.

[140] **STAR** Collaboration, J. Adams et al., "Multiplicity and pseudorapidity distributions of charged particles and photons at forward pseudorapidity in Au + Au collisions at $\sqrt{s_{NN}}$ = 62.4 GeV," *Phys. Rev.* **C73** (2006) 034906, arXiv:nucl-ex/0511026.

[141] J. Benecke, T. T. Chou, C.-N. Yang, and E. Yen, "Hypothesis of limiting fragmentation in high-energy collisions," *Phys. Rev.* **188** (1969) 2159–2169.

[142] **BRAHMS** Collaboration, I. G. Bearden et al., "Nuclear stopping in Au + Au collisions at $\sqrt{s_{NN}}$ = 200 GeV," *Phys. Rev. Lett.* **93** (2004) 102301, arXiv:nucl-ex/0312023.

[143] **BRAHMS** Collaboration, I. G. Bearden et al., "Charged meson rapidity distributions in central Au + Au collisions at $\sqrt{s_{NN}}$ = 200 GeV," *Phys. Rev. Lett.* **94** (2005) 162301, arXiv:nucl-ex/0403050.

[144] **BRAHMS** Collaboration, I. Arsene et al., "Quark gluon plasma and color glass condensate at RHIC? The perspective from the BRAHMS experiment," *Nucl. Phys.* **A757** (2005) 1–27, arXiv:nucl-ex/0410020.

[145] CMS-TOTEM Collaborations, "Prospects for Diffractive and Forward Physics at the LHC," *CERN/LHCC* **2006-039/G-124** (2006).

[146] C. M. G. Lattes, Y. Fujimoto, and S. Hasegawa, "Hadronic interactions of high-energy cosmic rays observed by emulsion chambers," *Phys. Rept.* **65** (1980) 151.

[147] J. D. Bjorken and L. D. McLerran, "Explosive Quark Matter and the 'Centauro' event," *Phys. Rev.* **D20** (1979) 2353.

[148] B. Mohanty and J. Serreau, "Disoriented chiral condensate: Theory and experiment," *Phys. Rept.* **414** (2005) 263–358, arXiv:hep-ph/0504154.

[149] **UA5** Collaboration, K. Alpgard et al., "Production of photons and search for Centauro events at the SPS collider," *Phys. Lett.* **B115** (1982) 71.

[150] **UA1** Collaboration, G. Arnison et al., "Search for Centauro-like events at the CERN proton-antiproton collider," *Phys. Lett.* **B122** (1983) 189.

[151] **MiniMax** Collaboration, J. D. Bjorken, "T864 (MiniMax): A search for disoriented chiral condensate at the Fermilab Collider," arXiv:hep-ph/9610379.

[152] **WA98** Collaboration, M. M. Aggarwal et al., "Search for disoriented chiral condensates in 158 AGeV Pb + Pb collisions," *Phys. Lett.* **B420** (1998) 169–179, arXiv:hep-ex/9710015.

[153] **NA49** Collaboration, H. Appelshauser et al., "Event-by-event fluctuations of average transverse momentum in central Pb + Pb collisions at 158 GeV per nucleon," *Phys. Lett.* **B459** (1999) 679–686, arXiv:hep-ex/9904014.

[154] **STAR** Collaboration, J. Adams et al., "Strangelet search at RHIC," arXiv:nucl-ex/0511047.

[155] E. Gladysz-Dziadus et al., "CASTOR: Centauro and strange object research in nucleus nucleus collisions at LHC," arXiv:hep-ex/0209008.

[156] **STAR** Collaboration, J. Adams et al., "Experimental and theoretical challenges in the search for the quark gluon plasma: The STAR collaboration's critical assessment of the evidence from RHIC collisions," *Nucl. Phys.* **A757** (2005) 102–183, arXiv:nucl-ex/0501009.

[157] C. Smith, "Event-by-Event Charged Multiplicity in Heavy-Ion Collisions with CMS Pixel Tracker," *CMS AN* **2003/015** (2003).

[158] "HIJING Web Site." Located at http://www-nsdth.lbl.gov/~xnwang/hijing/index.html.

[159] **PHOBOS** Collaboration, B. B. Back et al., "Charged-particle pseudorapidity density distributions from Au + Au collisions at s(NN)**(1/2) = 130-GeV," *Phys. Rev. Lett.* **87** (2001) 102303, arXiv:nucl-ex/0106006.

[160] G. Baur et al., "Heavy ion physics programme in CMS," *Eur. Phys. J.* **C 32 s02** (2003) 69. CMS-NOTE-2000-060.

[161] I. Damgov et al., "Heavy Ion Studies with CMS HF calorimeter," *CMS Note* **2001/055** (2001).

[162] "PYTHIA Web Site." Located at `http://www.thep.lu.se/tf2/staff/torbjorn/Pythia.html`.

[163] "HYDJET fast event generator." Located at `http://cern.ch/lokhtin/hydro/hydjet.html`.

[164] **ALICE** Collaboration, J. P. Revol, "Low-p_{T} Proton-Proton Physics at Low Luminosity at LHC," *Eur. Phys. J. direct* **C4S1** (2002) 14.

[165] C. Roland, "Track reconstruction in heavy ion events using the CMS tracker," *Nucl. Instrum. Meth.* **A566** (2006) 123–126. CERN-CMS-NOTE-2006-031.

[166] CMS Collaboration, "The TriDAS Project Technical Design Report, Volume 1: The Trigger Systems," *CERN/LHCC* **2000-38** (2000). CMS TDR 6.1.

[167] CMS Collaboration, "The TriDAS Project Technical Design Report, Volume 2: Data Acquisition and High-Level Trigger," *CERN/LHCC* **2002-26** (2002). CMS TDR 6.2.

[168] F. Sikler, "Reconstruction of low p_{T} charged particles with the pixel detector,". CMS Note AN-2006/100.

[169] F. Sikler, "Reconstruction of V0s and photon conversions with the pixel detector,". CMS Note AN-2006/101.

[170] F. Sikler, "Particle identification using energy loss in the pixel detector,". CMS Note in preparation.

[171] P. F. Kolb, U. W. Heinz, P. Huovinen, K. J. Eskola, and K. Tuominen, "Centrality dependence of multiplicity, transverse energy, and elliptic flow from hydrodynamics," *Nucl. Phys.* **A696** (2001) 197–215, `arXiv:hep-ph/0103234`.

[172] M. Gyulassy, I. Vitev, and X. N. Wang, "High p_{T} azimuthal asymmetry in noncentral A + A at RHIC," *Phys. Rev. Lett.* **86** (2001) 2537–2540, `arXiv:nucl-th/0012092`.

[173] **PHENIX** Collaboration, S. S. Adler, "A detailed study of high-p_{T} neutral pion suppression and azimuthal anisotropy in Au + Au collisions at s(NN)**(1/2) = 200-GeV," `arXiv:nucl-ex/0611007`.

[174] I. P. Lokhtin, S. V. Petrushanko, L. I. Sarycheva, and A. Snigirev, "Azimuthal anisotropy of jet quenching at LHC," *Pramana* **60** (2002) 1045–1050, `arXiv:hep-ph/0112180`.

[175] I. P. Lokhtin, S. V. Petrushanko, L. I. Sarycheva, and A. Snigirev, "Azimuthal asymmetry of jet production as a signal of parton energy losses in semicentral heavy-ion collisions," *Phys. Atom. Nucl.* **65** (2002) 943–952.

[176] A. M. Poskanzer and S. A. Voloshin, "Methods for analyzing anisotropic flow in relativistic nuclear collisions," *Phys. Rev.* **C58** (1998) 1671–1678, `arXiv:nucl-ex/9805001`.

[177] I. P. Lokhtin and A. M. Snigirev, "A model of jet quenching in ultrarelativistic heavy ion collisions and high-p_{T} hadron spectra at RHIC," *Eur. Phys. J.* **C45** (2006) 211–217, arXiv:hep-ph/0506189.

[178] CMS Collaboration, "The Hadron Calorimeter Technical Design Report," *CERN/LHCC* **97-031** (1997). CMS TDR 2.

[179] CMS Collaboration, "The Electromagnetic Calorimeter Technical Design Report," *CERN/LHCC* **97-033** (1997). CMS TDR 4, Addendum CERN/LHCC 2002-027.

[180] I. P. Lokhtin, S. V. Petrushanko, L. I. Sarycheva, and A. M. Snigirev, "Azimuthal anisotropy and jet quenching in heavy ion collisions with CMS calorimetry," *CMS Note* **2003/019** (2003).

[181] "OSCAR: CMS Simulation Package Home Page." http://cmsdoc.cern.ch/oscar.

[182] "ORCA: CMS Reconstruction Package." Site located at http://cmsdoc.cern.ch/orca.

[183] I. P. Lokhtin, L. I. Sarycheva, and A. M. Snigirev, "The method for analysing jet azimuthal anisotropy in ultrarelativistic heavy ion collisions," *Phys. Lett.* **B537** (2002) 261–267, arXiv:hep-ph/0203144. doi:10.1016/S0370-2693(02)01913-5.

[184] CMS Collaboration, "The Tracker Project Technical Design Report," *CERN/LHCC* **98-006** (1998). CMS TDR 5, Addendum CERN/LHCC 2000-016.

[185] G. Eyyubova et al., "Azimuthal Anisotropy in Heavy Ions Collisions with CMS Tracker," *CMS Analysis Note* **2007/004** (2007).

[186] N. Borghini, P. M. Dinh, and J.-Y. Ollitrault, "A new method for measuring azimuthal distributions in nucleus nucleus collisions," *Phys. Rev.* **C63** (2001) 054906, arXiv:nucl-th/0007063.

[187] N. Borghini, P. M. Dinh, and J.-Y. Ollitrault, "Flow analysis from multiparticle azimuthal correlations," *Phys. Rev.* **C64** (2001) 054901, arXiv:nucl-th/0105040.

[188] R. Mak, "Measurements of elliptic flow in ultrarelativistic heavy ion collisions," Master's thesis, University of Auckland, 2006.

[189] D. Krofcheck et al., "Simulations of Elliptic Flow in Heavy-Ion Collisions with the CMS Experiment at the LHC," *Quark Matter '06 poster Proceeds.* (2007).

[190] M. Ballintijn, C. Loizides, I. P. Lokhtin, K. Krajczar, C. Roland, A. M. Snigirev, and G. I. Veres, "Estimating the statistical reach for the charged particle nuclear modification factor in jet triggered heavy ion events," 2006. CMS AN-2006/109.

[191] M. Bedjidian and O. Kodolova, "Quarkonia measurements in heavy-ion collisions in CMS," *CMS Note* **2006/089** (2006).

[192] M. Ballintijn, C. Loizides, and G. Roland, "Studies of the High Level Trigger in CMS Pb+Pb running," 2006. CMS AN-2006/099.

[193] J. F. Gunion and R. Vogt, "Determining the existence and nature of the quark-gluon plasma by Υ suppression at the LHC," *Nucl. Phys.* **B492** (1997) 301–337, arXiv:hep-ph/9610420.

[194] **NA50** Collaboration, M. C. Abreu et al., "Observation of a threshold effect in the anomalous J/ψ suppression," *Phys. Lett.* **B450** (1999) 456–466.

[195] X.-N. Wang and M. Gyulassy, "HIJING: A Monte Carlo model for multiple jet production in p p, p A and A A collisions," *Phys. Rev.* **D44** (1991) 3501–3516.

[196] K. J. Eskola, V. J. Kolhinen, and C. A. Salgado, "The scale dependent nuclear effects in parton distributions for practical applications," *Eur. Phys. J.* **C9** (1999) 61–68, arXiv:hep-ph/9807297.

[197] O. Kodolova, M. Bedjidian, and S. Petrouchanko, "Dimuon reconstruction in heavy ion collisions using a detailed description of CMS geometry," *CMS Note* **1999-004** (1999).

[198] F. Gasparini, "A Study of Charged Particle Rates and Muon Backgrounds in the CMS Muon Chambers," *CMS Note* **1993/106** (1993).

[199] **ALICE** Collaboration, B. Alessandro et al., "ALICE: Physics performance report, volume II," *J. Phys.* **G32** (2006) 1295–2040.

[200] I. Kodolova and M. Bedjidian, "Quarkonia measurements in heavy-ion collisions in CMS," *CMS Analysis Note* **2006/089** (2006).

[201] **STAR** Collaboration, B. I. Abelev et al., "Identified baryon and meson distributions at large transverse momenta from Au + Au collisions at $\sqrt{s_{NN}}$ = 200 GeV," *Phys. Rev. Lett.* **97** (2006) 152301, arXiv:nucl-ex/0606003.

[202] **PHENIX** Collaboration, S. S. Adler et al., "Nuclear modification of electron spectra and implications for heavy quark energy loss in Au + Au collisions at $\sqrt{s_{NN}}$ = 200 GeV," *Phys. Rev. Lett.* **96** (2006) 032301, arXiv:nucl-ex/0510047.

[203] Y. L. Dokshitzer and D. E. Kharzeev, "Heavy quark colorimetry of QCD matter," *Phys. Lett.* **B519** (2001) 199–206, arXiv:hep-ph/0106202.

[204] Z.-W. Lin and R. Vogt, "Energy loss effects on heavy quark production in heavy-ion collisions at $\sqrt{s}$ = 5.5 ATeV," *Nucl. Phys.* **B544** (1999) 339–354, arXiv:hep-ph/9808214.

[205] I. P. Lokhtin and A. M. Snigirev, "Probing the medium-induced energy loss of bottom quarks by dimuon production in heavy ion collisions at LHC," *Eur. Phys. J.* **C21** (2001) 155–162, arXiv:hep-ph/0105244.

[206] I. P. Lokhtin and A. M. Snigirev, "High-mass dimuon and secondary J/ψ production at CMS as probes of medium-induced bottom quark energy loss in heavy-ion collisions," *CMS Note* **2001/008** (2001).

[207] I. P. Lokhtin, L. I. Sarycheva, A. M. Snigirev, and K. Y. Teplov, "Medium-modified fragmentation of b jets tagged by a leading muon in ultrarelativistic heavy ion collisions," *Eur. Phys. J.* **C37** (2004) 465–469, arXiv:hep-ph/0407109.

[208] **Particle Data Group** Collaboration, S. Eidelman et al., "Review of particle physics," *Phys. Lett.* **B592** (2004) 1. doi:10.1016/j.physletb.2004.06.001.

[209] "PYQUEN event generator." Located at http://cern.ch/lokhtin/pyquen.

[210] N. Borghini and U. A. Wiedemann, "Distorting the hump-backed plateau of jets with dense QCD matter," arXiv:hep-ph/0506218.

[211] **PHENIX** Collaboration, K. Adcox et al., "Centrality dependence of the high p_{T} charged hadron suppression in Au + Au collisions at $\sqrt{s_{NN}}$ = 130 GeV," *Phys. Lett.* **B561** (2003) 82–92, arXiv:nucl-ex/0207009.

[212] **STAR** Collaboration, J. Adams et al., "Evidence from d + Au measurements for final-state suppression of high p_{T} hadrons in Au + Au collisions at RHIC," *Phys. Rev. Lett.* **91** (2003) 072304, arXiv:nucl-ex/0306024.

[213] **PHENIX** Collaboration, S. S. Adler et al., "High-p_{T} charged hadron suppression in Au + Au collisions at $\sqrt{s_{NN}}$ = 200 GeV," *Phys. Rev.* **C69** (2004) 034910, arXiv:nucl-ex/0308006.

[214] **PHOBOS** Collaboration, B. B. Back et al., "Centrality dependence of charged hadron transverse momentum spectra in Au + Au collisions from $\sqrt{s_{NN}}$ = 62.4 GeV to 200 GeV," *Phys. Rev. Lett.* **94** (2005) 082304, arXiv:nucl-ex/0405003.

[215] O. Kodolova, I. Vardanian, A. Nikitenko, and A. Oulianov, "Algorithm for jet identification and reconstruction in densly populated calorimetric system,". CERN-CMS-NOTE-2006-050.

[216] **CMS** Collaboration, D. Acosta et al., "CMS Physics TDR Volume1, Section 10," *CERN/LHCC* **2006-001** (2006).

[217] **CDF** Collaboration, A. A. Affolder et al., "Measurement of the inclusive jet cross section in $\bar{p}p$ collisions at $\sqrt{s} = 1.8$ TeV," *Phys. Rev.* **D64** (2001) 032001, arXiv:hep-ph/0102074.

[218] N. Kruglov, L. Sarycheva, and I. Vardanyan, "Jet Finding Algorithms in Heavy Ion Collisions in CMS,". CERN-CMS-TECHNICAL-NOTE-1996-084.

[219] V. Gavrilov, O. Kodolova, A. Oulianov, and I. N. Vardanian, "Jet Reconstruction with Pileup Subtraction,". CERN-CMS-RAPID-NOTE-2003-004.

[220] M. Gyulassy, P. Levai, and I. Vitev, "Non-Abelian energy loss at finite opacity," *Phys. Rev. Lett.* **85** (2000) 5535–5538, arXiv:nucl-th/0005032.

[221] D. d'Enterria and C. Mironov, "Nucleon-nucleon reference spectrum for high-p_T inclusive charged hadron production in Pb+Pb collisions at $\sqrt{s_{NN}}$ = 5.5 TeV," 2006. CMS Note in preparation.

[222] I. P. Lokhtin and A. M. Snigirev, "Partonic energy loss in ultrarelativistic heavy ion collisions: Jet suppression versus jet fragmentation softening," *Phys. Lett.* **B567** (2003) 39–45, arXiv:hep-ph/0303121.

[223] F. Arleo et al., "Photon physics in heavy ion collisions at the LHC," arXiv:hep-ph/0311131.

[224] I. N. Vardanian, I. P. Lokhtin, L. I. Sarycheva, A. M. Snigirev, and C. Y. Teplov, "Modification of the jet fragmentation function for ultrarelativistic collisions of nuclei and its determination in the channel involving the production of a leading neutral pion," *Phys. Atom. Nucl.* **68** (2005) 332–339.

[225] V. Kartvelishvili, R. Kvatadze, and R. Shanidze, "On Z and Z + jet production in heavy ion collisions," *Phys. Lett.* **B356** (1995) 589–594, arXiv:hep-ph/9505418.

[226] M. van Leeuwen, "Quark Matter 2006: High-p_{T} and jets," arXiv:nucl-ex/0702011.

[227] X.-N. Wang, Z. Huang, and I. Sarcevic, "Jet quenching in the opposite direction of a tagged photon in high-energy heavy-ion collisions," *Phys. Rev. Lett.* **77** (1996) 231–234, arXiv:hep-ph/9605213.

[228] X.-N. Wang and Z. Huang, "Medium-induced parton energy loss in gamma + jet events of high-energy heavy-ion collisions," *Phys. Rev.* **C55** (1997) 3047–3061, arXiv:hep-ph/9701227.

[229] F. Arleo, "Photon-tagged correlations in heavy-ion collisions: Kinematic requirements and a case study," arXiv:hep-ph/0701207.

[230] I. P. Lokhtin and A. M. Snigirev, "Quenching of hard jets in viscous quark gluon plasma," *Phys. Atom. Nucl.* **60** (1997) 295–298.

[231] I. P. Lokhtin and A. M. Snigirev, "Probing the space-time evolution of hot parton matter by hard jets," *Z. Phys.* **C73** (1997) 315–320.

[232] P. Aurenche et al., "A critical phenomenological study of inclusive photon production in hadronic collisions," *Eur. Phys. J.* **C9** (1999) 107–119, arXiv:hep-ph/9811382.

[233] F. Arleo, "Hard pion and prompt photon at RHIC, from single to double inclusive production," *JHEP* **09** (2006) 015, arXiv:hep-ph/0601075.

[234] **CompHEP** Collaboration, E. Boos et al., "CompHEP 4.4: Automatic computations from Lagrangians to events," *Nucl. Instrum. Meth.* **A534** (2004) 250–259, arXiv:hep-ph/0403113.

[235] T. Sjöstrand, L. Lonnblad, S. Mrenna, and P. Skands, "PYTHIA 6.3: Physics and manual," arXiv:hep-ph/0308153.

[236] M. Cacciari, P. Nason, and R. Vogt, "QCD predictions for charm and bottom production at RHIC," *Phys. Rev. Lett.* **95** (2005) 122001, arXiv:hep-ph/0502203.

[237] M. L. Mangano, P. Nason, and G. Ridolfi, "Heavy quark correlations in hadron collisions at next-to- leading order," *Nucl. Phys.* **B373** (1992) 295–345.

[238] J. Pumplin et al., "New generation of parton distributions with uncertainties from global QCD analysis," *JHEP* **07** (2002) 012, arXiv:hep-ph/0201195.

[239] C. Peterson, D. Schlatter, I. Schmitt, and P. M. Zerwas, "Scaling Violations in Inclusive e^+e^- Annihilation Spectra," *Phys. Rev.* **D27** (1983) 105.

[240] **H1** Collaboration, A. Aktas et al., "Diffractive photoproduction of ρ mesons with large momentum transfer at HERA," *Phys. Lett.* **B638** (2006) 422–431, arXiv:hep-ex/0603038.

[241] L. Frankfurt, M. Strikman, and M. Zhalov, "Elastic and large t rapidity gap vector meson production in ultraperipheral proton ion collisions," *Phys. Lett.* **B640** (2006) 162–169, arXiv:hep-ph/0605160.

[242] L. Frankfurt, M. Strikman, and M. Zhalov, "Large t diffractive ρ-meson photoproduction with target dissociation in ultraperipheral p A and A A collisions at LHC," arXiv:hep-ph/0612072.

[243] J. Nystrand, "Electromagnetic interactions in nucleus nucleus and proton proton collisions," *Nucl. Phys.* **A752** (2005) 470–479, arXiv:hep-ph/0412096.

[244] S. R. Klein and J. Nystrand, "Photoproduction of quarkonium in proton proton and nucleus nucleus collisions," *Phys. Rev. Lett.* **92** (2004) 142003, arXiv:hep-ph/0311164.

[245] A. J. Baltz, S. R. Klein, and J. Nystrand, "Coherent vector meson photoproduction with nuclear breakup in relativistic heavy ion collisions," *Phys. Rev. Lett.* **89** (2002) 012301, arXiv:nucl-th/0205031.

[246] S. Klein and J. Nystrand, "Exclusive vector meson production in relativistic heavy ion collisions," *Phys. Rev.* **C60** (1999) 014903, arXiv:hep-ph/9902259.

[247] R. Vogt, "Heavy quark production in heavy ion colliders," *Heavy Ion Phys.* **18** (2003) 11–20, arXiv:hep-ph/0205330.

[248] P. Yepes, "Studying Light Objects in Ultra-Peripheral Heavy Ion Collisions," *CMS NOTE 2003/022* (2003).

[249] M. G. Ryskin, R. G. Roberts, A. D. Martin, and E. M. Levin, "Diffractive J/ψ photoproduction as a probe of the gluon density," *Z. Phys.* **C76** (1997) 231–239, arXiv:hep-ph/9511228.

[250] T. Teubner, "Diffractive production of vector mesons and the gluon at small x," *AIP Conf. Proc.* **792** (2005) 416–419.

[251] D. d'Enterria, "Hard spectra and QCD matter: Experimental review," *J. Phys.* **G30** (2004) S767–S774, arXiv:nucl-ex/0404018.

[252] M. Strikman, R. Vogt, and S. White, "Probing small x parton densities in ultraperipheral A A and p A collisions at the LHC," *Phys. Rev. Lett.* **96** (2006) 082001, arXiv:hep-ph/0508296.

[253] M. Strikman, M. Tverskoy, and M. Zhalov, "Neutron tagging of quasielastic J/ψ photoproduction off nucleus in ultraperipheral heavy ion collisions at RHIC energies," *Phys. Lett.* **B626** (2005) 72–79, arXiv:hep-ph/0505023.

[254] L. Frankfurt, V. Guzey, M. Strikman, and M. Zhalov, "Onset of perturbative color opacity at small x and Υ coherent photoproduction off heavy nuclei at LHC," *JHEP* **08** (2003) 043, arXiv:hep-ph/0304218.

[255] V. P. Goncalves and M. V. T. Machado, "Heavy quarks and meson production in ultraperipheral heavy ion collisions," arXiv:hep-ph/0601131.

[256] D. d'Enterria and A. Hees, "Measurement of $\Upsilon \to e^+e^-, \mu^+\mu^-$ in electromagnetic PbPb collisions at $\sqrt{s_{NN}}$ = 5.5 TeV in CMS," *CMS AN-2006/107* (2006).

[257] K. Piotrzkowski, "Tagging two-photon production at the LHC," *Phys. Rev.* **D63** (2001) 071502, arXiv:hep-ex/0009065.

[258] M. W. Krasny, J. Chwastowski, and K. Slowikowski, "Luminosity measurement method for LHC: The theoretical precision and the experimental challenges," arXiv:hep-ex/0610052.

[259] M. Klasen, "Hard photoproduction at HERA," arXiv:hep-ph/0702052.

[260] V. A. Khoze, A. D. Martin, and M. G. Ryskin, "Double-diffractive processes in high-resolution missing- mass experiments at the Tevatron," *Eur. Phys. J.* **C19** (2001) 477–483, arXiv:hep-ph/0011393.

[261] I. A. Pshenichnov, J. P. Bondorf, I. N. Mishustin, A. Ventura, and S. Masetti, "Mutual heavy ion dissociation in peripheral collisions at ultrarelativistic energies," *Phys. Rev.* **C64** (2001) 024903, arXiv:nucl-th/0101035.

[262] **Particle Data Group** Collaboration, W.-M. Yao et al., "Review of particle physics," *J. Phys.* **G33** (2006) 1–1232.

[263] M. Boonekamp et al. ATL-GEN-2004-001, March, 2004.

[264] **PHENIX** Collaboration, S. S. Adler et al., "Suppressed π^0 production at large transverse momentum in central Au + Au collisions at $\sqrt{s_{NN}}$ = 200 GeV," *Phys. Rev. Lett.* **91** (2003) 072301, arXiv:nucl-ex/0304022.

[265] S. Baffioni, C. Charlot, et al., "Electron Reconstruction in CMS," *CMS NOTE 2006/40* (2006).

[266] X.-f. Zhang and G. I. Fai, "Z0 production as a test of nuclear effects at the LHC," *Phys. Lett.* **B545** (2002) 91–96, arXiv:hep-ph/0205155.

[267] M. Arneodo, "Nuclear effects in structure functions," *Phys. Rept.* **240** (1994) 301–393.

[268] M. Cacciari and G. P. Salam, "Dispelling the N^3 myth for the k_{T} jet-finder," *Phys. Lett.* **B641** (2006) 57–61, arXiv:hep-ph/0512210.

[269] M. Cacciari, "FastJet: A code for fast k(t) clustering, and more," arXiv:hep-ph/0607071.

[270] P. Stankus, "Direct photon production in relativistic heavy-ion collisions," *Ann. Rev. Nucl. Part. Sci.* **55** (2005) 517.

[271] **PHENIX** Collaboration, S. S. Adler et al., "Common suppression pattern of η and π^0 mesons at high transverse momentum in Au + Au collisions at $\sqrt{s_{NN}}$ = 200 GeV," *Phys. Rev. Lett.* **96** (2006) 202301, arXiv:nucl-ex/0601037.

[272] **PHENIX** Collaboration, S. S. Adler et al., "Centrality dependence of direct photon production in $\sqrt{s_{NN}}$ = 200 eV Au + Au collisions," *Phys. Rev. Lett.* **94** (2005) 232301, arXiv:nucl-ex/0503003.

[273] **PHENIX** Collaboration, K. Adcox et al., "Centrality dependence of charged particle multiplicity in Au Au collisions at s(N N)**(1/2) = 130-GeV," *Phys. Rev. Lett.* **86** (2001) 3500–3505, arXiv:nucl-ex/0012008.

[274] T. Sjöstrand et al., "High-energy-physics event generation with PYTHIA 6.1," *Comput. Phys. Commun.* **135** (2001) 238–259. doi:10.1016/S0010-4655(00)00236-8.

[275] B. Andersson, G. Gustafson, and B. Soderberg, "A GENERAL MODEL FOR JET FRAGMENTATION," *Z. Phys.* **C20** (1983) 317.

[276] "LCG GENSER (Generator Services) subproject." Located at http://lcgapp.cern.ch/project/simu/generator/.

[277] M. K. Ballintijn, C. Loizides, et al., "HIROOT - tool for generator-level studies." Located at http://higweb.lns.mit.edu/hiroot.

[278] "ROOT : an Object Oriented Data Analysis Framework." Information available at http://root.cern.ch/.

[279] M. K. Ballintijn, C. Loizides, C. J. Reed, et al., "Tree Analysis Modules." Located at http://higweb.lns.mit.edu/tam.